

Seismic Vulnerability of Historical Structures
with the Discrete Element Method

by

Tommaso Pagnoni

Submitted to the Department of Civil and Environmental Engineering
in Partial Fulfillment of the Requirements for the Degree of

Doctor of Philosophy in Civil and Environmental Engineering

at the

Massachusetts Institute of Technology

February 2001

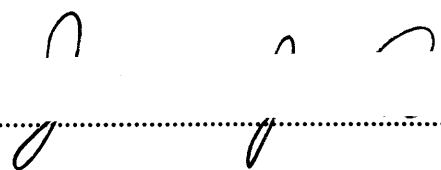
[February 2002]

© 2001 Massachusetts Institute of Technology
All rights reserved

Signature of Author 

Department of Civil and Environmental Engineering

January 12, 2001

Certified by 

Jerome J. Connor

Professor of Civil and Environmental Engineering

Thesis Supervisor

Accepted by 

Oral Buyukozturk

Chairman, Departmental Committee on Graduate Students

MASSACHUSETTS INSTITUTE
OF TECHNOLOGY

FEB 22 2001

ENG

Seismic Vulnerability of Historical Structures with the Discrete Element Method

by

Tommaso Pagnoni

Submitted to the Department of Civil and Environmental Engineering
on January 12, 2001, in Partial Fulfillment of the Requirements for the Degree of
Doctor of Philosophy in Civil and Environmental Engineering

ABSTRACT

It is widely recognized that historical structures represent a cultural heritage which should be preserved and transmitted to future generations. In several countries, and particularly, in the Mediterranean area, where a large number of important monuments are exposed to seismic hazard, there is a growing interest for the problem of strengthening such structures in order to reduce their seismic vulnerability, while preserving their original architectural integrity. However the seismic vulnerability assessment of historical block structures is still a challenging task.

In this work, after having explored the potentials and limitations of the Discrete Element Method for this type of problem, a new joint model for the quasistatic analysis of block structures is proposed. It accounts for (a) the non coplanarity of the contact surfaces, and (b) friction softening. The new model allowed a more accurate prediction of the in-plane failure load and corresponding failure mechanism of *opus quadratum* walls (walls made of regular squared blocks without mortar). In particular it predicts the development of progressive internal displacements, and the formation of localized sliding band as observed in the experimental models. Such results confirm that even apparently negligible joint imperfections should not be ignored since they may cause significant modifications in the response of a block structure subjected to gravity and lateral loading.

Thesis Supervisor: Prof. Jerome J. Connor

Title: Professor of Civil and Environmental Engineering

ACKNOWLEDGMENTS

I wish to express my sincere gratitude to Prof. J. Connor, Prof. D. Veneziano, Prof. A. Whittle, Prof. O. Buyukozturk and Prof. E. Kausel for their invaluable support and guidance throughout the duration of the thesis.

I would like, also, to thank Prof. P. Pinto for his precious guidance and support during my work at the University of Rome.

Table of Contents (summary)

1. INTRODUCTION

2. A SURVEY OF HISTORICAL STRUCTURES

3. REVIEW OF STATIC ANALYSIS METHODS FOR BLOCK STRUCTURES

4. REVIEW OF DYNAMIC ANALYSIS METHODS FOR BLOCK STRUCTURES

5. QUASISTATIC ANALYSIS OF BLOCK STRUCTURES WITH CURRENT D.E.M.

6. DYNAMIC ANALYSIS OF BLOCK STRUCTURES WITH CURRENT D.E.M.

7. A NEW JOINT MODEL FOR D.E. ANALYSIS OF HISTORICAL BLOCK STRUCTURES

8. CONCLUSION

9. RECOMMENDATIONS

APPENDIX A: OUT-OF-PLANE BEHAVIOR OF HISTORICAL MASONRY WALLS

APPENDIX B: IN-PLANE BEHAVIOR OF HISTORICAL MASONRY WALLS

REFERENCES

Table of Contents

1. INTRODUCTION, 13
1.1 DEFINITION OF PROBLEM, 13
1.2 FOCUS OF THE RESEARCH, 14
1.3 OVERVIEW, 15
2. A SURVEY OF HISTORICAL STRUCTURES, 19
2.1. MASONRY WALLS, 20
2.2. BLOCK STRUCTURES, 44
3. REVIEW OF STATIC ANALYSIS METHODS FOR BLOCK STRUCTURES, 71
3.1. RIGID CONTACT MODELS, 73
3.1.1. Limit Analysis and Mathematic Programming, 73
3.1.2. Livesley Model, 82
3.1.3. Lo Bianco-Mazzarella Model, 83
3.2. DEFORMABLE CONTACT MODELS, 88
3.2.1. Gap Elements, 89
4. REVIEW OF DYNAMIC ANALYSIS METHODS FOR BLOCK STRUCTURES, 91
4.1. RIGID CONTACT MODELS, 92
4.1.1. Milne's Studies, 95
4.1.2. Perry Model, 96
4.1.3. The Housner Model, 100
4.2. DEFORMABLE CONTACT MODELS, 104
4.2.1. The Angotti-Toni Model, 105
4.3. THE DISCRETE ELEMENT METHOD, 108
5. QUASISTATIC ANALYSIS OF BLOCK STRUCTURES WITH CURRENT D.E.M., 111
5.1. SEISMIC RESPONSE OF ANCIENT MASONRY BUILDINGS, 115
5.2. EXPERIMENTAL TESTS ON SMALL SCALE WALL MODELS, 120
5.2.1. In-plane failure tests of 3 small scale wall models, 121
5.2.2. Measure of friction parameters, 126
5.3. D.E.M. MODELING OF THE QUASISTATIC BEHAVIOR OF BLOCK STRUCTURES, 143

5.3.1. Modeling,	143
5.3.2. Validation of the analysis procedure,	146
5.3.3. Parametric study of model sensitivity,	149
5.3.4. Discrete Element simulation of the experimental tests,	151
5.4. CONCLUSION,	154
6. DYNAMIC ANALYSIS OF BLOCK STRUCTURES WITH CURRENT D.E.M.,	157
6.1. SINGLE BLOCK D.E.M. MODELING,	160
6.2. MULTIPLE BLOCK D.E.M. MODELING,	161
6.2.1. Harmonic Oscillations,	161
6.2.2. Seismic Oscillations,	164
6.2.2.1. Shaking Table Tests,	164
6.2.2.2. Numerical Simulations,	171
6.3. CONCLUSION,	176
7. A NEW JOINT MODEL FOR D.E. ANALYSIS OF HISTORICAL BLOCK STRUCTURES,	179
7.1. CRITICAL EVALUATION OF CURRENT DEM RESULTS,	182
7.2. FORMULATION OF A NON COPLANAR JOINT MODEL,	183
7.2.1. Experimental observations of out-of-plane wall failure,	187
7.2.2. Interpretation of experimental results,	190
7.2.3. The non coplanar joint model,	198
7.3. IMPLEMENTATION AND VERIFICATION,	198
7.3.1. Definition of polygonal joint reference base,	198
7.3.2. Modified DE solution algorithm,	200
7.3.3. Verification analyses,	203
7.4. SENSITIVITY ANALYSIS AND CALIBRATION,	225
7.4.1. Sensitivity with respect to joint geometry,	226
7.4.2. Sensitivity with respect to number of blocks,	233
7.4.2.1. Instability of a block column due to contact non coplanarity,	236
7.5. APPLICATIONS,	241
7.5.1. 14-block case,	243
7.5.1.1. 14-block case with planar joint model,	243
7.5.1.2. 14-block case with non coplanar joint model,	249
7.5.2. 21-block case,	257
7.5.3. 110-block case,	261

- 7.5.4. 231-block case, 265
- 7.5.5. Assessment of friction softening, 268
- 7.6. CONCLUSION, 272

8. CONCLUSION, 277

9. RECOMMENDATIONS, 283

APPENDIX A: OUT-OF-PLANE BEHAVIOR OF HISTORICAL MASONRY WALLS, 285

- A1. BACKGROUND, 286
- A2. THE OUT-OF-PLANE MODEL, 289
- A3. NUMERICAL ANALYSES, 300
- A4. DISCUSSION OF RESULTS, 306
- A5. CONCLUSIONS, 311

APPENDIX B: IN-PLANE BEHAVIOR OF HISTORICAL MASONRY WALLS, 313

- B1. BACKGROUND, 314
- B2. EXPERIMENTAL INVESTIGATION, 316
- B3. NUMERICAL ANALYSIS, 322
- B4. DISCUSSION OF RESULTS, 324
- B5. CONCLUSION, 330

REFERENCES, 333

1. INTRODUCTION

1.1 DEFINITION OF PROBLEM

It is widely recognized that historical structures represent a cultural heritage which should be preserved and transmitted to future generations. In several countries, and particularly, in the Mediterranean area, where a large number of important monuments are exposed to seismic hazard, there is a growing interest in the problem of strengthening such structures in order to reduce their seismic vulnerability (see for example the Proceedings of the US-Italy Workshop on Guidelines for Seismic Evaluation and Rehabilitation of Unreinforced Masonry Buildings [Abrams D.P., 1994], and the recent guidelines for evaluating the seismic vulnerability of historical masonry buildings in [Applied Technology Council, 1999]). In designing these interventions, a constraint, which is often undervalued, is the requirements of preserving, whenever it is possible, the architectural and structural integrity of the original construction. Consequently, the interventions should be respectful of the traditional construction techniques and strictly kept to the minimum necessary to ensure the required level of safety [Giuffrè, A., 1994].

To this respect, two problems unavoidably arise: (a) firstly, the modern engineer having lost the empirical knowledge of traditional building techniques, is unprepared to understand the intentions of the ancient builders, and therefore difficulties may arise in understanding the presence, or the absence, of those structural provisions which may be beneficial to an acceptable mechanical response; (b) secondly the methods of structural analysis which have been developed for modern constructions - essentially based on continuum mechanics - are generally inadequate for studying the response of inherently discontinuous structures such as the majority of the historical constructions. The consequence of this lack of knowledge is a tendency to replace, rather than improve, the original structure with a great loss in the cultural value associated to the integrity of the monument.

In this work an attempt is made to overcome the two problems mentioned above by proposing an innovative method of analysis which may be used for both (a) improving the basic understanding of block structure behavior under earthquake action, and, (b) assessing the seismic vulnerability of specific monuments.

1.2 FOCUS OF THE RESEARCH

In the following we will consider mainly those structures where the blocks or bricks interact among themselves only through frictional contacts, therefore masonry walls with mortar are beyond the scope of this work. In addition, given the low stress level generally found in historical structures, material failure of the single units is disregarded, while emphasis is placed on the failure mechanisms due to loss of equilibrium induced by large rotations and displacements of the units.

It is recognized that this problem is still a challenging task: the opening and closure of the joints, and the sliding and rotation of the single blocks determine a complex nonlinear response which is not fully described by existing analysis methods. Finite elements models with both smeared and localized cracks have been developed for masonry ([Kelly, T., 1996], [Mamaghani, 1999]). However, since they are primarily based on continuum formulations, their numerical effectiveness strongly decreases when the system approaches failure and a large number of openings, closures, and sliding take place. Limit analysis has also been used to study the stability of block structures ([Livesley, 1992], [Baggio, 2000]): it accounts for separations of blocks and Coulomb friction, but, in addition to the numerical problems which are often encountered when the number of element increases, it is restricted to static equilibrium problems. The dynamic behavior of a single block sliding and rocking on its foundation has been the object of several researches (see for a review of recent studies [Sinopoli, 1998]), however very limited work is available on the dynamic response of multiple block systems and furthermore it is mainly restricted to predefined structural typologies such as the multi-block column or the trilite ([Manos, 1994], [Wilson, 1999]).

The objective of this work is to provide a more general and realistic modeling of the seismic behavior of complex block structures. The Discrete Element Method (DEM), which has been developed in the field of rock mechanics, and employed in various problems of dynamic interaction of multiple bodies, appears appropriate for overcoming the previously mentioned limitations. In the first part of the study, the DEM is evaluated by comparing the numerical simulations with a series of experimental tests on small scale model of block structures. Subsequently, in order to overcome certain observed discrepancies between experimental and numerical results, a new joint model for the DE analysis of historical block structures will be developed.

1.3 OVERVIEW

In chapter 2 a brief review of some significant examples of historical constructions is presented. Despite the great variety of building techniques, depending from the geographical location and historical period, the use of stone blocks for important constructions has been extensive, as documented in a series of figures illustrating the various types of masonry and block structures. In chapters 3 and 4 a critical review of the analysis methods currently used for the study of the static and dynamic response to seismic actions of block structures is presented.

Chapters 5 and 6 are devoted to the exploration of the potential and limitations of the current DEM to, respectively, the quasistatic and dynamic analysis of historical block structures subjected to seismic actions. Subsequently, in chapter 7, a new DE joint model will be proposed for overcoming the observed limitations.

More specifically, chapter 5, focuses on the performance of the DEM for the prediction of the mechanical response of *opus quadratum* walls (regular masonry of

squared stone with no mortar)¹, subjected to slowly increasing in-plane lateral forces simulating the seismic actions.

First, as described in section 5.2, a series of experimental tests on 3 small scale wall models have been performed in order to obtain data (not available in the literature) on the in-plane failure of opus quadratum walls subjected to quasistatic loading. Tests on the friction behavior of the specific type of stone blocks used in the wall models (including the dependency of the friction coefficient with: (a) the normal contact force, (b) the degradation of the contact surfaces, and (c) the sliding velocity), were also performed with the objective of evaluating the friction parameters to be used in the DE simulations.

Subsequently, in section 5.3, the DE analysis of opus quadratum walls subjected to quasistatic in-plane lateral forces is presented. After a series of DE analyses were executed for evaluating the sensitivity of the response with respect to various model parameters, the DE simulations of the experimental tests on the 3 small scale wall models (illustrated in section 5.2) were performed. The DE predictions compared well with "exact" limit analysis results. However a number of discrepancies were observed with respect to the experimental data. It appeared that such differences could be attributed to the presence of geometrical imperfections in the experimental model which are not considered either in the limit analysis or in the DE model.

For the dynamic case, which is discussed in chapter 6, the main additional difficulty with respect to the quasistatic case lies in the appropriate prediction of the energy loss at the impact among blocks. In reality, energy dissipation is associated to friction and internal material damping, and a realistic prediction of such phenomena even for the simplest case of 2 impacting blocks would require a very complex numerical model. For a block system of realistic size, such an approach becomes practically impossible. An attempt has been made, in the context of the DEM, to model the internal material damping with a lumped viscous element acting at the interface between the

¹ A survey of historical structures including opus quadratum walls is illustrated in Chapter 2.

blocks, and retaining a simple representation of the block interior. For the case of rocking of a slender block on a rigid base, an empirical expression for the parameter of the viscous element has been obtained by minimizing errors of predicted restitution ratios with respect to “exact” values obtained with the Housner model. Good agreement with experimental results has been found for a range of slenderness ratios (from 2 to 5). Using the same parameter, acceptable agreement with experimental results has also been found for the case of harmonic base shaking of the single block. For a case of a multibody arch structure subjected to ground shaking, the same viscous parameter obtained for the case of a single block has been assumed. A reasonable agreement was found with experimental results, however it was noted that for this particular case the system response was dominated by the rocking of the two columns, which, as previously reported, is well described by this model.

Based on the evaluation of the applicability of the DEM to the study of block structures presented in chapters 5 and 6, it appears that the quasistatic approach is promising even if a number of discrepancies in the response prediction have been observed and need to be resolved. In the more complex dynamic case a strong assumption is made in the representation of the damping at impact, and while it may be acceptable for single block structures or for certain types of multibody systems, additional work is needed for defining a more general interface dissipation mechanism. Since the problems identified in the quasistatic analyses will have an impact also on the dynamic case it was decided to approach them.

Based on various experimental observations it appeared that the microrotations due to the non coplanarity of the contacts may play an important role in explaining the observed discrepancies. Consequently the development of a new joint model for the DE analysis of historical block structures was undertaken. In chapter 7 the formulation, implementation and verification of the model are described. A series of DEM analyses of various block structures were carried out, and the results demonstrate that a substantial improvement of the DEM predictions is possible with the proposed joint model.

Chapter 2. A SURVEY OF HISTORICAL STRUCTURES

2.1 MASONRY WALLS

2.2 BLOCK STRUCTURES

2. A SURVEY OF HISTORICAL STRUCTURES

The objective of this survey is to illustrate the relevance and variety of the monumental structures in which the main interaction mechanism among their components is essentially friction. As already noted the types of masonry with mortar are not addressed by the proposed DEM procedure and are reported here only for completeness. First, various types of masonry walls are presented, and later some significant example of block structures are illustrated.

2.1 MASONRY WALLS

A study, however brief, of ancient masonries immediately brings out the great variety of construction techniques, owing both to the evolution in time of the technologies for working materials, and to the various geographic contexts considered. It is however possible, and very convenient for the purposes of clarity of explanation, to classify them chronologically and, then, typologically.

THE ARCHAIC AND CLASSICAL PERIOD

The various masonry typologies of this period, even if there are variations, may be grouped into three main categories, which differ from each other substantially:

- masonry structures composed of large stone blocks;
- masonry structures having an opus caementicium core;
- masonry mixed structures.

MASONRY STRUCTURES COMPOSED OF LARGE STONE BLOCKS

These may be classified into structures having *polygonal blocks*, and structures built of squared stones.

Polygonal-block structures (opus siliceum).

This kind of masonry is certainly to be considered among the most widespread construction techniques in continental Greece, especially in Attica, the Peloponnese, and Acharnaia, from the 5th through the 3rd centuries BC. It can also be often traced in the pre-Roman Italic culture between the end of the 6th and the 1st centuries BC, used mainly to build city walls. The blocks used, of considerable size, are cut more or less carefully and are set without the use of mortar. It is just the accuracy of the working, which improved as time passed, that makes it possible to classify the various kinds of polygonal-block structures.

- *Formless masses*. This kind of masonry (6th century BC) displays crude masses set run-of-the-mine fashion, with interstices of considerable size, closed rather approximately using small-size stones (Figure 2-1).

- *Irregular polygons*. In this kind of masonry (5th-4th centuries BC) the blocks are only roughly hewn, the outside face is not worked, and the resulting cracks are carefully closed with stone chips (Figure 2-2).

- *Regular polygons*. In this kind of masonry (4th through last part of the 2nd century BC) the blocks are cut with great precision, so that the connections perfectly meet. The outside surface of the blocks is smoothed (Figure 2-3).

- *Trapezium-style*. In this kind of masonry (3rd through 1st centuries BC) the parallelism of the two sides of the blocks produces the tendency to form more or less obvious horizontal lays (Figure 2-4).

Squared-block structures (opus quadratum).

This typology differs from the preceding in that the blocks are worked to form regular parallopipeds, so that they are assembled to form horizontal courses. As for the polygonal structures, the connection between the blocks is made dry, i.e. without mortar. The main areas in which opus quadratum is to be found are Greece and Magna Graecia, where it was used for monumental architecture and, after the 5th century, for city walls (Figure 2-5), and Etruria, where, starting from archaic times, tuff was in widespread use as the raw material (Figure 2-6). With the Hellenistic age the squared-block structure was introduced into Roman monumental architecture (Figure 2-7, Figure 2-8, Figure 2-9). It has been observed, apropos the polygonal-block structure, that the evolution of the technique coincided with an ever more accurate working of the stones: from this standpoint it is therefore legitimate to see in the squared blocks a natural development of the polygonal stones, subjected to a gradual process of regularization that generated not just perfect stability for the individual elements, but also a very different esthetic harmony. The aspect of the opus quadratum masonry varies considerably depending on the arrangement of the stones, which may be set headwise -- the so-called *diatoni* -- or along their lengths, *orthostats*. There may be courses made up of diatoni and orthostats alternating according to a certain scheme, or courses of diatoni only with superposed orthostats only (Figure 2-10).



Figure 2-1. Cori, wall [Marta R., 1987].



Figure 2-2. Amelia, wall [Marta R., 1987].



Figure 2-3. Palestrina, Sanctuary of Fortune [Marta R., 1987].



Figure 2-4. Poggio Mirteto, villa [Marta R., 1987].

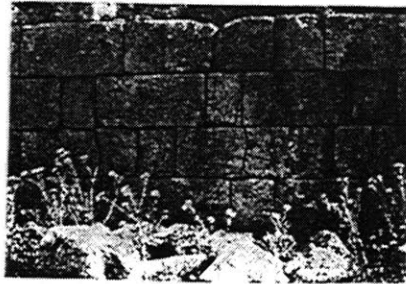


Figure 2-5. Selimunte, wall [Marta R., 1987].



Figure 2-6. Fiesole, wall [Marta R., 1987].



Figure 2-7 - Rome (Viminale), the “Servian” walls [Adam J.P., 1984].

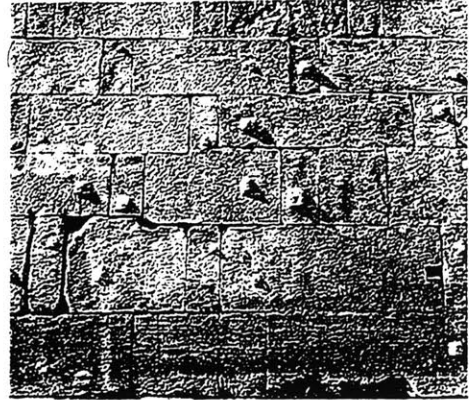


Figure 2-8 - Rome, Appian gate [Adam J.P., 1984].

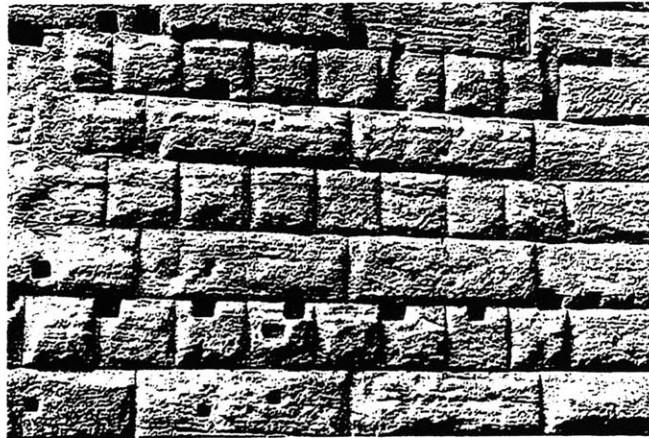


Figure 2-9 - Rome, forum of Augustus [Adam J.P., 1984].

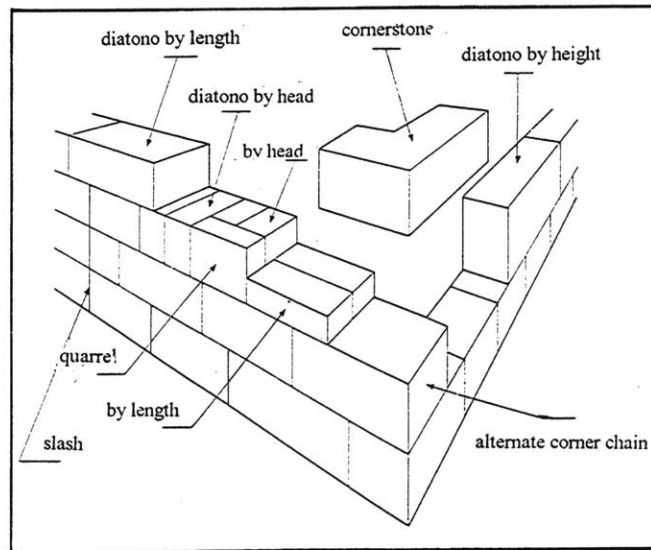


Figure 2-10 - Opus quadratum, arrangement of the stones [Adam J.P., 1984].

In structures of Roman age, six main periods may be identified, depending on the materials used and on the dimensions of the blocks.

- *Period I*, from 754 to 390 BC: the blocks are in cappellaccio and are set in alternating courses of diatoni and orthostats. The height of each course is around 29 cm (Figure 2-11).

- *Period II*, from 390 to 210 BC: the main materials are tuff and black scoria, and porous yellow tuff; course height reaches 61 cm (Figure 2-12).

- *Period III*, from 210 to 121 BC: the 59 cm high blocks are of peperino (volcanic) stone, of sperone stone, and of tuff from the Anio river (Figure 2-13).

- *Period IV*, from 121 to 36 BC: this sees the union of opus quadratum and opus caementicium, together with the introduction of travertine marble (Figure 2-14).

- *Period V*, from 36 BC to 41 AD: the most-used material is Lunae marble. The blocks are used either as the cladding for concrete walls, or by themselves (Figure 2-15).

- *Period VI*, from 41 to 68 AD: the prevalent use of rustic travertine is observed (Figure 2-16).

After the end of the first century AD the use of opus quadratum was limited exclusively to the construction of bearing structures.



Figure 2-11 - Rome, base of Temple of Juppiter [Marta R., 1987].



Figure 2-12 - Civita Castellana, via Flaminia [Marta R., 1987].



Figure 2-13 - Rome, Tullianum, lower room [Marta R., 1987].

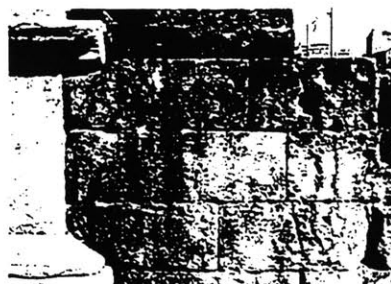


Figure 2-14 - Rome, Temple of Portunno [Marta R., 1987].



Figure 2-15 - Rome, wall of forum of Augustus [Marta R., 1987].



Figure 2-16 - Rome, Templum Divi Claudi [Marta R., 1987].

MASONRY STRUCTURES WITH AN OPUS CAEMENTICIUM CORE

This category of masonry structure includes various typologies, all featuring a central core, built of concrete, enclosed between two facings. The type was commonly called the "sack wall".

The concrete was made up of stone fragments, the *caementa*, with a binder of lime and sand (or preferably pozzolana) mortar. The *caementa* comprises stones and stone fragments. The mortar was made up of three parts of pozzolana and one of slaked lime, or else of two parts of river sand and one of slaked lime (Figure 2-17).

The masonry technique calling for an opus caementicium core was developed around the end of the 3rd century BC in Latium and in the Campania region, and its economy brought about its very rapid dissemination throughout the whole Roman world. Depending on the type of face, generally built of elements of small size bonded with mortar, numerous variations of this kind of structure can be distinguished: *opus incertum*, *opus quasi reticulatum*, *opus reticulatum*, *opus vittatum* and *opus testaceum*.

Opus incertum.

The facing is made up of stone elements of irregular shape and size (Figure 2-18); in its most ancient form it was made up of the opus caementicium wall itself, left fair face. Chronologically it appeared in Rome starting from the 2nd century BC.

Opus quasi reticulatum and Opus reticulatum.

Opus reticulatum is nothing else than the final stage of transformation and regularization of opus incertum, through the intermediate phase of opus quasi reticulatum. In this latter the blocks of stone, called *cubilia*, display various forms, the inclination being toward irregular laying and large amounts of mortar (Figure 2-19). The adoption of pyramidal blocks of tuff, all equal, set with the base to form the facade and in regular courses with the sides inclined at 45 degrees to the horizontal, forms the passage to opus reticulatum, which was the most widespread technique in Rome for around one century, starting from 55 BC (Figure 2-20).

Opus vittatum

This involves the laying of simple quadrangular stone blocks of small size in horizontal courses all of the same depth (Figure 2-21). This masonry technique did not start its spread into Rome and its immediate suburbs until the 2nd century AD. Its use was interrupted during the Antonine age, but it reappeared under Maxentius (307-312). In Gaul this technique was in very widespread use.

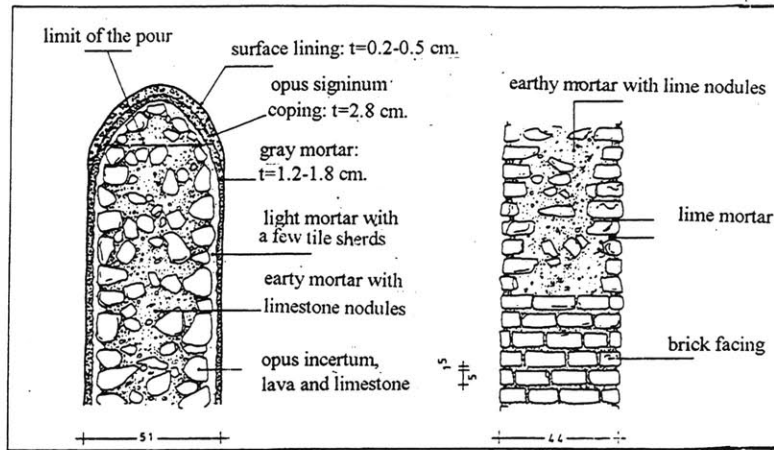


Figure 2-17 - Pompeii, street of Sepulchres [Adam J.P., 1984].



Figure 2-18 - Palestrina, Sanctuary of Fortuna Primigenia [Adam J.P., 1984].

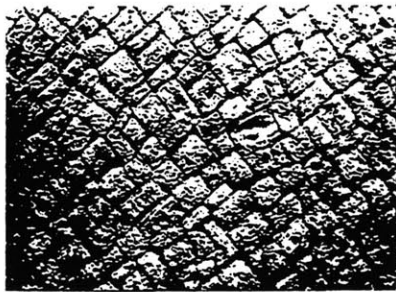


Figure 2-19 - Sepino, city walls [Marta R., 1987].



Figure 2-20 - Rome, mausoleum of Augustus [Marta R., 1987].

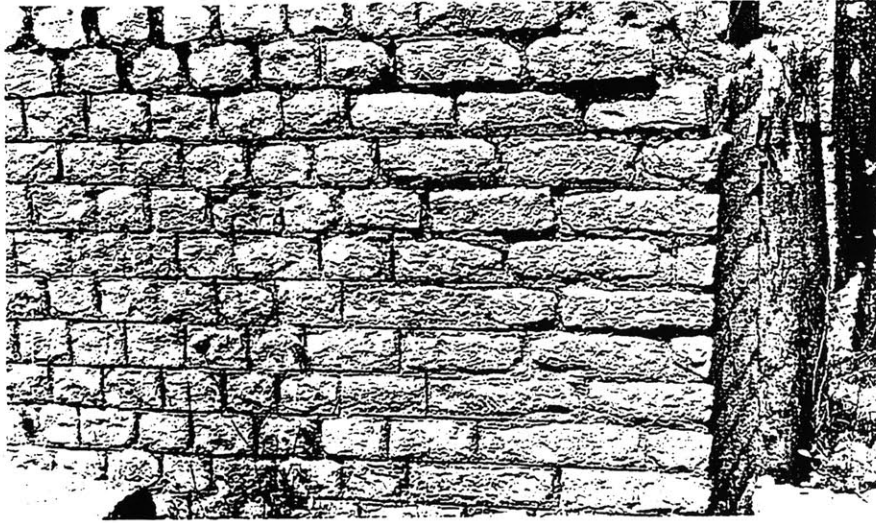


Figure 2-21 - St. Marcel, theatre of Argentomagus [Adam J.P., 1984].

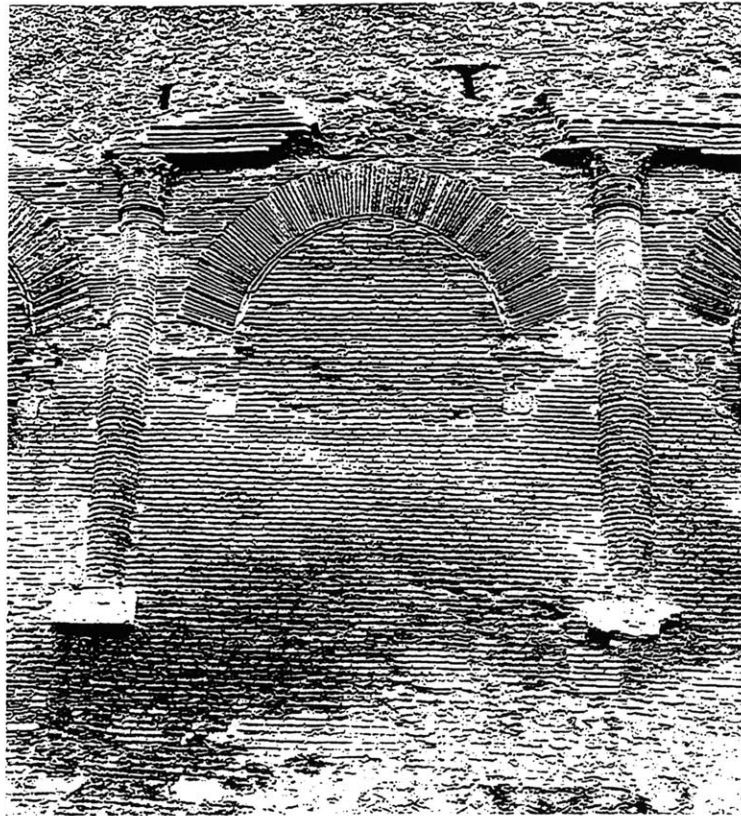


Figure 2-22 - Rome, Castrensian amphitheatre [Adam J.P., 1984].

Opus testaceum.

In this case the face of the opus caementicium was formed of fired bricks (Figure 2-22). The brick was in extremely widespread use in the Roman world owing to its economy and to the simplicity of its laying relative to stone materials, for example. This technique appeared around the middle of the 1st century BC with the use of bricks presenting a depth that continually decreased down to the start of the 3rd century, it then growing again down to Constantine. The brick curtain walls were clad with plaster and this made it possible to tolerate slight non-uniformities in the sizes and colors of the bricks. The fair-face masonry walls, however, were built with more care, using lower-depth bricks having more regular dimensions. Very rarely in Roman building construction were crude bricks used to build walls wholly of brick, that is, without the opus caementicium core, they being called opus latericium. The remains of such are found in constructions dating to the first century of the empire, especially in structures featuring military architecture.

MIXED STRUCTURE MASONRY

These may be classified into *checkerboard*, *frame* and *grating*.

Checkerboard structures

In the masonry structures described to this point the blocks displayed dimensional uniformity within the various typologies: that is, elements exclusively of large size were used in the polygonal and squared-stone structures, and elements of small size were used in the structures having an opus caementicium core. The special feature of the checkerboard structures consists instead just in the joint use of stones of strongly differing dimensions. Their arrangement called for the alternation of large squared blocks with, as filler, stones of small size (Figure 2-23). The large blocks always bear one on the other, acting as the bearing elements. The stone filler could be removed without jeopardizing the building's stability in any way.

Frame structures (Opus africanum)

The area in which this typology was most widespread, as the name indicates, was North Africa, and examples of it have been found in Sicily too, where it was imported by the Carthaginians. In this case too, as in the checkerboard structures, there is a mingling of elements of very different dimensions. The idea of the frame is suggested by the arrangement of the larger stone blocks, which form vertical supports in which stones of vertical and horizontal development alternate (Figure 2-24). These supports form the bearing elements of the wall, connected together by horizontal files of smaller stones.

Finally, this is a technique that calls for the separation of the functions, identifying, that is, within the whole of the wall a bearing frame and a curtain filler.

Grating structures (Opus craticium)

This is certainly the mixed-structure typology in most widespread use, even if its archaeological vestiges are few, just because of the perishableness of the materials used. The basic idea is still that of the frame structure, with the difference that in this case the framing is of wood (a material easily found in Italy at the time, unlike Africa). The filling was stones and cement, the whole then being plastered (Figure 2-25, Figure 2-26). Characteristics of the walls in opus craticium were the possibility of obtaining low thicknesses (20 cm) and lightness, to the detriment, however, of its strength, which was low.

THE MEDIAEVAL PERIOD

During this period the masonries can also be classified to facilitate their recognition. The main typologies that can be traced follow closely in the footsteps of those analyzed for the Roman period, confirming a more or less accentuated continuity in construction techniques¹. The categories analyzed are as follows:

- masonry structures composed of blocks;
- masonry structures of cement concrete;
- masonry special structures.

¹ In the analysis of mediaeval masonry, owing to the many typological variations to be found, the attention has been focussed on Rome and Latium.



Figure 2-23 - Velia, wall
[Adam J.P., 1984].

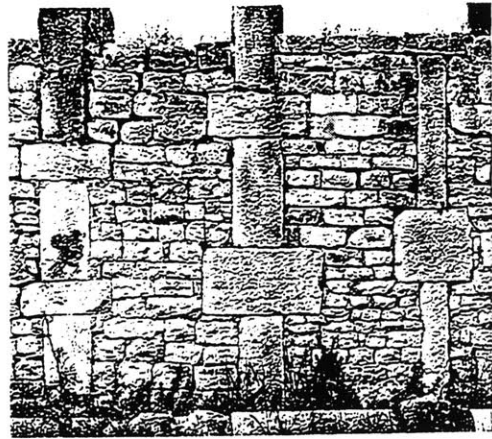


Figure 2-24 - Douggia (Tunisia)
[Adam J.P., 1984].

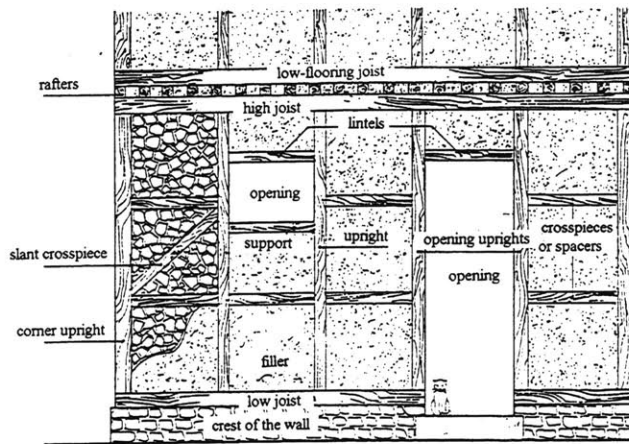


Figure 2-25 - Frame structure [Adam J.P., 1984].

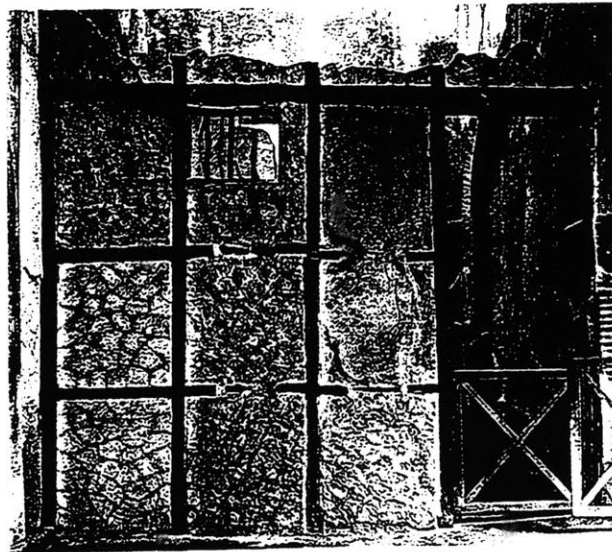


Figure 2-26 - Herculaneum, College of Augustali [Adam J.P., 1984].

STRUCTURES MADE UP OF BLOCKS

Stone masonry

This substantially derives from the reuse of the large blocks used in the previous classical Roman construction. The reference model is opus quadratum, but the masonry system resulting almost never displays either regularity or expertness in the arrangement of the blocks. Irregularities are found both in the dimensions of the materials used and in the techniques of working and laying them. On the wall face there are visible cavities filled with cement mortar, bricks, stones, etc. (Figure 2-27).

Brick masonry

The masonry derives from the classical Roman opus testaceum and the masonry walls are made using bricks coming from stores or from occasional reserve supplies. One consequence of this practice is that the material available is non-uniform in dimensions and color, so that glaring increases in the depth of the mortar beds are required. The passing of the centuries saw an ever more accentuated deterioration in the materials and, most especially, in their laying, assigned to workmen who were ever less qualified. In particular in the 8th, 9th and 10th centuries that obvious deterioration is noted that takes the form of out-of-plumbs, swellings and undulations visible on the surfaces. The mortar depths are quite variable (Figure 2-28, Figure 2-29).

Striped-work masonry

This is characterized by the alternation of courses of bricks and of parallelepipedal blocks of tuff or similar stone. Its origin may be traced to the Roman *opus vittatum* and its use was limited relative to brick-only masonry. The number of courses of brick and stone varies and depends on the availability of the materials. The masonry systems built display a workmanship that varies depending on the capabilities of the workmen. In most cases there is an alternation of one or two courses of bricks and one or two of tuff, but in some cases it reaches four or five courses (Figure 2-30).

Masonry with tuff blocks ("tuffelli")

Masonry facings built of tuff blocks were seen in Rome as far back as the Republic. During the period of the empire this facing displayed an elegant weave, owing to the proper squaring of the elements and therefore to the regularity of the mortar beds. During the mediaeval period, then, the tuffelli masonry was not an innovation; at first the tuffelli were well cut and the mortar joints were finished with flush plastering (Figure 2-31). As times became harder economically speaking there was a deterioration in technique: the tuffelli became less well finished and the mortar beds, without flush plastering, had less care taken with their depths (Figure 2-32). At the start of the 15th century these walls were made up with pieces that were vaguely squared and of various dimensions, utilizing, together with tuff, salvaged materials and brick fragments. The frequent use of tuffelli can be explained by noting a number of factors:

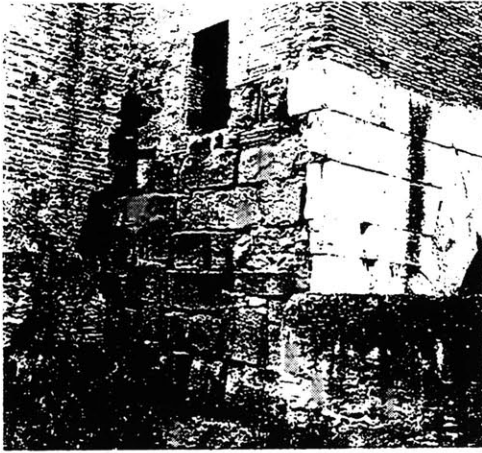


Figure 2-27 - Rome, Latina gate
[Marta R. 1989].

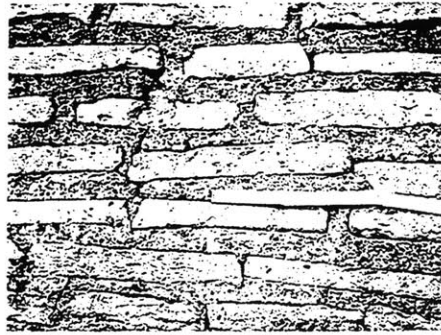


Figure 2-28 - Rome, B. of St. Nereo, St.
Achilleo [Marta R. 1989].

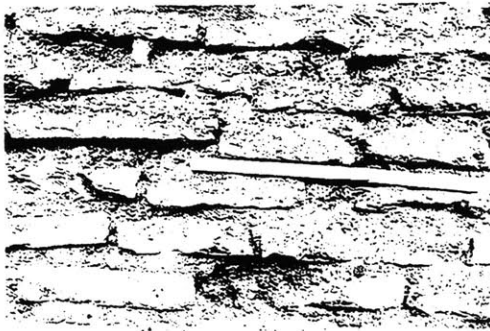


Figure 2-29 - Rome, B. of S. Francesca
R. [Marta R. 1989].

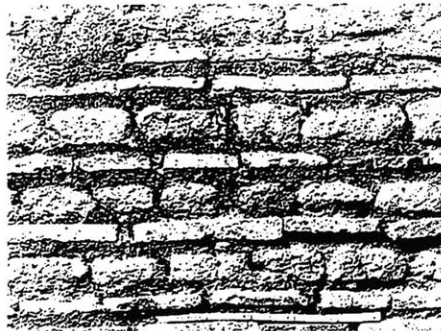


Figure 2-30 - Rome, B. of S. John at the
Latina gate [Marta R. 1989].



Figure 2-31 - Rome, Bas. of St. Lorenzo
[Marta R. 1989].



Figure 2-32 - Rome, Bas. of St. Pancrazio
[Marta R. 1989].

- the progressive exhaustion of the supplies of brick;
- the ease of finding tuff deposits (especially in some areas of Latium);
- tuff's easy workability and good mechanical strength;
- its imitation of the generic brick in size, aspect, texture and color.

The tuffello usually presents as its proportion between depth and length the value of 1:2. This ratio in some cases grows to reach 1:3: The length runs between 5 and 37 cm, and the depth between 3 and 12.5 cm. As time passed tuff blocks were set whose dimensions tended ever to increase.

CEMENT CONCRETE STRUCTURES

This construction technique too draws its origins from a structure used in the Roman world: *opus caementicium*. The concrete used during mediaeval times is composed of fragments of tuff, marble, travertine, bricks, flint, etc., held together by a lime and pozzolana mortar. The concrete masonry does not constitute, except in rare cases, a definite structure to itself, since the facies is characterized by cladding elements that give rise to well connoted masonry systems. For the construction of the core the concrete masonry was formed by laying down abundant mortar beds and then drowning in them, with care, rock fragments, travertine, brick etc. This stratification, on being finished, formed the sturdy and economical skeleton, which was then clad with a brick or tuff or stone lining (Figure 2-33, Figure 2-34).

SPECIAL STRUCTURES

This name has been given to a number of mediaeval masonry typologies that appear in wholly singular fashion; they are mentioned below.

Irregular masonry

This typology is occasionally seen in mediaeval construction technique and the arrangement of the elements varies case by case and often within the same masonry system. It appeared during the middle of the mediaeval period, during the 9th century. The masonry is made up irregularly both as regards the materials and the course alignments. Cases are seen of the use of special materials such as fragments of column drums, sculptural decorations, pieces of trabeations, inscriptions; and all this without being concerned to follow any compositionnal design whatever (Figure 2-35).

Dry masonry

Depending on the material available, through the whole of the mediaeval period the model of the polygonal-stone structure of Roman times acting as containment or as the bounds delimiting agricultural lands was imitated. The walls were executed without mortar, of any stone that was found, and accurately set to make the pieces fit together, without forming horizontal courses. It is a masonry that relies, statically speaking, on the stabilizing force of its weight.

Herringbone masonry

This appears episodically in a few religious constructions (Figure 2-36). It is found, then, almost as a construction intercalation, without ever rising to the dignity of a true autonomous typology, built in imitation of Byzantine structures or as a memory of the Roman opus spicatum.

Stone frame masonry

This follows the opus africanum of Roman construction technique, at the time imported from the Carthaginian area and applied rather seldom. It is a masonry made up of large stone blocks set both vertically and horizontally, with the vacant spaces between the blocks filled with small material to complete the masonry core (Figure 2-37).



Figure 2-33 - Rome, Bas. of St. Clemente
[Marta R. 1989].



Figure 2-34 - Velletri, villa of the Ottavi
[Marta R. 1989].



Figure 2-35 - Rome, Bas. of St. Stefano
Rotondo [Marta R. 1989].



Figure 2-36 - Rome, Bas. of St. Stefano
Rotondo. [Marta R. 1989].



Figure 2-37 - Rome, Bas. of St. Lawrence outside the walls [Marta R. 1989].

2.1 BLOCK STRUCTURES

MEGALITHIC WORKS

The use of stone as a construction material goes back to the most remote periods of prehistory. The first appearances of man's construction activities are megalithic constructions made of natural masses of enormous size. These works are given various names, arising from the genius of the language of the country in which they are found (e.g. dolmen, cromiech, menhir, etc.). The oldest go back to the New Stone Age.

THE SARDINIAN NURAGHI

When bronze appeared construction stones no longer had to be worked by breaking or spalling, but could be worked in forms more suited to construction. Belonging to the first period of this age are the Sardinian Nuraghi, enormous towers built of stone blocks, some of which rudely worked and arranged in horizontal courses the one overhanging the one below, so as to form a kind of dome.

EGYPTIAN WORKS

In the second millennium BC the Egyptian civilization was thoroughly acquainted with the art of stone working, as the monolithic obelisks and the works built of huge overlapping stone blocks bear witness to.

Examples of these works are:

- the obelisk built in Heliopolis by Sesostris I (circa 1950 BC) (Figure 2-38);
- the great banquet hall built at Karnak by Tuthmose III (circa 1450 BC) (Figure 2-39);
- the temple of Amun built in Karnak by Tuthmose III (circa 1450 BC) (Figure 2-40);
- the temple of Amenophis III at Luxor (circa 1350 BC) (Figure 2-41).

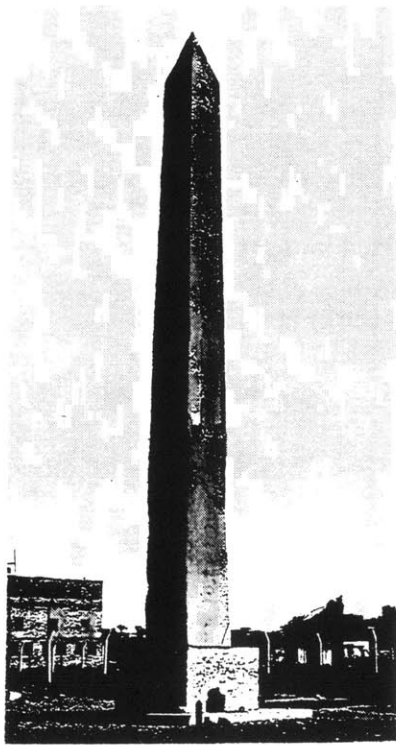


Figure 2-38. Eliopoli, the obelisk of Seostris I (circa 1950 BC).



Figure 2-39. Karnak, the great banquet hall built by Tuthmose III (circa 1450 BC).



Figure 2-40. Karnak, the temple of Amun built by Tuthmose III (circa 1450 BC).



Figure 2-41. Luxor, the temple of Amenophis III, detail of colonnade (circa 1350 BC).

THE WORKS OF CRETE AND MYCENAE

In the period running from 2000 to 1400 BC important large stone works were built in Crete and Mycenae. In particular, Cretan architecture is characterized by residential constructions having more than one storey and open to the landscape; the Mycenaean architecture instead features imposing walls built of huge cyclopean blocks, at times barely squared, within which have been cut pedestrian corridors (Figure 2-42 and Figure 2-43), and royal palaces and tombs roofed by domes similar to the nuraghi but using stones worked with greater precision (see as an example the tomb called The Treasure of Atreus of Mycenae, shown in Figure 2-44).

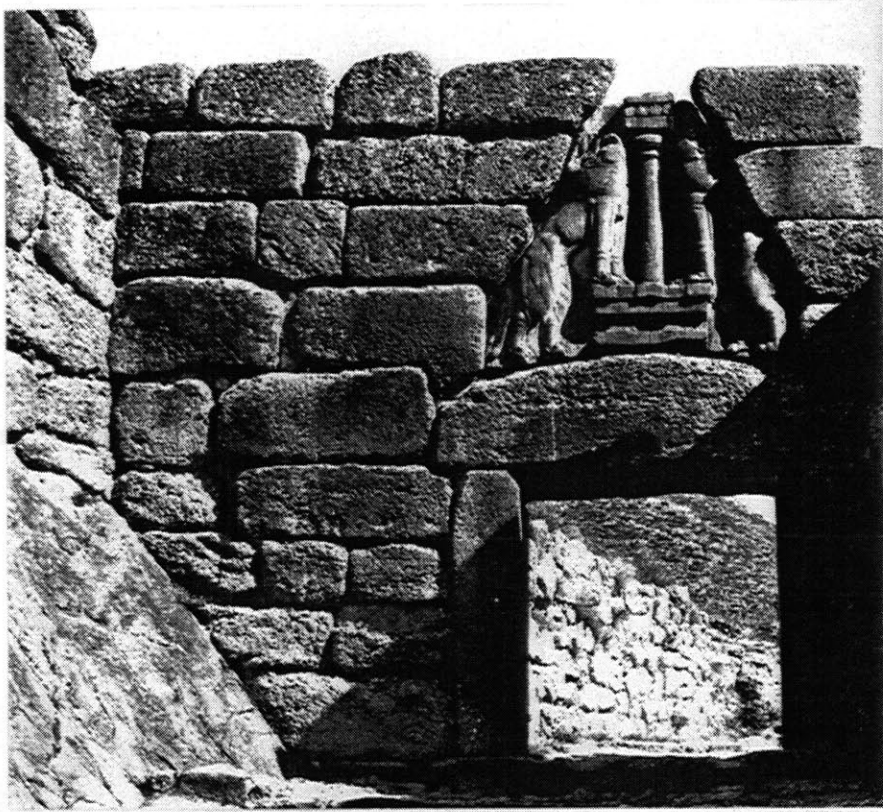


Figure 2-42. Micenae, The Lion Gate.

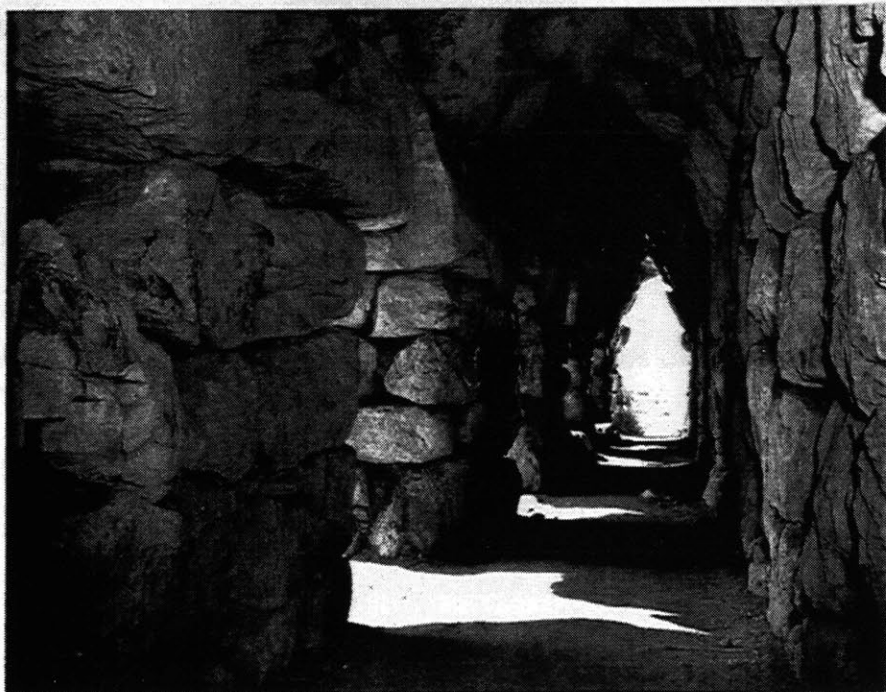


Figure 2-43. Tirinto, pedestrian corridors inside the wall.



Figure 2-44. Micenae, inside of the royal tomb called *Treasure of Atreus*.

THE GREEK WORKS

Greek architecture adopted the cut stone at first for those works for which considerable strength was needed (fortifications, bearing walls, substructures, etc.), and then for all architectural works of the monumental type, in particular for temples, which were the constructions of most interest. Some examples of Greek temples are the Parthenon, built in Athens in 450 BC (Figure 2-45) and the Treasury of the Athenians, built at Delphi in 490 BC (Figure 2-46). The stone blocks forming the temple structures were worked with great precision and very carefully set in place. Observe for example the arrangement of the blocks forming the trabeation of the temple of Aphaia at Egina (Figure 2-47). To obtain blocks that precisely fit, the contact surfaces of the block faces were often limited to the outermost margins, worked with extreme exactness, the innermost part being recessed and left rustic. To give the structure more stability, the stones were often tied together by metal cramps (Figure 2-48). Cut stones were used in the form of parallelepipedal blocks, generally of moderate size and set in horizontal courses, except for those cases in which the proportions of the building or the use assignment of the item demanded monolithic stones of considerable size. During the Hellenistic age the arch and the vault definitively entered the repertoire of the Greek architect; see for example the vaulted accessway to the stadium of Olympia (Figure 2-49), and the arch of the Agora gate at Pirene (Figure 2-50).

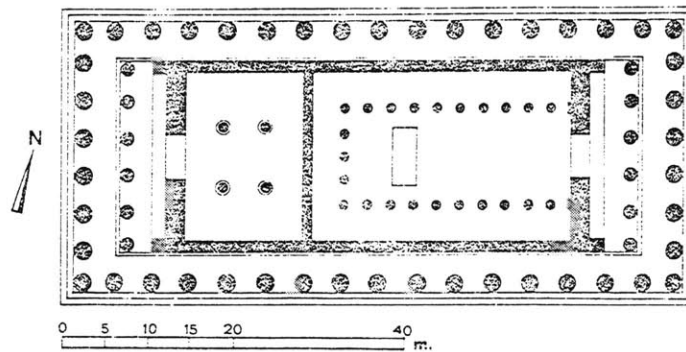
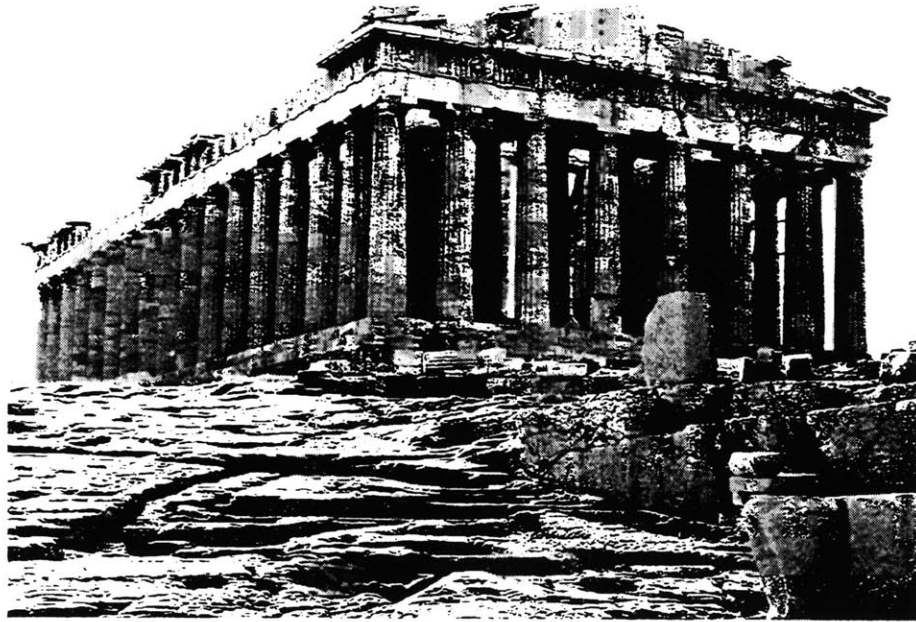


Figure 2-45. Athens, view and plant of the Parthenon temple (450 BC).



Figure 2-46. Delphi, the Treasury of the Athenians (490 BC).



Figure 2-47. Egina, particular of the trabeation of the temple of Aphaia.

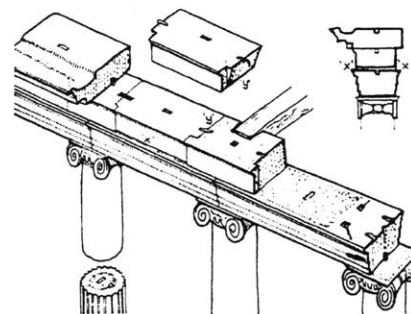


Figure 2-48. Typical scheme of the disposition of the blocks in a Greek trabeation.



Figure 2-49. Olympia, the vaulted accessway to the stadium (circa 300 BC).

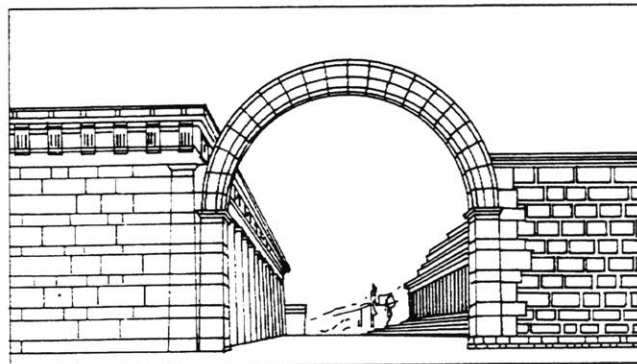


Figure 2-50. Scheme of the Agora Gate at Pirene.

ANCIENT ROMAN WORKS

Most Roman constructions were composed of brick-and-cement-mortar structural members; but stone block constructions are numerous too. In particular, most monumental works were built of stone blocks, such as temples, obelisks, tombs, city gates, and commemorative arches. Some of these works, especially the temples, were a more or less faithful reproduction of Greek constructions. Examples of Roman temples are:

- the temple of Fortuna Virilis, also called the Rectangular Temple, built in Rome in 70 BC (Figure 2-51);
- the temple of Castor and Pollux, built in Rome in 484 BC, and then rebuilt by Tiberius in 6 AD (Figure 2-52);
- the temple of Vesta, also called the Round Temple, built in Rome in 80-100 BC (Figure 2-53).

A famous example of an obelisk is Trajan's column, built in Rome in 113 AD (Figure 2-54), while examples of monumental tombs (not very widespread in Italy) are the Roman-Libyan tower tombs at El Mselleten (Figure 2-55).

In all Roman installations the city gates were built of stone blocks: see for example Porta Maggiore, built in Rome in 52 AD (Figure 2-56); while commemorative arches were mostly built in towns of major importance.

Stone blocks were also used by the Romans to build imposing infrastructures, such as bridges (Figure 2-57) and aqueducts (Figure 2-58); for the construction of important public buildings such as the baths (Figure 2-59), theatres (Figure 2-60 and

Figure 2-61) and amphitheatres (Figure 2-62), and for the construction of high-prestige private residences (Figure 2-63) and buildings used for manufacturing purposes (Figure 2-64).

Some works were built with mixed structures, and thus only partly of stone blocks; such is the case of many buildings built with brick and cement mortar structures and given a stone-block portico in front; one of the most famous works built with this structure is the Pantheon in Rome (Figure 2-65).



Figure 2-51. Rome, Boario Forum, temple of Fortuna Virilis, also called the *Rectangular Temple* (70 BC).

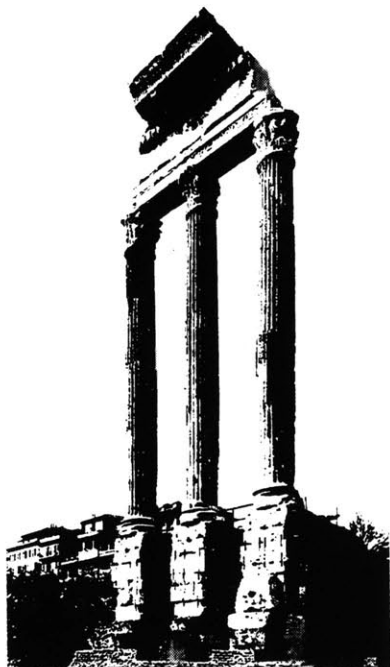


Figure 2-52. Rome, remains of the temple of Castor and Pollux (484 BC and 6 AD).



Figure 2-53. Rome, Boario Forum, temple of Vesta, also called the *Round Temple* (80-100 BC).



Figure 2-54. Rome, Trajan's column.
(113 AD).

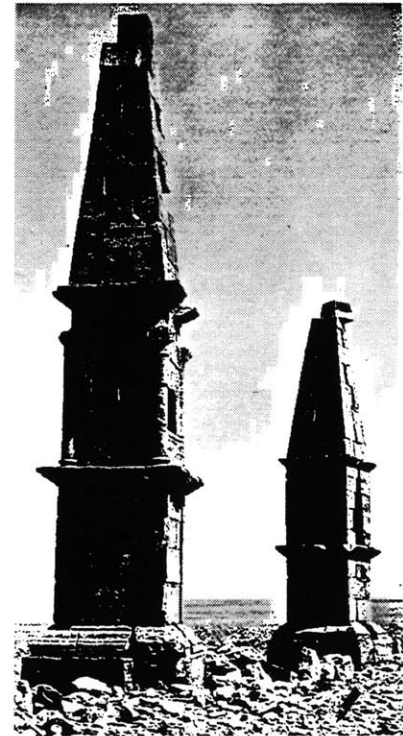


Figure 2-55. El-Mselleten, Roman-Libyan
tower tombs.



Figure 2-56. Rome, Porta Maggiore (52 AD).



Figure 2-57. Prenestina Road, *Di Nona* Bridge.

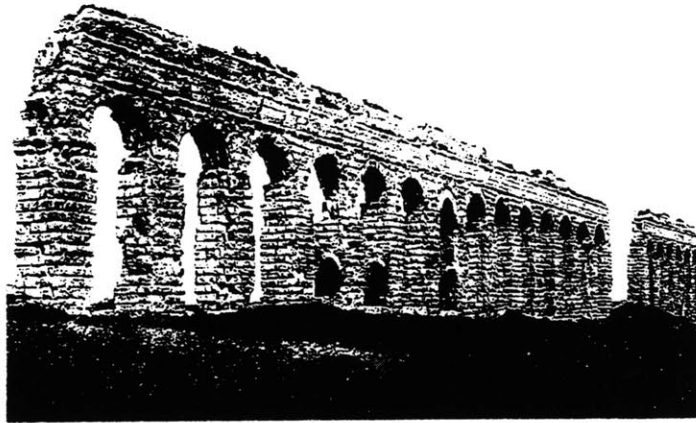


Figure 2-58. Rome, *Claudio* aqueduct (50 AD).



Figure 2-59. Hierapolis, vaulted frigidarium of a bath building.



Figure 2-60. Meridia, theatre.



Figure 2-61. Sabratha, theatre.

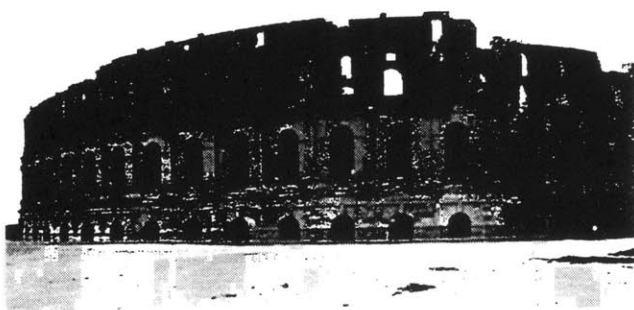


Figure 2-62. El-Djem, amphitheatre.

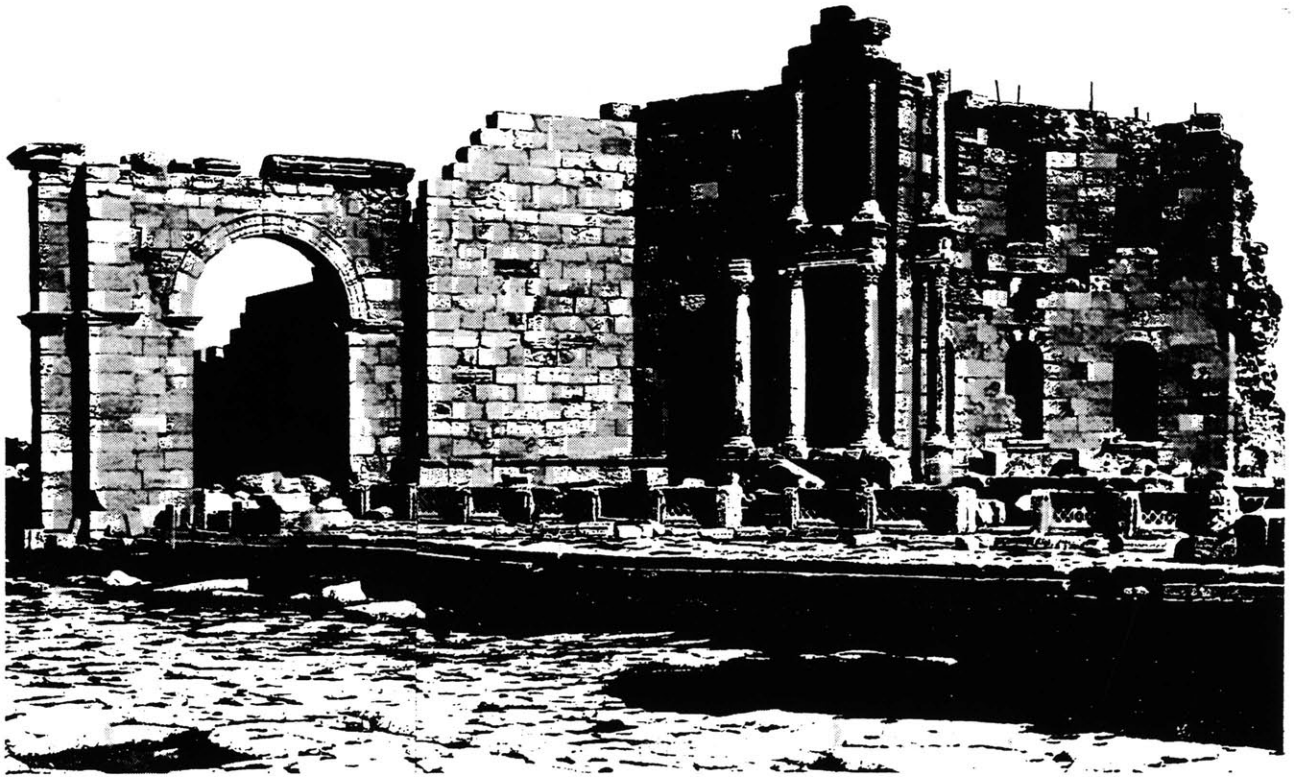
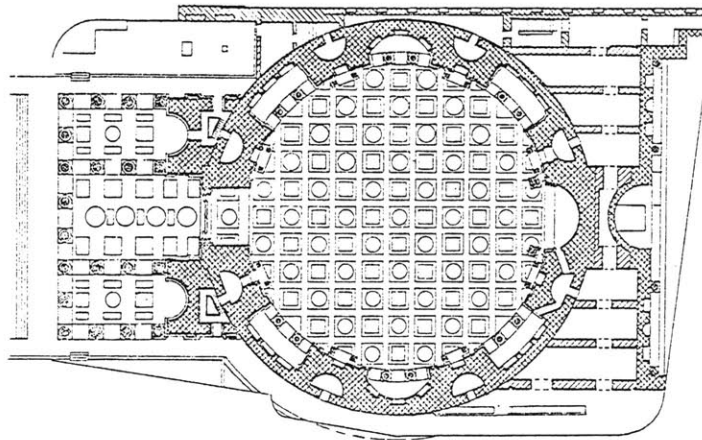
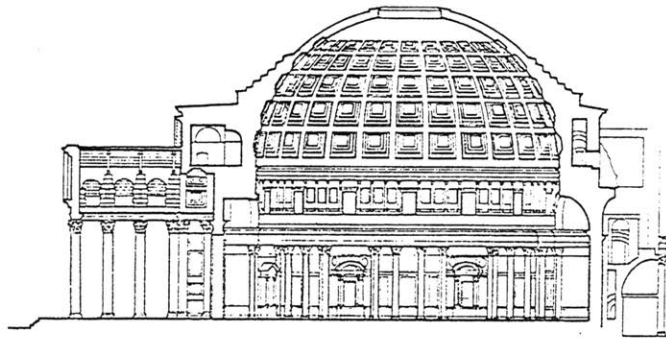


Figure 2-63. Leptis Magna, Severian building of the fountain (circa 200 AD).



Figure 2-64. Brisagane (near Tébessa), oil production building.



0 10 40 m



Figure 2-65. Rome, section, plant and view of Pantheon (25 BC).

ROMANESQUE CONSTRUCTIONS

During the Romanesque period, which runs from the end of the 8th century through the middle of the 13th (Middle Ages), the common people's residences (throughout the territory of old Europe) were constructed mostly of wood and masonry (as was the case for the preceding centuries as well), while works of greater importance (churches, castles, city walls) were built of stronger and more lasting materials that could be found on the spot (only rarely were materials used that came from localities distant from the construction site, owing to the enormous difficulties involved in their transport). Thus thousands of constructions were built with bearing structures of stone blocks or fired brick, many of which have been well conserved through the centuries. The fired brick constructions are characteristic of areas poor in rocks useable for construction, in particular the Po Valley Plain and Tuscany (in Italy), and the Low Countries and Northern Germany's lowlands. Fired bricks differ from stone blocks most especially in the fact that their crushing strength is lower and, generally, they are smaller in size. In stone block structures, the largest and smoothest blocks are used for the outside surfaces, while the more angular blocks and the working residues are in general used as filler, in addition to the mortar, for the construction of sack wall.

The typical construction of Romanesque architecture is the masonry church, but there are examples of them, even if their morphological characteristics differ, dating from the period preceding the Romanesque (the pre-Romanesque period). An example of a pre-Romanesque church is San Pedro de la nave, of 691, built wholly of stone blocks (Figure 2-66).

Many Romanesque works feature structures that thrust horizontally (arches, vaults, domes), which demand suitable support elements that can counter both the vertical forces arising from weight and the horizontal forces generated by the arch effect; these thrusts depend on the size of the structure (its span), on its form (round or pointed) and on the specific gravity of the material used. The horizontal thrusts are met by counterthrusts (thrusting structures set beside the main structure), or by the thickness of the bearing walls or also by suitable local reinforcements (exterior or interior buttresses). One of the first Romanesque constructions using buttresses and stone-block masonry is the church of Santa Maria de Naranco, built near Oviedo (northern Spain) between 842 and 848 (Figure 2-67). Examples of Romanesque churches with stone block structures and thrusting roofs are:

- the church of Sant Ponç at Corbera (1074) (in Catalonia, in southwestern Europe), having a nave alone with a ribbed barrel vault roof;
- the abbey church of Fontevault (1119) (in Aquitaine, in southwestern Europe), having a nave only, with a dome roof (Figure 2-68);
- the church of St. Etienne at Nevers (1063-1097) (in Burgundy, in central western Europe), nave and two aisles, the nave being roofed by a ribbed cylindrical barrel vault.
- the cathedral of Le Mans (north of the Loire), nave and two aisles, with the nave roofed by ogival cross-vaults;
- the church of St. Pierre at Moissac (France), central plan, with a ribbed-dome roof.

In some regions, for example Italy, Romanesque churches were built with non-thrusting roofs (wood-beam), supported on vertical bearing walls. Such is the case for the following examples:

- the church of Santa Maria Maggiore in Tuscania (1206), nave and two aisles;
- the church of San Tommaso at Alemno (11th-12th centuries) (in northern Italy) central plan (Figure 2-69).

And finally, deserving of mention are the Romanesque churches of central Europe, mostly built of stone block masonry and characterized by the basilica plan and by being surmounted by towers. Some examples of these structures are:

- the Abbey church of Notre Dame at Jumièges (in Normandy) (11th century);
- the abbey church of Gundersheim (in Lower Saxony) (11th century);
- the church of St. Pantaleon in Cologne (circa 1100).



Figure 2-66. Spain, church of San Pedro de la nave.

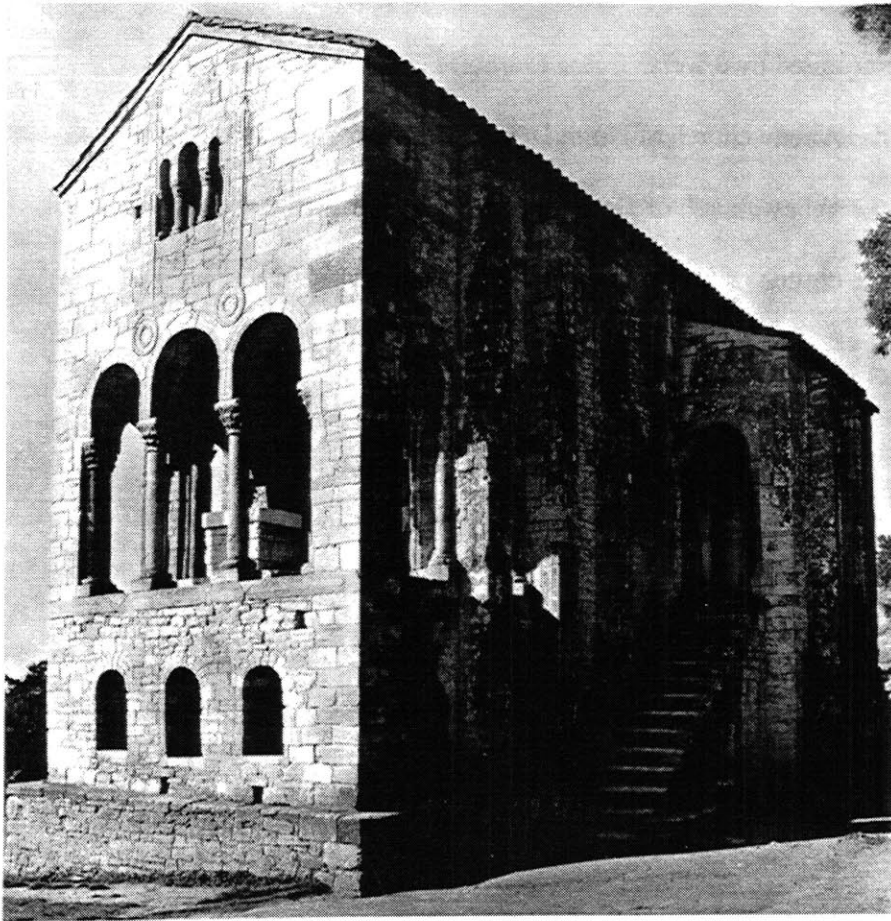


Figure 2-67. Oviedo, church of Santa Maria de Naranco (842-848 AD).

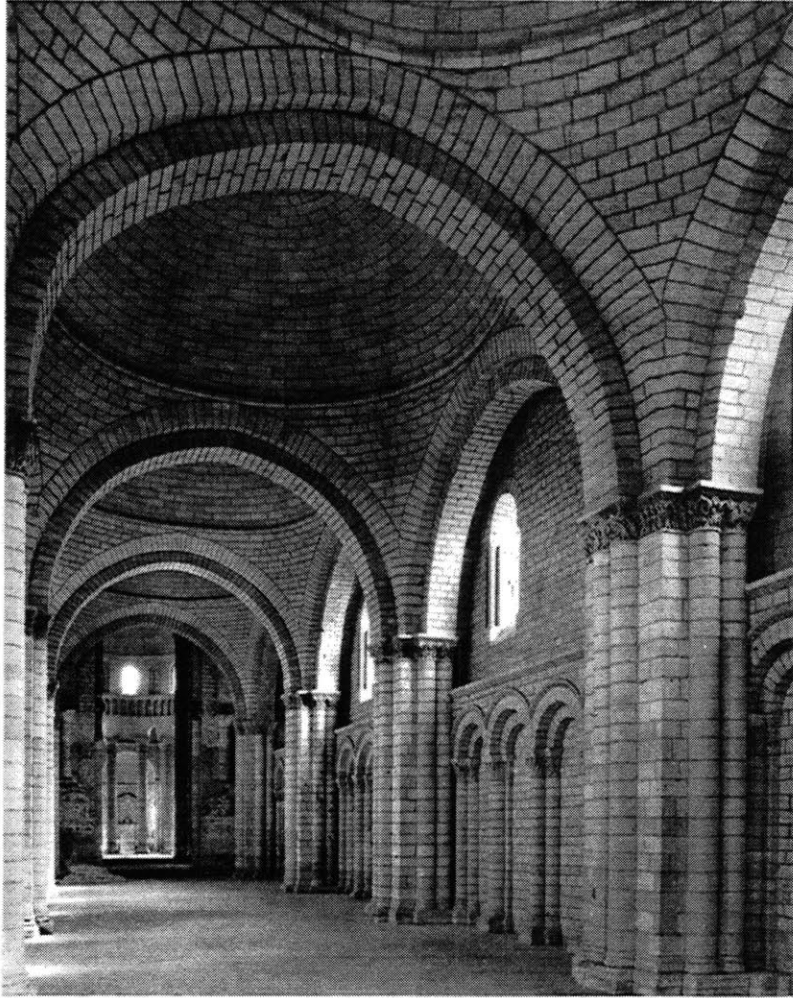


Figure 2.68. Fontevrault (Aquitania), the abbey church (1119 AD).



Figure 2.70. Alemno (Italy), San Tommaso (11th-12th centuries).

GOTHIC AND RENAISSANCE CONSTRUCTIONS

The monumental works of the Gothic period, characterized by tall and slender forms, were mostly built of cut stone, and this because it was the only material at the time capable of the necessary crushing strength.

Afterward, from the Renaissance on, the tendency was more and more to forsake the use of stone in building structures, it being relegated mainly to the decorative elements.

Chapter 3: REVIEW OF STATIC ANALYSIS METHODS FOR BLOCK STRUCTURES

3.1. RIGID CONTACT MODELS

3.1.1. Limit Analysis and Mathematics Programming

3.1.2. Livesley Model

3.1.3. Lo Bianco-Mazzarella Model

3.2. DEFORMABLE CONTACT MODELS

3.2.1. Gap Elements

3. STATIC ANALYSIS METHODS FOR BLOCK STRUCTURES

The main difficulty in the numerical modeling of block structures lies in the mechanical characterization of the contact forces. Current models can be conveniently classified into rigid contact and deformable contact models. The first exclude the mechanical characterization of the joints assuming appropriate constraints on the contact forces and, in the dynamic case, also on the resulting motion after the impact. The second determine the contact forces assuming that the joints between blocks are constituted by conveniently chosen deformable elements.

The rigid contact models can be considered as limit analysis problems characterized by non associated flow rules, due to the presence of friction forces [Drucker D.C., 1954]. Livesley [Livesley R.K., 1978] provides the first applications, but the roots of this method can be found in Heyman [Heyman J., 1966, 1969] who applies for the first time limit analysis methods to block masonry structures assuming, however, associated flow rules. Livesley's hypotheses are later taken up and modified in [Lo Bianco M., 1984; 1985], and further extended to the 3D case in [Baggio C., 2000]. It is interesting to observe, as it will be illustrated in detail in the following, that the Livesley model may be interpreted as a linear mathematics programming problem, while the one proposed by Lo Bianco and Mazzarella as a non linear one.

The elastic contact models describe the contact between blocks with the so called gap elements, that are elements with axial and tangential stiffness, capable of transmitting compressive and shear stresses respectively (see for example [Mamaghani I., 1999]).

3.1 RIGID CONTACT MODELS

3.1.1 Limit Analysis and Mathematic Programming

Limit analysis is based on the use of the perfectly plastic model for the description of the structural behavior and on the use of the limit theorems of plasticity (*upper bound theorem* and *lower bound theorem*). The rigid perfectly plastic model is particularly suitable for describing the behavior of a rigid block on a plane surface with friction. If r_n and r_t are the resultants of the normal and tangential forces between the block and the base, the states of incipient sliding may be described by a relationship between r_n and r_t (the failure or limit curve). Such relationship depends from the morphology of the contact surfaces and from the mechanical properties of the materials. A generic limit equilibrium curve in the $r_n - r_t$ plane is given in Figure 3-1, in the same figure p_n and p_t represent the external loads in the normal and tangential direction respectively.

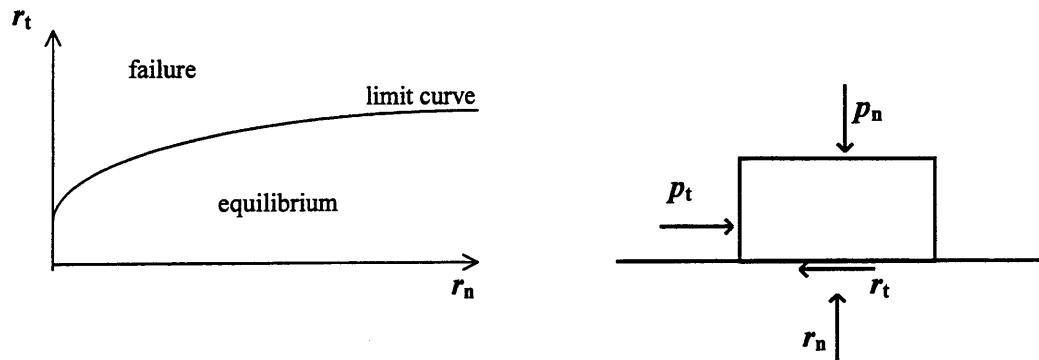


Figure 3-1. A failure criterion for a rigid block on plane with friction contact.

In general, the solution of the perfectly plastic problem requires that equilibrium, geometric compatibility, and constitutive relationship are simultaneously satisfied. The general procedure may be simplified using the *lower bound* theorem (in the static approach), which states that:

the set of values of external loads which are in equilibrium with a set of internal forces (the contact force, in this case) satisfying at any point both equilibrium and the failure criterion, is a lower bound approximation of the failure;

or using the *upper bound* theorem (kinematic approach), according to which:

the values of external loads determined equating the work of external forces in any failure mechanism which satisfies kinematic compatibility and the work of the corresponding internal forces (satisfying the failure criterion) are an upper bound approximation of the failure.

Expressing the external loads with λp , in which λ is a scalar representing the multiplicative factor of the load vector p , we have the problem to determine the value λ_c for which the structure collapse. If r is the vector of internal forces, d the vector of displacements and e the vector of strains, we have that the equilibrium equation may be written as:

$$\lambda p = H r$$

the kinematic compatibility equations as:

$$H^T d = e.$$

and the equation of balance of internal and external work as:

$$\lambda p^T d = (r^*)^T e.$$

where (r^*) is the value of r during sliding.

Assuming for the failure criterion the following law:

$$-r^l \leq r \leq r^u$$

and expressing, for convenience, the vectors r , d and e as the difference between two orthogonal vectors with positive non zero components:

$$r = r_1 - r_2 \quad \text{with: } r_1 \geq 0, \quad r_2 \geq 0 \quad \text{and} \quad r_1^T r_2 = 0$$

$$d = d_1 - d_2 \quad \text{with: } d_1 \geq 0, \quad d_2 \geq 0 \quad \text{and} \quad d_1^T d_2 = 0$$

$$e = e_1 - e_2 \quad \text{with: } e_1 \geq 0, \quad e_2 \geq 0 \quad \text{and} \quad e_1^T e_2 = 0$$

we have that the lower bound theorem of plasticity may be given by the following relationships:

$$\lambda_c = \max(\lambda),$$

$$\lambda p - H(r_1 - r_2) = 0, \quad r^l \leq (r_1 - r_2) \leq r^u,$$

$$\lambda \geq 0, \quad r_1 \geq 0, \quad r_2 \geq 0$$

which may also be written in matrix form as:

$$\lambda_c = \max(\lambda)$$

$$\begin{bmatrix} p & -H & H \\ -p & H & -H \\ 0 & I & -I \\ 0 & -I & +I \end{bmatrix} \begin{bmatrix} \lambda \\ r_1 \\ r_2 \end{bmatrix} \leq \begin{bmatrix} 0 \\ 0 \\ r^u \\ r^l \end{bmatrix}$$

$$\begin{bmatrix} \lambda \\ r_1 \\ r_2 \end{bmatrix} \geq 0$$

whose solution is a typical problem of mathematic programming.

Analogously, the upper bound theorem of plasticity may also be expressed from:

$$\lambda_c = \min(\lambda),$$

$$H^T (d_1 - d_2) = (e_1 - e_2), \quad \lambda p^T (d_1 - d_2) = (r^*)^T (e_1 - e_2),$$

$$\lambda \geq 0, \quad e_1 \geq 0, \quad e_2 \geq 0, \quad d_1 \geq 0, \quad d_2 \geq 0$$

where the vector e has an arbitrary length. Again, the corresponding matrix expression is:

$$\lambda_c = \min(\lambda)$$

$$\begin{bmatrix} p^T & -p^T & 0 & 0 \\ -H^T & H^T & I & -I \\ H^T & -H^T & -I & I \end{bmatrix} \begin{bmatrix} d_1 \\ d_2 \\ e_1 \\ e_2 \end{bmatrix} \geq \begin{bmatrix} 1/\lambda \\ 0 \\ 0 \end{bmatrix}$$

$$\begin{bmatrix} \lambda \\ d_1 \\ d_2 \\ e_1 \\ e_2 \end{bmatrix} \geq 0$$

assuming for the length of vector e , a value which always satisfies: $(r^*)^T (e_1 - e_2) \geq 1$.

It is recognized that the previously described problems, formulated with the static and kinematic approach, are two dual problems and it follows that the multipliers coincide.

The problem has been simplified by assuming a particularly simple failure criterion. Let us study now the case of contact forces with a generalized Coulomb friction behavior given by the following relationship:

$$-r_0^l - T^l r \leq r \leq r_0^u + T^u r$$

Assuming that the external loads are described as the sum of a constant vector p_1 and a variable vector λp_2 :

$$p = p_1 + \lambda p_2$$

the two problems of mathematic programming formulated in the preceding paragraph, with the new position of the constraints, become:

$$\lambda_c = \max(\lambda)$$

$$\begin{bmatrix} p_2 & -H & H \\ -p_2 & H & -H \\ 0 & (I - T^u) & (-I + T^u) \\ 0 & (-I - T^l) & (I + T^l) \end{bmatrix} \begin{bmatrix} \lambda \\ r_1 \\ r_2 \end{bmatrix} \leq \begin{bmatrix} -p_1 \\ p_1 \\ r_0^u \\ r_0^l \end{bmatrix}$$

$$\begin{bmatrix} \lambda \\ r_1 \\ r_2 \end{bmatrix} \geq 0$$

and:

$$\lambda_c = \min(\lambda)$$

$$\begin{bmatrix} p_2^T & -p_2^T & 0 & 0 \\ -H^T & H^T & I & -I \\ H^T & -H^T & -I & I \end{bmatrix} \begin{bmatrix} d_1 \\ d_2 \\ e_1 \\ e_2 \end{bmatrix} \geq \begin{bmatrix} 1/\lambda \\ 0 \\ 0 \end{bmatrix}$$

$$\begin{bmatrix} \lambda \\ d_1 \\ d_2 \\ e_1 \\ e_2 \end{bmatrix} \geq 0$$

having assumed for the length of vector e , a value for which $(r^*)^T (e_1 - e_2) \geq 1$.

In this case, the problems of maximum and minimum are not dual ones, unless the matrices T^u and T^l are identically null; such a condition, for a system of reactive forces with generalized Coulomb friction, exists only if the friction angles are null and the resistant force tangent to the joint comes entirely from cohesion of the restraint. The presence of Coulomb friction determines that the problem of limit analysis requires a non-associated flow rule. A rectangular block is considered subject to two forces N and F respectively perpendicular and parallel to the supporting surface (Figure 3-2).

The limit criterion in the space of the forces is the following:

$$\begin{aligned} F - c - N \times \operatorname{tg} \varphi &\leq 0 \\ F + c + N \times \operatorname{tg} \varphi &\leq 0 \\ F \times h - N \times b &\leq 0 \\ -F \times h + N \times b &\leq 0 \\ N &\leq N_0 \end{aligned}$$

Overlapping the space of the displacements (u, v) with the space of the forces (F, N) it is possible to relate the displacements following a given collapse mechanism with

the failure domain (Figure 3-3). One finds in fact that in the segments OA and OA' the mechanism is one of pure rotation with centers of rotation o' and o and the field of displacements defined by the following relationships:

$$u^{OA} = -v^{OA} \cdot \frac{h}{b}$$

$$u^{OA'} = v^{OA'} \cdot \frac{h}{b}$$

in the segments AB and A'B' the mechanism is of pure translation and the field of displacement is the following:

$$v^{AB} = 0, \quad u^{AB} = u_0,$$

$$v^{A'B'} = 0, \quad u^{A'B'} = -u_0;$$

in the segment BB' one has joint failure due to crushing and the field of displacement is the following:

$$u^{BB'} = 0$$

$$v^{BB'} = v_0.$$

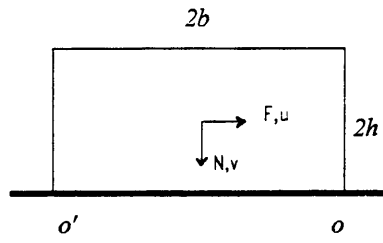


Figure 3-2. Rectangular block subjected to a system of centroidal forces.

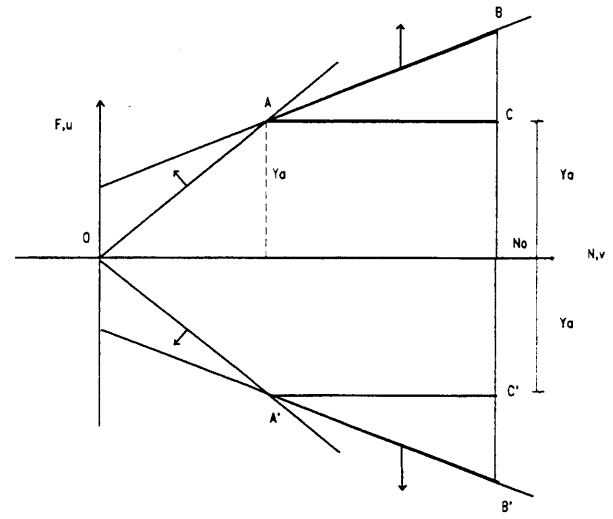


Figure 3-3. Failure limit and compatible displacements for a rectangular block, in the presence of Coulomb friction.

One has therefore that in the segments AB and A'B' the law of normality is not respected. For materials with non-associated flow rule it is possible to identify a reduced limit domain such that in correspondence with the activation of one of its sides the normality law would be respected and at the same time there would be a dissipation of energy equal to the lowest value of the energy that would dissipate following the activation of the corresponding face of the real domain. In the case in question (figure), the reduced domain coincides with the domain that one would obtain by choosing a friction criterion of the type:

$$F \leq \pm y_A$$

where:

$$y_A = \frac{c \cdot b \cdot h}{b - h \cdot \operatorname{tg} \varphi}$$

The identification of the reduced domain allows, on the basis of the two Radenkovic theorems for non-standard materials (materials that do not have an associated flow rule), the determination of a lower or upper approximation of the collapse multiplier. In fact it is found *that the failure load of a body with non-standard material is upwards-limited by the failure load that the same body would have if the material were standard and the criterion of resistance were the real one ($F(\sigma) \leq 0$); further, the failure load for a body whose material is not standard is downwards-limited by the failure load that the body would have if the material were standard and the criterion of resistance were ($G(\sigma) \leq 0$), where $G(\sigma) = 0$ is a convex function entirely contained in the yielding surface $F(\sigma) = 0$, such that at each stress state σ on $F(\sigma) = 0$, there is a corresponding stress state σ' in $G(\sigma') = 0$ and in σ' one has that ε'_p is perpendicular to $G(\sigma') = 0$, and $(\sigma_{ij} - \sigma'_{ij})\dot{\varepsilon}_{ij} \geq 0$.*

It is therefore possible to find an upper bound and lower bound of the failure load by solving two linear mathematic programming problems: the first one can be found solving the problem of maximum; the other may be obtained solving the problem of minimum, substituting the nonlinear constraints with the constraints resulting from having used the reduced domain.

3.1.2 Livesley Model

In [Livesley R. K., 1975], the author illustrates a numeric procedure for the evaluation of the collapse multiplier for 2D frames. The procedure utilizes the static approach. In [Livesley R. K., 1978] he adopts the same procedure for the study of rigid block structures considering two different cases:

- 1) independence of the friction forces from the forces (N) acting perpendicular to the planes of sliding;
- 2) dependence of friction forces from N .

In order to apply the algorithms developed for the frame case, the block structures are modeled as nodes with finite dimensions and elements with rigid-plastic behavior: the nodes represent the blocks, the elements represent the joints. On each element (joint) a system of equilibrated forces r is applied, and the field of possible displacement is represented by the vector e such that the work is $r^T e$ (Figure 3-4). In the type 1 case, given that there is duality between the static and the kinematic problem, the correct value of the collapse multiplier is obtained; in the type 2 case, the author points out that, even though there is no duality, the multiplier obtained is correct if the field of displacement is such that the work $r^T e$ is null. To say that $r^T e$ is null means to exclude the cases in which the failure implies sliding, admitting that for each single block one can have exclusively a rotation mode.

In [Livesley R. K., 1992], the author extends the procedure to the calculation of three-dimensional block structures.

3.1.3 Lo Bianco-Mazzarella Model

Lo Bianco and Mazzarella take up the Livesley hypothesis and write the equilibrium and compatibility equation as follows:

$$\begin{aligned} r &= A_0^T p + A^T r_x & (a) \\ p &= p_1 + \lambda p_2 & (b) \\ d &= A_0 e & (c) \\ d_x &= A e = 0 & (d) \end{aligned} \tag{3-1}$$

where:

- p = generalized vector forces;
- p_1 = constant generalized vector forces;
- λp_2 = variable generalized vector forces;
- λ = load multiplier;
- d = generalized nodal vector displacements;
- r = generalized vector stress (contact forces);
- e = generalized vector of deformations
- r_x = statically indeterminate forces vector;
- d_x = non compatibilities vector.

The constraints on the contact forces are formulated as it follows:

$$f = T r - r_0 \leq 0 \tag{3-2}$$

and dictate that the perpendicular stress at the joint is either null or compression, that the eccentricity of the perpendicular stress must fall within the section and finally that the generalized rule of Coulomb must be respected. The relative displacement between the two joint faces are described as linear combination with non negative coefficients of four elementary displacements (Figure 3-5):

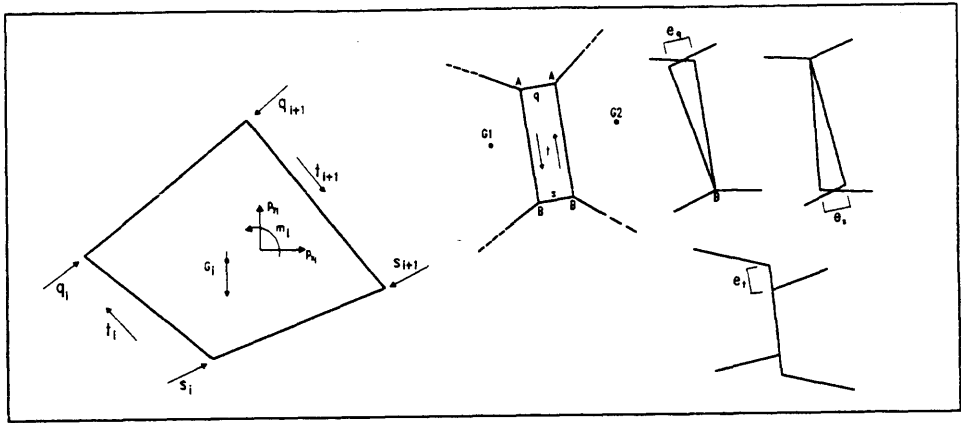


Figure 3-4. Scheme of Livesley model.

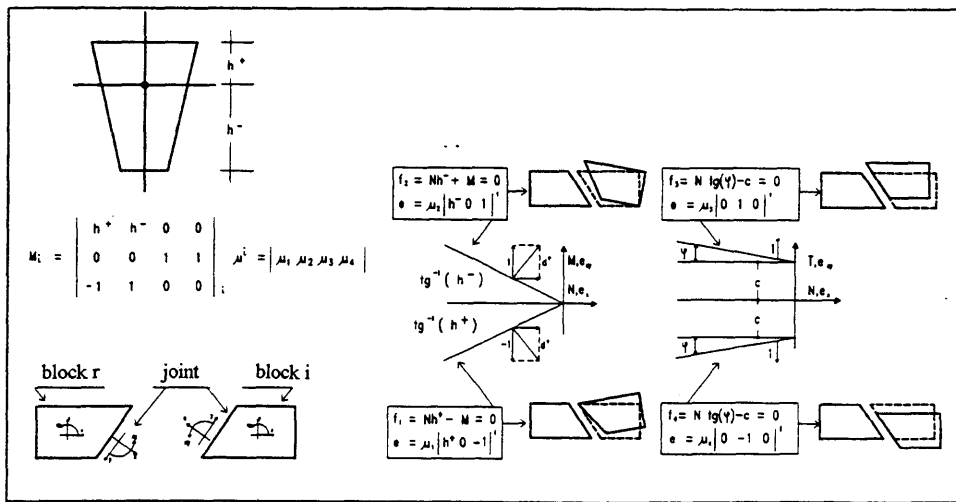


Figure 3-5. Scheme of Lo Bianco-Mazzarella model.

μ_1 = unit rotation in negative direction and center on the upper edge of the joint;

μ_2 = unit rotation in positive direction and center on the lower edge of the joint;

μ_3 = unit positive sliding;

μ_4 = unit negative sliding.

The allowable displacements are thus expressed by the following relationship:

$$e = M \mu \quad (3-3)$$

while since the variable loads are positive one has:

$$d^T p_2 = 1 \quad (3-4)$$

According to the authors, for structural safety purposes, the only significant multiplier is the minimum, obtainable by the following non-linear programming problem:

$$\begin{aligned} \min(\lambda) & \quad (a) \\ r &= A_0^T (p_1 + \lambda p_2) + A^T r_x \quad (b) \\ \lambda &\geq 0 \quad (c) \\ f &= T r - r_0 \leq 0 \quad (d) \\ \mu &\geq 0 \quad (e) \\ f^T \mu &= 0 \quad (f) \\ e &= M \mu \quad (g) \\ d &= A_0 e \quad (h) \\ d_x &= A e = 0 \quad (i) \\ d^T p_2 &= 1 \quad (l) \end{aligned} \quad (3-5)$$

Putting (3-3) into (3-5h) one obtains:

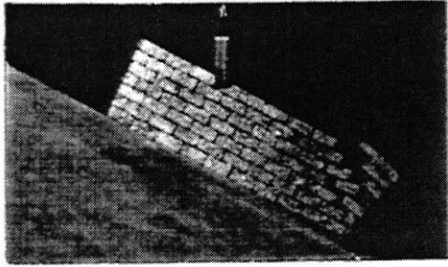
$$d = A_0 M \mu$$

which allows the calculation of the displacement vector u .

The authors emphasize how it is possible to find a lower and upper estimate of the multiplier from the solution of the preceding problem. The first one coincides with the collapse multiplier of a structure which has the same kinematic laws ($e = M \mu$) of the real one, but a reduced domain. The evaluation of the lower estimate, however, become meaningless in the case in which the resistance to sliding is assigned entirely to friction. In the absence of cohesion, in fact, the reduced limit domain (Figure 3-3) coincides for each element with the axis of equation $F = 0$; it follows that the lower estimate is zero. The upper one coincides with the collapse multiplier of a structure which differs from the real one only for the kinematic behavior which is of the associated type.

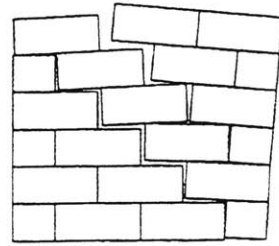
In [Trovalusci P., 1992] the formulation in (3-5) is applied for the identification of the collapse multiplier of small block masonry structures made with rectangular blocks (Figure 3-6). The authors highlight that the value of the multipliers obtained experimentally are lower than the ones obtained with limit analysis, and that the numeric procedure of minimization has convergence problems even for a limited number of blocks as in the case of Figure 3-6b, where the mechanism reported is not correct, but rather refers to an intermediate iteration far from the exact solution. An improved implementation of (3-5) with extension to the 3D case, and better convergency performances is given in [Baggio C., 2000].

It should be noticed that the Discrete Element Method, which will be described in the following, does not show convergence problems, but still predicts failure loads which are higher than the experimental ones (see Chapter 5). In Chapter 7 a new joint model for the DEM is proposed in order to overcome such discrepancy, and among the applications which will be presented, there will be also the case illustrated in Figure 3-6a (21-block case), in which the failure load has been overestimated by the Limit Analysis method.

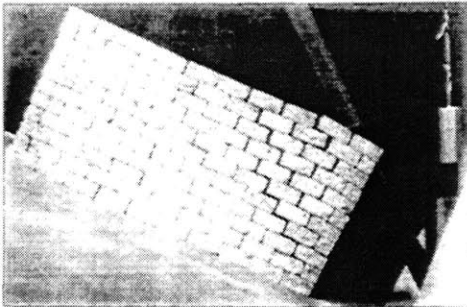


(a)

$\lambda = 0.5$

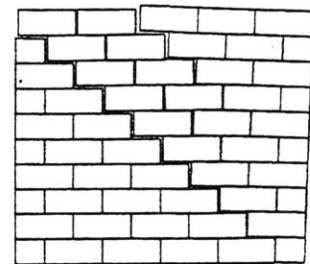


$\lambda = 0.64$



(b)

$\lambda = 0.47$



$\lambda = 0.545$

Figure 3-6. Application of the Lo Bianco-Mazzarella model [Trovalusci P., 1993].

3.2 DEFORMABLE CONTACT MODELS

In block structures, in some cases, the hypothesis of rigid plastic joints can turn out to be inadequate for the modeling of contact forces. In a masonry wall, for example, even when the mortar is degraded, the deformability of the joints is much higher than that of the bricks which may be modeled instead with rigid elements. But even in the absence of mortar, a rough joint has contact points which may be modeled in terms of deformability and resistance with constitutive relations which are different from those of the element itself.

In this second case, the studies performed in the field of rock mechanics have yielded useful indications: the morphology of a rock fracture is often classifiable based on its roughness measurable using the *JRC* (Joint Roughness Coefficient). As it will be described more in detail in Chapter 5, in stone blocks the *JRC* is about 2, since the roughness of the joint is classifiable as type-I [Barton N. R., 1978]. It seems reasonable to assume that the contact is localized in a discrete number of points with given mechanical characteristics, such as:

k_n = stiffness in a direction perpendicular to the joint surface;

k_t = stiffness in a direction tangent to the joint surface;

N_s^* = resistance to compression at the contact point;

F_s^* = resistance to sliding at the contact point.

For a rigid block placed on a horizontal plane (3-7a) and supposing that the contact points coincide with its corners it is possible to model the contact points with two deformable elements: one with stiffness $k_n \neq 0$ and $k_t = 0$, the other with stiffness $k_n = 0$ and $k_t \neq 0$. The contact element with stiffness k_n is characterized by the force displacement law shown in 3-7b: it has a no tension resistance, and an infinite resistant in compression and has a constant stiffness.

The contact force increases therefore linearly with the increase of the displacement u_n of the block corner (contact point) in direction n with respect to the position that it had in the absence of interaction forces. The contact element with stiffness k_t is characterized by the force displacement rule shown in Figure 3-7c: it has an elastic-plastic behavior whose variable elasticity threshold is a function of the normal force acting in the contact point. For Coulomb friction the tangential ultimate force is provided by:

$$|F^u| = N \operatorname{tg} \varphi \quad (3-6)$$

3.2.1. Gap Elements

For the study of the failure load of multi-block structure it is possible to use finite elements models with the so-called gap elements whose behavior is analogous to the one previously described in section 3.2. In [Trovalusci P., 1992] a series of FE analysis of block walls have been performed. The blocks were considered rigid while the joints were modeled as in section 3.2. The Newton-Raphson algorithm was used for the solution of the system of non linear equilibrium equations. However, the numerical procedure, as reported by the author, became particularly unstable when several openings occurred, and convergence was not easily obtained.

A recent work presented in [Mamaghani I., 1999] falls in this category of models for block structures.

In addition, it is noted that, since the FEM is not suited for detecting new contact surfaces during the evolution of the system response, cases in which a local instability is followed by a global stable configuration are not captured by the FE analysis, whereas the Discrete Element Method will generally predict the correct solution.

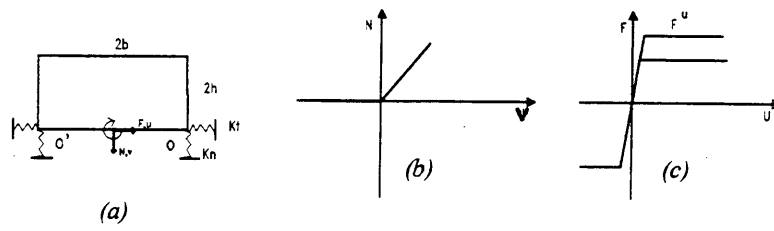


Figure 3-7. Modeling of a block with elastic contacts.

Chapter 4. REVIEW OF DYNAMIC ANALYSIS METHODS FOR BLOCK STRUCTURES

4.1. RIGID CONTACT MODELS

4.1.1. Milne's Studies

4.1.2. Perry Model

4.1.3. The Housner Model

4.2. DEFORMABLE CONTACT MODELS

4.2.1. The Angotti-Toni Model

4.3. THE DISCRETE ELEMENT METHOD

4. REVIEW OF DYNAMIC ANALYSIS METHODS FOR BLOCK STRUCTURES

In the field of block dynamics the first studies date back to the last century, when in [Milne J., 1881] were presented the first investigations aimed at the estimation of earthquake intensity based on the study of its effects on columns and obelisks. Systematic studies of the dynamic behavior of blocks, however, begins with the work by [Housner G.W., 1963] aimed at the study of seismic behavior of storage tanks. Many studies have been devoted to this subject, an extended review is contained in [Sinopoli A., 1998]. However the available dynamic models, with the exception of the Discrete Element Method, tend to be limited by the simplicity (both in the shape and in the number of elements) of the structures which may be considered.

4.1 RIGID CONTACT MODELS

The dynamic behavior of a block structure is characterized by the presence of impulsive interaction forces associated to the impact. Impact is a highly dissipative phenomenon which is generally quantified by the restitution coefficient, defined as it follows:

$$e = \frac{\int F_d \cdot dt}{\int F_r \cdot dt} \quad (4-1)$$

where $\int F_d \cdot dt$ and $\int F_r \cdot dt$ are respectively the impulses acting during the period of deformation and of restitution. In the case of frictionless impact, for regular contact surfaces, it may be assumed that impulses act perpendicularly to the surfaces, and it can be shown [Beer, 1957] that, in the case of both direct central and oblique impact, and the case of eccentric impact, (4-1) becomes:

$$e = \frac{(v_B^+ - v_A^+)_n}{(v_B^- - v_A^-)_n} \quad (4-2)$$

where A and B indicate the contact points of the bodies, n the direction perpendicular to the surface of the bodies at the contact points and $v_A^+, v_B^+, v_A^-, v_B^-$ the velocities of the contact points respectively after and before the impact. In the case of impact with friction, the direction of the acting impulse is not known a priori, and in general it has two components, one perpendicular and one tangential to the contact surfaces. See [Levi-Civita, 1927] for a discussion of the problem.

After having defined for a system of bodies the internal impulses, it is possible to write, for each body and for the system as a whole, the equations of impulsive motion as it follows:

$$\begin{aligned} \Delta Q &= R \\ \Delta K &= M \end{aligned} \quad (4-3)$$

where ΔQ and ΔK represent respectively the variations of the quantity of motion and of the momentum of the quantity of motion, or rather, with obvious meaning of the symbols:

$$\begin{aligned} \Delta Q &= Q^+ - Q^- \\ \Delta K &= K^+ - K^-, \end{aligned}$$

R is the resultant of the external impulses, and M is the corresponding resulting moment.

From (4-3) it is deduced that for a system of bodies, in the absence of external forces, since the resultant of the external impulses is zero, the quantity of motion and its momentum is conserved after the impact.

The equations in (4-3) do not usually suffice for the solution of the problem, that is the determination of the motion of the single bodies after the impact, since in general the number of unknowns (acting impulses and velocities of the bodies after the impact) is greater than the number of available equations and therefore the problem is indeterminate. From this comes the necessity of introducing, in addition to the geometric constraints, also mechanical (temporary) constraints during the impact. Such constraints may be characterized directly if an actual constitutive relation for the joint is assumed, or indirectly if additional supplementary hypotheses related to the resulting motion of the body after the impact are introduced.

Such additional hypotheses can be:

- a) limitations of the degrees of freedom of the system, such as in [Housner G. W., 1963]; and
- b) quantification of the restitution coefficients, such as in [Ishiyama Y., 1982].

The preceding hypotheses can be seen as a particular case of mechanical characterization of the joints. It results in fact that a) often coincides with the introduction of infinitely rigid joints; and b) can be seen as a quantification of the impulses in the phases of deformation and restitution, which implies the definition of a constitutive relation for the joint.

In the field of block dynamics, analysis methods are usually classified into those that consider deformable and rigid contacts. The first group hypothesize a constitutive relation for the temporary joint; the second hypothesize rigid contacts, without describing the characteristics of motion during the impact. An alternative approach is represented by the methods that identify the act of motion after the impact (for the case of bodies with rigid joints) with a variational approach, by minimizing a functional which in the case of [Sinopoli A., 1987] is Robin's functional.

4.1.1. Milne's Studies

Milne (1881) studied the problem of columns overturning when subjected to seismic activity, pointing out that the period of oscillation of a column depends on the maximum rotation to which it was subjected and that the initiation of rocking doesn't necessarily imply overturning since the seismic activity provides the column with "overturning energy acting in opposite directions".

He has conducted experimental studies, subjecting cylindrical columns to alternating displacements using a rudimental, but effective vibrating table (Figure 4-1).

The columns had a diameter of 2.5 *cm* and varied in height from 5 to 8 *cm*; the objective of the test was to evaluate for which displacement of the weight (*W*) there would be column overturning. With known initial displacement which yields the period of oscillation *T*, the maximum oscillation width (*S*), and the maximum velocity (*V*) of the "vibrating table", one can determine the average acceleration (\bar{A}) and the maximum acceleration (*A*) that causes the overturning of the column:

$$\bar{A} = 4 \frac{V}{T}; \quad A = \frac{V^2}{S}$$

4.1.2 Perry Model

Perry (1881) studied the rotation of a column (Figure 4-2), whose center of rotation coincides with a corner of the base, hypothesizing the friction to be such that relative translations are avoided.

The author does not address the problem of impact, but defines the equations which govern motion between one impact and the next.

$$\ddot{\theta} = -\frac{m \cdot g \cdot r}{m \cdot i_o^2} \sin(\alpha - \theta)$$

where m is the mass of the body, g the acceleration of gravity, r the distance of the centroid from the center of rotation and i_o is the gyrotory radius around the center of rotation. The precedent equation for slender blocks becomes:

$$\ddot{\theta} = -\frac{m \cdot g \cdot r}{m \cdot i_o} (\alpha - \theta)$$

and its solution is:

$$\theta = \alpha + C_1 \cdot e^{nxt} + C_2 \cdot e^{-nxt}$$

where : $n = \sqrt{\frac{g \cdot r}{i_o}}$

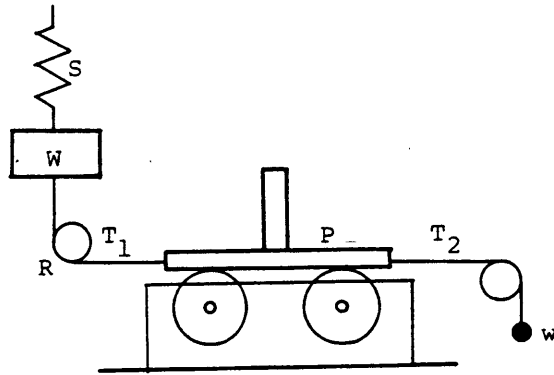


Figure 4-1. Scheme of the shaking table used by Milne.

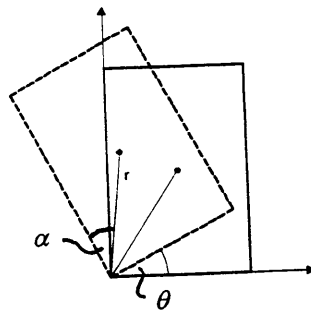


Figure 4-2. Scheme of the Perry Model.

The author, from the precedent expression evaluates the time necessary for angle θ to go from the initial value θ_0 to an assigned value θ_* , hypothesizing two different initial conditions:

$$\begin{aligned} \text{a)} \quad & \theta = \theta_0, \quad \dot{\theta}_0 = 0; \\ \text{b)} \quad & \theta = 0, \quad \dot{\theta} = \dot{\theta}_0. \end{aligned}$$

The type-a conditions refer to the case of a block subjected to an initial rotation around its base edge and it gives (with $\theta_*=0$):

$$t' = \frac{1}{n} \cdot \ln \left[\frac{\alpha}{(\alpha - \theta_0)} \pm \sqrt{\left(\frac{\alpha}{(\alpha - \theta_0)} \right)^2 - 1} \right]$$

where $\alpha = \arctg(b/h)$.

The type-b conditions refer to the case of a block, initially motionless, and subjected to a given initial angular velocity and the solution is:

$$\theta = \alpha - \frac{n \cdot \alpha - \dot{\theta}_0}{2n} e^{nt} - \frac{n \cdot \alpha + \dot{\theta}_0}{2n} e^{-nt}.$$

We further have:

$$t = \frac{1}{n} \cdot \ln \left[\frac{n \cdot (\alpha - \theta)}{n \cdot \alpha - \dot{\theta}_0} \pm \sqrt{\left(\frac{n \cdot (\alpha - \theta)}{n \cdot \alpha - \dot{\theta}_0} \right)^2 - \frac{n \cdot \alpha + \dot{\theta}_0}{n \cdot \alpha - \dot{\theta}_0}} \right],$$

that for $\theta = \alpha$ becomes:

$$t' = \frac{1}{n} \cdot \ln \left(\frac{\dot{\theta}_0 + n \cdot \alpha}{\dot{\theta}_0 - n \cdot \alpha} \right)^{\frac{1}{2}}$$

Thus if $\dot{\theta}_0 < n\alpha$ the block will be subjected to a rocking motion, if $\dot{\theta}_0 = n\alpha$, the block reaches the unstable position $\theta = \alpha$ for $t = \infty$ with zero angular velocity, and finally if $\dot{\theta}_0 > n\alpha$ the block reaches the position $\theta = \alpha$ in a finite period and will later overturn. Further, for a given value of $\dot{\theta}_0$, the time necessary to reach the unstable position increases with the increase of $n\alpha$ and it follows that the probability of toppling diminishes with the reduction of the slenderness.

Perry examines further the case of a block subjected, during the rocking motion and in the absence of impact, to an acceleration parallel to the supporting plane, of the type:

$$\ddot{X} = a \cdot \sin(pt)$$

In this case he provides the equation for slender blocks:

$$\ddot{\theta} = \frac{g \cdot r}{i_o} (\theta - \alpha) + a \cdot \sin(pt)$$

and the relative solution:

$$\theta = \alpha - \frac{a}{2n} \left[\frac{p \cdot \cos(pt) + n \cdot \sin(pt)}{n^2 - p^2} - \frac{n \cdot \sin(pt) - \cos(pt)}{n^2 + p^2} \right] + C_1 \cdot e^{nt} + C_2 \cdot e^{-nt}$$

4.1.3 The Housner Model

Housner's studies [Housner G. W., 1963] on block dynamics arise from the necessity to provide an explanation of the dynamic behavior of a certain storage tanks ("Golf Ball Tanks") which, during the 1960 earthquake in Chile, showed an apparently abnormal behavior. Thus he systematically examines rigid block dynamics, subjected to both free oscillations and external actions and arrives at the conclusion that, given equal slenderness, rigid blocks are more stable with increasing height. The preceding conclusion thus explains the good static behavior of some tall slender storage tanks when compared to shorter but equally slender ones.

The author takes Perry's model, posing however the problem of the complete characterization of block motion, studying the effect of the impacts that occur during rocking. With regard to free oscillations, with initial conditions of type-a of the Perry model (4.1.2), one finds that it is possible to distinguish four types of motion which act in succession (Figure 4-3):

- 1) the block, starting from an initial condition $\theta = \theta_0$ and $\dot{\theta}_0 = 0$, reaches, turning on edge o , the resting position $\theta = 0$ with angular velocity $\dot{\theta}_1$, at time t_1 ; occurring a phenomenon of impact with consequent dissipation of energy;
- 2) the block begins a rotation around corner o' , with initial angular velocity $\dot{\theta}_2 < \dot{\theta}_1$, reaching at time t_2 the position $\theta_1 < \theta_o$, characterized by a maximum of potential energy;
- 3) the block initiates a new motion around the corner o' , with zero initial angular velocity, and initial rotation equal to θ_1 , reaching the resting position with angular velocity $\dot{\theta}_2$, at time t_3 ;
- 4) the block rotates around corner o with initial angular velocity $\dot{\theta}_3 < \dot{\theta}_2$, reaching at time t_4 the position $\theta_2 < \theta_1$, characterized by a maximum of potential energy.

In the Housner model the following parameters are significant:

$\frac{\theta_{n+1}}{\theta_n} \left(\frac{\theta_2}{\theta_1}, \frac{\theta_1}{\theta_o} \right)$	relationship between two maximum consecutive rotations, in correspondence with the times at which the potential energy is at its maximum;
$\frac{\dot{\theta}^+}{\dot{\theta}^-} \left(\frac{\dot{\theta}_2}{\dot{\theta}_1}, \frac{\dot{\theta}_3}{\dot{\theta}_2} \right)$	relationship between the angular velocities before and after each impact;
$\frac{T}{2} = 2 \cdot t_2$	time interval between two consecutive impacts

The author determines the above quantities starting with the motion equation:

$$\ddot{\theta} = -\frac{g \cdot r}{i_o} \cdot \sin(\alpha - \theta)$$

and assuming equality of the moments of the quantity of motion around the corner in which the impact takes place in the instant immediately before and after the impact.:

$$i_o \dot{\theta}^- - 2 \cdot r \cdot b \cdot \dot{\theta}^- \cdot \sin(\alpha) = i_o \dot{\theta}^+$$

It in fact results that:

$$\sigma = \frac{\dot{\theta}^+}{\dot{\theta}^-} = 1 - \frac{2 \cdot r^2 \cdot \sin^2(\alpha)}{i_o} \quad (4-4)$$

$$\frac{\theta_n}{\alpha} = 1 - \sqrt{1 - \sigma^{2n} \left[1 - \left(1 - \frac{\theta_o}{\alpha} \right)^2 \right]} \rightarrow \frac{\theta_{n+1}}{\theta_n} = \frac{1 - \sqrt{1 - \sigma^{2(n+1)} \left[1 - \left(1 - \frac{\theta_o}{\alpha} \right)^2 \right]}}{1 - \sqrt{1 - \sigma^{2n} \left[1 - \left(1 - \frac{\theta_o}{\alpha} \right)^2 \right]}} \quad (4-5)$$

$$\frac{T_n}{2} = \frac{2}{n} \tanh^{-1} \sqrt{\sigma^{2n} \left[1 - \left(1 - \frac{\theta_o}{\alpha} \right)^2 \right]} \quad (4-6)$$

From (4-4) the relationship between kinetic energy before and after impact can be calculated, which is the restitution coefficient $r = \sigma^2$, which for rectangular blocks ($2b \times 2h$) becomes:

$$r = \left[\frac{2h^2 - b^2}{2(b^2 + h^2)} \right]^2 \quad (4-7)$$

Removing the hypotheses of contact at the corners of the block, and hypothesizing that the point of contact during the impact is placed at the distance ηb from the corner (Figure 4-4), the value of the restitution coefficient varies according to [Giannini R., 1985]:

$$r = \left[\frac{4 \left(\frac{h}{b} \right)^2 - 2 + 3\eta}{4 \left(\frac{h}{b} \right)^2 + 4 - 3\eta} \right]^2 \quad (4-8)$$

that for $\eta = 0$ coincides with the value given by Housner, while for $\eta \rightarrow 1$ it tends toward 1. The case in which $\eta \rightarrow 1$ is a limit condition in correspondence to which the contact points between the block and the supporting base coincides which is the case, for example, if the base is convex.

The principal conclusions deducible from the Housner model are that the restitution coefficient depends exclusively on the slenderness of the block, and in particular it increases with increasing slenderness, and also that the time interval between two consecutive impacts decreases with the number of impacts.

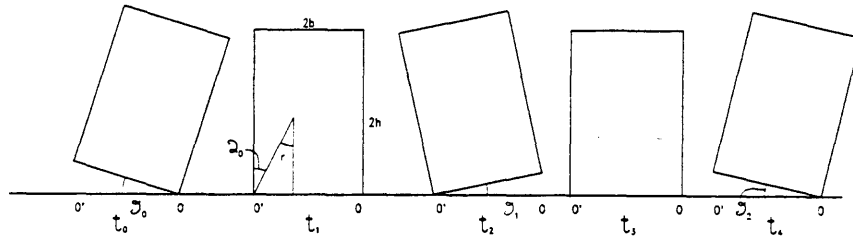


Figure 4-3. Housner model.

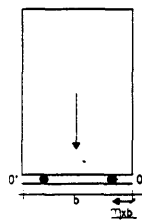


Figure 4-4. Block with eccentric contacts.

4.2 DEFORMABLE CONTACT MODELS

Among the deformable contact models one can identify two different approaches. The first considers elastic contacts as monolateral-type constraints, and it may be considered an extension to the dynamic case of the gap element model described in the previous chapter; in this case the modeling of the dissipative effects during impact can be obtained introducing viscous-type forces. The second approach considers bilateral-type constraints, and the constitutive relationship is such as to simulate also the gravity force. In fact, a block subjected to rotation, with a center coinciding with one of its corners, is subject to an equilibrating moment M which is a function of the rotation angle:

$$M(\theta) = \pm P r \sin (\alpha - \theta) \quad (4-9)$$

(4-9) can be approximated with a continuous softening rule such as:

$$M^* = -a(\text{sign}\theta)(e^{-\gamma (\text{Sign}\theta)\theta} + \frac{(\text{sign}\theta)\theta}{a} - 1)$$

which is the sum of two equations, one of which represents the two straight lines passing through the point at which (4-9) intersect the axes (M , θ), the other is an exponential-type curve which varies with γ which represents initial stiffness of the joint (Figure 4-5a). The first part of the curve $M^*(\theta)$ (Figure 4-5b), gives the elastic deformations of the block before it can rotate rigidly. If $\theta > \alpha$, the block exceeds the position of maximum potential energy and becomes unstable. The block can therefore be modeled with a one degree of freedom elastic oscillator (Figure 4-5c) of the softening-type approximating the forces given by (4-9). The equation which govern the equivalent elastic oscillator motion is:

$$m^* \ddot{\theta} + c \dot{\theta} + M^* = 0,$$

where m^* is the generalized mass and $c\dot{\theta}$ are viscous-type forces.

4.2.1. The Angotti -Toni Model

The authors Angotti and Toni [Angotti F., 1982] study the dynamic behavior of a rigid block with three degrees of freedom resting on a monolateral elastic half space. (Figure 4-6a). The model is aimed at the study of the interaction between electrical equipment or low rise buildings and the foundation soil in case of dynamic actions. The elastic half-space is modeled as a layer of independent no tension vertical springs, with piecewise linear constitutive relation (Figure 4-6b). The lateral reaction of the foundation is modeled by independent bilateral springs whose constitutive relation is described in Figure 4-6c.

In [Angotti F., 1984] the authors introduce into the preceding model viscous elements for the simulation of the dissipative effects of the soil-structure interaction, and further study the dynamic behavior of two overlapping blocks (Figure 4-7). The joint between the two blocks is rigid, and the lower block rests on a monolateral elastic half space. The motion of the upper block can only be rocking, even if the possibility of total detachment of the bodies, as final limit condition, is considered. The system is subjected to a sinusoidal base acceleration, and its response to increasing amplitude of the oscillation (with all other parameters fixed) is studied. The authors point out how the time necessary to reach the total detachment of the bodies doesn't always decrease with increasing amplitude of the base oscillation.

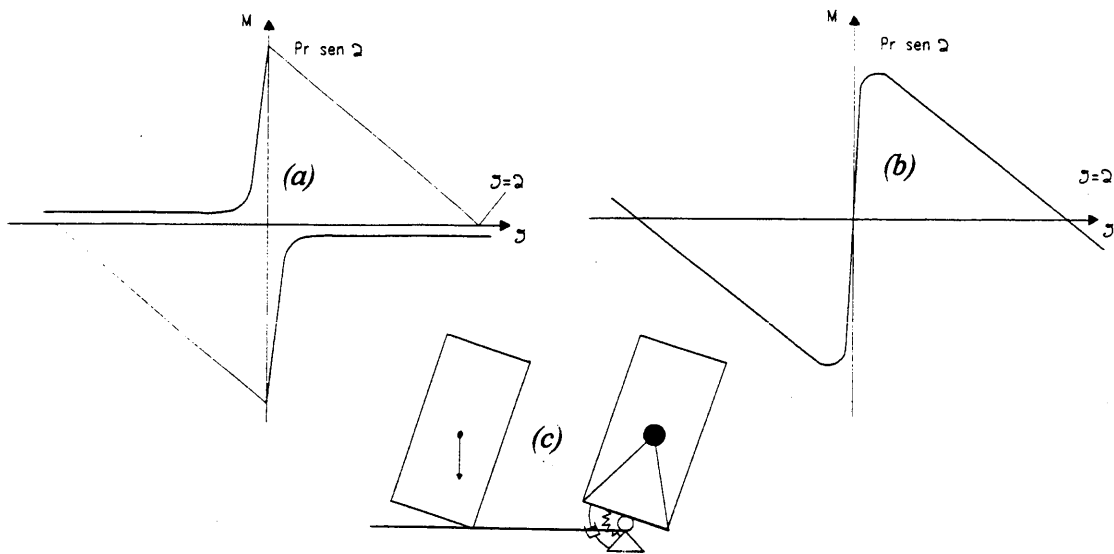


Figure 4-5. Scheme of equivalent elastic oscillator model.

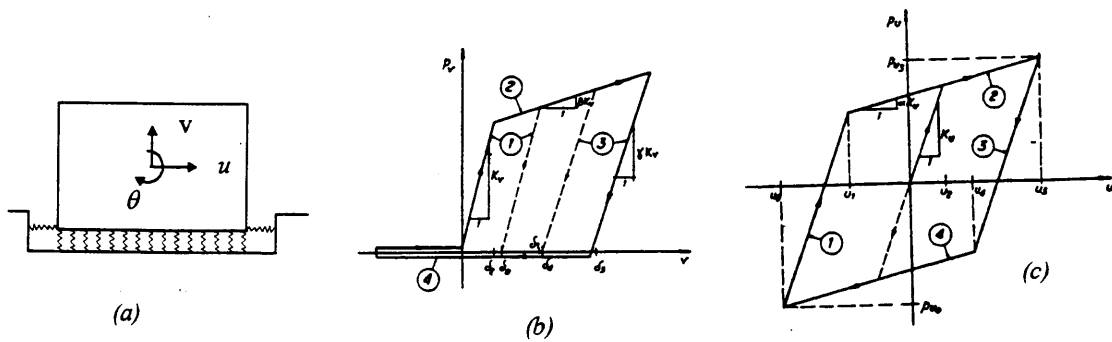


Figure 4-6. Block on monolateral elastic soil [Angotti F., 1982].

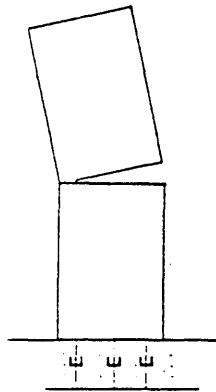


Figure 4-7. Overlapping block structure [Angotti F., 1984].

4.3 THE DISCRETE ELEMENT METHOD

From the previous review of available methods for the study of block dynamics, it appears that most of them are restricted in their use to simple, predefined structural configurations, whereas the study of historical structures, viewed as assemblages of blocks, require the maximum flexibility and generality in defining the structural configuration. Such flexibility is provided by the DEM, which was initially developed in the field of rock mechanics, and it is proposed in this work as a powerful numerical methodology for studying the seismic response of historical block structures.

The DEM, after being applied to the investigation of the stability of fractured rocks, has later been used for various problems of dynamic interaction of multiple bodies in fields ranging from constitutive modeling of concrete and granular material to blasting. In the following only general concepts on the DEM will be presented, while details concerning its formulation can be found elsewhere (e.g. [Cundall, 1989], and [Williams, 1985]).

In the implementation adopted in this work (both in the program DECICE [Intera Technologies, 1988], and UDEC [UDEC, 1996]), the element has a quadrilateral shape and 4 nodes at its corners. It can translate and rotate freely (3 d.o.f in 2D) and it can deform elastically similarly to a finite element. It is subjected to gravity and boundary forces coming from the interaction with other elements.

The motion of its centroid is governed by the dynamic equations, while its deformations are described by linear elasticity. An explicit integration scheme for the time domain solution of the dynamic equations is adopted.

The interaction between elements is provided by contact elements which are located in the nodes and become active only when the node gets close to the surface of

another element. When the contact between a node and a surface is active two interaction forces are updated at each time step: one normal and another tangential to the contact surface. The normal force N may be viewed as generated by a no-tension linear spring with stiffness K_n which deforms according to U_n , the normal component of the relative displacements between node and surface, while the tangential force T , which simulates the Coulomb friction force, is obtained by an elastoplastic spring with initial stiffness K_t , which deforms according to the tangential component of the relative displacement U_t , and whose plastic limit is given by $T = N \eta$ (where η is the friction coefficient, and N is the current normal force at the node).

Note that the contact may occur between any node and any surface of two different elements therefore the number of potential contacts is in the order of n^2 (where n is the number of nodes). Since the time step dt is usually very small, to ensure stability and accuracy of the solution, and given that at every time step all potential contacts have to be checked for activation or de-activation, an efficient algorithm for contact detection is one of the essential features of the DEM (consider that in the case studies examined in this work n was in the order of 10^2 and the number of time steps for each analysis in the order of 10^5 to 10^6).

The energy dissipation which takes place during the impact is a complex phenomenon which, in this approach, is simply modeled by a linear viscous element in parallel with the normal interaction spring. The parameter C defining the viscous element is chosen proportional to the normal interaction stiffness K_n : $C = \alpha K_n$. Care should be used in selecting α , since it determines the range of high frequencies which are overdamped and therefore cannot be transmitted through a given contact affecting, consequently, both the numerical stability and the accuracy of the solution. In quasistatic problems, where loads are applied slowly and a static solution is searched, a viscous damping proportional to the mass M of the element, and defined by a parameter $C = \beta M$, may be applied to the motion of its centroid in order to expedite solution convergence. In this case β determines the range of low frequencies which are overdamped. Its

selection does not affect numerical stability, but it is critical for solution accuracy since low frequencies generally govern the system response.

In summary, in a DEM model it is required to define the following critical interaction parameters: K_n , K_t , η , α , and/or β . While the friction coefficient η , may be taken from standard lab tests, the remaining 4 parameters, which represent in a lumped form the mechanical property of the joint, are not easily measured with direct tests and should be assigned with care as described in the following chapters.

It can be noticed that a major advantage in using the DEM is the capability of retaining all the degrees of freedom of each element (for example, it does not restrict the analysis to pure rocking of the blocks); and of accurately describing the closure and opening of joints without the need of specifying where they will occur. On the other hand, the phenomena which accompany the interaction among blocks are described by simple discrete frictional and impact models. Nevertheless, the DEM proves to be a valuable tool when the interest is in the prediction of the collapse mechanisms and in the determination of the global force transfer among blocks, more than in the detailed characterisation of the local stress and strain fields in the vicinity of the contact.

**Chapter 5. QUASISTATIC ANALYSIS OF BLOCK STRUCTURES WITH
CURRENT D.E.M.**

- 5.1. SEISMIC RESPONSE OF ANCIENT MASONRY BUILDINGS
- 5.2. EXPERIMENTAL TESTS ON SMALL SCALE WALL MODELS
 - 5.2.1 In-plane failure tests of 3 small scale wall models
 - 5.2.2. Measure of friction parameters
- 5.3. D.E.M. MODELING OF THE QUASISTATIC BEHAVIOR OF BLOCK STRUCTURES
 - 5.3.1. Modeling
 - 5.3.2. Validation of the analysis procedure
 - 5.3.3. Parametric study of model sensitivity
 - 5.3.4. Discrete Element simulation of the experimental tests
- 5.4 CONCLUSION

5. QUASISTATIC ANALYSIS OF BLOCK STRUCTURES WITH CURRENT D.E.M.

From the review of the methods currently available for the quasistatic analysis of seismic response of block structures, presented in Chapter 3, it appears that this problem is still a challenging task. The opening and closure of the joints, and the sliding and rotation of the single blocks determine a complex nonlinear response which is not fully described by the existing analysis methods.

In fact, limit analysis, recently extended to include also the dependence of friction from the normal load [Livesly,R.,1992, Baggio, C.,2000], in addition to being restricted to static equilibrium problems, can predict only the initial motion of the system, without being able to capture a subsequent stabilization of the structure and a possible different global failure mechanism for higher loads. Also in the context of deformable contact models, it was noted that, specialized finite elements such as "gap elements", are not particularly suited for automatically detecting the activation and deactivation of a large number of contact surfaces during the evolution of the system response [Mamaghani,I.,1999]. The method of finite elements with the smeared crack approach, not mentioned in the previous review because not specific to block structures, has also been used for modeling brick walls [Kelly,T.,1996]. However it is limited by the impossibility of considering the effects of the layout of the bricks and of the presence of well defined lines of fracture within the structure.

The Discrete Element Method, as illustrated in the previous section, with the explicit modeling of discontinuities, and its sophisticated contact detection algorithms, appears to be capable of overcoming some of the previous limitations. However, the DEM, developed in the field of rock mechanics, and employed in various problems of dynamic interaction of multiple bodies, has not been systematically applied yet to the study of the seismic vulnerability of historical block structures, and this is the purpose of the current work.

In this chapter, the DEM will be applied to the quasistatic analysis of block structures. The next chapter discusses the applicability of the DEM for the dynamic analysis of block structures. Subsequently, in Chapter 7, a new DE joint model is proposed for overcoming the observed limitations.

In the following of this chapter we will focus on the seismic behavior of opus quadratum walls (regular masonry of squared stone with no mortar)¹, both for the simplicity of their geometrical layout, and for the historical importance of the constructions in which they are found.

In section 5.1, some basic observations on how masonry buildings tend to fail under seismic actions are presented. Based on such considerations the relevance of the in-plane response of opus quadratum walls is explained, and consequently such type of behavior will become the focus of most of the rest of this work.

In section 5.2, a series of experimental tests on small scale wall models made of stone blocks and subjected to in-plane lateral loads (simulating the seismic action) is illustrated. Such tests were performed mainly for obtaining well documented data to be used in the evaluation of the DE predictions. Tests for measuring the friction parameters related to the specific type of stone blocks used in the wall models were also performed with the objective of measuring the friction coefficient to be used in the analysis, and also for evaluating other aspects of the friction behavior, not accounted for in the basic Coulomb friction model (usually adopted in DEM), such as the dependency of the friction coefficient with: (1) the normal contact force, (2) the degradation of the contact surfaces, and (3) the sliding velocity.

In section 5.3, the analysis, with current DEM, of opus quadratum walls subjected to quasistatic in-plane lateral forces is presented. After a series of analyses were performed for evaluating the sensitivity of the response with respect to certain model

¹ A survey of historical structures including opus quadratum walls is illustrated in Chapter 2.

parameters, the DE predictions were compared with limit analysis results and the experimental data obtained in section 5.2.

Finally the potentials and the limitations of the DE method for the quasistatic analysis of block structure are highlighted in the conclusion.

It should be mention also that the practical application of current DEM to the quasistatic analysis of historical structures is further illustrated in the Appendices, where two pilot studies concerning respectively the out-plane and in-plane behavior of masonry walls are presented.

5.1 SEISMIC RESPONSE OF ANCIENT MASONRY BUILDINGS

Preliminary to the experimental and analytical study of the seismic response of historical structures, it is useful to briefly review the usual failure modes observed in such type of buildings during past earthquakes. Extended information of this topic may be found in the proceedings of specialized conferences such as the "US-Italy Workshop on Guidelines for Seismic Evaluation and Rehabilitation of Unreinforced Masonry Buildings" [Abrams,D.,1994], and the "International Conference on Structural Repair and Maintenance of Historical Buildings" [Brebbia, C., 1991].

A simple scheme of an historical buildings consists of three elements: roofing, horizontal and vertical elements. The vertical elements can be classified as walls and columns and both can be either monolithic or multiblock. They are considered monolithic if composed of a single block or if the constituent blocks are strongly connected between each other by well conserved and effective mortar.

The block structures, which are the specific subject of this investigation, are those in which the elements are not strongly interconnected. Such lack of connection in the building may occur both at a global level between roofing, horizontal structures and vertical elements, and at the component level in case of columns or walls composed of multiple blocks interacting only through frictional contacts. From the post-earthquake observations it can be stated that the stronger are the connections among the building elements, the higher is the seismic resistance of the building which tends to behave as a monolithic box type structure as opposed to a set of disconnected walls and columns. In this last case the failure occurs according to the so called "first collapse mode", while in presence of a box type structure the "second collapse mode" may take place [Giuffrè, A., 1994].

It is of interest to notice that in the renowned construction manual of Rondelet published in France in 1802, reflecting the empirical knowledge on masonry constructions accumulated over centuries of experience, the importance of the

slenderness of a masonry wall for its stability with respect to lateral loads was precisely stated as it follows: *"Therefore through observations made on a very large quantity of buildings of all kinds it is found that a wall will have great stability if its thickness is the eighth part of its height; that the tenth part gives it medium stability, and the twelfth one the lowest degree of stability it can have"*. But even more interesting is the understanding, by Rondelet, of the influence of the connections between the walls on the overall strength with respect to lateral loads, as it is reflected by the collapse mechanisms illustrated in Figure 5-1.

In the **first collapse mode** the walls, which are not well connected to rest of structure, tend to fail out of the plane by rotating monolithically around the base as shown in Figure 5-2. In theory, sliding of the base could also be possible, but the typical dimensions of the walls (height over thickness) exclude this possibility. The cases reported in Figure 5-3 and Figure 5-4 clearly refer to mechanisms of the first type. They regard, respectively, the 1906 Messina earthquake, and the 1990 earthquake that also occurred in Sicily. If the wall does not interact with other building elements and it remains monolithic while rotating under the cyclic action of the earthquake, it behaves similarly to a rigid rectangular block rocking on a rigid base. In such case the response is governed by the slenderness and height of the wall, and by the dissipation which takes place during the impacts with the base (as illustrated in Chapter 4). In some cases, the lack of connection between the building elements may even cause the building to behave as the 2D model represented in Figure 5-5 constituted by rigid blocks (interacting through frictional contact only) representing the walls and the floors of a 2-story building. Even such simple model is not easily studied with traditional analysis methods when the number of elements increases, as observed in [Angeletti, P., 1994], while it can be readily analyzed with the DEM as it will be illustrated in the following. In particular, in Appendix A, we will illustrate the use of the DEM for analyzing a similar scheme describing the critical section of a typical medieval church subjected to lateral loads.

In the **second collapse mode**, which arises when the orthogonal walls are well connected among themselves, failure may occur due to the forces acting in the plane of the wall (Figure 5-6). Such wall may collapse by separation of large portions of material which may rotate monolithically, or it may be subjected to a disgregation due to the sliding, rotation, and eventually separation of the blocks constituting the wall, or else it may be interested by a localized, or diffuse, sliding of the blocks without rotation. The possibility of predicting which one of the previous mechanisms will take place is of particular interest for the evaluation of the seismic vulnerability of the structure. Such problem, as we have already noted, is not well studied with currently used analysis methods, and in this chapter we will illustrate that the DEM is, in fact, quite appropriate for approaching this category of problems. More specifically, Appendix B will be dedicated to the study, with DEM, of the factors which may influence the type of in-plane failure mechanism of an opus quadratum wall. These factors, as it will be discussed later, involve the slenderness ratio of the blocks, and the loading conditions of the wall.

Before discussing the applications, however, we need to evaluate the performances of the DEM, and for this purpose it is necessary to obtain well documented experimental data, not available in the literature, on the behavior of opus quadratum walls subjected to lateral loads. This type of experimentation is described in the following section..

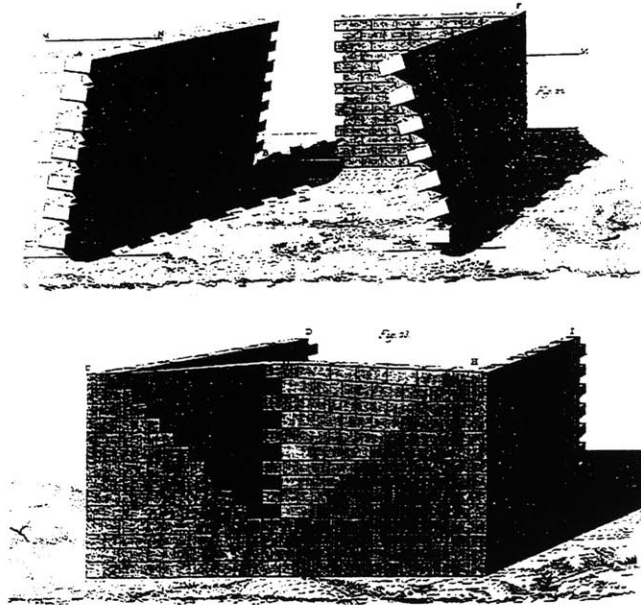


Figure 5-1. Failure modes of a masonry wall according to Rondelet.

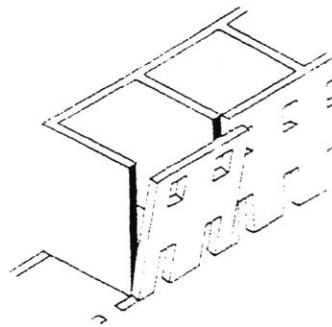


Figure 5-2 *First collapse mode* of a masonry building.



Figure 5-3. Messina, 1906.



Figure 5-4. Carlentini, 1990.

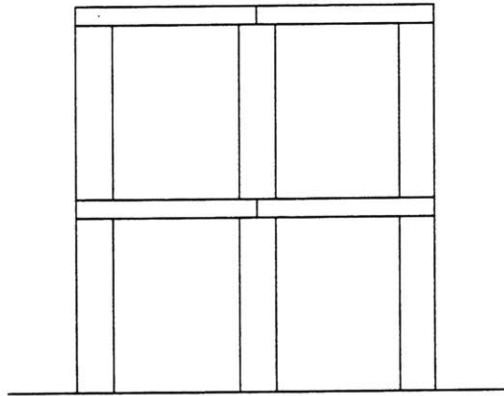


Figure 5-5. "Disconnected" frame.

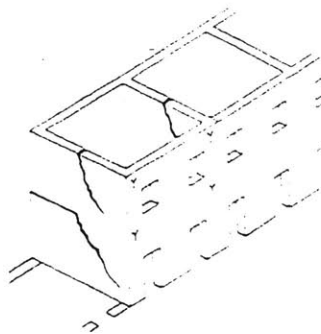


Figure 5-6. *Second collapse mode* of a masonry building.

5.2 EXPERIMENTAL TESTS ON SMALL SCALE WALL MODELS

The purpose of this section is the experimental investigation of the mechanical response of *opus quadratum* walls subjected to slowly increasing lateral forces, acting in the plane of the wall, simulating the seismic action. We consider the *opus quadratum* because of its well defined geometrical layout - which simplify the modeling - and also because it is utilized in the most important ancient constructions. Moreover, as it will be observed later in Appendix B, it can serve as a qualitative mechanical model for the evaluation of the behavior of other types of masonry such as the irregular stone masonry. Three small scale wall models constituted by stone blocks have been tested as reported in the following section 5.2.1.

Since the objective of the experimentation is that of acquiring data for evaluating the predictions of the DEM, and given that in this method it is necessary to explicitly model the friction between the blocks, a series of experimental tests for measuring the friction parameters of the specific type of blocks used in the wall models have been performed and will be described in section 5.2.2, where also a brief review of some analytical model proposed for friction is presented.

5.2.1 In-plane failure tests of 3 small scale wall models

The in-plane failure behavior of small scale models of opus quadratum walls has been studied experimentally applying slowly increasing horizontal forces proportional to the mass of each element. Such forces simulated the earthquake action. This loading condition was obtained with a simple experimental set-up consisting of a plane with variable inclination angle (as already adopted in [Ceradini V, 1992]). In order to obtain in-plane lateral forces the wall was positioned in a plane orthogonal to the axis of rotation of the base. The objective of the tests was the determination of the failure load and the corresponding failure mechanism of the brick walls.

The models have been assembled, without mortar, with tuff peperino blocks with average dimensions of $17.5 \times 40 \times 80$ mm, and an average weight of 120g. Despite the attention used in accurately cutting the bricks, variations of the order of 10^{-1} mm were found. The average friction coefficient of the material was approximately $\alpha=0.6$, as it will be illustrated in detail in the next section.

The analogy between the seismic action and the loading condition obtained with the tilting table is quite clear. In fact, a rigid block of mass m placed on a base subjected to an acceleration $a(t)$ undergoes an horizontal inertia force $m a(t)$ (in the hypothesis of no displacement of the block with respect to the base). If the friction angle between the block and the base is φ , and referring to Figure 5-7-a for the meaning of the symbols, we have the following two conditions for the stability of the block:

$$\frac{a}{g} \leq \frac{b}{h} \tag{5-6}$$
$$\frac{a}{g} \leq \text{tg}(\varphi)$$

The first is the condition for preventing a collapse by overturning of the block, the second one for preventing failure by sliding.

Analogously, if a block is placed on an inclined plane with angle ϕ (see Figure 5-7-b), the corresponding stability conditions are:

$$\begin{aligned} \operatorname{tg}(\phi) &\leq \frac{b}{h} \\ \operatorname{tg}(\phi) &\leq \operatorname{tg}(\varphi) \end{aligned} \quad (5-7)$$

Comparing (5-6) with (5-7) it results that the maximum value of $\operatorname{tg}(\phi)$ for which the wall on the inclined plane is stable, coincides with the maximum base acceleration, given in terms of g , for which a block on a horizontal plane would not slide or rotate.

In the following we will refer to the failure load λ obtained from the test of a certain wall on the inclined plane. This means that if at failure the component of the gravity load normal to the block layers is N , then the one perpendicular to it is λN (see Figure 5-7-c). In other terms λ is the ratio of the parallel and normal components of the gravity load and it can be determined experimentally by the value of $\operatorname{tg}(\phi)$ at failure.

Three brick walls with increasing number of elements (labeled WALL1, WALL2, and WALL3), have been tested on the inclined plane. The blocks were positioned with the longer side orthogonal to the wall, so that the block dimensions, in the plane of the wall, were: base $b=40\text{mm}$, and height $h=17.5\text{mm}$. All walls had equal base length, measuring $H=400\text{mm}$, and equivalent to the length of 10 full blocks. The 3 walls had, respectively, 7, 11, and 23 number of layers. Notice that the bricks of the bottom layer were fixed to the base plane in all 3 cases, therefore the effective height of the walls were: $6 \times 17.5 = 105\text{mm}$ for WALL1, $10 \times 17.5 = 175\text{mm}$ for WALL2, and $22 \times 17.5 = 385\text{mm}$ for WALL3.

The failure configurations and the failure load λ obtained with the inclined plane for the 3 walls are given in Figure 5-8.

A complex mixed mode of collapse involving the combined rotation and sliding of several bricks took place in all three cases as shown in figure.

Concerning WALL1, in addition to the collapse mode shown in figure, other tests have yielded a partial failure of the wall involving only the right brick of the top 2 layers, initiated by sliding of the top one (see Figure 7-62b). Such partial failure mode occurred for the same failure load $\lambda=0.5$ observed in the mixed mode. This variability in the experimental response should be attributed mainly to the geometrical imperfections of the bricks, and the slight variations in the geometrical configuration of the system due to the manual repositioning of the blocks. Such causes are particular evident in WALL1 due to the limited number of blocks involved in the failure mechanism.

In WALL3 it should be noticed the presence of a localized diagonal band in which most of the sliding takes place at failure.

It is also important to notice, that in all 3 cases slight displacements of the blocks were observed starting from approximately 80% of the failure load.

It should be mentioned that other similar tests, to be described in Chapter 7 and in Appendix B, have been performed on the inclined plane with the same type of blocks, in order to study certain specific aspects of the mechanical response of a brick wall, such as the effects of the geometrical imperfections of the blocks, and the influence of the loading conditions on the in-plane failure load and corresponding collapse mechanisms of the opus quadratum wall.

Before approaching the Discrete Element modeling of the opus quadratum walls, the frictional behavior of the specific blocks used in the experimental tests will be investigated as illustrated in the next section.

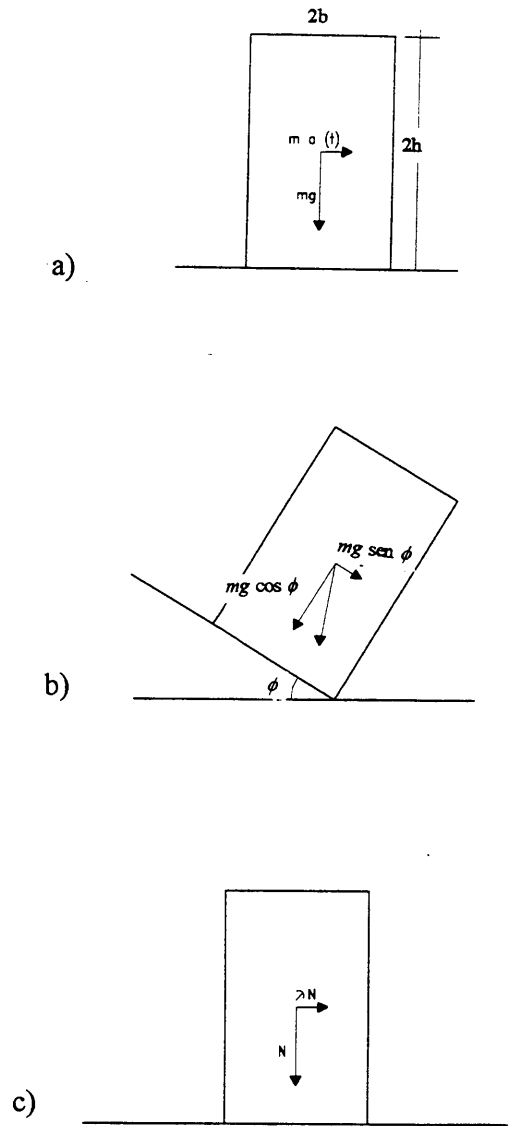
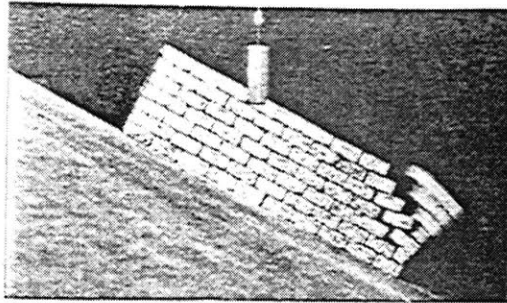
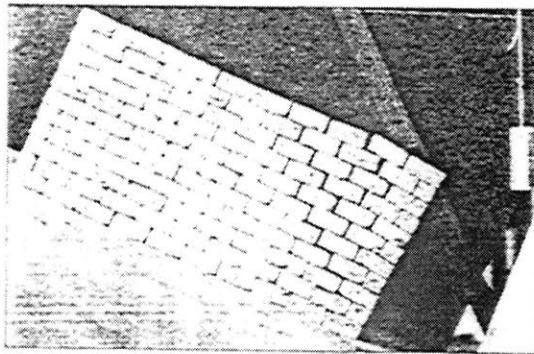


Figure 5-7. (a) Block on a moving base, (b) block on an inclined plane, and (c) block subjected to a centroidal force.



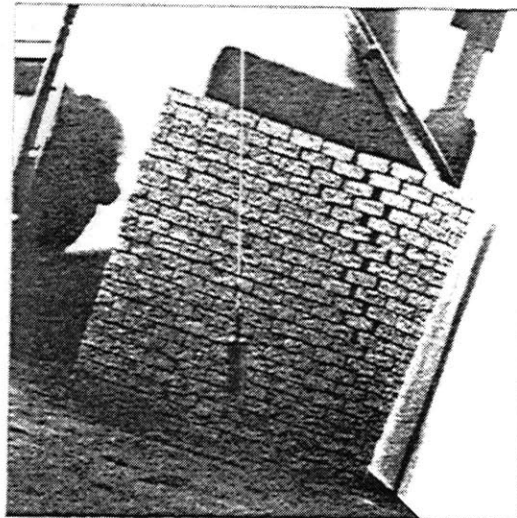
WALL1

$$\lambda = 0.5$$



WALL2

$$\lambda = 0.47$$



WALL3

$$\lambda = 0.35$$

Figure 5-8. Experimental failure configurations of small scale brick walls on inclined plane.

5.2.2 Measure of friction parameters

Given the essential importance of friction in the in-plane response of an opus quadratum wall, we have performed a series of tests in order to characterize the frictional behavior of the peperino blocks used in the previously described experimental tests. This has provided data for the calibration of the DE models and a better understanding of the phenomenon.

It should be reminded that the frictional behavior of a joint is a complex phenomenon which has been studied extensively, and for which comprehensive constitutive models have been proposed both in the fields of structural engineering (Fardis and Buyukozturk, 1979), and rock mechanics (Plesha, 1987), which, among other aspects, account also for dilatancy and contact surface degradation. In the following we will restrict our review to some basic analytical models of friction in order to better plan and understand the experimental tests which are of interest for the specific problem under investigation.

Analytical Models

In [Coulomb C.A., 1776] it is postulated that two bodies in contact interact through reciprocally orthogonal forces (F , N). Force F lies in the plane tangential to the two bodies and can assume, in it, whatever direction. Based on the experiments carried out by M. Amontons he further states that there is no relative displacement between the two bodies if:

$$|F| \leq c|N| \quad (5-1)$$

where c is the friction coefficient. Coulomb's formulation is a phenomenological model, because it does not specify the mechanical reasons from which eq. (5-1) derives. The determination of (5-1) on the ground of a mechanical models requires that the

morphology of the interacting surfaces is known. These rough contact surfaces can be considered either deformable or rigid.

As an example of the first type of contact models, in [Ruina A. L., 1985] the interacting surfaces, referred to as joints in the following (see Figure 5-9), contain intervals of length P (called *continuum points*), formed by microscopic asperities of dimension m_1 , (called asperities of the first order) mixed with other intervals containing asperities of dimension $m_2 \ll m_1$ (called asperities of the second order). The asperities can fracture, deform or slide and their dimension is negligible with respect to P (so that many of them are contained in a continuum point). Initially the resisting mechanism of the joint depends upon the contact forces generated among the first order asperities on one surface and the second order asperities of the other one. Later, due to the micro displacements occurred in the first phase, the continuum points of the two joints come in contact up to when local failures take place. When these occur, the asperities of the second order can come into contact, thus generating contact intervals whose length is comparable with that of the joint.

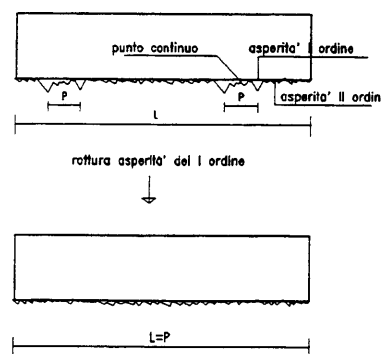


Figure 5-9. Morphology of a joint [Ruina A.L., 1985].

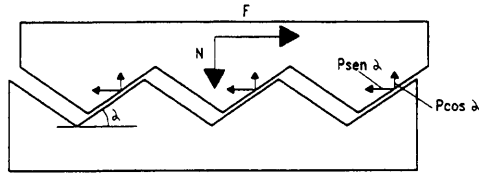


Figure 5-10. Morphology of a rough and rigid joint.

For models in which rigid surfaces are assumed, a schematic description of the surfaces of a joint can be given with a rough contour (Figure 5-10) whose n asperities, with triangular section, interact through forces (P) normal to the surfaces. If this is the case, eq. (5-1) can be deduced through simple conditions of limit equilibrium of interacting bodies. It results in fact:

$$F = n P \sin(\alpha)$$

$$N = n P \cos(\alpha)$$

and therefore:

$$\frac{F}{N} = \operatorname{tg}(\alpha) = c.$$

Note that in this model sliding is accompanied by a normal relative displacement of the two surfaces which may be associated to the well known phenomenon of dilatancy.

In the previous models the friction coefficient is assumed to be constant, however this is not always observed experimentally. In fact, among the classical constitutive relationships for friction the Barton's law [Barton N.R., 1978] postulates, on the basis of experimental data, that the ratio of the ultimate resistant tangential force and the normal

one is not constant, but it decreases with increasing normal stress. Barton proposes for the friction coefficient the following expression:

$$tg(\varphi) = tg \left[JRC \log_{10} \left(\frac{JCS}{\sigma_N} \right) + \varphi_R \right] \quad (5-2)$$

where *JRC* (Joint Roughness Coefficient) is a nondimensional parameter that characterizes the roughness of the joint, *JCS* (Joint Compressive Strength) is the normal stress that produces the compression failure of the element, φ_R is the residual friction angle, i.e. the minimum value that friction coefficient assumes when normal tension σ_N is maximum ($\sigma_N = JCS$). The author supplies the value of *JRC* in function of the morphology of the joint as illustrated in Figure 5-11.

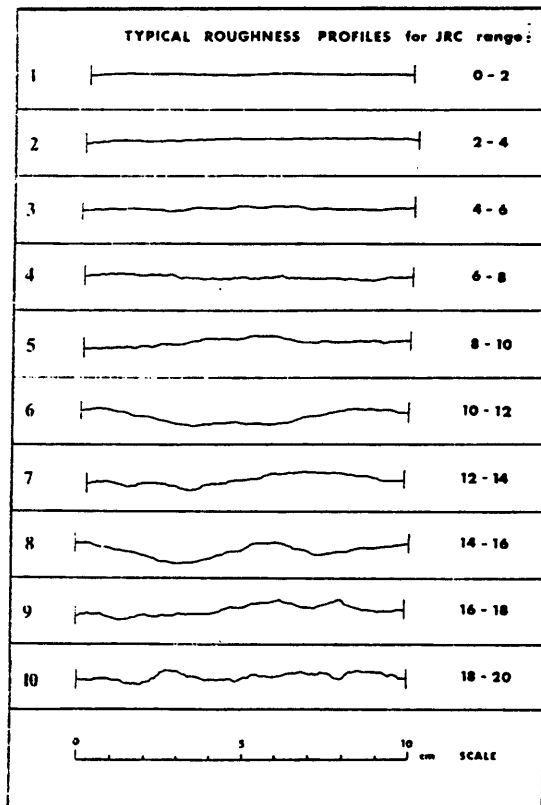


Figure 5-11. Morphology of a joint in function of *JRC* [Barton N.R., 1978].

The models and the laws previously presented, aim exclusively to determine the limit conditions that guarantee the absence of relative displacement between two bodies. An analytical solution to the problem regarding the determination of the velocity field of a body with a base subjected to frictional forces was proposed for the first time by Den Hartog [Den Hartog J.P., 1931]. More recently Ruina [Ruina A.L., 1983], on the basis of experimentation and analytical studies, has defined a constitutive relationship characterized by phenomenological parameters called state variables, whose general formulation is of the following type:

$$\tau = F(V, \sigma_N, \theta_1, \theta_2, \dots, \theta_m)$$

$$\frac{d\theta_i}{dt} = G_i(V, \sigma_N, \theta_1, \theta_2, \dots, \theta_m) \quad (i = 1, 2, \dots, m)$$

A simple special case of the previous relationship is given by:

$$\tau = F(V, \theta) = \tau_* + \theta + A \ln\left(\frac{V}{V_*}\right)$$

$$\frac{d\theta}{dt} = G(V, \theta) = -\frac{V}{L} \left(\theta + B \ln\left(\frac{V}{V_*}\right) \right)$$

where τ_* represents the tangential frictional stress acting on the block when it slides at a constant velocity V_* ; A and B are two empirical positive constants having the dimensions of a stress and their values depending upon τ_* and V_* ; L is an empirical positive constant with the dimensions of a length and it represents the characteristic distance of relaxation for the state variable θ .

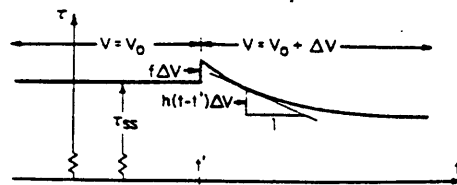


Figure 5-12. Variation of friction force as a function of velocity [Ji-Cheng G., 1983].

Figure 5-12 [Ji-Cheng G., 1983] shows the variation of τ with time for the case of an initial velocity V_0 which is increased an amount ΔV . The value of frictional resistance has an immediate increase, and subsequently an exponential relaxation which is function of the characteristic length L .

The proposed relationship is in good agreement with experimental observations, which are:

- (a) the frictional resistance has a logarithmic dependence upon velocity;
- (b) it increases instantaneously with an increase of velocity and subsequently tends towards the value it would have at steady state:

$$\frac{\partial \tau(v, \theta)}{\partial v} > 0 \quad (5-3)$$

- (c) the steady state frictional resistance is inversely proportional to velocity:

$$\frac{\partial \tau_*(v)}{\partial v} < 0 \quad (5-4)$$

- (d) the characteristic distance of relaxation is independent of velocity.

Equation (5-3) identifies a frictional behavior of viscous type, while (5-4) identifies the dependence of frictional resistance upon velocity which is in agreement with the observation that the "static" frictional force is higher than the "dynamic" one.

Experimental observations

On the basis of the analytical models described in the previous section a series of tests of the friction properties of the blocks used in the small scale wall model described in section 5.2.1 were performed. It is recalled that the blocks are made of peperino stone and measured $17.5 \times 40 \times 80$ mm, with an accuracy of the order of 10^{-1} mm, and had a weight of 120 gr. The specific objectives of the tests were to measure the dependence of the friction coefficient upon three factors:

- (1) the value of the normal stress,
- (2) possible phenomena of degradation of the contact surfaces,
- (3) the sliding velocity.

The tests aimed at goals 1 and 2 were carried out laying two blocks (one on top of the other) on a horizontal plane. The lower block was fixed while the upper one, which was free to slide, was connected by a wire with a pulley (Figure 5-13). A container was connected with the other end of the wire and it was slowly filled with water.

With this simple device it was possible to determine the lowest value F_u of the force parallel to the joint causing the initiation of the sliding motion of the block. F_u was evaluated for 20 couples of blocks. Four values of N were considered, and for each value, F_u was evaluated for 5 different couples of blocks. For each pair of blocks only one test was carried out. Mean value and standard deviation of the measured friction coefficients for each level of normal stress are given in Table 5-1.

$N(g)$	Normal stress (Kg/cm^2)	Friction coefficient: $F_w/N = tg(\varphi)$	
		Mean	Standard Deviation
120.6	0.005	0.61	0.00694
2120.32	0.088	0.551	0.00225
4618.76	0.192	0.579	0.006
10521.22	0.441	0.534	0.003

Table 5-1. Friction coefficient of peperino blocks with varying normal stress.

From such data a dependency of the friction coefficient from the normal stress level is observed. As presented in the previous section, Barton's law (eq. 5-2) accounts for this type of dependency, and therefore it may be appropriate for generalizing the previous experimental observations. In fact, based on the previous data, the parameters of Barton's law are estimated as follows: $JRC = 1.96$; and $\varphi_R = 23.14$. Then, measuring the compression strength of peperino: $JCS = 281.53 Kg/cm^2$, the relationship between friction coefficient, and normal stress for the peperino blocks used in the wall models experiments may be assumed as:

$$\tau / \sigma = tg [1.96 \times \log_{10} (281.53/\sigma) + 23.14] \quad (5-5)$$

which is plotted in Figure 5-14.

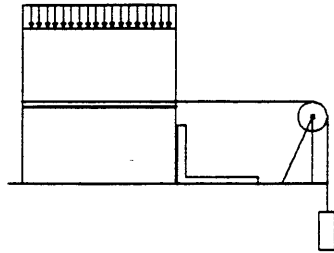


Figure 5-13. Scheme of the device used for the evaluation of static friction coefficient.

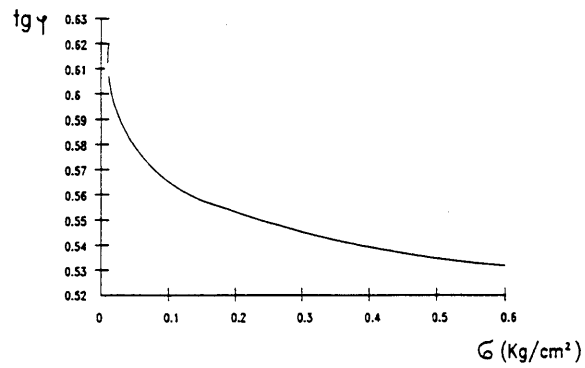


Figure 5-14. Graph of Barton's law for peperino blocks.

Further tests have been carried out in order to evaluate the influence of possible degradation factors: five pairs of blocks were considered; for each pair a sequence of tests were carried out assigning different values to the normal force N and evaluating the value of the corresponding friction force F_u . For each pair of blocks, after a sliding length of 1 cm had taken place, the units were repositioned and were subjected to the subsequent test. The last test of each sequence was performed with a different procedure: it was repeated several times trying to achieve, by carefully positioning the blocks, the best possible interlocking among the two surfaces with the objective of identifying the presence of first order asperities despite the degradation which the joint had been subjected to.

The results of the five series of tests are presented in Figures 5-15 to 5-19. In each figure the x axis represents the test number, while the y axis is the normal force, in figure (a), and the corresponding friction coefficient in figure (b). In Figure 5-20 we report, for each sequence of test performed on a couple of blocks, the ratio of the friction coefficient measured in the last (regular) test and in first one. Note how in each set of tests, the ratio, which may be regarded as a measure of the degradation of the friction surface, is always less than 1. The lowest value, 0.483, is for the block pair C which was tested with the highest normal force N .

These tests show a substantial reduction of the friction coefficient after the contact surfaces have undergone repeated sliding phases (an average reduction of 32% was observed for the previous 5 series). Such phenomenon may be important in the modeling of the dynamic response of a block structure subjected to seismic actions when sliding in alternating directions takes place before failure.

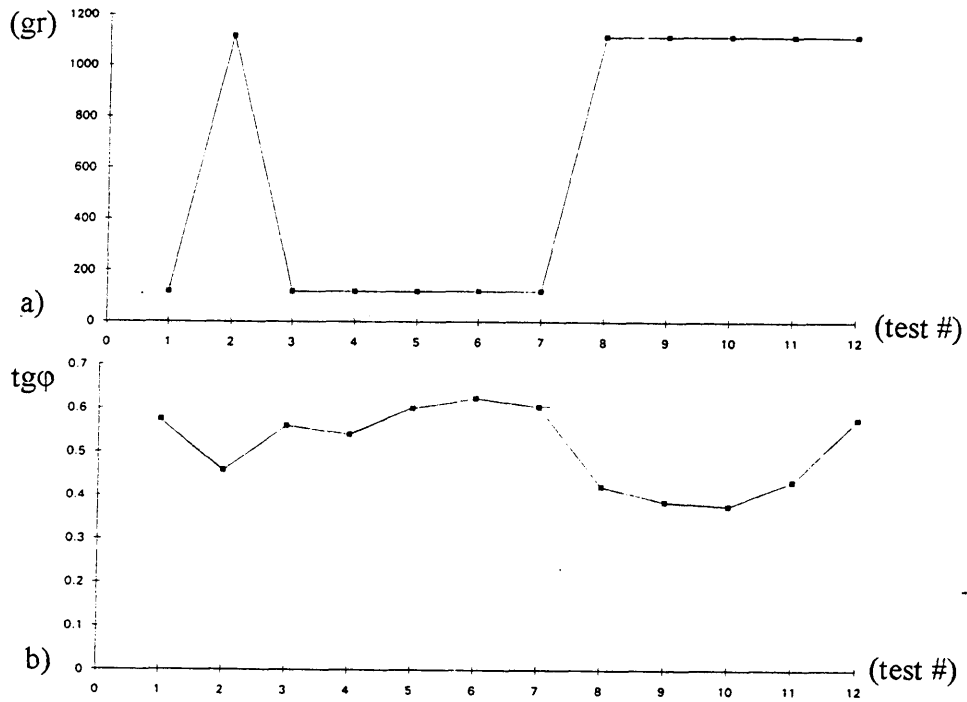


Figure 5-15. Block pair (A). For each test: (a) value of normal stress; (b) value of friction coefficient.

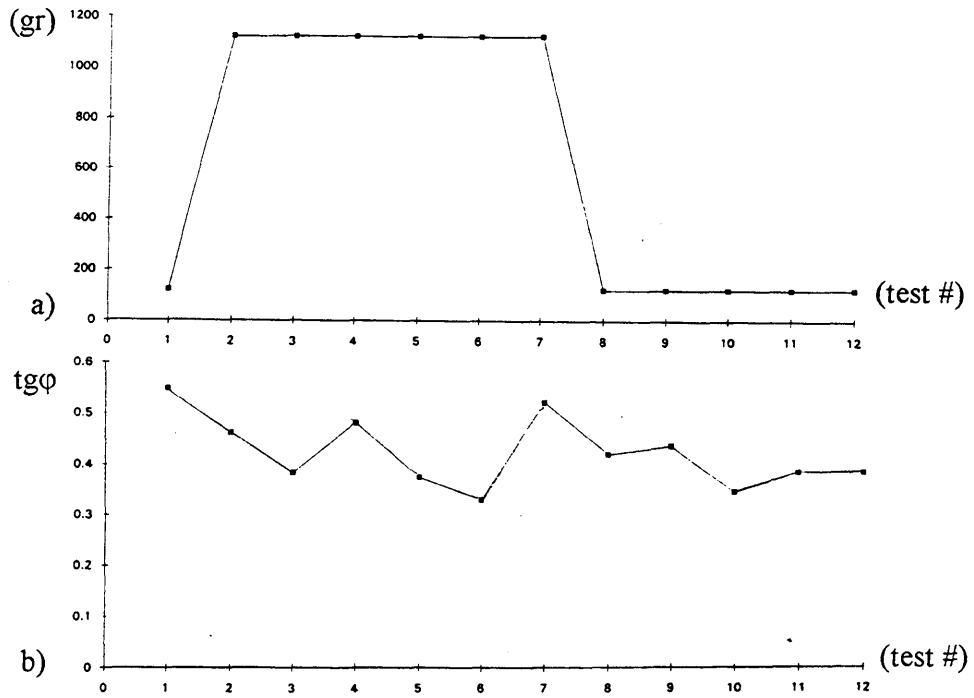


Figure 5-16. Block pair (B). For each test: (a) value of normal stress; (b) value of friction coefficient.

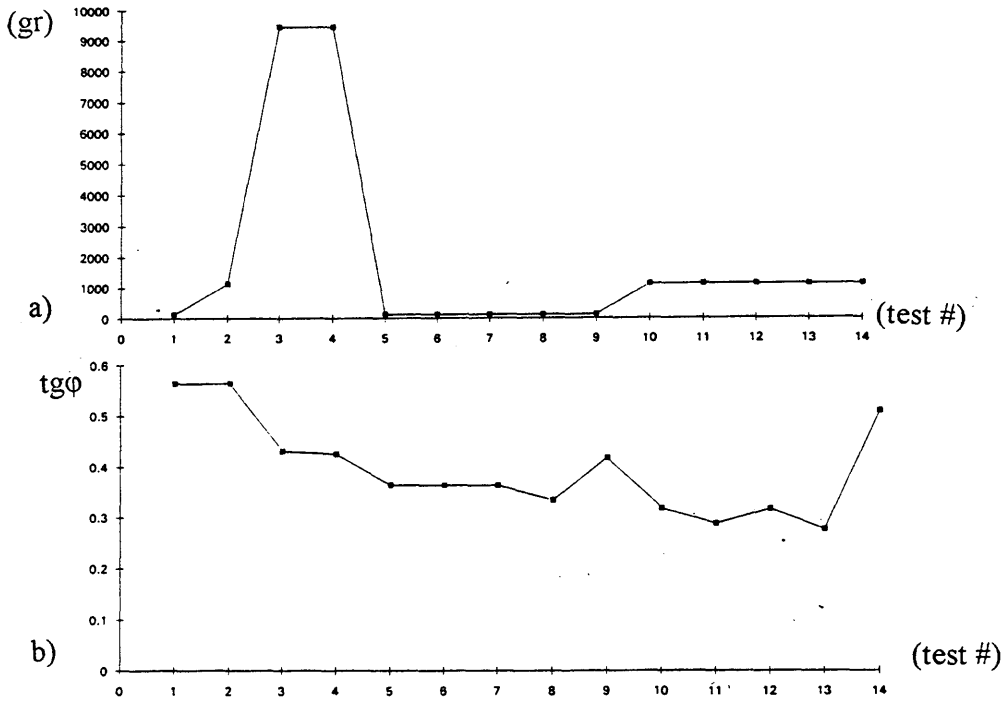


Figure 5-17. Block pair (C). For each test: (a) value of normal stress; (b) value of friction coefficient.

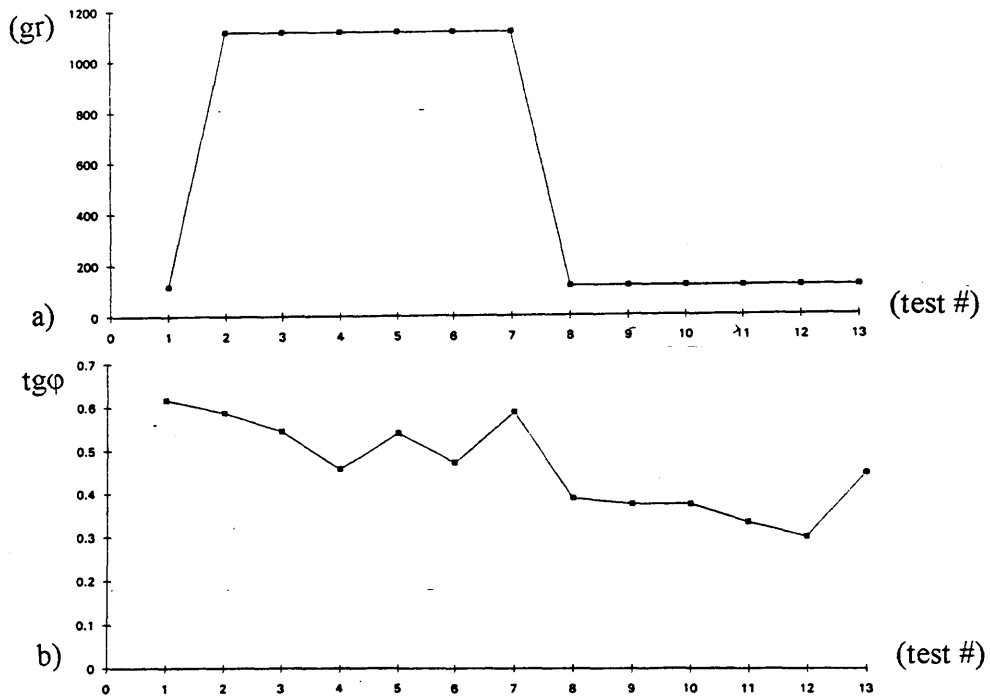


Figure 5-18. Block pair (D). For each test: (a) value of normal stress; (b) value of friction coefficient.

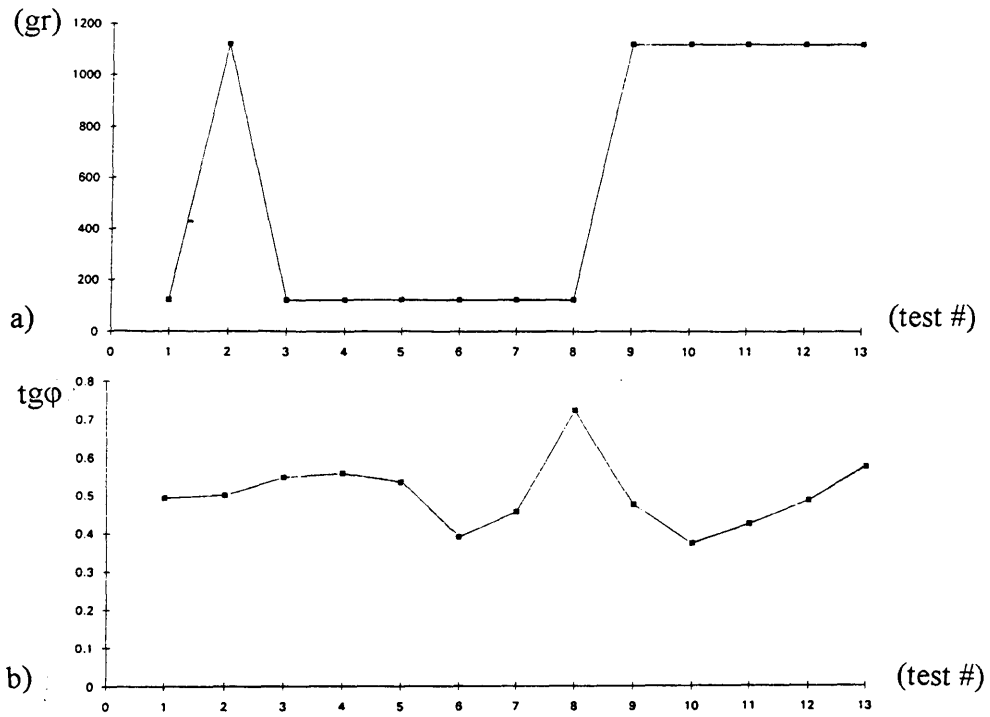


Figure 5-19. Block pair (E). For each test: (a) value of normal stress; (b) value of friction coefficient.

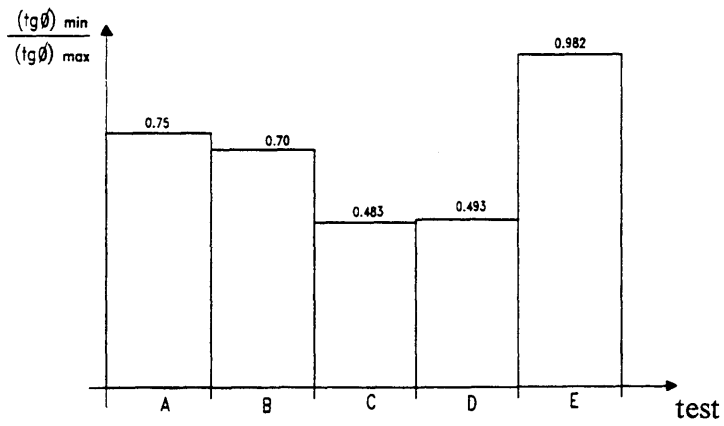


Figure 5-20. Friction coefficient "decay index" for the block pairs A,B,C,D and E.

In order to evaluate the dependence of the friction coefficient with the sliding velocity, we conducted several tests on block pairs with a special device, schematically illustrated in Figure 5-21. The bottom block is fixed while the top one is free to slide and is subjected to a certain normal force N . The top block is connected with a spring of stiffness K to a slider which moves at a constant velocity v . The slider, by moving away from the block, deforms the spring and applies an increasing horizontal force to the top block which will initiate moving when such force exceeds the static friction resistance. As a consequence of the block displacement the spring unloads and the block may keep moving at the same speed of the slider (allowing the measure of the dynamic frictional force) or it may find a new static equilibrium position in which it will remain until the static friction force is exceeded and so on. Such an unstable behavior can be avoided increasing the stiffness of the spring. It may be demonstrated, in fact, [Rice J.R., 1983] that the motion of a rigid block connected in series with a spring of stiffness K , moving with constant velocity, is unsteady if the elastic system is not sufficiently stiff and if the frictional contact force depends upon velocity (as in the case of the constitutive relationship proposed by Ruina and previously described). In fact, it exists a critical value of stiffness K_c such that if $K < K_c$ the system oscillations will increase whereas if $K > K_c$ they will decrease, and the system is stable if $K \gg K_c$.

After some preliminary tests we verified that an elastic element with $K = 5.5$ kg/mm yielded a stable behavior for speed ranging from 0.75 and 3.5 mm/min. We monitored the block displacements and the elastic force acting on the block. Although results were influenced by undesired vibrations of the motor of the slider which could not be completely eliminated, it is interesting to notice the various types of responses which have occurred. Some examples are given in Figure 5-22, where for the case (a) the dynamic friction force (on average) is equal to the initial one, whereas in cases (b) and (c), after an initial displacement the friction force, as expected, decreases below its initial value. Finally in case (d) we notice that, while the block is sliding, the friction force has a sudden increase probably due to an interlocking of the first order asperities of the two contact surfaces.

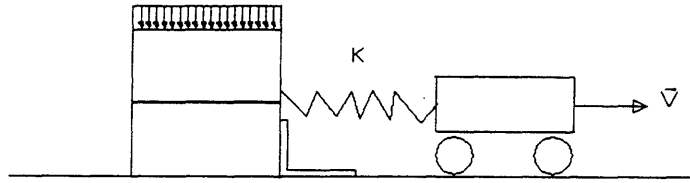


Figure 5-21. Scheme of the device used for evaluation of the dynamic friction properties of peperino blocks.

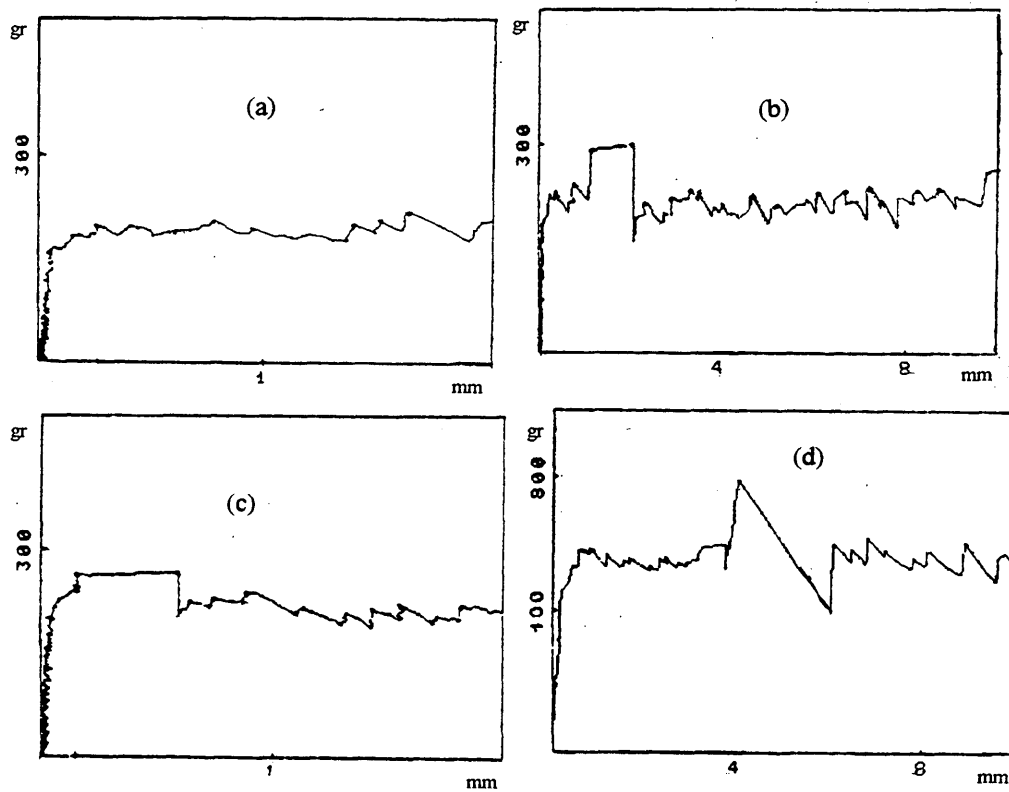


Figure 5-22. Tests carried out for the evaluation of “dynamic” friction coefficient: qualitative diagrams of applied tangential force vs. sliding distance.

Based on the results of the experimental tests described in this section we can observe the following:

1. A small scattering of the values of the friction coefficient for "new" surfaces (with a variation coefficient of less than 2% for normal stress $\sigma < 0.441 \text{ kg/cm}^2$), and a high scattering (up to 21%) for the "degraded" ones.
2. A noticeable variability of friction coefficient φ with normal stress σ (e.g. from 0.61 to 0.53 for normal stress ranging from 0.005 to 0.441 kg/cm^2). Such variability can be described by Barton's law whose parameters have been identified from the experimental results.
3. A remarkable variability of the friction coefficient with the level of degradation of the contact surfaces as observed from a 32% average reduction of the friction coefficient after a series of 13 sliding tests with various normal forces.
4. A reduction of the dynamic with respect to the static friction coefficient as indicated in the responses reported in Figure 5-22.

The previous observations have some implications on the DE modeling:

- since the blocks used in the models were "new", the random variability of the friction coefficient can be neglected;
- the variation of the friction coefficient due to the variation of the normal stress found inside the wall models is quite small and it is not expected to influence the system response;
- the reduction of the friction coefficient due to the degradation of the contact surfaces clearly does not affect the quasistatic test, but should be considered in a dynamic simulation; and finally

- the reduction of the dynamic vs. static friction coefficient should not affect the determination of the quasistatic failure load and initial failure mechanism, however if the evolution of the failure mode is of interest, then such reduction should be considered (see the friction softening mechanism proposed in the new non coplanar joint model shown in Figure 7-10).

In conclusion, after having acquired (in section 5.2.1) data on the experimental in-plane failure of 3 opus quadratum walls models, and (in section 5.2.2) data on the friction parameters of the specific blocks used in the wall experiments, we can now proceed, as it will be illustrated in the next section, to the DE modeling of such tests with the objective of evaluating the numerical predictions which can be obtained with current DEM.

5.3 D.E.M. MODELING OF THE QUASISTATIC BEHAVIOR OF BLOCK STRUCTURES

The effectiveness of the Discrete Element Method for the study of the quasistatic response of brick walls has been investigated through a series of numerical simulations of the experimental tests of the 3 small scale wall models reported in section 5.2.1.

The presentation is structured in the following four sections regarding:

- (1) the modeling and analysis procedure used in the DE simulations;
- (2) the validation of the DE results of a 21-block wall² with respect to limit analysis;
- (3) a parametric study for evaluating the sensitivity of the solution with respect to model parameters, and improving the efficiency of the analysis; and finally
- (4) the comparison of the numerical and experimental results for WALL1, WALL2 and WALL3.

5.3.1. Modeling

It should be noticed that, in the 3 wall models described in section 5.2.1, the stress level at failure was always very low with respect to strength of the block material (peperino stone), and therefore the corresponding material deformations were negligible both in the interior and in the joint area. In fact, the collapse did not occur due to material failure but to the loss of equilibrium accompanied by sliding and rotation of the blocks which behaved essentially as rigid blocks. As a consequence, a simple linear elastic behavior or even a rigid body model can be acceptable for the material modeling of the blocks.

² The 21-brick wall represents a model of the portion of WALL1 where failure takes place (see Figure 5-10).

In the following, each brick has been modeled with a plane stress elastic element. The material parameters have been chosen as follows:

- (1) The experimental values of the elastic moduli E and ν , and of the mass density of the peperino bricks have been used;
- (2) The stiffness of the interaction springs have been selected such that the displacements due to the elastic joints were of the same order of magnitude, but smaller than the displacements caused by the elastic deformations of the elements. The normal and tangential interaction stiffnesses have been chosen equal.
- (3) Based on the considerations illustrated in the previous section, the friction behavior has been described by the Coulomb model.

The simulation of the loading corresponding to the inclined plane experiments has been performed according to the standard DE procedure:

- (1) An instantaneous gravity load is applied without damping and the lower frequency F_V of the vibrations induced by the vertical forces is measured.
- (2) The analysis is repeated applying the gravity load and a mass damping corresponding to 30% of the critical damping of the measured frequency F_V and the simulation is carried on up to $t=t_0$, when the residual vibrations are damped out.
- (3) At time $t=t_0$ a horizontal force - proportional to the brick weight and small with respect to the failure force - is applied instantaneously to each element in order to determine the lower frequency F_H of the vibrations caused by the horizontal forces.

- (4) Then the quasistatic application of the horizontal forces begins. The analysis is restarted from time $t=t_0$ with the application of slowly increasing horizontal forces varying in time according to a function made of linear ramps and flat sections. The ratio between the horizontal and vertical forces at any given time is equal for all the elements. The ramp duration is generally greater or equal to $1/F_h$, and the flat section is at least twice the ramp duration for allowing the system response to stabilize. A mass damping corresponding to 10 - 30% of the critical damping of the frequency F_h is applied. Due to the high non linearity of the system, other frequencies may arise during the loading, and care has to be used in order to reduce any residual vibrations without overdamping the response.

After each load increase - if the failure load has not been reached - the system undergoes small displacements and deformations until it finds a new configuration of static equilibrium. Conversely, when the failure load has been reached or exceeded, the system cannot find a new static equilibrium configuration for small displacements and it is affected by large displacements, describing the kinematics of the failure mechanism.

5.3.2 Validation of the analysis procedure

In order to validate the previously described DE analysis procedure, a series of numerical tests have been performed on a 21-brick wall representing WALL1, and the responses, in terms of failure loads λ and failure mechanisms, have been compared with the results of limit analysis which provides exact results in the hypothesis of rigid blocks and perfect Coulomb friction.

The analysis has been repeated for six values of the friction coefficient α (from 0.5 to 1.0) in order to obtain a variety of different (and representative) friction mechanisms. In Figure 5-23 the predicted DE failure mechanisms are presented for four values of α (the results for $\alpha = 0.5$ and 1.0 are not shown since they are similar to those obtained respectively for $\alpha = 0.6$ and 0.75).

For low friction coefficients, such as $\alpha \leq 0.6$, failure occurs in a purely diffuse sliding mode when the lateral load λ exceeds the value of the friction coefficient; rotations take place later, when sufficiently large displacements have developed.

For high friction coefficients, $\alpha \geq 0.75$, the system separates in two portions and the system fails in a purely rotating mode.

For intermediate cases both rotations and sliding occur and a complex mixed mode of failure takes place.

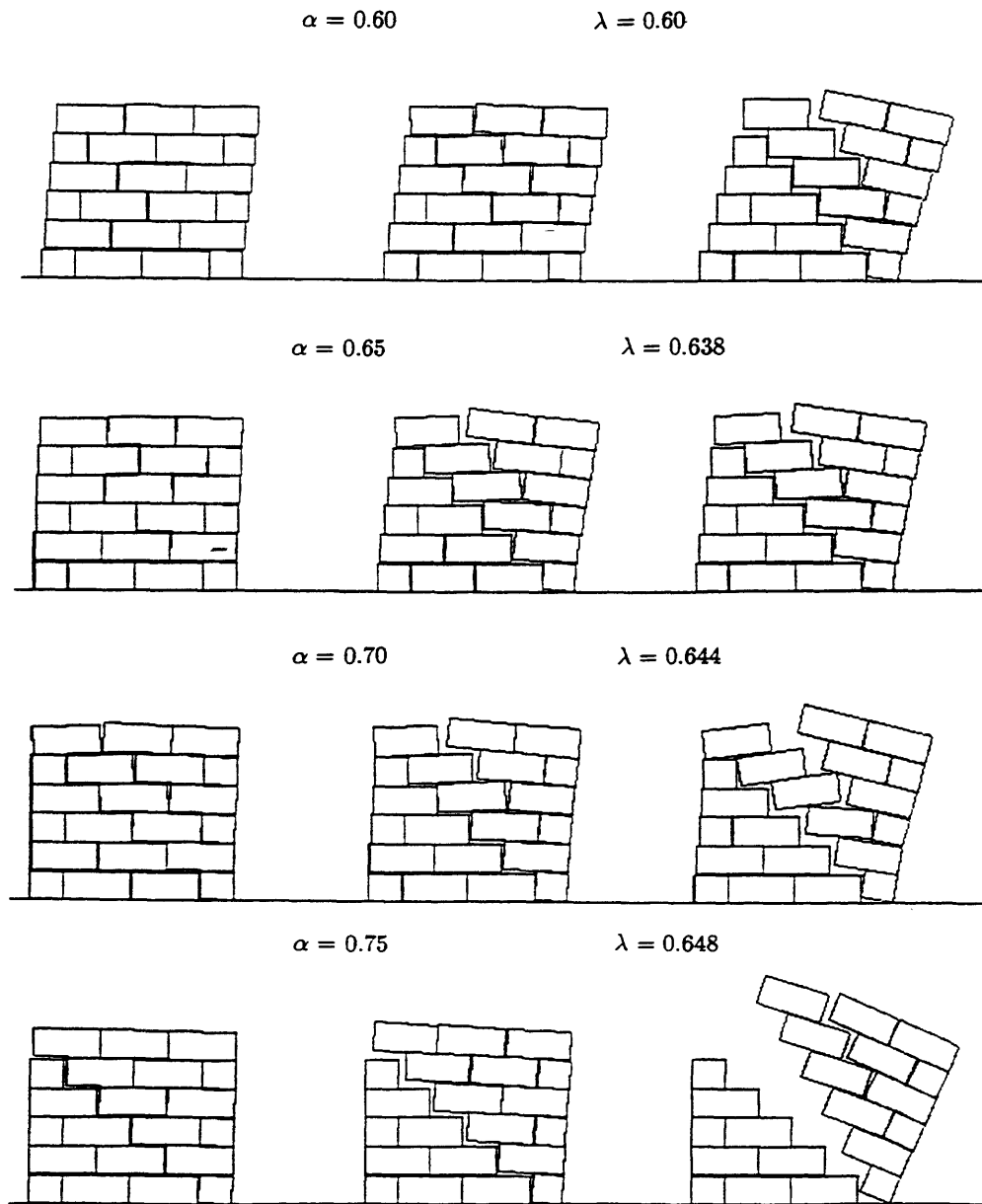


Figure 5-23. Failure mechanism and failure loads λ of a 21-brick wall subjected to gravity and increasing horizontal forces for various friction coefficients α .

The outcomes of the numerical tests are summarized in Table 5-3. The DE predictions appear to be successfully validated with respect to the "exact" results, which are obtained from a limit analysis study [Baggio,C., 1993] of the same 21-brick wall. The previously mention study perfectly confirms also the failure mechanisms predicted by the DE analysis.

α	<i>Failure mode</i>	λ <i>predicted</i>	λ <i>exact</i>
0.50	sliding	.5	.5
0.60	sliding	.6	.6
0.65	mixed	.638	.64
0.70	mixed	.644	n/a
0.75	rotating	.648	.646
1.00	rotating	.648	.646

Table 5-3. Failure modes and predicted vs. "exact" failure loads λ for various friction coefficients α .

5.3.3 Parametric study of model sensitivity

The numerical efficiency of the discrete element method is limited by the size of the time step required for a stable and accurate solution. Since the required time step is a fraction of the smallest period of the structure it has been attempted to increase such period by increasing the masses and decreasing the stiffness of the system. The justifications for modifying the real material parameters of the structure are: (1) the quasistatic application of the load determines negligible inertial effects, and (2) the deformations which occur before failure are small and unimportant. It is therefore reasonable to increase the masses and decrease the stiffness if care is taken not to introduce noticeable inertial effects or considerable deformations.

A parametric study has been performed to verify the sensitivity of the response of the brick wall to these parameters. The following cases have been tested on the 21-brick wall:

- (1) Simultaneous reduction of E , K_n , K_t (Young's modulus of bricks, normal and tangential stiffness of interaction springs respectively) by a factor of 10^{-2} and 10^{-4} .
- (2) Increase of masses by a factor of 10^2 and 10^4 .
- (3) Combined reduction of E , K_n , K_t by a factor of 10^{-2} and increase of masses by a factor of 10^2 .

All of the above extreme cases have failure loads which are close (within 2%) to the values obtained for the exact material parameters, and a considerable gain in efficiency is observed. For example, for case (3) the time step has increased of a factor of 100. This has not changed noticeably the CPU time required for determining the failure load since the response time of the system before failure has increased of the same factor.

However, the CPU time required to obtain the response after failure, which is mainly a rigid body motion, has substantially decreased.

Another model parameter which has been studied is the ratio between the normal and tangential stiffness K_n / K_t . In this case, the concern was the sensitivity of the solution to this parameter which was not determined experimentally.

In addition to the original analysis where K_n was equal to K_t , three additional cases have been studied: $K_n / K_t = 10^2$, 10^{-1} , and 10^{-2} . All results were similar to those of the original analysis, showing that the solution is rather insensitive to this parameter. However when $K_n / K_t < 1$ more care has to be taken in the analysis in order to damp out undesired vibrations during the quasistatic loading.

5.3.4 Discrete Element simulation of the experimental tests

After the calibration and validation of the analysis procedure, the experimental tests performed on the 3 wall models (illustrated in Figure 5-8), have been simulated according to the DE procedure described in the previous section. The friction coefficient has been set to the experimental value 0.6 (corresponding to the low normal stress level found in the 3 wall models). The results, in terms of failure loads, are summarized in Table 5-4.

For WALL1 we notice a substantial overestimation of the failure load, in fact, while the experimental one was $\lambda_{exp}=0.5$, the numerical model failed at $\lambda_{DE}=0.6$, with a 20% overestimation. Also the predicted failure mechanism shown in Figure 5-23 (for $\alpha=0.6$) is not in perfect agreement with the experimental result (shown in Figure 5-8). DE analysis predicted a failure which initiated with a diffuse sliding, while in the experimental case it occurred with a mixed sliding and rotating mechanism (similar to the one obtained with DE for $\alpha=0.65$).

WALL3 has been modeled with a system of 220 elements, the stiffness has been reduced of a factor of 10^{-2} and the mass has been increased of a factor of 10^2 in order to expedite the solution. The failure mechanism obtained from the DE analysis is displayed in Figure 5-24. If we compare such failure mode with the experimental one shown in Figure 5-10, we can observe a reasonably good agreement. The DE analysis is capable of predicting the complex kinematics involving the sliding and rotation of many blocks, which would be impossible with analysis methods based on continuum mechanics. However, we notice that in the experimental case the portion affected by sliding appears to be localized in a narrower area than the one predicted by the DE analysis. In addition the failure load is also substantially overestimated: $\lambda_{DE}=0.47$ vs. $\lambda_{exp}=0.35$. A similar result is obtained for WALL2 with a predicted failure load of $\lambda_{DE}=0.56$ vs. the experimental one $\lambda_{exp}=0.47$.

Finally, we also mention that in the experimental tests, starting from approximately 80% of the failure load, slight internal displacements were observed, while in the DE analyses the wall remained practically undeformed up to failure.

<i>Model</i>	<i>WALL1</i> λ	<i>WALL2</i> λ	<i>WALL3</i> λ
Experimental	0.50	0.47	0.35
DE analysis	0.60	0.56	0.47
Overestimation	20%	19%	34%

Table 5-4. Experimental and analytical failure loads λ .

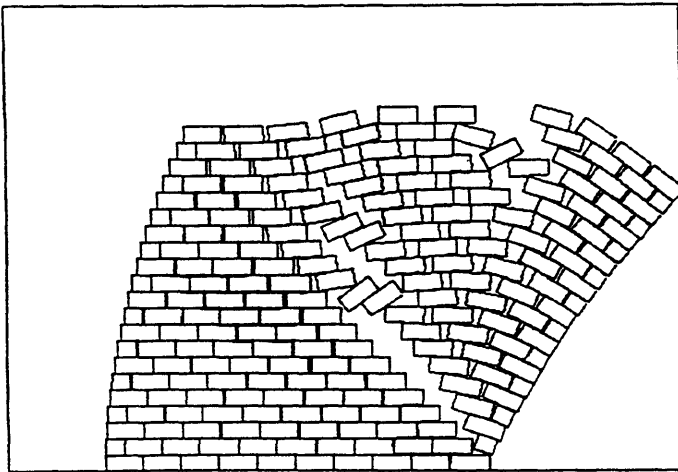
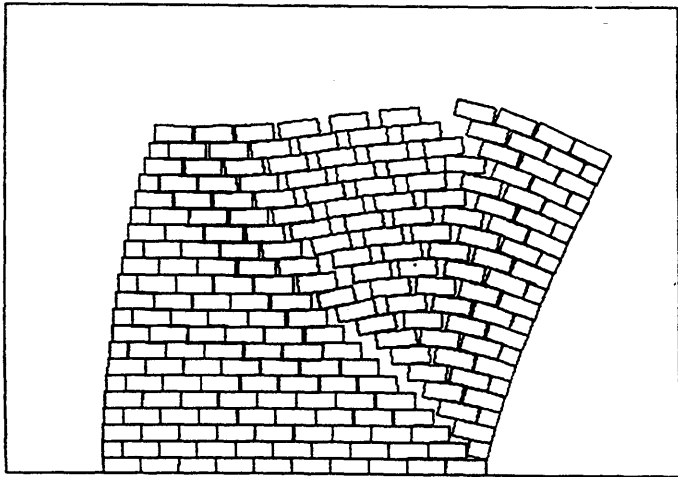
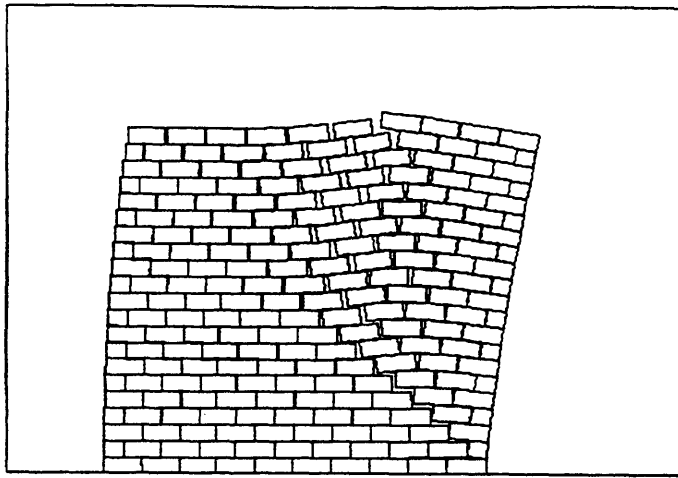


Figure 5-24. Failure mechanism of a 220-brick wall.

5.4 CONCLUSION

The objective of this chapter has been the evaluation of current Discrete Element Method for the numerical simulation of the mechanical response of brick walls subjected to in-plane quasistatic lateral loading.

Preliminary to the numerical analysis, a series of experimental tests on 3 small scale wall models, made of peperino stone, have been performed in order to acquire benchmark data for assessing the numerical predictions. Various aspects of the friction behavior of the peperino blocks (such as the dependency of friction from: normal stress, surface degradation, and sliding velocity) have also been tested to measure the friction coefficient to be used in the DE models, and also for evaluating the appropriateness of the simple Coulomb friction model for this case.

Subsequently, the DE modeling and loading procedure for the quasistatic in-plane loading of a brick wall has been illustrated in detail, and successfully validated with respect to limit analysis results for a 21-brick wall. A parametric study has shown that a careful selection of certain material parameters can increase the efficiency of the solution without losing the required accuracy, and that the results of the proposed analysis procedure are relatively insensitive to the ratio of the normal and tangential interaction stiffnesses.

The DEM simulations of the experimental tests on the 3 wall models have shown how the complexities of the highly nonlinear behavior of the brick wall near failure, such as the opening and closures of joints, and the sliding and rotations of the elements, are handled well with this approach.

However, certain discrepancies between the experimental and the DE results were noticed. In particular a systematic overestimation of the failure load was observed. This occurred despite the fact that the DE results had been successfully validated by the limit analysis for the 21-brick wall. Thus, it seems that possible numerical inaccuracies are

sufficiently small, and also that the fundamental assumptions of this method - including the elastic pointwise contact - are reasonably adequate for an effective modeling of the mechanical behavior of an "idealized" wall with regular geometry. Therefore, it seems that the irregularities of the experimental model, such as the variability of the geometrical dimensions, the non perfect coplanarity of the contact surfaces, and the rounded corners, are responsible for the reduction of the failure load.

Based on this observation, an attempt has been made to employ the DEM for investigating the effects of carefully defined imperfections on the response of the brick wall. As an example, the effect of small plausible geometrical imperfections has been studied on the 21-brick wall model by reducing the heights of the two elements indicated with (a) and (b) in Figure 5-25. The reduction of 1 mm of the height of element (a) has lowered the failure load from 0.6 to 0.51 (close to the experimental value $\lambda_{exp}=0.5$). The reduction of 0.5 mm of the height of element (b) has lowered the failure load from 0.6 to 0.54. A mixed mode failure mechanism, shown in Figure 5-25, occurred for both cases.

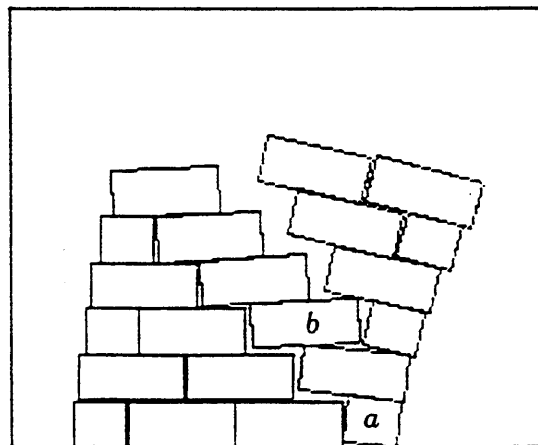


Figure 5-25. Failure mechanism of a 21-brick wall with geometrical imperfections.

The previous results are an indication that small geometrical imperfections play an important role in the failure response of the opus quadratum wall. However we are still faced with the uncertainty of defining the type, the number, the location, and the size of such imperfections.

We can conclude that the current DEM is promising for the modeling of the seismic response of historical block structures. However it appears that more work is necessary to formulate a rational and general approach to the modeling of the geometrical imperfections which constitute an inherent feature of block structures. This formulation is considered in Chapter 7 where a new joint model accounting for the non coplanar contact between blocks will be presented.

**Chapter 6: DYNAMIC ANALYSIS OF BLOCK STRUCTURES WITH
CURRENT D.E.M.**

6.1. SINGLE BLOCK D.E.M. MODELING

6.2. MULTIPLE BLOCK D.E.M. MODELING

6.2.1. Harmonic Oscillations

6.2.2. Seismic Oscillations

6.2.2.1. Shaking Table Tests

6.2.2.2. Numerical Simulations

6.3. CONCLUSION

6. DYNAMIC ANALYSIS OF BLOCK STRUCTURES WITH CURRENT D.E.M.

In the previous chapter the seismic action has been modeled with equivalent static forces because of the complexity of the response of a block structure. However the ultimate objective of a seismic vulnerability study is a dynamic analysis. In this chapter we will explore, for a single block structure, and for a system of a limited number of blocks, the potential and limitations of a fully dynamic analysis of such typology of structures with the DEM.

In Chapter 4 it was noted how the difficulty in using the DEM, especially for a dynamic problem, lies in the determination of the interaction parameters: K_n , K_t (the normal and tangential interaction stiffness), η (the friction coefficient), and α the proportionality parameter defining the viscous damping factor C ($C=\alpha K_n$) of a linear viscous element acting in parallel with K_n for the modeling of the energy dissipation which takes place during the impact. The parameter selection and the modeling procedure will be discussed first for the single block case, and later for a multi-block system.

Differently from other studies which have applied dynamic DE analysis to historical buildings (e.g. [Sinclair,G.,1999], [Brookes,C.L.,1998]), the numerical modeling which will be illustrated in the following, has been supported by a series of experimental tests involving the study of the rocking of single blocks with various slenderness ratios, and the investigation, with shaking table tests, of the response of a small scale model of an 8-block arch structure subjected to simulated earthquake accelerograms. The arch structure, has been selected for this study, because it shows how the DEM may handle much more complex cases than the ones usually found in the literature (single block or multiblock column, and the trilite), and, at the same time, it is an idealized model of several monuments of considerable architectural and historical

value such as, for example, the ancient Roman arch of Trajan found in Leptis Magna in North Africa (Figure 6.1).



Figure 6-1. Leptis Magna (North Africa), arch of Trajan (109-110 AD).

6.1 SINGLE BLOCK DEM MODELLING

The following procedure was applied to the modeling of free rocking oscillations of a single block of mass M :

1. The interaction stiffnesses ($K_n = K_t$) are equal to γK_e , where K_e is the vertical elastic stiffness of the block, and γ is an empirical factor which should be small for improving numerical efficiency, and large enough for determining only negligible elastic displacements (with respect to the size of the block).
2. The friction coefficient η is equal to the average experimental value.
3. The stiffness damping parameter α is determined such that the "block reference frequency ω " is subjected to a certain fraction ϕ of the critical damping. The block reference frequency ω is the natural frequency of a 1 d.o.f. oscillator with mass M and stiffness K_n .

In order to determine the optimal critical damping fraction ϕ the following experimental tests were performed. A series of 4 marble blocks with aspect ratios $b/h = 2, 2.9, 3.6,$ and 5 were subjected to free rocking oscillations and their average restitution ratios were determined. Then the same tests were simulated with the DEM according to the previous procedure, with $\gamma \approx 10^{-2}$ and with various values of $\phi = 0.15, 0.35, 0.45,$ and 0.75 . By minimizing the differences between the numerical and experimental restitution ratios, it was determined that the optimal value is $\phi = 0.35$ (for such value the maximum difference of the restitution ratios did not exceed 5%).

6.2 MULTIPLE BLOCK D.E.M. MODELLING

The previously described modeling procedure was extended to the case of multiple block structures in the numerical and experimental study of the seismic response of an 8-block arch structure (Figure 6-3). An experimental model of the arch was made with peperino blocks (the same type of material used in the wall models studied in the previous Chapter). As a preliminary analysis one of the two columns was studied according to the procedure described in the previous section. A critical damping fraction of $\phi = 0.35$ at the block reference frequency $\omega = 180$ Hz, yielded a predicted average restitution ratio ($r_1 = 0.55$) in free rocking oscillations which was only 10% higher than the experimental one ($r_2 = 0.5$). This result could be further improved by increasing the damping fraction, however for the subsequent analyses the previous value ($\phi = 0.35$) was used.

6.2.1 Harmonic Oscillations

The second step was the study, both experimental and with the DEM, of the response of the single column to harmonic ground motion. The previous interaction parameters have been used. Both experimental and numerical results confirm that rocking does not occur until the peak ground acceleration a - normalized with respect to λg - (where λ is the normalized static lateral failure load, and g is the acceleration of gravity) does not exceed 1. For the cases tested experimentally, when $a > 1$, the column responds with a periodic non symmetrical rocking motion. In the case of $a = 1.02$ and ground shaking frequency $f = 10.5$ Hz. the average predicted rotation amplitude was 0.008 rads which compares reasonably well with the experimental value of 0.007 rads.

The next step was the modeling of the response of the entire 8-block arch structure subjected to harmonic ground motion. Since the column is expected to provide a major contribution to the frequency content of the global response, the previously determined column interaction parameters have been used throughout the multi-block structure. The system response is generally periodic with the same frequency of the ground motion, and it involves both sliding and rocking of blocks. Typical experimental and numerical oscillation modes compare quite well as shown Figure 6-3. A quantitative comparison of rotation amplitudes was not possible since, due to geometrical imperfections of the experimental model, column rocking in the experimental tests initiated for peak ground acceleration $a < 1$. Several numerical tests were performed with various ground shaking frequencies $f = 2.5, 5, \text{ and } 10$ Hz. The duration of each simulation was 5 sec. At the lowest frequency, $f = 2.5$ Hz, the system collapsed even for the low value of $a = 1.1$, while at higher frequencies ($f = 5$ and 10 Hz), failure was not reached even for $a = 2.0$.

Harmonic shaking, which has been studied here for comparing experimental and numerical results of a dynamic multi-block problem, does not provide, however, conclusive information on the seismic response of the system. To this purpose an extensive series of experimental and numerical analyses, which will be described in the next section, has been undertaken in order to demonstrate how an estimate of the seismic vulnerability of the arch can be obtained with the proposed DEM procedure.

MODEL THICKNESS = 70 mm

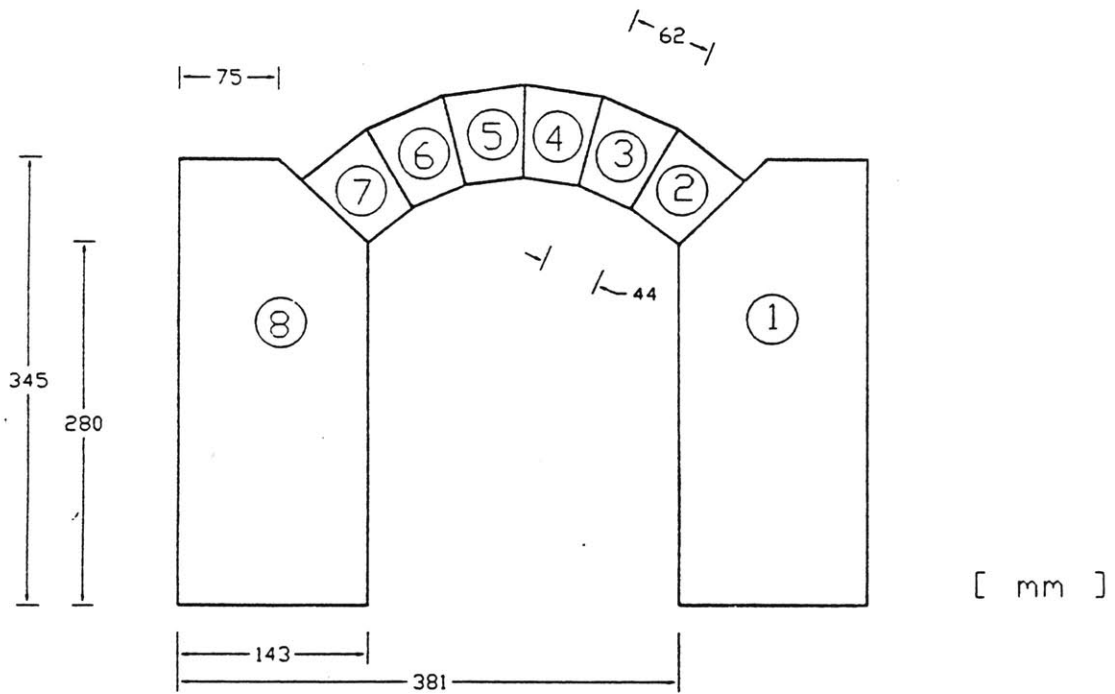


Figure 6-2. Geometric dimensions of the arch model.

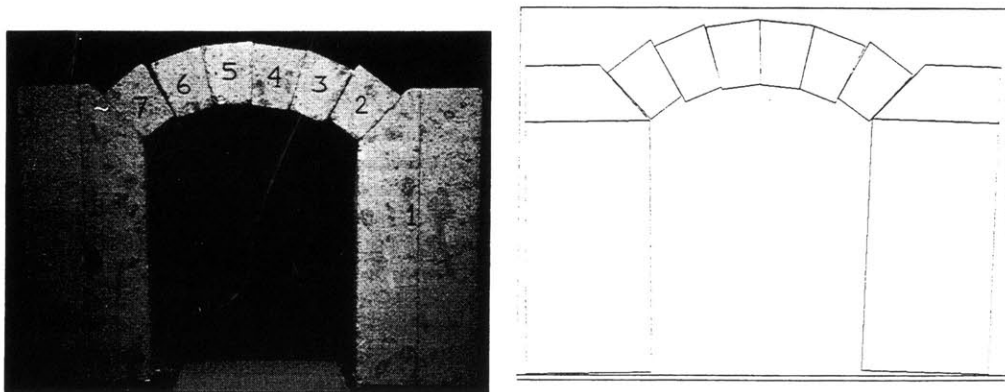


Figure 6-3. Experimental and numerical oscillation modes of an arch structure subjected to harmonic shaking

6.2.2. Seismic Oscillations

The object of the investigation is the same arch model studied in the previous section. The experimental tests consisted of applying simulated earthquake motions to the model, and were performed using the shaking table of the National Laboratory of Civil Engineering in Lisbon. Subsequently, a series of numerical simulations based on DEM, were performed in order to obtain the seismic vulnerability curve of the arch structure.

6.2.2.1 Shaking Table Tests

The geometry of the stone model is illustrated in Figure 6-2. The shaking table size is very large with respect to the model: it measures 3.26 by 2.26 meters, and it has a weight of 30 kN. The table has a steel structure with an horizontal displacement degree of freedom activated by an hydraulic system controlled by a self-tuning algorithm using the displacement as the control variable. The instrumentation consisted of 5 displacement and 3 acceleration transducers placed as indicated in Figure 6-4 and in Figure 6-6.

CHANNELS	MEASURED VARIABLES	TRANSDUCER
1	Displacement of the shaking table	LVDT
2	Displacement at the top of column 8	LVDT
3	Displacement at the top of column 1	LVDT
4	Displacement at the bottom of column 8	LVDT
5	Displacement at the bottom of column 1	LVDT
6	Acceleration at the top of column 8	Piez. Accelerometer
7	Acceleration at the top of column 1	Piez. Accelerometer
8	Acceleration of the shaking table	Piez. Accelerometer

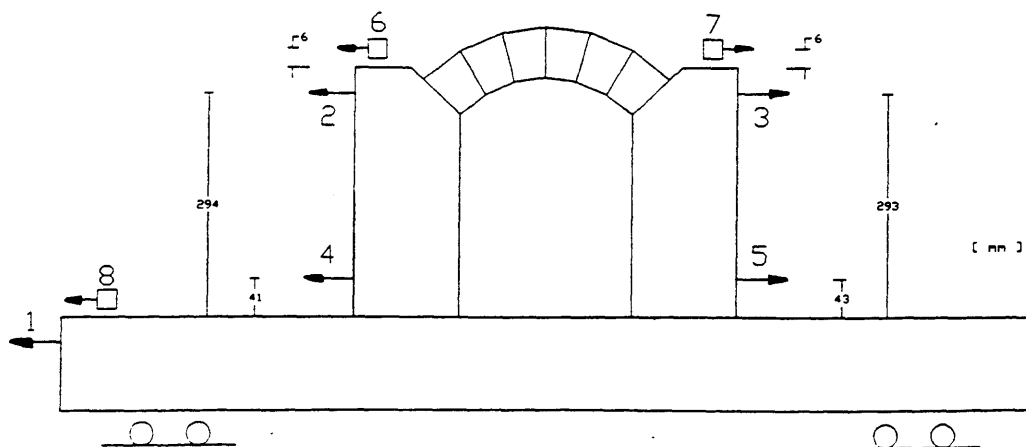


Figure 6-4. General scheme showing the measure channels.

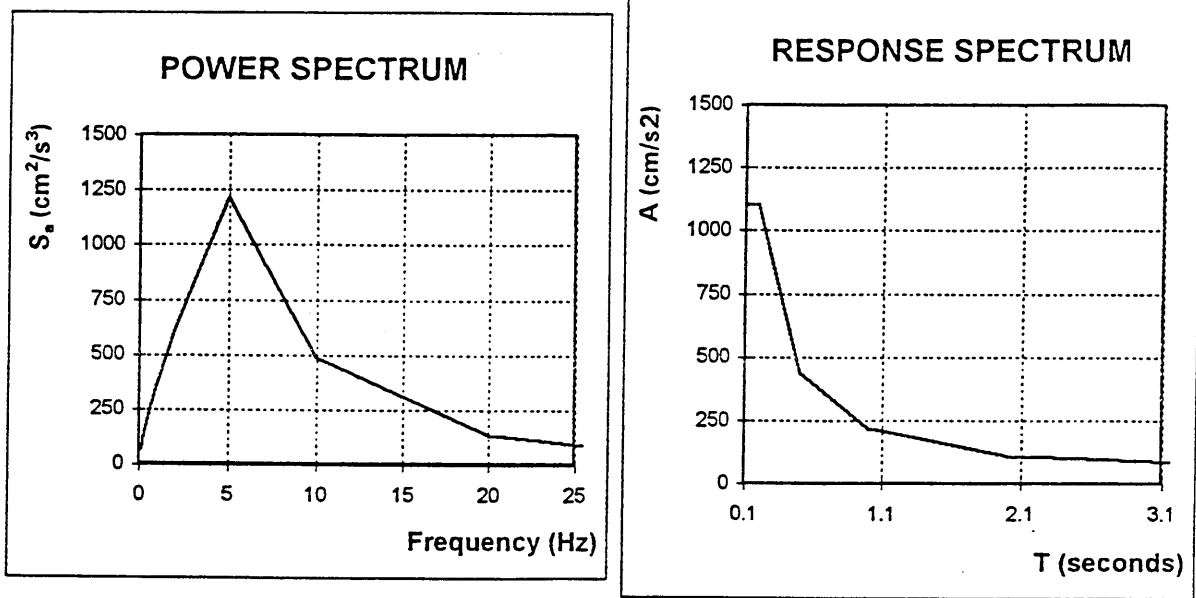


Figure 6-5. Power and response spectra used in the shaking table tests.

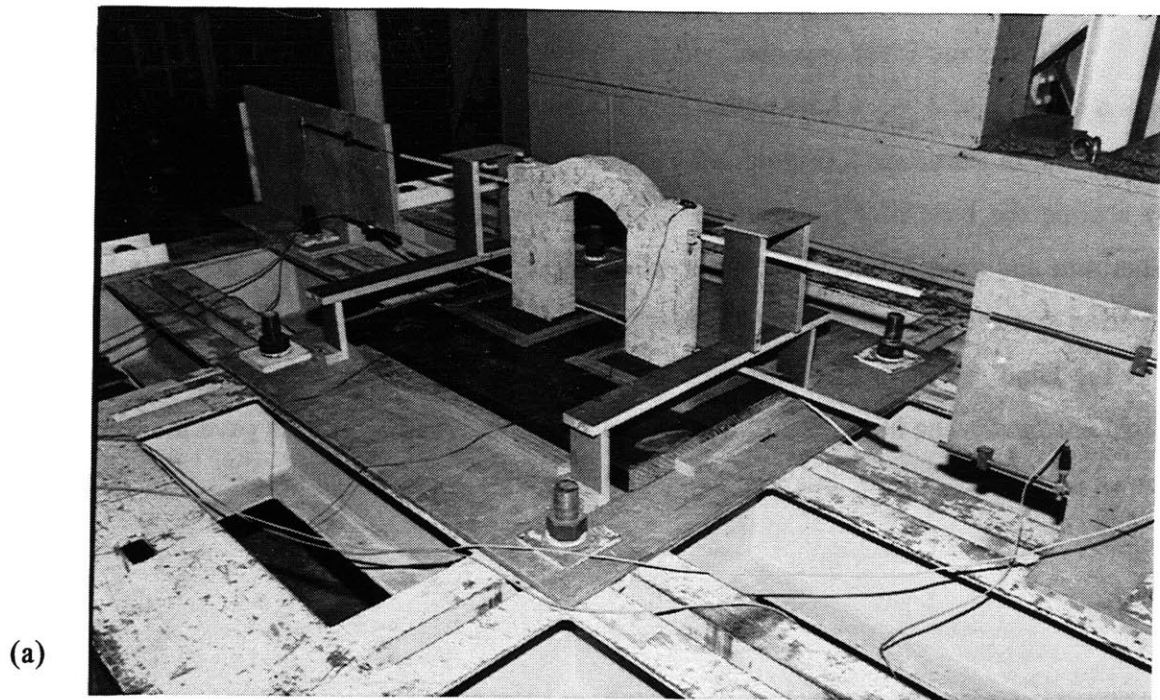


Figure 6-6. (a) Instrumented arch model on shaking table; (b) Displaced arch configuration after a test.

The seismic input was obtained by generating 3 independent base time-histories with a duration of 8 sec. whose power spectrum corresponds to the response spectrum for soil type B in Eurocode 8 (Figure 6-5). Three series of accelerograms were generated by scaling the base time histories by appropriate factors. Due to the type of control algorithm and system tolerances, recorded accelerograms generated with the same base function and scaling factor were not exactly the same. Another element of randomness was the hand replacement of the structure after each test which inevitably introduced slight changes in the initial conditions of each test. The 3 series of tests gave the results shown in Table 6-1, Table 6-2, and Table 6-3.

Test No.	Peak accel. (cm/sec ²)	Collapse
1	155	no
2	163	no
3	175	no
4	155	no
5	305	no
6	355	no
7	515	no
8	640	no
9	770	no
10	1035	yes
11	1000	yes

Table 6-1. Test results for Base Time-History 1

Test No.	Peak accel. (cm/sec ²)	Collapse
12	240	no
13	590	no
14	815	no
15	970	no

Table 6-2. Test results for Base Time-History 2

The third series was performed to estimate the peak failure acceleration distribution by increasing the scaling (by small increments) until collapse occurred and then decreasing it until the arch was able to resist the shaking.

Test No.	Peak accel. (cm/sec ²)	Collapse
16	758	no
17	819	no
18	944	no
19	917	yes
20	935	yes
21	926	yes
22	880	yes
23	889	no
24	894	no
25	893	no
26	937	yes
27	887	no
28	940	no
29	972	yes
30	927	no
31	935	yes

Table 6-3. Test results for Base Time-History 3.

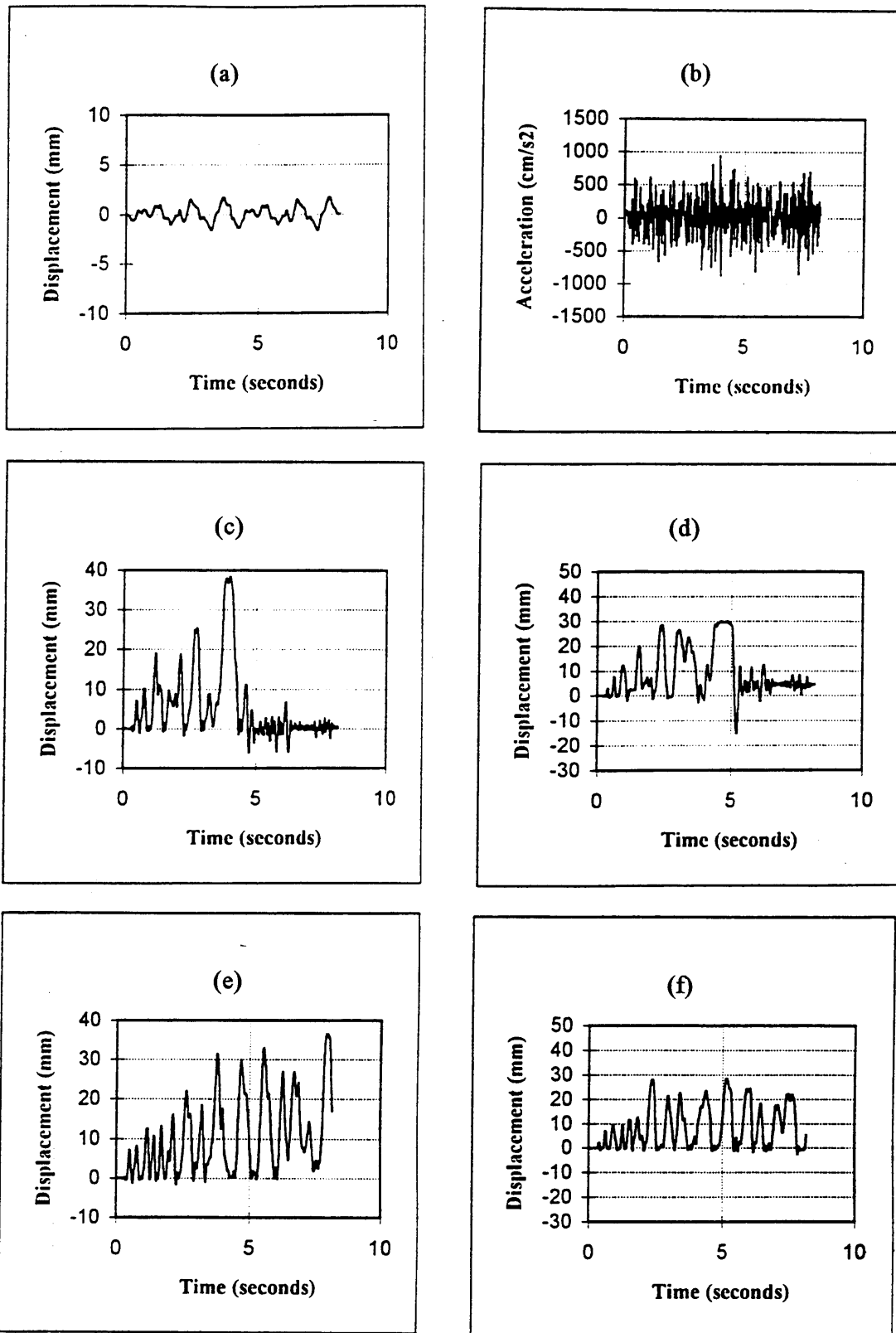


Figure 6-7. Recorded shaking table results:

- (a) Base displacement in test 26; (b) Base accelerogram in test 26;
 (c) Top displ. of left column in test 26; (d) Top displ. of right col. in test 26;
 (e) Top displ. of left column in test 25; (f) Top displ. of right col. in test 25.

Some results are presented in Figure 6-7. The time-history of base displacements and accelerations for the third series of tests are shown in Figure 6-7 (a) and (b) respectively (test No. 26). Figures 6-7c and 6-7d show the displacements of the top of the left and right columns respectively (test No. 26) for the case where the arch fails. The behavior of the columns before failure is characterized by low frequency large amplitude oscillations. A half cycle with large period and amplitude occurs when the arch falls down. The right column undergoes a permanent displacement of approximately 5 mm due to outward sliding. In Figure 6-7 (e) and (f), the top columns displacements for the non collapse case are plotted (test No. 25). Note the low frequency large amplitude oscillations and the large residual displacement in the left column due to its outward tilt (associated to the lowering of the arch) in the final configuration as it can also be seen in Figure 6-7 (b).

6.2.2.2 Numerical Simulations

The same stiffness and damping interaction parameters used for the study of the harmonic oscillations of the arch were adopted here. A series of twenty different earthquake accelerograms with a duration of 20 sec have been simulated using the SIMQKE program. They have been derived from the response spectrum of the EC8 Seismic Code corresponding to soil type B.

Each accelerogram has been scaled several times such that its peak acceleration a ranged from 1.15 to 1.40 with 0.05 intervals (acceleration is normalized with respect to $\lambda g = 0.325 * 981$ (cm/sec²) which is the minimum constant acceleration causing the arch failure). A DEM analysis has been performed for every scaled version of the 20 accelerograms, and for each one the lowest peak ground acceleration which caused failure was determined. Results are reported in Figure 6-8 in the form of cumulative density function of the lowest failure peak ground acceleration a_{max} which constitutes the vulnerability curve of the arch.

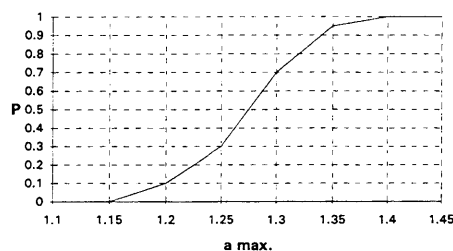


Figure 6-8. DEM estimate of the seismic vulnerability of the 8-node arch using 20 simulated accelerograms with a duration of 20 sec.

In Figure 6-9 the comparison of the numerical and experimental failure mechanism of the arch subjected to one of the simulated accelerograms is presented.

The shaking table results (Table 6.3)¹ show that in the range $2.76 < a < 2.95$ there is an overlapping of the survival and collapse cases, the average being $a_{exp} = 2.85$. In the discrete element analyses the analogous range is $1.15 < a < 1.40$ with average $a_{num} = 1.27$. The great difference between the two values is due, in the first place, to the longer duration of the accelerograms used in DE analysis (20 sec), with respect to the duration of those used in the lab tests (8 sec). In fact the progressive damage accumulation which takes place during the longer accelerograms, determines substantially lower failure accelerations than for the shorter earthquakes. However, also for the harmonic oscillations case, the experimental model failed for a lower peak acceleration than the numerical one. This tendency is similar to the one observed in the previous chapter for the quasistatic case, and it may again be explained by the presence of geometric imperfections in the experimental model which are not accounted for in the current DEM analysis.

¹ Note that the peak acceleration given in Table 6-3 is normalized with respect to $\lambda g = 0.325 * 981$ (cm/sec²) which is the minimum constant acceleration causing the arch failure.

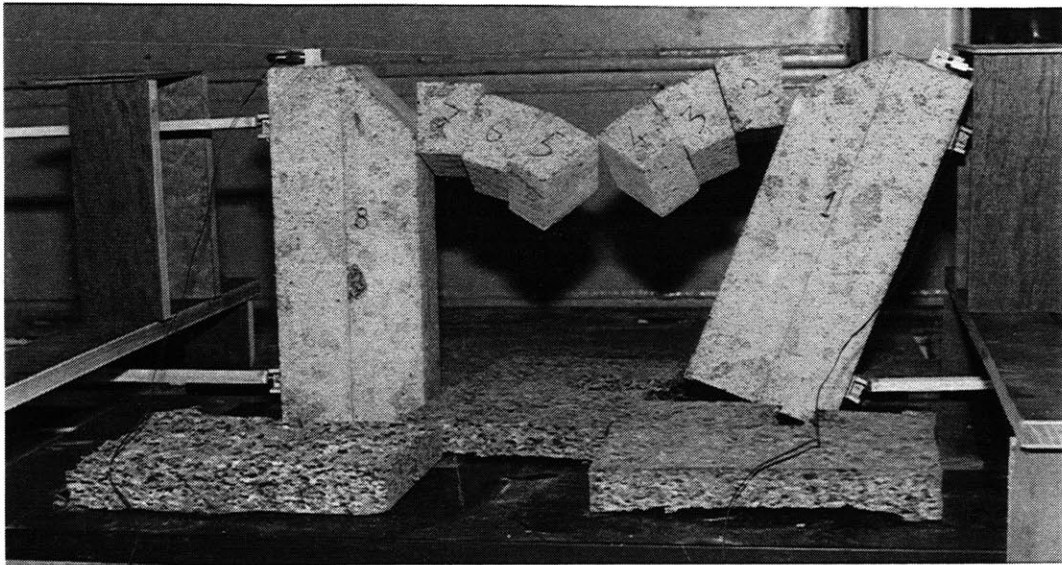
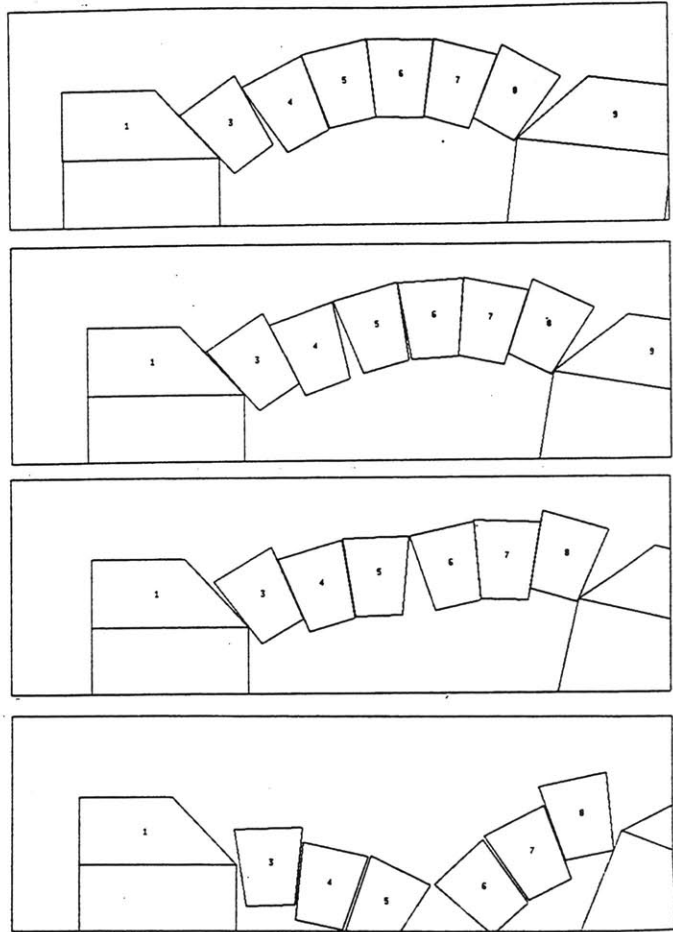


Figure 6-9. Comparison of numerical and experimental failure mechanisms of an arch subjected to seismic ground motion.

It is of interest to observe that, comparing the system configurations corresponding to quasi-static lateral loading (Figure 6-10), harmonic shaking (Figure 6-11), and a simulated earthquake ground motion (Figure 6-12), it appears that the DEM is capable of capturing these remarkably complex and differentiated responses. In the quasi-static application of a lateral load, the failure is reached when the ratio λ of horizontal and vertical load is 0.325. Both the predicted failure load and collapse mechanism are in very good agreement with the experimental observations. The failure mode involves the rocking of one column, with the formation of one sliding surface and several hinges. The harmonic shaking at 5 Hz with $a_{\max} = 1.5$ does not cause failure, and the system response reaches a steady oscillation mode after the 4 central blocks have progressively sledded down and the columns have tilted outward. In the simulated earthquake motion the response is fairly complex and it varies with the type and amplitude of the accelerogram, however, it usually involves the sliding down of the central blocks, the outward tilting of the columns, and impacting between blocks with wide joints openings and closures before failure, which occurred for $1.2 \leq a_{\max} \leq 1.4$. In particular the response due to the accelerogram n.3 is illustrated in Figure 6-12 and Figure 6-13, where the configurations near failure, and the time history of the rotation of the right hand column are given.

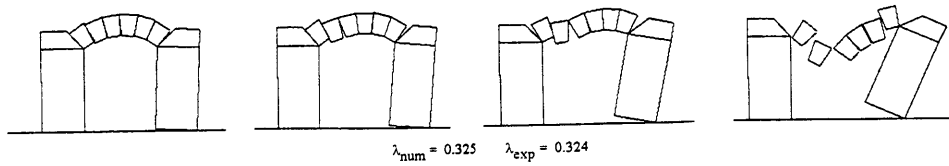


Figure 6-10. Predicted failure mode, and numerical vs. experimental failure loads λ due to quasi-static lateral loading.

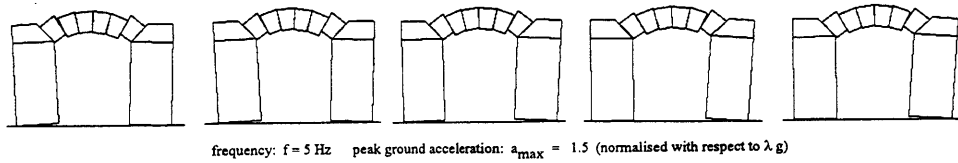


Figure 6-11. Predicted steady state oscillation mode due to **harmonic** ground shaking.

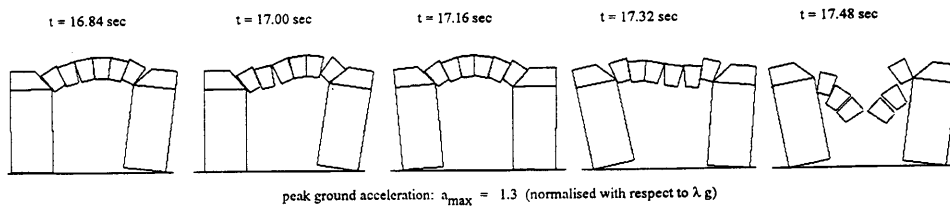


Figure 6-12. Predicted failure mode due to a **simulated earthquake ground motion** (accelerogram n. 3).

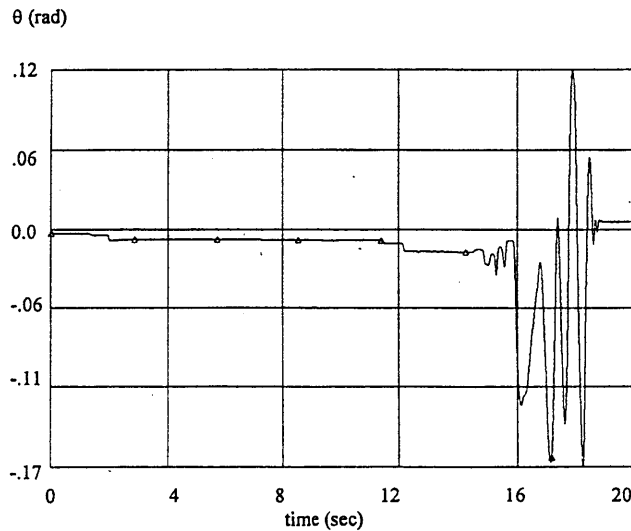


Figure 6-13. Predicted time history of rotation θ of right hand column of the 8-node arch due to simulated earthquake ground motion (accelerogram n. 3 with duration of 20 seconds).

6.3 CONCLUSION

A series of laboratory tests for the investigation of the dynamic behavior of block structures were performed. They included the study of the response of:

- (1) single blocks with aspect ratios from 2 to 5 subjected to free rocking;
- (2) a single block subjected to harmonic shaking with various shaking frequencies and amplitudes;
- (3) a multi-block arch structure subjected to harmonic shaking with various shaking frequencies and amplitudes;
- (4) a multi-block arch structure subjected to a series of simulated earthquake accelerograms applied with shaking table.

The DE model was calibrated using the free rocking experimental results, and then verified by comparing the numerical predictions with the experimental results for the harmonic oscillations of a single block (section 6.2.1).

For the 8-block arch structure subjected to harmonic oscillations, the experimental failure acceleration was lower than the numerical one. This difference is probably due to the geometric imperfections of the experimental model which are not accounted for in the DE model. In addition, it was shown how a seismic vulnerability analysis of the 8-block arch structure can be performed based on the proposed DEM analysis procedure.

It may be concluded that the Discrete Element Method - coupled with simple laboratory tests for the calibration of the block interaction parameters - may be a promising tool for predicting the highly nonlinear dynamic response of multi-block structures characterized by sliding, rocking, and impacting between blocks. However, more work is necessary for accounting for the geometrical imperfections, and developing a more general model for the energy dissipation associated to the impact.

Chapter 7: A NEW JOINT MODEL FOR D.E. ANALYSIS OF HISTORICAL STRUCTURES

- 7.1 CRITICAL EVALUATION OF CURRENT DEM RESULTS
- 7.2 FORMULATION OF A NON COPLANAR JOINT MODEL
 - 7.2.1 Experimental observations of out-of-plane wall failure
 - 7.2.2 Interpretation of experimental results
 - 7.2.3 The non coplanar joint model
- 7.3 IMPLEMENTATION AND VERIFICATION
 - 7.3.1 Definition of polygonal joint reference base
 - 7.3.2 Modified DE solution algorithm
 - 7.3.3 Verification analyses
- 7.4 SENSITIVITY ANALYSIS AND CALIBRATION
 - 7.4.1 Sensitivity with respect to joint geometry
 - 7.4.2 Sensitivity with respect to number of blocks
 - 7.4.2.1 Instability of a block column due to contact non coplanarity
- 7.5 APPLICATIONS
 - 7.5.1 14-block case
 - 7.5.1.1 14-block case with planar joint model
 - 7.5.1.2 14-block case with non coplanar joint model
 - 7.5.2 21-block case
 - 7.5.3 110-block case
 - 7.5.4 231-block case
 - 7.5.5 Assessment of friction softening
- 7.6 CONCLUSION

7. A NEW JOINT MODEL FOR DE ANALYSIS OF HISTORICAL STRUCTURES

It is recalled that the general objective of this research is the improvement of the seismic vulnerability assessment of historical structures using the Discrete Element Method. The types of structures which have been addressed are those constituted by blocks which interact mainly through frictional contacts. They can be either masonry structures without mortar¹, such as ancient opus quadratum constructions, or megalithic structures made by few large blocks such as Egyptian, Greek and Roman columns, trilites, and temples. These structures are characterized by low stress levels, and, under seismic actions, they generally collapse by overall loss of equilibrium rather than by material failure. In other words, the response of block structures to strong ground motion is often governed by sliding, rotations, and separation between blocks. The prediction of this highly non linear mechanical behavior still constitutes a challenging task. Currently used analysis methods such as Finite Elements, Limit Analysis, or special purpose dynamic analysis procedures, as discussed in the previous chapters, are generally recognized as either inadequate or not sufficiently general for the prediction of the mechanical response of complex and inherently discontinuous block structures to seismic actions.

In this work, the approach adopted for modeling historical structures is based on abandoning equivalent continuum schemes in favor of a representation of such structures as a system of distinct elements. As illustrated in the previous chapters, the application of the DEM to this area has yielded very promising results. However certain discrepancies with respect to the experimental results have been observed. The new developments presented in this chapter are aimed at overcoming the observed limitations, and consequently extending the applicability of the DEM to the seismic vulnerability of historical structures.

¹ The case of historical masonry structures with ineffective mortar are also in the scope of this study.

7.1 CRITICAL EVALUATION OF CURRENT DEM RESULTS

Before presenting the formulation of the new constitutive model, the previous work performed in the present study, employing current DEM, is briefly summarized and evaluated.

The seismic load was modeled both as a system of *quasistatic* lateral forces applied to the centroid of the elements, and also as a fully *dynamic* action caused by the ground shaking. Full details of such analyses were given in the previous chapters.

Within the context of the standard DEM, the strength and deformation characteristics of the joint were represented in a lumped form at the contact nodes. In the normal direction, a linear compression behavior with zero tensile strength has been assumed. In the tangential direction, an elastoplastic model with yield strength equal to Coulomb friction was selected.

For the quasistatic case, the objective has been the determination of the lateral failure loads and associated failure mechanisms of opus quadratum walls² subjected to gravity and slowly increasing lateral load. The work included the verification of the accuracy of the model predictions with respect to limit analysis for a series of representative cases, and a study of the sensitivity of the solution with respect to essential parameters of the DEM model. Both provided good results. When compared with experimental tests, the numerical predictions of the failure mode were in reasonable agreement.

However, several differences between the DEM results and the experimental response were observed³:

² Opus quadratum is the classical masonry typology made by regular squared blocks interacting only through friction.

³ see Chapter 5 for details on experimental and numerical tests.

- (1) the numerical predictions systematically overestimated the actual experimental failure load;
- (2) at failure, the sliding and rotations among blocks were generally localized in relatively narrow diagonal bands, on the contrary the numerical model predicted sliding and rotations over a wider area of the wall⁴;
- (3) micro-sliding progressively developed starting from 80% of the failure load, while in the numerical model the wall remained practically undeformed up to failure;
- (4) for the case of long and short walls with long blocks (where collapse occurred by sliding only) the failure load was 10% lower than the friction coefficient, whereas the numerical model did not predict this apparent shear strength reduction; and
- (5) in the case of the in-plane loading of the 21-block wall the failure mode was incorrectly predicted as pure sliding while in fact it was a mixed sliding and rotating mode.

For the dynamic case the main additional difficulty with respect to the quasistatic case lies in the appropriate prediction of the energy loss at the interfaces between blocks. Energy dissipation is associated to friction and internal material damping, and a realistic prediction of such phenomena even for the simplest case of 2 impacting blocks would require a very complex numerical model. For a block system of realistic size, such approach becomes practically impossible. An attempt has been made, in the context of the DEM, to model the internal material damping with a lumped viscous element acting at the interface between the blocks, and retaining a simple representation of the block interior. For the case of rocking of a slender block on a rigid base, an empirical expression for the parameter of the viscous element has been obtained by minimizing errors of predicted restitution ratios with respect to “exact” values obtained with the Housner model. Good agreement with experimental results has been found for a range of slenderness ratios (from 2 to 5). Using the same parameter, acceptable agreement with experimental results has also been found for the case of harmonic base shaking of the single block. For a case of a multibody arch structure subjected to ground shaking, the same viscous parameter obtained for the case of a single block has been assumed. A

⁴ see as an example WALL3 in Chapter 5

reasonable agreement was found with experimental results. However it was noted that for this particular case the system response was dominated by the rocking of the two columns, which, as previously reported, is well described by this model.

From the work performed it appears that the quasistatic approach is promising even though a number of discrepancies in the response prediction were observed and need to be resolved. In the more complex dynamic case, a simplifying assumption is made in the representation of the damping at impact, and while it may be acceptable for single block structures or for certain types of multibody systems a more general interface dissipation mechanism needs to be defined. Since the problems identified in the quasistatic analyses will have an impact also on the dynamic case, it was decided to approach them first.

7.2 FORMULATION OF A NON COPLANAR JOINT MODEL

In order to propose an improved DE model which may overcome the observed limitations, it is necessary to understand the causes of such discrepancies. Several aspects need to be considered: the randomness of the friction coefficient, the variability of the friction coefficient with normal load, the softening behavior of the joint in the tangential direction, and possible relative microrotations of blocks at the joints due to either the deformability of the asperities, or to the non coplanarity of the contact surfaces.

The frictional behavior of a joint is a complex phenomenon which has been studied extensively (as already illustrated in Chapter 5). Comprehensive constitutive models have been proposed both in the fields of reinforced concrete (Fardis and Buyukozturk, 1979), and rock mechanics (Plesha, 1987), which, among other aspects, account also for dilatancy and contact surface degradation which are not considered in the current DE model. However, based on the observations of the failure of small scale walls subjected to out-of-plane loading, in which no sliding takes place, it appears that the microrotations at the joints play an important role and should be investigated further.

In fact, the out-of-plane failure mode of a brick wall had not been previously investigated in this study because of its apparent simplicity when compared to the in-plane failure of the same wall. However, the same ease of interpretation has yielded some interesting observations with regard to the identification of the causes of the previously mentioned limitations of the current DEM.

7.2.1 Experimental observations of out-of-plane wall failure.

Experiments on small scale models of walls subjected to out-of-plane lateral forces have been reported in (Ceradini, V. 1992). The walls were built with peperino blocks⁵ with dimensions of 17.5 x 40 x 80 mm, weight of 120 g, and average friction coefficient of 0.6. The blocks had been cut very carefully with an accuracy of the order of 10^{-1} mm. Increasing lateral forces were generated using a tilting table. Out-of-plane lateral forces were obtained by placing the wall in a plane parallel to the axis of rotation of the tilting table. Defining α as the angle of the base plane with respect to the horizontal plane, the gravity force F acting on each block had components F_n and F_p , respectively normal and parallel to the wall

$$F_n = F \sin \alpha \quad \text{and} \quad F_p = F \cos \alpha \quad (7-1)$$

A normalized measure λ of the lateral forces acting on the wall is given by:

$$\lambda = \frac{F_n}{F_p} = \tan \alpha \quad (7-2)$$

Figure 7-1 shows the 14-layer wall tested in (Ceradini, V. 1992). In the loading plane, the dimensions were: $b = 40$ mm, and $h = 245$ mm. The wall failed by rigid body rotation around its base corner at a failure load $\lambda_{\text{exp}} = 0.132$. The exact failure load of a rectangular rigid body with same base and height which is given by $\lambda_{\text{rig}} = b/h = 0.163$. Note that the failure load λ_{DE} obtained with DE analysis using the current joint model is $\lambda_{\text{DE}} = \lambda_{\text{rig}} = 0.163$.

It appeared that the experimental failure load was only 81% of the predicted failure load:

$$\frac{\lambda_{\text{exp}}}{\lambda_{DE}} = 0.81 \quad (7-3)$$

The cause of the overestimation of the failure load predicted with DEM is quite clear. In the experiment, before failure, the wall appeared slightly bent⁶ in the direction of the horizontal forces, and consequently the projection of the wall centroid on its base had moved closer to the corner around which the rotation takes place at failure (Figure 7-1c). As a consequence the stabilizing moment was reduced, and therefore failure became possible for a lower value of lateral forces. Such deformation before failure is not predicted with the DE model, where instead the wall behaves essentially as a rigid body.

The apparent bending of the wall takes place gradually with the increase of lateral load λ . In Figure 7-2 the dashed curve O-C shows an indicative relationship between the lateral displacement of the wall centroid δ_g and the lateral load λ . The curve starts in O and increases monotonically up to a point C with coordinates: δ_g^* ; λ_{exp} , which corresponds to the failure configuration.

In general, for any rectangular wall with base b and height h , that fails by overturning - after some internal displacements had taken place, the following relationship between the lateral centroid displacement at failure, δ_g^* , and the failure load λ_{exp} can be obtained using simple equilibrium considerations:

$$\lambda_{\text{exp}} = \left(1 - \frac{2\delta_g^*}{b}\right) \lambda_{\text{rig}} \quad (7-4)$$

⁵ these were the same type of blocks used in all other experimental small scale tests of walls presented in this thesis.

where $\lambda_{\text{rig}} = b/c$, is the rigid body failure load.

The line A-B in Figure 7-2 represents the above relationship.

Note that if the apparent bending of the column at failure is small, point C tends to A, and the column behaves as a rigid body with a failure load close to λ_{rig} . If the bending is more pronounced, δ_g^* tends to $b/2$ and the resulting failure load tends to zero. The conditions under which this limit situation takes place - due to microrotations at the joints - is discussed in section 7.4.2.1.

⁶ with a top displacement $\delta_{\text{top}} = 11.5$ mm, and a centroid displacement $\delta_g = 3.8$ mm

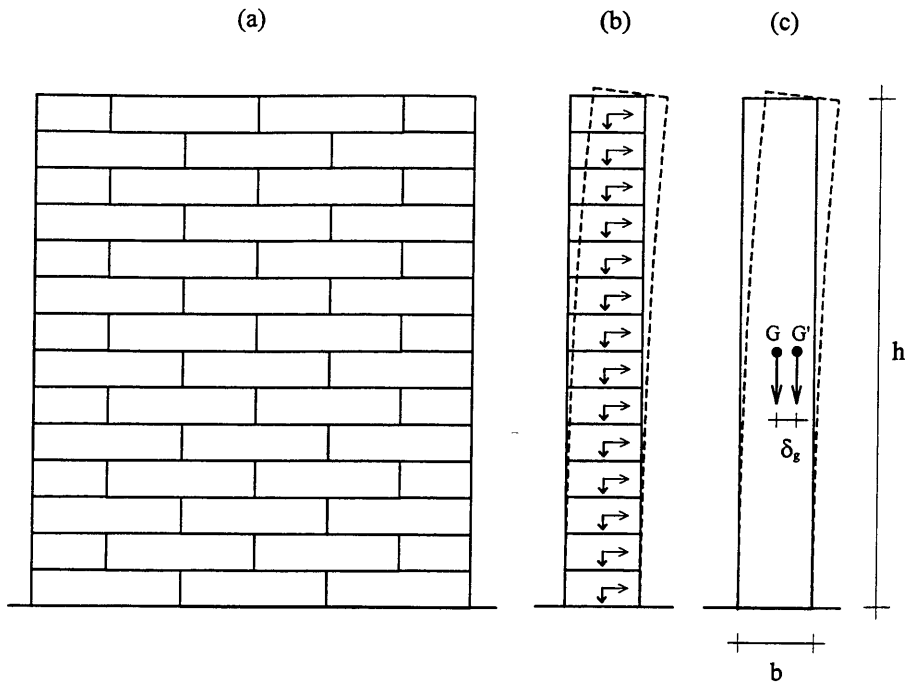


Figure 7-1. Out-of-plane loading of a 14-layer wall. The lateral load causes an apparent bending due to microrotations at the joints. (a) view in the plane perpendicular to lateral forces; (b) view in the plane parallel to lateral forces; (c) lateral displacement δ_g of wall centroid.

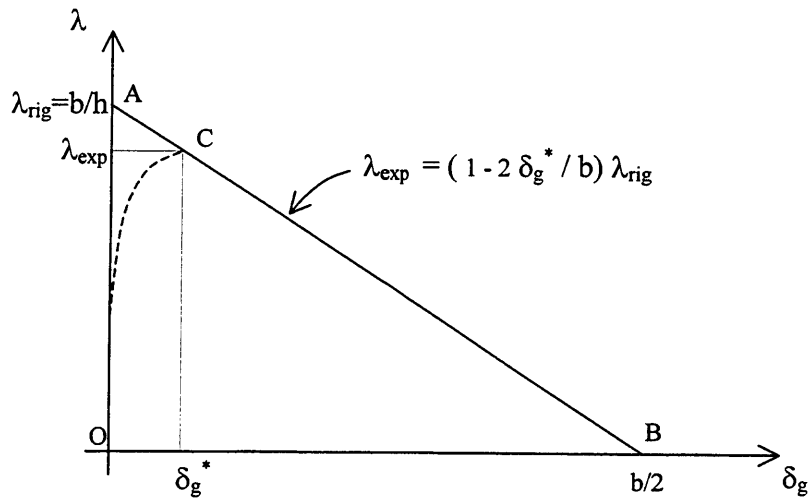


Figure 7-2. The curve O-C is an indicative relationship between lateral load λ , and centroid lateral displacement δ_g for the 14-layer wall up to failure. The segment A-B delimitates the curve $\lambda(\delta_g)$ for any rectangular wall.

7.2.2 Interpretation of experimental results

The observed apparent bending could not be attributed to internal strain because of the very low stress level⁷ with respect to the compressive strength of the stone block, but rather to the accumulation of microrotations at the joints, and again, for the same reason, it appears more likely that such microrotations were due to the noncoplanarities of contact surfaces as opposed to deformations of the joints.

In fact, due to the irregularities of the surfaces of the blocks, only a few points along the joint can be in contact, as illustrated in Figure 7-3. In 2D, a stable contact between two blocks generally requires two contact points, and also requires that the resultant N_a of the active forces acting on each block intersects the joint in a point P which lies between the 2 contact points. When the resultant of the active forces N_a , shifts from a point P included in the interval delimited by the contact points B and C , to a point P' in the adjacent interval C - D , the block goes through an unstable phase where the contact occurs only in C and a rotation $\Delta\theta$ takes place due to the unbalanced moment $M = e N_a$ (e is the eccentricity of N_a and is measured by the distance between C and P')⁸.

Therefore, in the out-of-plane loading of the 14-layer wall described in the previous section, we can assume that the observed apparent bending before failure, was due to the small rotations occurred at the joints related to the non perfect planarity of the contact surfaces. As the horizontal load increases the resultant of the active forces N_a moves from the center of the joint in the direction of the lateral load. This shift is higher for the bottom blocks which will tend to rotate first. A rotation at a joint will cause the rigid body rotation of the entire portion of the wall above such joint. This rotation will determine a further shift of N_a in all joints, and this in turn may determine further rotations and so on until either a new stable configuration is obtained, or failure is reached.

⁷ not exceeding 0.674 psi for the 14-layer wall.

⁸ note that, in the expression of the unbalanced moment, N_a represents the component of the resultant of the active forces normal to the joint.

Such behavior, quite evident in the out-of-plane case, is expected to have a lower, but still significant impact also in the in-plane case, and possibly explain some of the previously mentioned discrepancies observed using the current DE model. In the following a joint model which account for the non coplanarity of the contact surfaces between blocks is presented.

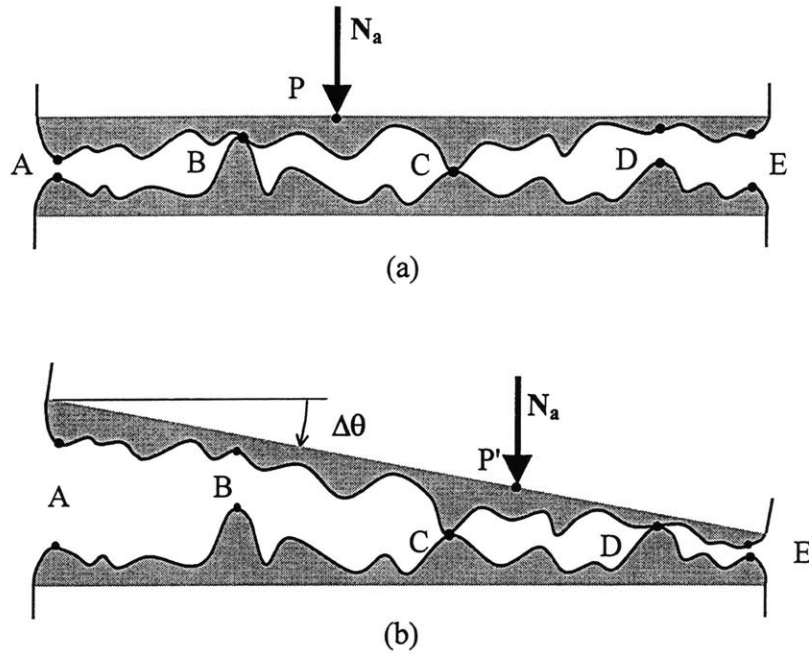


Figure 7-3. Effect of irregular contact: relative microrotation $\Delta\theta$ of two contacting blocks due to a shift of the resultant of the active forces N_a .

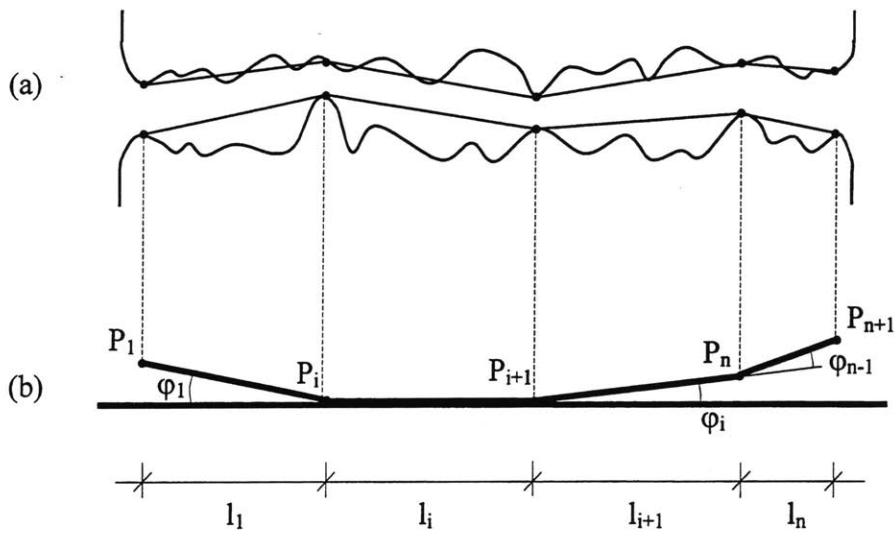


Figure 7-4. Convex polygon on a flat surface as the representation of the contact between two irregular surfaces.

7.2.3 The non coplanar joint model

In the following we will first consider the normal behavior of the joint which is directly related to the microrotations of the blocks. Subsequently, a modified friction softening tangential constitutive relation for addressing the problem of sliding localization will be presented.

Concerning the non coplanarity of the joint, in the first place, it is necessary to simplify the geometric representation of the two irregular surfaces at a joint without modifying the kinematics of the system.

It is observed that along a generic joint of length l there are in general $n+1$ possible contact points P_i , which define n possible stable contacts c_i between any two consecutive contact points P_i and P_{i+1} positioned at a distance l_i one from the other. For changing contact from c_i to c_{i+1} a slight relative rotation φ_i among the two blocks has to take place.

Consider the convex polygon with n sides of length l_i , in which each side s_i forms an angle $\varphi_i' = 180 - \varphi_i$ with the following side s_{i+1} . For the purpose of describing the possible relative microrotations of two adjacent blocks it is clearly possible to replace the complex profiles of the asperities of the two surfaces in contact (Figure 7-4a) with the previously defined convex polygonal base in contact with a flat surface⁹ (Figure 7-4b). In the following we will refer to this geometrical representation of the joint, and particular attention will be given to the definition of the polygonal base.

The parameters which define such polygon are the lengths l_i and the angles φ_i which can be considered as random variables. The distribution of such variables could be derived directly from experimental measures of surface roughness, or indirectly from the measurement of global parameters (such as the failure load λ^* , or the maximum

⁹ The only negligible difference is that the centers of rotation in the polygonal contact are aligned along the flat surface, while in the real case they may be slightly up or down with respect to such surface.

centroid lateral displacement δ_g^*) of the response of a simple block assemblage subjected to lateral loads.

Let us look more carefully to the behavior of the joint, represented now by the previously defined polygon, when a rotation takes place due to a shift of the resultant of the active forces N_a . In the following we consider separately the forces normal and tangential to the contact surface. The normal forces are directly related to the microrotations and will be addressed first.

Initially, the position P of the projection of the resultant of the active forces N_a along the joint will determine which of the n possible contacts will be activated. In fact, it is quite clear that the contact will be at the two consecutive points P_i and P_{i+1} which include P as shown for example in Figure 7-5a. In the same figure also the reactive forces N_i and N_{i+1} and their resultant N_r are indicated. Since the system is in equilibrium: $N_r = -N_a$, and they are applied to the same point.

When N_a moves from P in the interval $[P_i, P_{i+1}]$, to P' in $[P_{i+1}, P_{i+2}]$, the system goes through an unstable phase in which the blocks are in contact only in P_{i+1} , and the unbalanced moment $M = e N_a$ will cause the block rotation $\Delta\theta$ as shown in Figure 7-5b. In this phase while N_a is applied to P' , the reactive force N_r is still applied in P_{i+1} .

Finally when the rotation $\Delta\theta$ is equal to φ_i a new stable contact at points P_{i+1} and P_{i+2} is re-established. The resultants of the active and reactive forces, N_a and N_r respectively, are again applied in the same point P' (Figure 7-5c).

Clearly in the current DE planar joint model, when there is a shift of the resultant of the active forces N_a , (from P to P' as indicated in Figures 7-6a and 7-6b), the reactive forces F_1 and F_2 , which are generated by the two normal stiffness K_1 and K_2 located at the two ends of the joint, will tend to equilibrate the active forces. As a consequence N_a and N_r will always be aligned causing no unbalanced moment and no relative rotation.

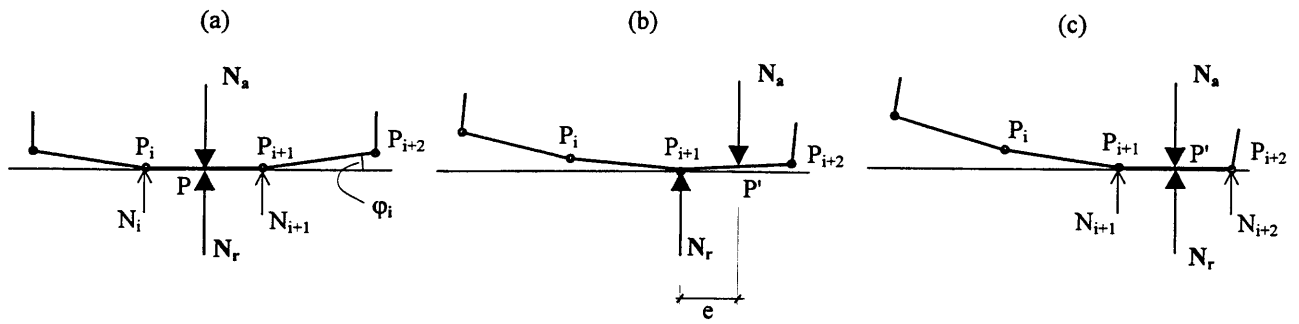


Figure 7-5. Forces acting on a block during a shift of the resultant of the active forces N_a from P to P' . A microrotation $\Delta\theta = \phi_i$ takes place.

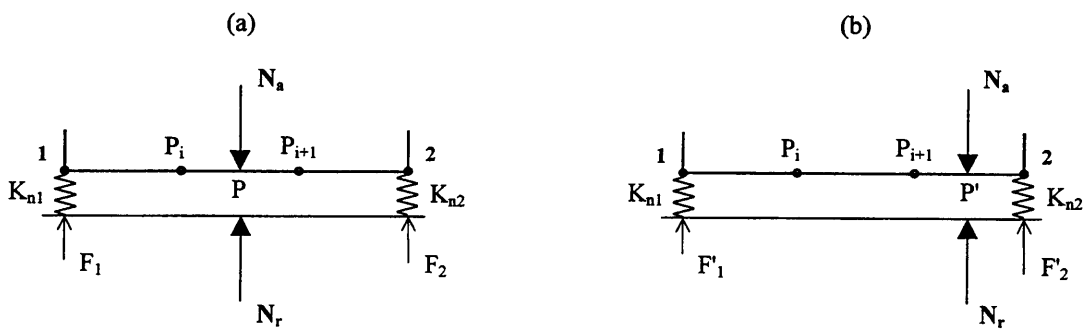


Figure 7-6. Current DE model: forces acting on a block during a shift of the resultant of the active forces N_a from P to P' . No microrotation takes place.

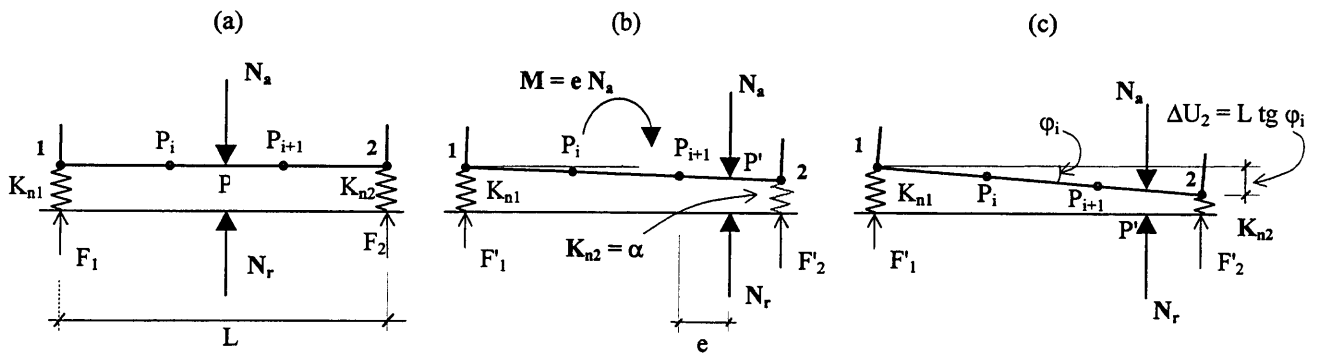


Figure 7-7. Scheme of proposed modifications to DE joint model to account for microrotations.

Based on the previous considerations, in order to account for the relative joint rotations the following modifications to the current DE joint model are proposed. The location of the point P (the intersection of the projection of the resultant N_a of the active forces and the joint) is monitored during the analysis, and when it moves from a position P in the interval $[P_i, P_{i+1}]$ to a position P' in the adjacent one $[P_{i+1}, P_{i+2}]$, a microrotation of the joint is allowed by:

- (a) softening the normal stiffness K_n on the side of the direction of the movement of N_a ; and
- (b) applying two opposite unbalanced moments of intensity $M = |e N_a|$ to the two blocks.

The normal stiffness K_n is set to a value α close to zero until a relative rotation $\Delta\theta = \varphi_i$ has been achieved. Subsequently the eccentricity e is reset to zero, and K_n is reassigned to its original value (see Figure 7-7).

More in detail, referring to Figure 7-8, where the subscripts “n” and “t” indicates the normal and tangential directions with respect to the contact surface, the following quantities are defined:

- K_{ni} and K_{ti} are the interaction stiffness at the node i ;
- F_{ni} and F_{ti} are the contact forces at the node i ;
- U_{ni} and U_{ti} are the relative displacements of the 2 blocks at the node i ;
- $e(F_{in}, \theta, j, \varphi_i, l_i)$ is the eccentricity of the contact forces, and $e \neq 0$ when an unstable contact is detected; more specifically $e = 0$ if the resultant of the active forces N_a is applied inside the current contact side of the reference polygon, or otherwise it is the distance between the current contact side and N_a ; e is taken positive in the direction from node 1 to node 2.
- θ is the current angle between the two blocks;
- j is the joint index indicating on which base or corner (of the reference polygonal base) the contact is currently taking place.

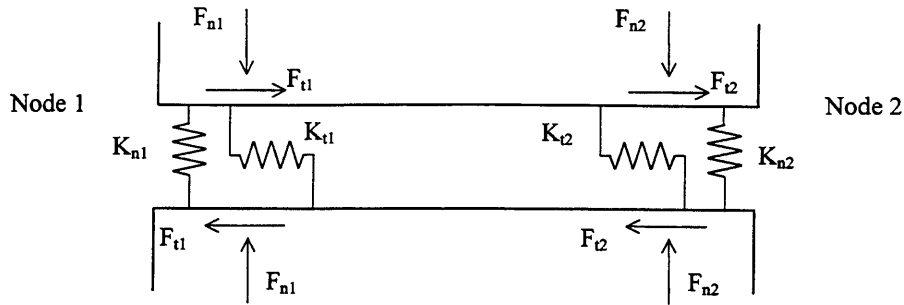


Figure 7-8. Interaction elements, and corresponding contact forces in the DE joint model.

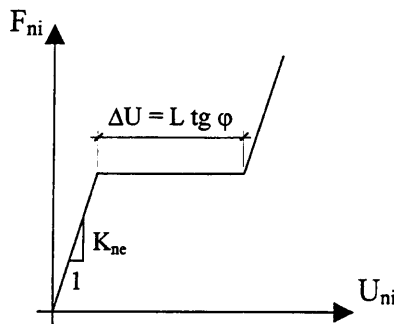


Figure 7-9. Modified joint behavior in the normal direction to allow microrotation φ : F_{ni} and U_{ni} are the force and the displacement in the normal direction at node i ; K_{ne} is the normal elastic stiffness of the joint; L is the joint length.

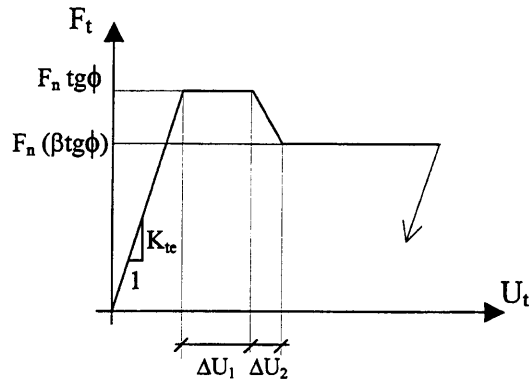


Figure 7-10. Modified joint behavior in the tangential direction to allow for friction softening: F_{ti} and U_{ti} are the force and the displacement in the tangential direction at node i ; K_{te} is the tangential elastic stiffness of the joint; $\text{tg}\phi$ is the friction coefficient; β , ΔU_1 , ΔU_2 are the parameters of the friction softening model.

The incremental constitutive relationship for the proposed joint model assumes the following form:

$$\begin{Bmatrix} dF_{n1} \\ dF_{t1} \\ dF_{n2} \\ dF_{t2} \end{Bmatrix} = \begin{bmatrix} K_{n1} & 0 & 0 & 0 \\ 0 & K_{t1} & 0 & 0 \\ 0 & 0 & K_{n2} & 0 \\ 0 & 0 & 0 & K_{t2} \end{bmatrix} \begin{Bmatrix} dU_{n1} \\ dU_{t1} \\ dU_{n2} \\ dU_{t2} \end{Bmatrix} \quad (7-5)$$

where the normal interaction elements control the development of microrotations:

$$K_{ni} = K_{ne} \text{ if } U_{ni} > 0 \text{ and } e(F_{in}, \theta, j, \phi_i, l_i) = 0; \quad (7-6)$$

$$K_{n1} = \alpha; K_{n2} = K_{ne} \text{ if } U_{ni} > 0 \text{ and } e(F_{in}, \theta, j, \phi_i, l_i) < 0; \quad (7-7)$$

$$K_{n1} = K_{ne}; K_{n2} = \alpha \text{ if } U_{ni} > 0 \text{ and } e(F_{in}, \theta, j, \phi_i, l_i) > 0; \quad (7-8)$$

$$K_{ni} = 0 \text{ if } U_{ni} < 0 \text{ (lost contact)} \quad (7-9)$$

and the tangential interaction elements have been modified to account for the friction softening behavior illustrated in Figure 7-10 and described in the following.

$$K_{ti} = K_{te} \text{ if } U_{ni} > 0 \text{ and } F_{ti} \leq F_{ni} \text{ tg}(\phi); \quad (7-10)$$

$$K_{ti} = 0 \text{ if } U_{ni} > 0 \text{ and } F_{ti} > F_{ni} \text{ tg}(\phi) \text{ and } 0 < U_s < \Delta U_1; \quad (7-12)$$

$$K_{ti} = -F_{ni} (1-\beta) \text{ tg}(\phi) / \Delta U_2 \text{ if } U_{ni} > 0 \text{ and } F_{ti} > F_{ni} \text{ tg}(\phi) \text{ and } \Delta U_1 < U_s < \Delta U_2 \quad (7-13)$$

$$K_{ti} = 0 \text{ if } U_{ni} > 0 \text{ and } F_{ti} > F_{ni} \text{ tg}(\phi) \text{ and } U_s > \Delta U_1 + \Delta U_2 \quad (7-14)$$

$$K_{ti} = 0 \text{ if } U_{ni} < 0 \text{ (lost contact);} \quad (7-15)$$

In the previous expressions:

- K_{ne} and K_{te} are the normal and tangential elastic stiffness of the joint;
- α is a value close to zero (e.g. $10^{-6} K_{ne}$) to which the normal stiffness is assigned when an unstable contact is detected (that is $e \neq 0$);
- $\text{tg}(\phi)$ is the friction coefficient for the two blocks;
- β , ΔU_1 , ΔU_2 are the parameters of the friction softening (as indicated in Figure 7-10), and U_s is the sliding distance.

It is observed that the microrotations allowed by the proposed model are around the limiting points of the joint while in reality they take place around a point in the interior of the joint. However a slight approximation in the location of the center of rotation should not significantly affect the overall response of the system. In fact, the essential feature which we are trying to describe with the proposed modifications to the model, is that relative rigid body rotations of given magnitude take place between contacting blocks when certain conditions are met. The rationale is that even if the magnitude of such rotations is small, if they take place in the lower part of the wall, they can result in non negligible horizontal displacements of the upper part of the same wall, with a reduction of the resulting failure load. This effect should not be affected by the slight approximation in the horizontal location of the relative center of rotation between the blocks.

In addition to accounting for the non coplanarity of the contact surfaces, another factor which could be important in explaining the localization of sliding, in the in-plane response of walls, and which is not considered in the current DE model, is the reduction of the friction coefficient when sliding has initiated (as described by eq. 7-10 to 7-15). It is well known, in fact, that the "static" frictional force is higher than the "dynamic" one. A complete description of such phenomenon is quite complex since the friction force depends upon many variables including: velocity, normal force, sliding distance, and material parameters. However it is thought that, considering that the current DE model uses a constant friction coefficient, even a simple description of such phenomenon may contribute to overcome the observed discrepancies between the DE predictions and the experimental response. Another consideration in favor of a simple frictional model relates to the difficulty in obtaining accurate estimates of the many parameters which are required in more complex frictional models for materials used in historical structures.

In the adopted model the friction coefficient $\text{tg}(\phi)$ is gradually reduced to $\beta \text{tg}(\phi)$ as indicated in Figure 7-10 (and described by eq. 7-13). The reduction initiates at a sliding distance $U_s = \Delta U_1$. Then the friction coefficient varies linearly for an additional

distance ΔU_2 , and subsequently is kept constant for any further displacement. The 3 parameters of the model: β , ΔU_1 , and ΔU_2 have to be obtained experimentally.

In the next section the implementation of the proposed model is presented.

7.3 IMPLEMENTATION AND VERIFICATION

The proposed joint model has been implemented in the Discrete Element program UDEC using the dedicated programming language FISH (UDEC, 1996).

7.3.1 Definition of polygonal joint reference base

Since the main objective of the new model is the simulation of the response of a block with a convex polygonal base - representing the non coplanarity of the contact, the first step in building its constitutive relation consists in defining the geometry of such reference polygonal base.

To this purpose it has been assumed that the polygon is always inscribed in a circumference of given radius r . The number n of sides and their lengths l_i (with $i = 1$ to n) complete the definition of the reference base. Instead of directly assigning r , it has been chosen to specify the maximum joint aperture d (see Figure 7-11) which has a more direct physical meaning¹⁰. Therefore for any joint of length L , the following $(n+1)$ parameters have to be defined:

- the number of sides n ,
- the lengths of $n-1$ bases¹¹: l_i with $i=1$ to $n-1$, and
- the maximum joint aperture d .

If a regular polygon is assumed then the geometrical parameters to be assigned for each contact are only two: n and d .

¹⁰ The exact definition of d , which may be viewed as a measure of the magnitude of the imperfection of the contact, is the distance between a straight line r_1 joining the ends of the polygon and the straight line r_2 tangent to the polygon and parallel to r_1 .

¹¹ The length of the n th base is obtained as $l_n = L - \sum_{(i=1, n-1)} l_i$, where L is the length of the joint.

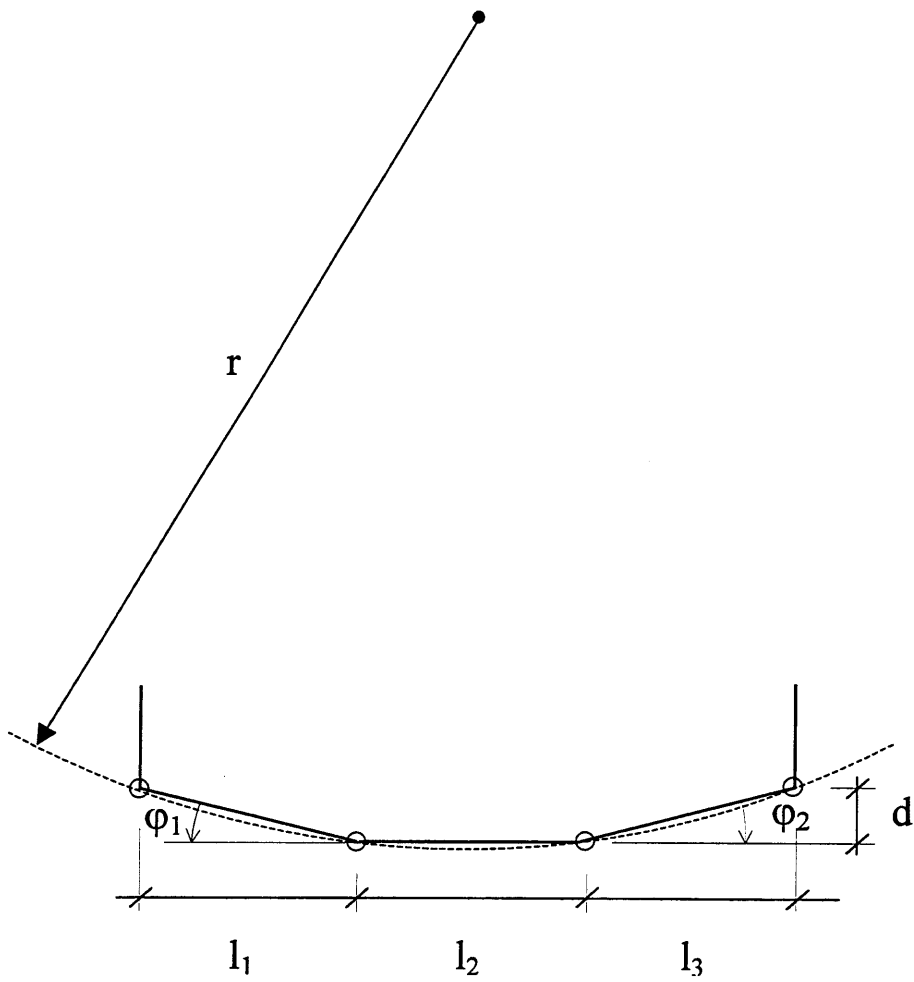


Figure 7-11. Definition of polygonal reference base underlying new DE joint model.

In order to account for the inherent randomness of irregularities of the contacts, the possibility of generating different reference polygons for each contact has been implemented. Their parameters may have a deterministic or a stochastic definition. In the last case, each parameter is assigned a uniform distribution between two prescribed limiting values:

- number of sides: n_{\min}, n_{\max}
- length of each base: l_{\min}, l_{\max}
- max joint aperture: d_{\min}, d_{\max}

Based on the previous data the angles of rotation φ_i (required to change contact from a base i to the adjacent one $i+1$) are computed. Thus the geometrical parameters l_i and φ_i required by the constitutive model are available.

7.3.2 Modified DE solution algorithm

An important aspect in the implementation of the joint constitutive model relates to the difference between the standard DE contact model which is oriented towards point contacts (corner-edge), and the new model which instead considers an extended linear joint between two edges of adjacent blocks. In other words in the standard DE model an edge-to-edge contact between two blocks is represented as two independent contacts which behave independently, instead, in the new joint model the behavior of the two contacts is a function of the state of the linear joint. This has required, the computation - at each time step - of the following variables which are associated to the state of the joint:

- the joint index j indicating on which base or corner (of the reference polygonal base) the contact is currently taking place¹²,
- the relative angle of rotation θ of the two blocks,
- the resultant N_r (in the direction normal to the joint) of the two contact forces (F_{n1}, F_{n2}) at the two nodes delimiting the joint,

¹² If a stable contact is taking place the joint index indicates the corresponding base, otherwise it indicates the corner around which a rotation is occurring.

- the position of N_r along the joint (given as distance d from the first contact of the joint),
- the eccentricity e of the force N_r with respect to the current stable base inside the joint,
- the unbalanced moment $M = N_r e$.

The determination of the lateral failure load requires first the application of the gravity forces (with a standard DE procedure), and then the incremental application of the lateral load λ .

After each increment of lateral load $\Delta\lambda$ is applied to the system, the standard DE time stepping is performed with the objective of determining a new static equilibrium configuration. If no equilibrium is possible the current lateral load is the failure load, otherwise a new increment $\Delta\lambda$ is applied. The difference with respect to the standard DE solution process is that checks have to be performed at every joint, and at every time step, in order to verify if a new unstable contact is detected, or if a previously unstable contact has become stable; in such cases the modifications to the stiffness elements, and to the forces acting on the blocks, as described in the formulation of the constitutive model, have to be accomplished.

A detailed scheme of the modified solution process for the new joint model is presented in Figure 7-12. The steps required by the standard DE algorithm are indicated in the same figure with a dashed line in order to clearly show the changes associated to the new model.

In the following sections after the verification tests, some applications to the in-plane failure of the opus quadratum walls (for which experimental results are available) will be performed in order to evaluate the actual improvement in the numerical predictions achieved with the new joint model.

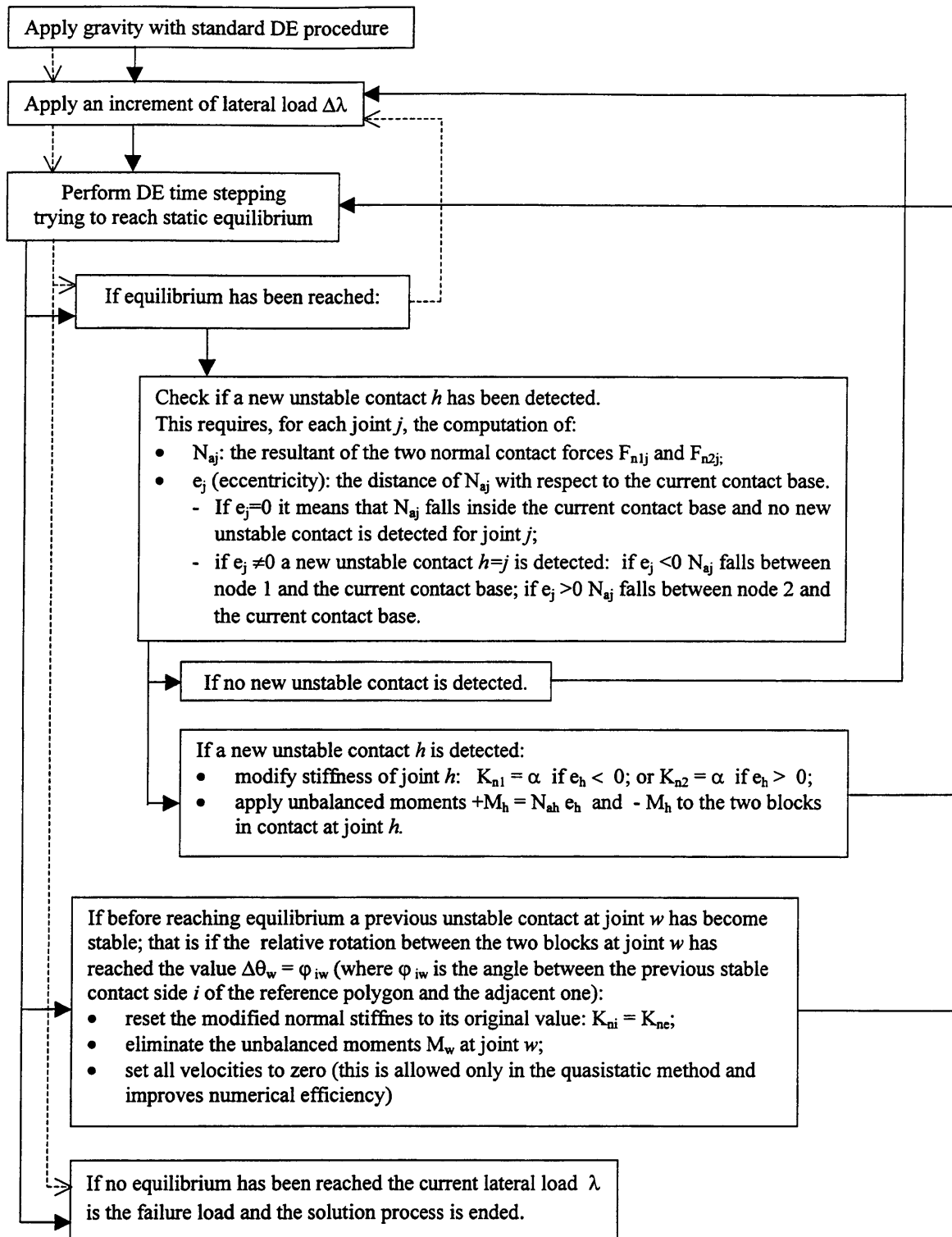


Figure 7-12. Solution process for determination of lateral failure load λ with new joint model (solid lines). Standard DE algorithm is indicated with dashed lines.

7.3.3 Verification analyses

In order to verify the behavior of the proposed joint model, a quasistatic analysis of a single rigid block subjected to gravity and a slowly increasing lateral force is performed. For such case the exact results are easily computed and therefore the evaluation of the proposed model is straightforward. First, the case of a monotonic loading up to failure is studied, subsequently the case of a cyclic loading is presented.

The block has a squared shape, with $b = h = 1$ m. The joint interaction elastic stiffness K_{ne} and K_{te} have been assigned to an arbitrary high value ($5 \cdot 10^6$ N/m) such that displacements due to elastic joint deformations are negligible with respect to those due to microrotations. A reference polygonal base with 5 sides of equal length, and a maximum joint aperture $d = 0.01 \cdot h = 1$ cm, has been assumed (see Figure 7-13 and Table 7-1). The corresponding geometric parameters of the joint model are $l_i = b/5 = 0.2$ m and $\varphi_i = 0.0166$ rad.

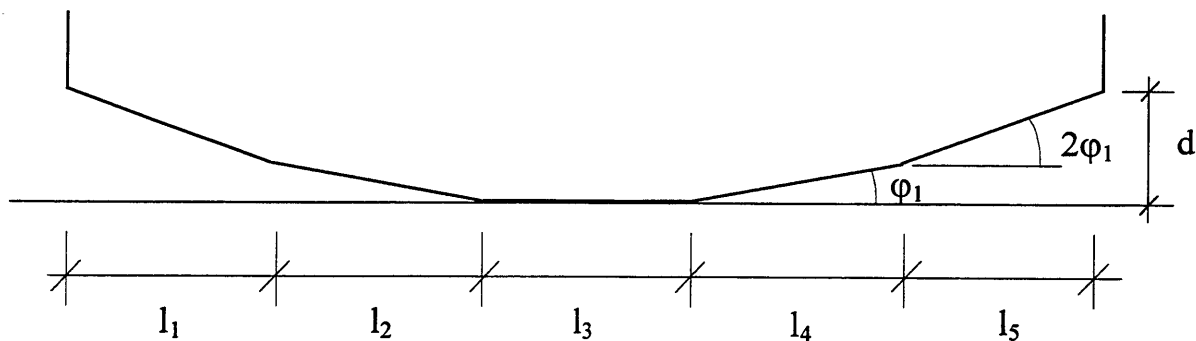


Figure 7-13. Reference polygonal base for verification test.

The objective of the first test is the study of the response of the block when subjected to a constant vertical force, $F_y = 10$ N, simulating gravity, and an increasing horizontal force F_x , simulating the seismic load, up to failure (both F_y , and F_x being applied to the block centroid). In particular it is of interest to verify: the formation of microrotations, the levels of lateral force which cause such microrotations, the associated displacements, and the failure load. The exact values of the previous quantities can be computed as illustrated in the following.

If the previously described block had a perfectly planar base, its normalized lateral failure load λ_{pl} would be:

$$\lambda_{pl} = F_x / F_y = b / h = 1, \text{ corresponding to a lateral force: } F_x = \lambda_{pl} F_y = 10 \text{ N}$$

For the block with the 5-sided polygonal base, assuming that after the application of gravity the contact occurred on the central base, the increasing lateral load will determine a first rotation φ_1 at a load level $\lambda = \lambda_1$, followed by a second rotation φ_1 at a load level $\lambda = \lambda_2$, and finally the overturning of the block at a load level $\lambda = \lambda_3$. It is easy to demonstrate that:

$$\lambda_1 = (b/5) / h = 0.200; \quad \text{corresponding to } F_x = \lambda_1 F_y = 2.00 \text{ N}$$

$$\lambda_2 = [3 b/5 - h \text{tg}(\varphi_1)] / h = 0.583; \quad \text{corresponding to } F_x = \lambda_2 F_y = 5.83 \text{ N}$$

$$\lambda_3 = [b - h \text{tg}(2 \varphi_1)] / h = 0.966; \quad \text{corresponding to } F_x = \lambda_3 F_y = 9.66 \text{ N}$$

The top horizontal displacements of the block due to the 2 microrotations can also be easily computed as :

$$\Delta U_1 = h \operatorname{tg}(\varphi_1) = 1.67 \text{ cm} \quad \text{and} \quad \Delta U_2 = h \operatorname{tg}(2\varphi_1) = 3.33 \text{ cm}$$

In order to verify the prediction of λ_1 , λ_2 , λ_3 , and ΔU_1 , ΔU_2 a DE analysis using the new joint model has been performed. First a vertical force $F_y = 10 \text{ N}$ has been applied to the block centroid, then the horizontal force (also applied to the block centroid) has been gradually increased with load steps equal to $\Delta F_x = 0.2 \text{ N}$ up to $F_x = 9.60 \text{ N}$, and subsequently $\Delta F_x = 0.01 \text{ N}$ up to failure.

Microrotations took place at $F_x = 2.2 \text{ N}$, and $F_x = 6.0 \text{ N}$, while failure occurred at $F_x = 9.66 \text{ N}$. The 3 values λ_{1nc} , λ_{2nc} , λ_{3nc} predicted with the non coplanar joint model are included in the following intervals and compare well with the exact values:

$$\begin{aligned} 0.200 < \lambda_{1nc} < 0.220, & \quad (\text{exact value } \lambda_1 = 0.200); \\ 0.580 < \lambda_{2nc} < 0.600, & \quad (\text{exact value } \lambda_1 = 0.583); \\ 0.965 < \lambda_{3nc} < 0.966, & \quad (\text{exact value } \lambda_1 = 0.966); \end{aligned}$$

Also the horizontal top displacements associated to the microrotations have been accurately predicted:

$$\begin{aligned} \Delta U_{1nc} &= 1.66 \text{ cm} \quad (\text{exact value } \Delta U_1 = 1.67 \text{ cm}) \text{ and} \\ \Delta U_{2nc} &= 3.30 \text{ cm} \quad (\text{exact value } \Delta U_2 = 3.33 \text{ cm}) \end{aligned}$$

Block data:

Base:	$b = 1 \text{ m,}$
Height:	$h = 1 \text{ m,}$
Mass density:	$M = 2 \text{ kg / m}^2$
Contact elastic interaction stiffness:	$K_{ne} = K_{te} = 5 \cdot 10^6 \text{ N/m}$
Friction coefficient:	$f = 1$

Reference polygon parameters:

Number of sides:	$n = 5$
Lengths of each side:	$l_i = 0.2 \text{ m}$
Maximum joint aperture:	$d = 1 \text{ cm}$
Angle between 2 adjacent sides:	$\varphi_1 = 0.0166 \text{ rad}$

Loading:

Centroidal Vertical forces:	$F_y = 10 \text{ N}$
Centroidal Horizontal forces:	
- loading sequence:	
$\Delta F_x = 0.20 \text{ N}$ from $F_x = 0.0 \text{ N}$ to $F_x = 9.6 \text{ N}$	
$\Delta F_x = 0.01 \text{ N}$ from $F_x = 9.6 \text{ N}$ to $F_x = 9.66 \text{ N}$	
- key values of horizontal forces:	
$F_x = 2.0, 2.2, 5.8, 6.0, 9.65, 9.66 \text{ N}$	

Table 7-1. Summary of data for first verification test.

In the following a series of figures document in detail the system response predicted by the non coplanar joint model.

To fully document the two microrotations and the initiation of the overturning it is useful to show the status of the system immediately before and after the instability has occurred, therefore a total of 6 states of the system have been presented. They correspond to the following levels of lateral load: $F_x = 2.0 \text{ N}$, 2.2 N , 5.8 N , 6.0 N , 9.65 N , 9.66 N . For each of them 3 figures are provided: (a) the global view of the

system, where a slight change in the configuration may be noted, (b) the magnified view of the contact area, where the amplitude of the base displacements can be quantified, and (c) the time history of the horizontal displacement of the top right corner up to specified level of lateral load (Figures 7-17 to 7-34). The same type of plots are also provided for documenting the initial response of the system to the vertical force $F_y = 10.0 \text{ N}$ (in Figures 7-14, to 7-16).

Note that each figure reports also the values of the lateral force F_x acting on the block, the simulation time, and the cycle number, corresponding to the time in which the figure was generated during the solution process¹³.

Finally in order to verify the response of the system to non monotonic loading an analysis of the same block with the same parameters, but subjected to one full cycle of lateral forces has been performed. The lateral force has been varied quasistatically between the following values: $F_x = 0 \text{ N}; +8 \text{ N}; 0 \text{ N}; -8 \text{ N}; 0 \text{ N}$. A series of 8 phases of instability, each one followed by a stable configuration, corresponding to 2 clockwise, 4 counterclockwise, and finally 2 clockwise microrotations have been correctly predicted. The load levels corresponding to such microrotations, and their magnitudes, have also been exactly predicted as documented in Figures 7-35 to 7-37.

After having verified the behavior of the new joint model, in the next section a series of calibration tests will be performed in order to select the appropriate values of the joint parameters which will be used in the application studies presented in section 7.5.

¹³ F_x is given in the title, the simulation time, and the cycle number are given in the top of the left panel of the figure. In addition, for the time history, the left panel contains also the maximum and minimum values of the quantities represented on each Cartesian axis.

$$F_x = 0.2 \text{ N} \quad F_y = -10 \text{ N}$$

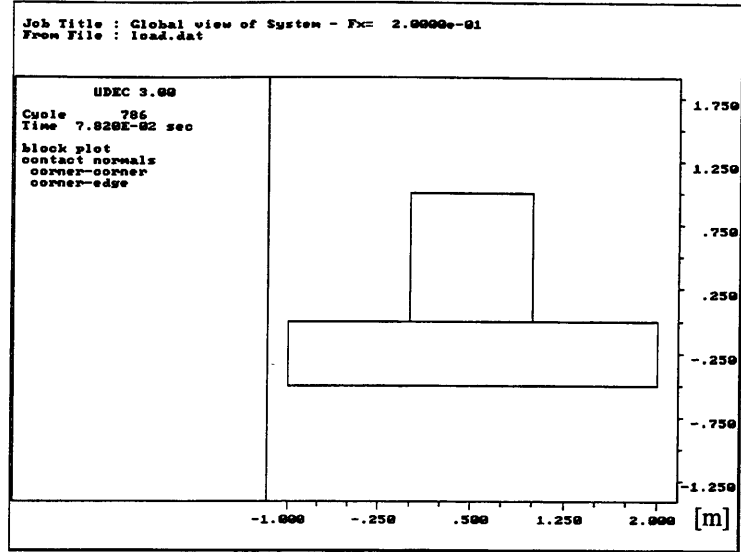


Figure 7-14. Configuration of the system after application of gravity force ($F_y = -10 \text{ N}$).

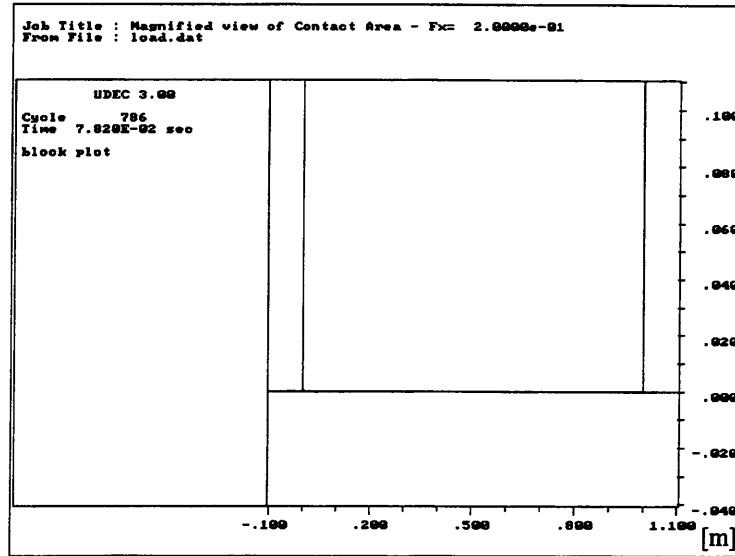


Figure 7-15. Magnified view of contact area after application of gravity force ($F_y = -10 \text{ N}$).

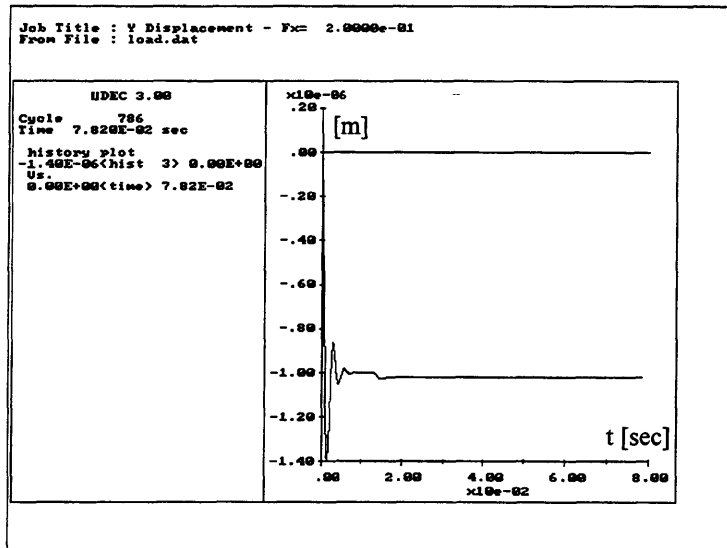


Figure 7-16. Time history of vertical displacement of top right corner after application of gravity force ($F_y = -10$ N). Negligible displacements (10^{-6} m) are caused by the joint elastic deformability in the vertical direction. Note vertical oscillations of the block before steady state is reached.

$$F_x = 2.0 \text{ N} \quad F_y = -10 \text{ N}$$

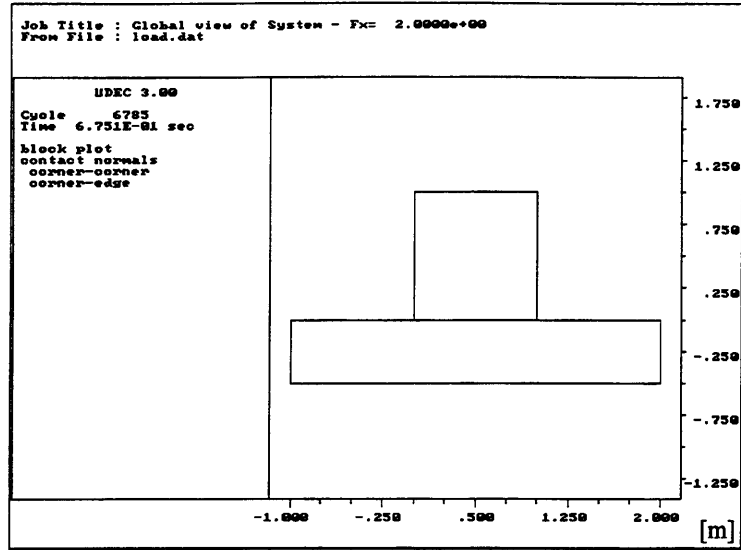


Figure 7-17. Global view of the system after application of forces: $F_x = 2.0 \text{ N}$, $F_y = -10 \text{ N}$. No microrotation has taken place.

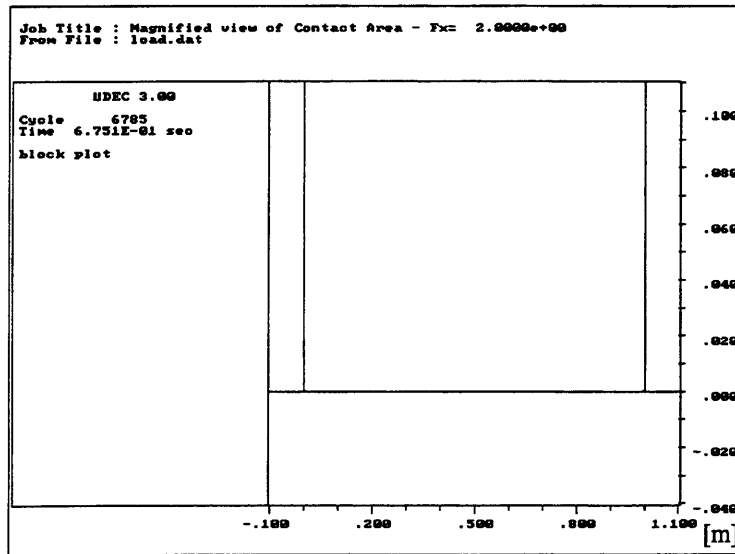


Figure 7-18. Magnified view of contact area after application of forces: $F_x = 2.0 \text{ N}$, $F_y = -10 \text{ N}$. No microrotation has taken place.

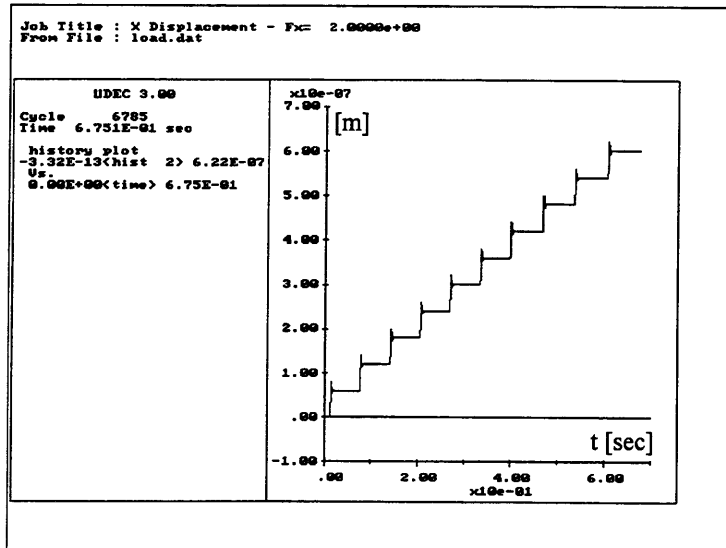


Figure 7-19. Time history of horizontal displacement of top right corner after application of forces: $F_x = 2.0$ N, $F_y = -10$ N. It can be observed the response to the first 10 load steps $\Delta F_x = 0.20$ N. The total displacement is negligible (of the order of 10^{-7} m), and it is due only to elastic deformations of the joint.

$$F_x = 2.2 \text{ N} \quad F_y = -10 \text{ N}$$

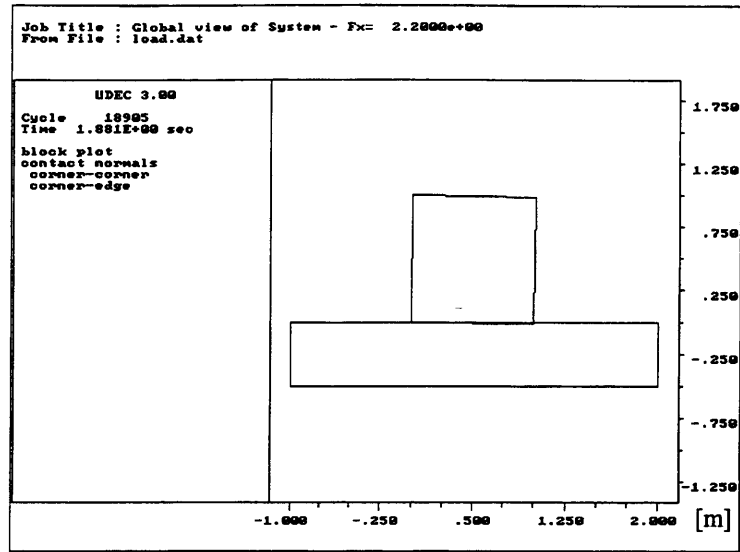


Figure 7-20. Global view of the system after application of forces $F_x = 2.2 \text{ N}$, $F_y = -10 \text{ N}$. A first microrotation can be observed.

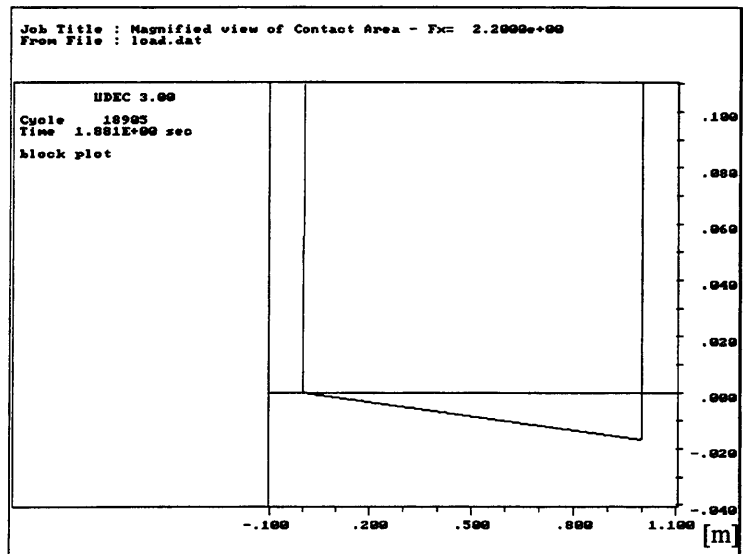


Figure 7-21. Magnified view of contact area after application of forces $F_x = 2.2 \text{ N}$, $F_y = -10 \text{ N}$. A first microrotation has taken place.

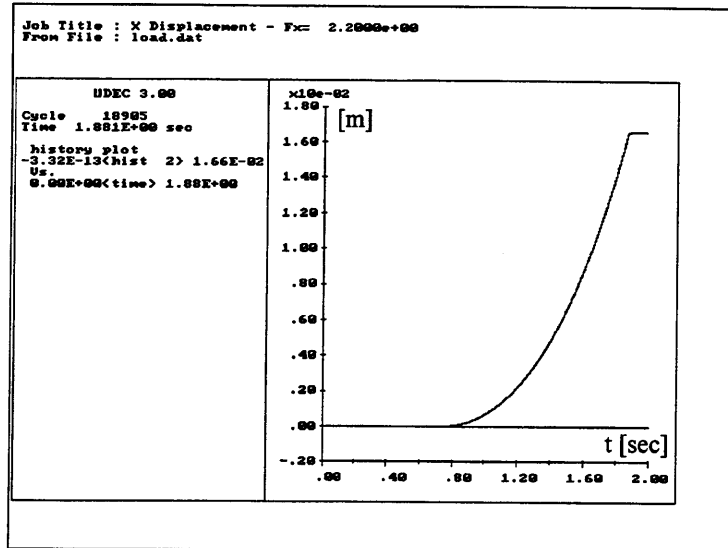


Figure 7-22. Time history of horizontal displacement of top right corner after application of forces $F_x = 2.2 \text{ N}$, $F_y = -10 \text{ N}$. A local instability has taken place, and then a new stable configuration is achieved.

$$F_x = 5.8 \text{ N} \quad F_y = -10 \text{ N}$$

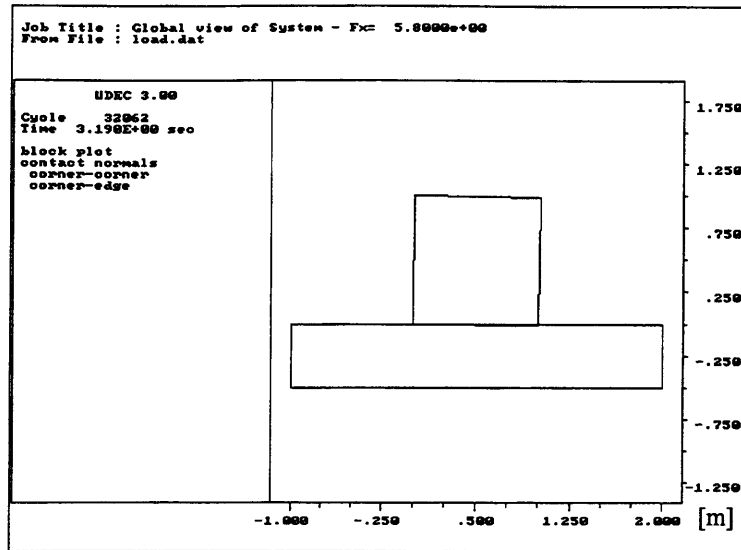


Figure 7-23. Global view of the system after application of forces $F_x = 5.8 \text{ N}$, $F_y = -10 \text{ N}$. No additional microrotation has taken place.

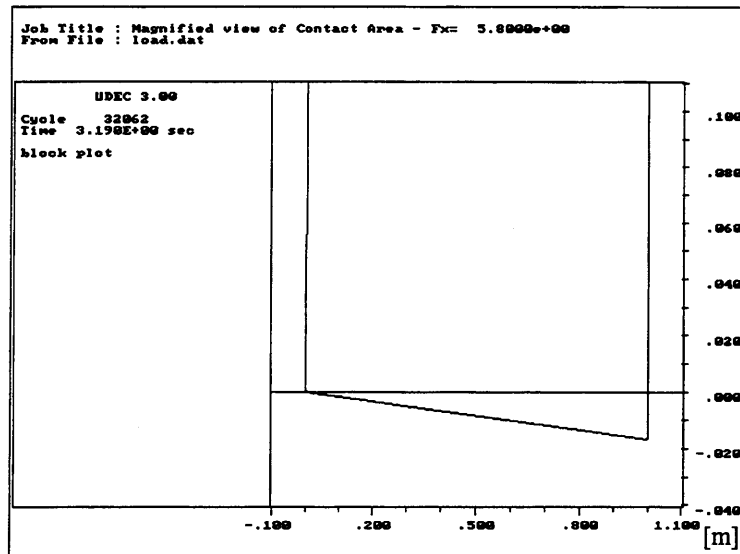


Figure 7-24. Magnified view of contact area after application of forces $F_x = 5.8 \text{ N}$, $F_y = -10 \text{ N}$. No additional rigid body microrotation has taken place.

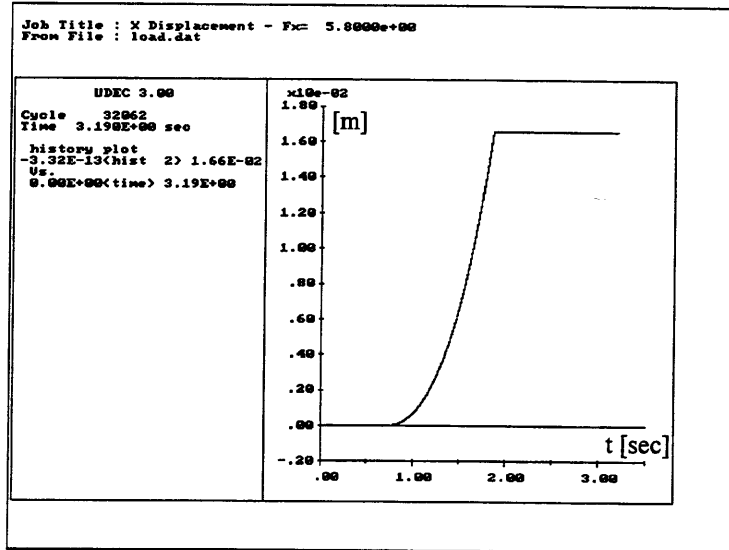


Figure 7-25. Time history of horizontal displacement of top right corner after application of forces $F_x = 5.8 \text{ N}$, $F_y = -10 \text{ N}$. The system remains in a stable configuration.

$$F_x = 6.0 \text{ N} \quad F_y = -10 \text{ N}$$

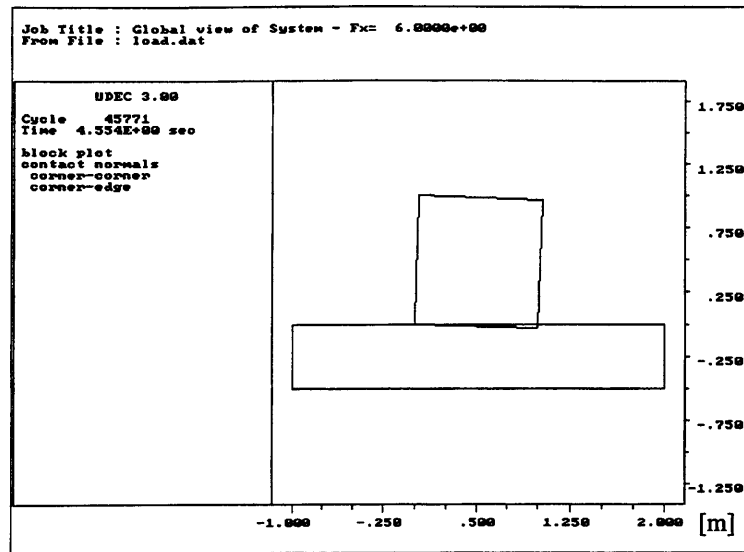


Figure 7-26. Global view of the system after application of forces $F_x = 6.0 \text{ N}$, $F_y = -10 \text{ N}$. A second microrotation can be seen.

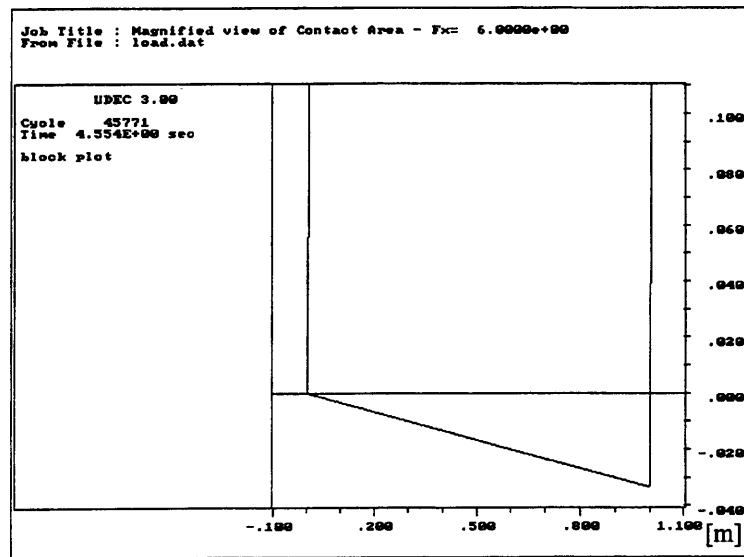


Figure 7-27. Magnified view of contact area after application of forces $F_x = 6.0 \text{ N}$, $F_y = -10 \text{ N}$. A second microrotation has taken place.

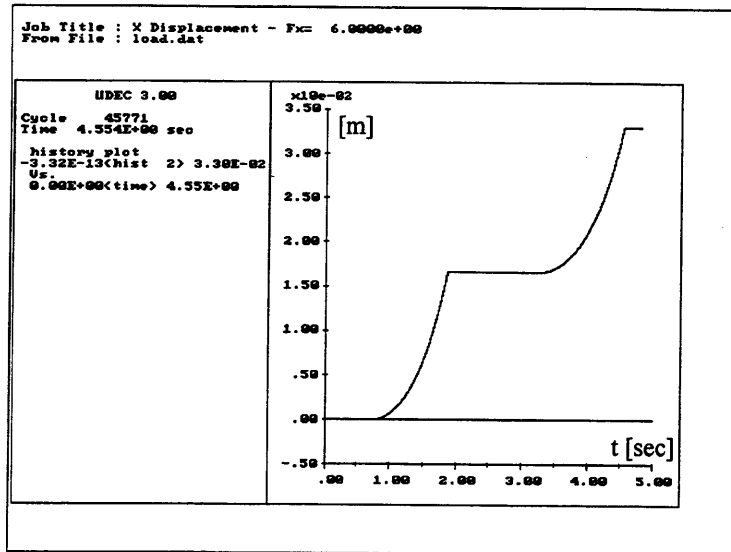


Figure 7-28. Time history of horizontal displacement of top right corner after application of forces $F_x = 6.0$ N, $F_y = -10$ N.

$$F_x = 9.65 \text{ N} \quad F_y = -10 \text{ N}$$

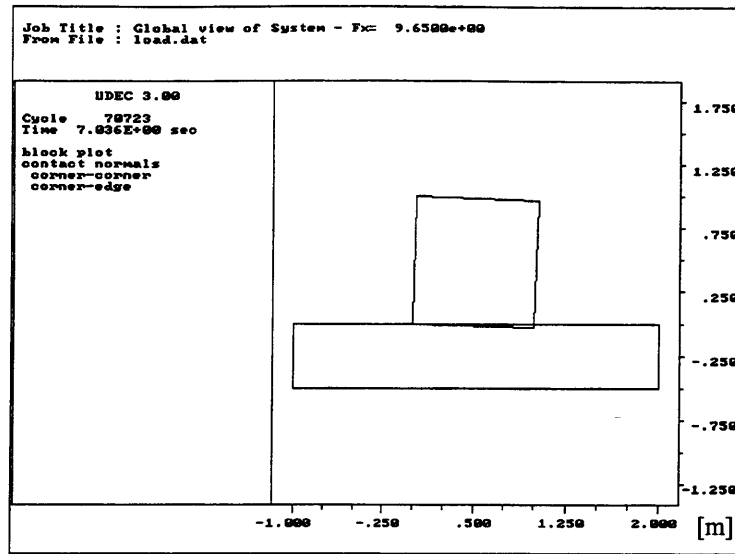


Figure 7-29. Global view of the system after application of forces $F_x = 9.65 \text{ N}$, $F_y = -10 \text{ N}$. No additional rigid body microrotation has taken place.

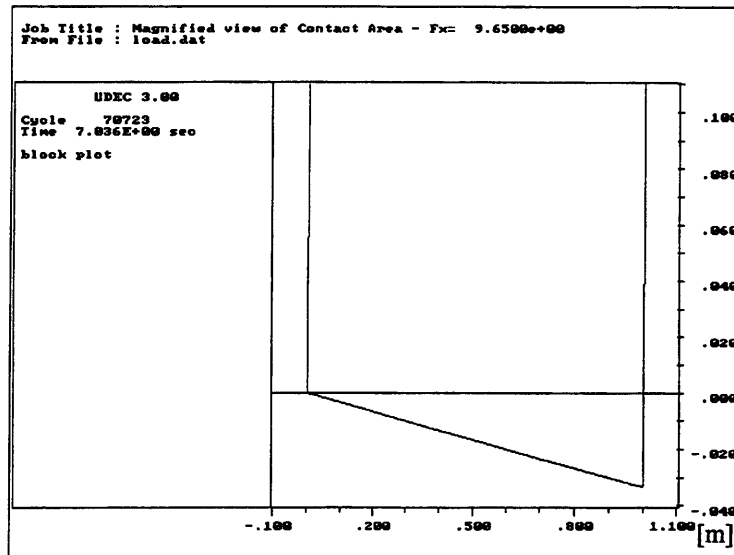


Figure 7-30. Magnified view of contact area after application of forces $F_x = 9.65 \text{ N}$, $F_y = -10 \text{ N}$. No additional rigid body microrotation has taken place.

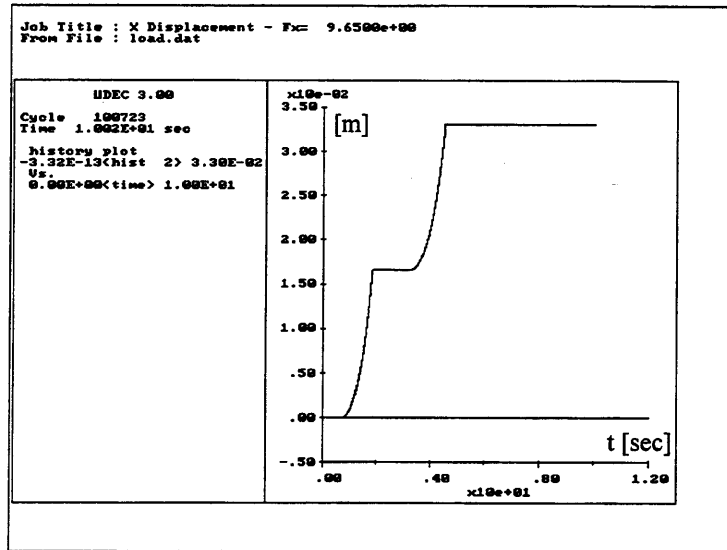


Figure 7-31. Time history of horizontal displacement of top right corner after application of forces $F_x = 9.65 \text{ N}$, $F_y = -10 \text{ N}$. The system is in a stable configuration.

$$F_x = 9.66 \text{ N} \quad F_y = -10 \text{ N}$$

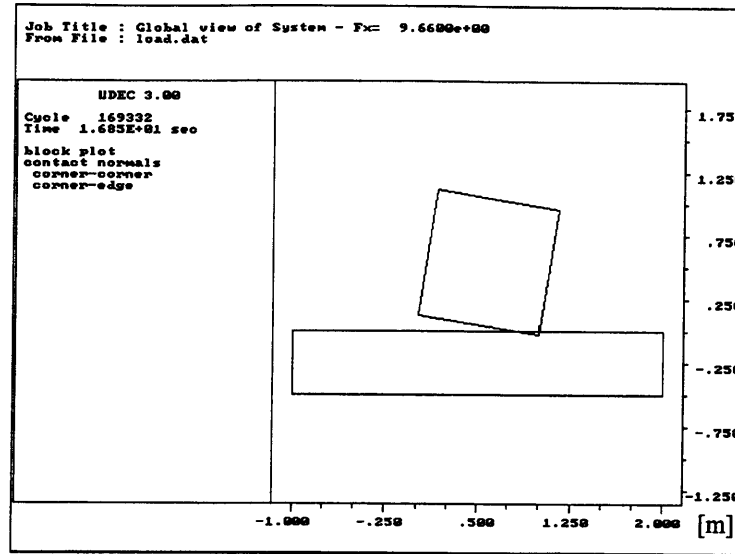


Figure 7-32. Global view of the system after application of forces $F_x = 9.66 \text{ N}$, $F_y = -10 \text{ N}$. Global failure by overturning is taking place. Note the reduction (from $\lambda = 1.0$ to $\lambda = 0.966$) of failure load due to non coplanar joint.

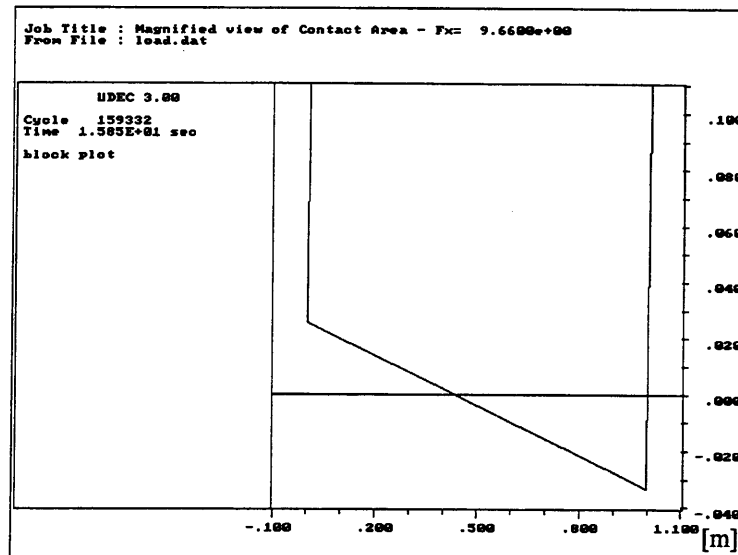


Figure 7-33. Magnified view of contact area after application of forces $F_x = 9.66 \text{ N}$, $F_y = -10 \text{ N}$. Global failure by overturning is taking place.

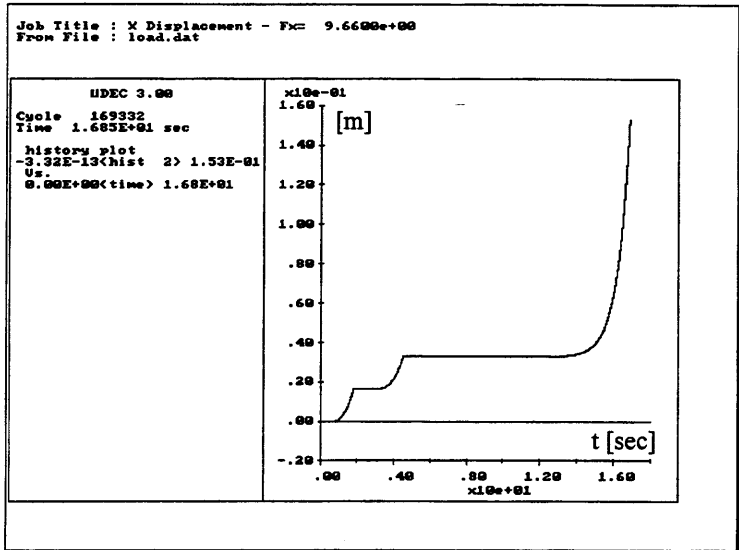


Figure 7-34. Time history of horizontal displacement of top right corner after application of forces $F_x = 9.66 \text{ N}$, $F_y = -10 \text{ N}$. Displacement keeps increasing and no further stable configuration is possible.

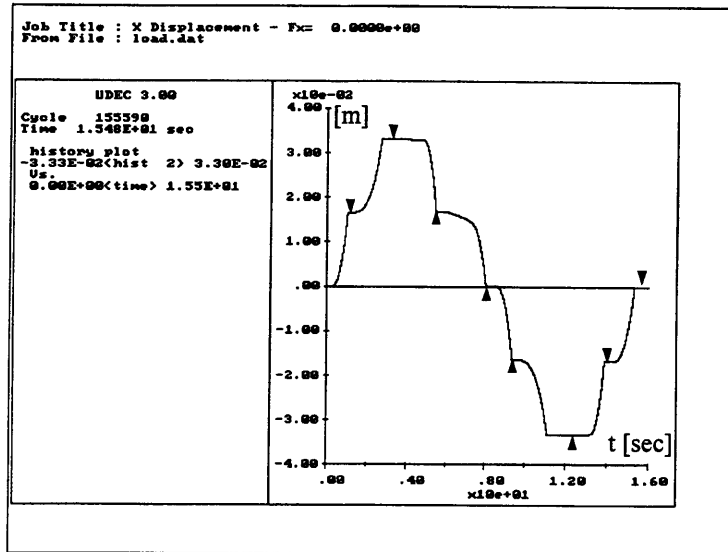
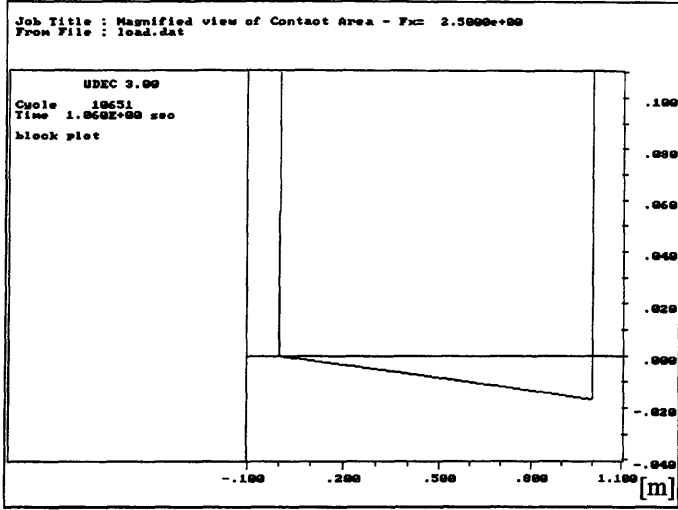
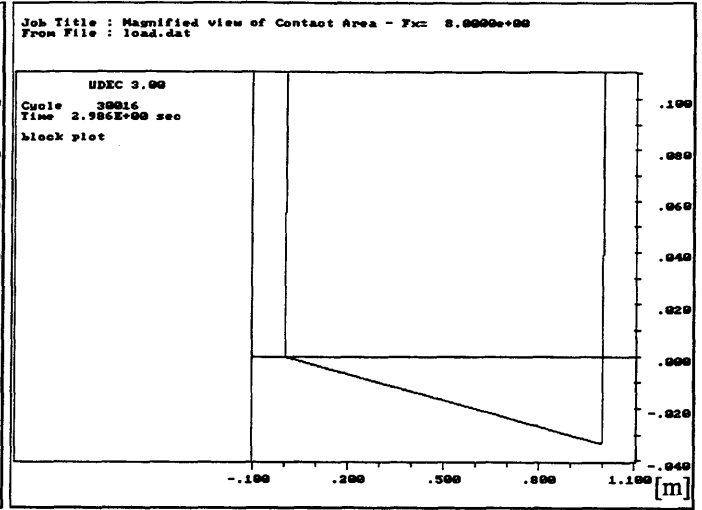


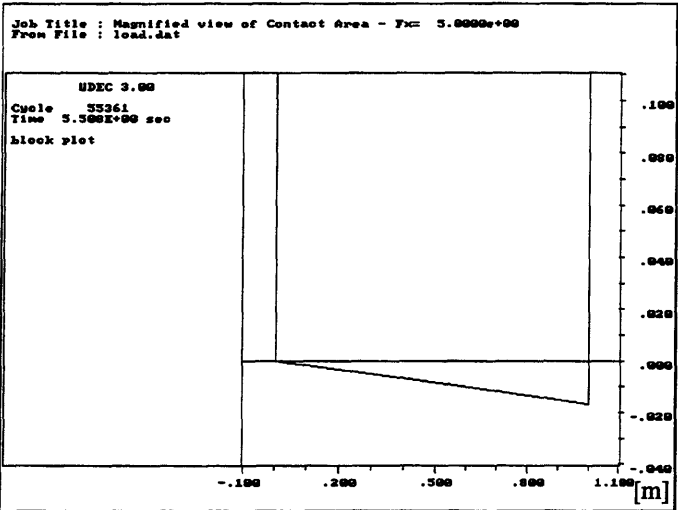
Figure 7-35. Cyclic loading: time history of horizontal displacement of top right corner during quasistatic application of a complete cycle of lateral force between the following values: $F_x = 0 \text{ N}$; $+8 \text{ N}$; 0 N ; -8 N ; 0 N . Note 8 phases of instability, each one followed by a stable configuration, corresponding to 2 clockwise, 4 counterclockwise, and finally 2 clockwise microrotations. The 8 different stable configurations (corresponding to the points indicated by triangles) are shown in following two figures.



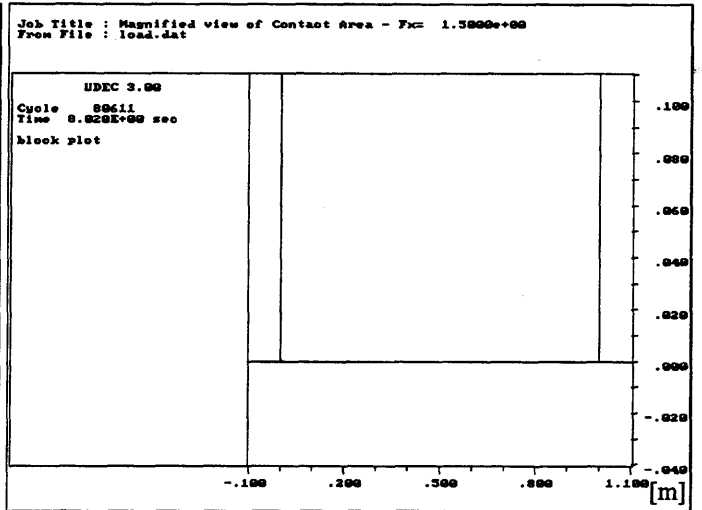
(a)



(b)

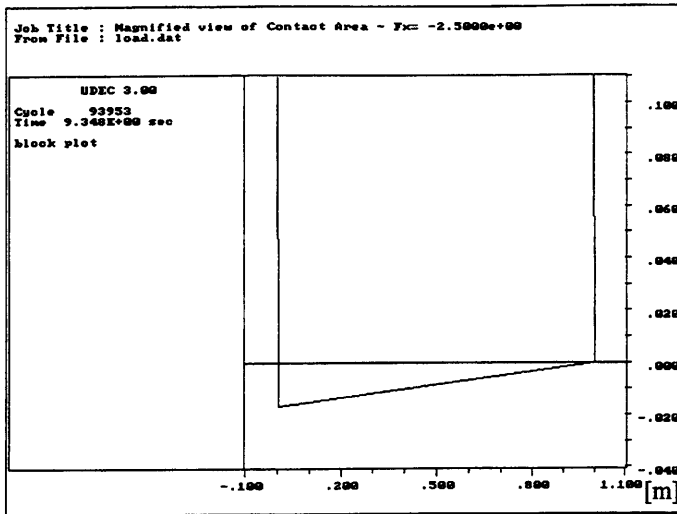


(c)

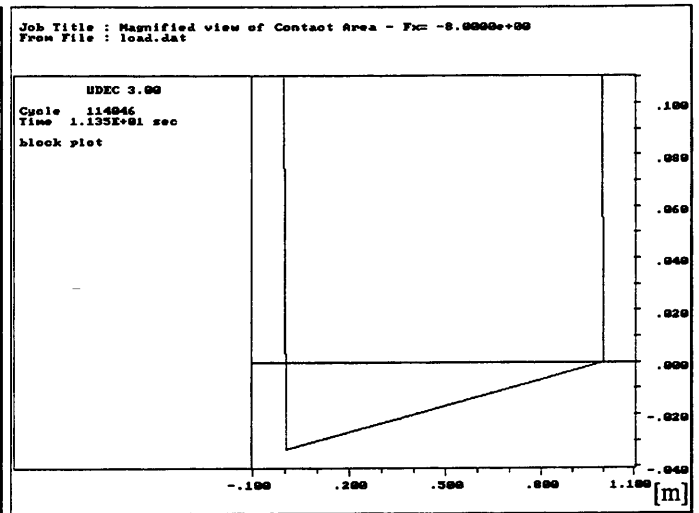


(d)

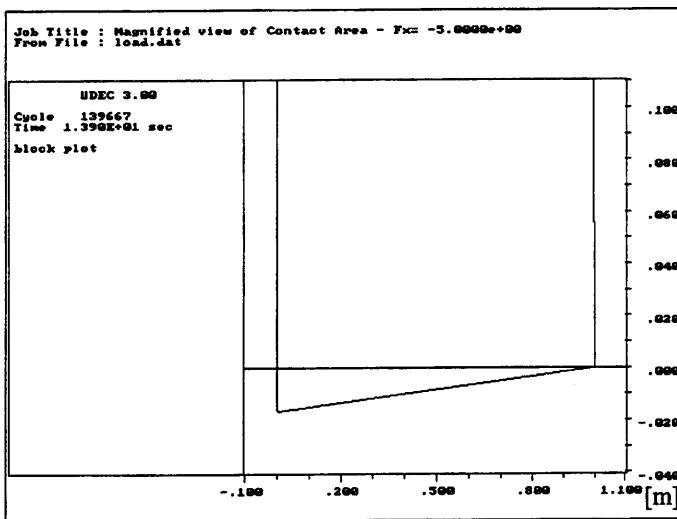
Figure 7-36. Cyclic loading: magnified view of contact area. Stable configurations at $F_x = 2.5 \text{ N}$; 8.0 N ; 5.0 N ; 1.5 N .



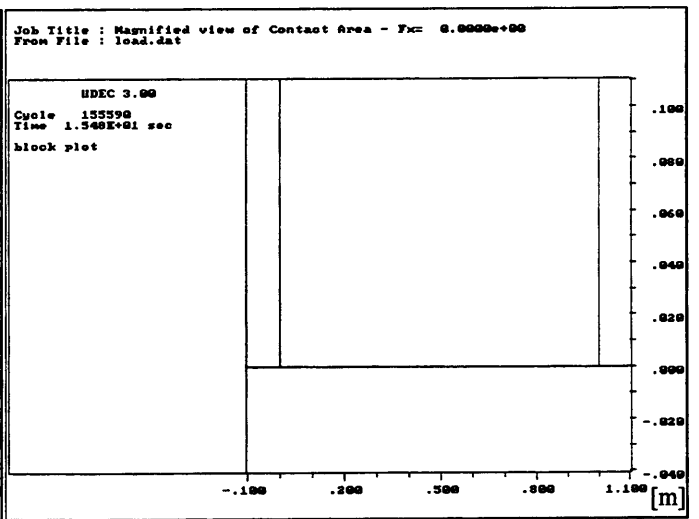
(a)



(b)



(c)



(d)

Figure 7-37. Cyclic loading: magnified view of contact area. Stable configurations at $F_x = -2.5 \text{ N}$; -8.0 N ; -5.0 N ; 0.0 N .

7.4 SENSITIVITY ANALYSIS AND CALIBRATION

The development of the non coplanar joint model had been stimulated by certain observed discrepancies between the results of a series of experimental tests and the numerical predictions of DE analyses using the current planar joint model. It is now necessary to perform the same DE analyses with the new joint model in order to evaluate the improvements in the numerical predictions, but first it is needed to select a joint reference surface which is representative of the irregularities of the blocks used in the experimental tests, in other words it is necessary to calibrate the joint model.

Since in the experimental tests (consisting in the in-plane loading of various small scale models of opus quadratum walls) only one type of block has been used¹, it has to be defined just one polygonal reference surface to be used in all analyses.

It is proposed to select the appropriate parameters of the joint reference surface on the base of the experimental results of the out-of-plane test of a 14-layer wall presented in section 7.2.1 (see Figures 7-1, and 7-2). In fact, in this test it was used the same type of blocks which had been employed in the in-plane experiments. It seems, also, appropriate to use the out-of-plane results for calibrating the joint model since in such case the effect of the non coplanarity is particularly pronounced.

After having studied the sensitivity of the out-of-plane response of the 14-layer wall with respect to the geometrical parameters of the joint, and having calibrated such parameters on the base of the experimental results, a study of the sensitivity of the out-of plane lateral failure load of the wall with respect to the number of layers is also performed.

¹ Peperino blocks with dimensions of 17.5 x 40 x 80 mm (cutting accuracy of approximately 0.1 mm), weight of 120 g, friction coefficient of 0.6.

7.4.1 Sensitivity with respect to joint geometry

In the following we illustrate a series of DE analyses which have been performed with the objective of determining the influence of the shape of the polygonal reference surface and of the size of the joint irregularity on the lateral failure load λ of a 14-layer wall subjected to out-of-plane loading. As shown in Figure 7-1b, such behavior may be studied with a 2D model constituted by a column of 14 blocks².

The system was subjected to gravity and quasistatic increasing lateral load up to failure. The detailed features of the response, including plots of the system configuration at various levels of lateral load, and the time histories of the applied lateral forces, and of the resulting lateral displacement will be given in section 7.5 dedicated to the presentation of the applications of the new joint model. Here only the features regarding the sensitivity study will be discussed.

It is recalled that the parameters required for the definition of the reference surface are:

- n : number of sides;
- l_i : length of each side ($i = 1, n$);
- d : maximum joint aperture.

Based on the previous data the program computes the value of the radius of the circumference in which the polygon is inscribed, and subsequently the angles of rotation φ_i required to move from each base (i) to the subsequent one (i+1), as illustrated in section 7.3.1.

² This is the reason why in the following we will refer indifferently to a 14-layer wall (loaded outside its plane) or a 14-block column.

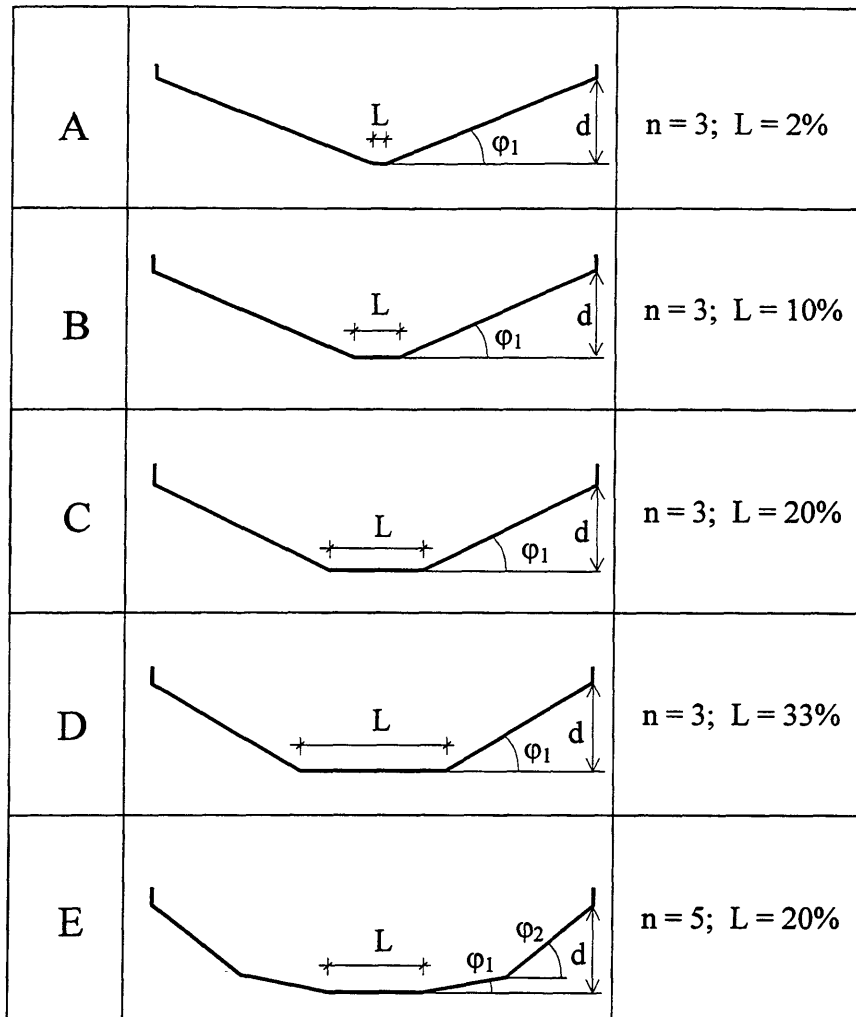


Figure 7-38. Shapes of reference polygon used for parametric analysis: n is the number of sides; L is the length of the central base as a percentage of the joint length; d is the maximum joint aperture.

The shape of the contact surface profile is defined by the values of n and l_i , while d may be viewed as the size (or intensity) of the joint irregularity. In the following, 5 shapes, illustrated in Figure 7-38, have been considered.

The number of sides which have been examined were: $n=3$ and $n=5$, the length of the central side has been varied from $L=2\%$ to $L=33\%$ of the contact length, and the joint opening ranged from $d=0.34\%$ to $d=0.69\%$ of the block height. The results of the 20

analyses (5 shapes, and 4 values of joint aperture), in terms of failure load λ , and lateral displacement of the top of the column before failure, δ_{top} , are summarized in Table 7-2. Note that the failure loads λ are normalized with respect to the failure load λ_{pl} obtained with the planar joint model (that is neglecting the imperfections of the joint)³. It is recalled that the normalized experimental failure load is $\lambda_{exp} = 0.81$, while the experimental top displacement is $\delta_{top-exp} = 11.5$ mm.

SHAPE	CASE	Max joint aperture d (%)	Failure load λ	Top lateral displacement δ_{top} (mm)
A	N=3 L=2%	0,34	0,91	4.9
		0,46	0,88	6.6
		0,57	0,84	8.1
		0,69	0,80	10.2
B	N=3 L=10%	0,34	0,89	6.2
		0,46	0,85	8.0
		0,57	0,81	9.7
		0,69	0,79	11.4
C	N=3 L=20%	0,34	0,88	7.0
		0,46	0,84	8.9
		0,57	0,80	10.5
		0,69	0,77	12.6
D	N=3 L=33%	0,34	0,84	8.3
		0,46	0,79	11.0
		0,57	0,75	13.2
		0,69	0,70	15.5
E	N=5 L=20%	0,34	0,86	7.3
		0,46	0,79	11.0
		0,57	0,72	14.6
		0,69	0,67	17.1

Table 7-2. Failure loads λ and top lateral displacements δ_{top} before failure in 20 out-of-plane DE analyses with non coplanar joint model of a 14-layer wall. Analyses were performed with 5 shapes of reference polygon and 4 values of maximum joint aperture d for each shape (d is given as a percentage of block height). In bold is indicated the case which better approximates the experimental response: $\lambda_{exp} = 0.81$; $\delta_{top-exp} = 11.5$ mm.

³ $\lambda_{pl} = b/H = 0.163$, as obtained also with DE analysis in section 7.5.1 where $0.162 < \lambda_{pl} < 0.164$.

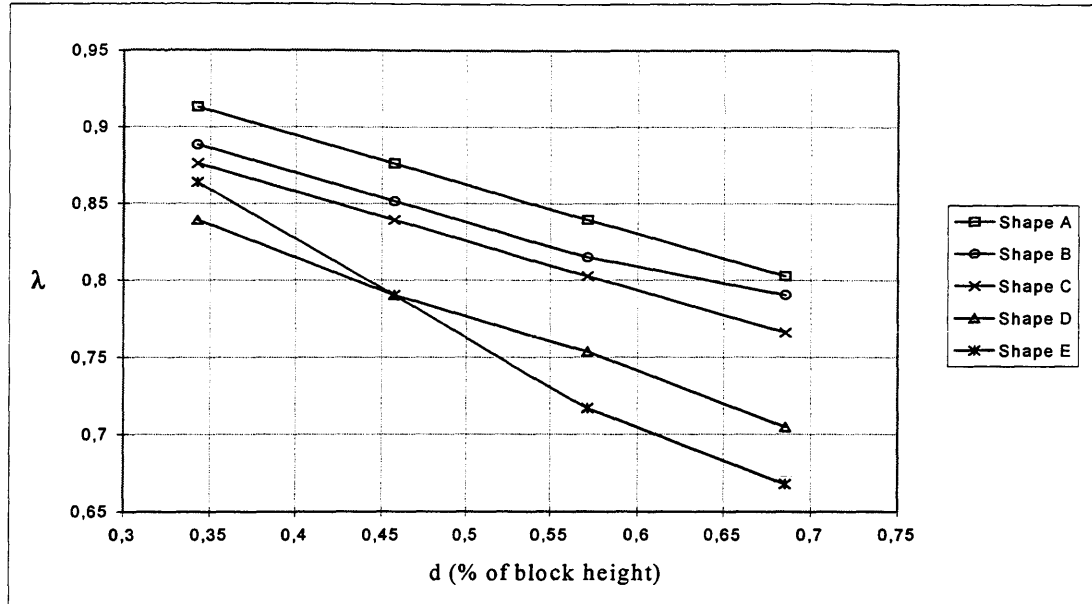


Figure 7-39. Failure loads λ versus maximum joint aperture d obtained in 20 out-of-plane DE analyses with non coplanar joint model of a 14-layer wall. Each line indicates the type of shape used in the analyses for the reference polygon. λ is normalized with respect to the failure load obtained with the planar joint model. Normalized experimental failure load is: $\lambda_{\text{exp}} = 0.81$.

It is noted, in the first place, that the failure load predicted by the non coplanar joint model is always lower than the one obtained without accounting for contact imperfections, and this tendency agrees with the experimental results.

Second, in the numerical predictions, a lateral top displacement is always observed before failure⁴ as expected from the lab experiments ($\delta_{\text{top-exp}} = 11.5$ mm), while with the planar joint model the system did not show any significant one.

The relationship between failure load λ , and joint aperture d is presented in Figure 7-39. Three observations can be made:

- λ decreases with increasing joint opening d

⁴ In both experimental and numerical tests the wall failed by rigid body overturning of the entire wall.

- λ decreases with increasing L , which corresponds to steeper angles of the lateral sides of the polygonal reference surface
- λ does not have a monotonic tendency with respect to n (number of sides). In fact if we consider the last two cases (D and E), where $n=3$, and $n=5$ respectively, and in which for both cases the polygon had sides of equal length ($L=20\%$), we can observe that:
 - for $d > 0.46$ λ decreases with n ,
 - for $d < 0.46$ λ increases with n , and
 - for $d = 0.46$ λ does not change with n .

This behavior is explained by the fact that, for case E, with small joint openings failure is obtained with several blocks resting on the second base, while with higher values of d the first rotation of the lower block causes the higher blocks to move directly to the third base and therefore causing large lateral displacements and lower global stability.

With regard to the sensitivity of the failure load λ with respect to the selected geometrical parameters (d, n, L) we can observe the following:

1. a high sensitivity with respect to variations of the joint opening d since a $\Delta d = 0.35\%$ of the block height (0.06 mm) causes a $\Delta\lambda = 10$ to 20%
2. a low sensitivity with respect to the number of sides n since going from $n=3$ to $n=5$, the variation of failure load $\Delta\lambda$ is from 0 to 5%
3. a moderate sensitivity with respect to the length L since a variation of L from 2 to 20% determines a variation of failure load $\Delta\lambda = 5\%$

In addition, Figure 7-40 shows an essentially linear relationship between maximum top lateral displacements δ_{top} and failure loads λ for all of the 20 cases previously described regardless the type of shape of the reference polygon. It is also noted that there are cases in which 2 (or more) different couples of shape type and maximum joint aperture d yield the same value of the failure load λ . This is the case, for

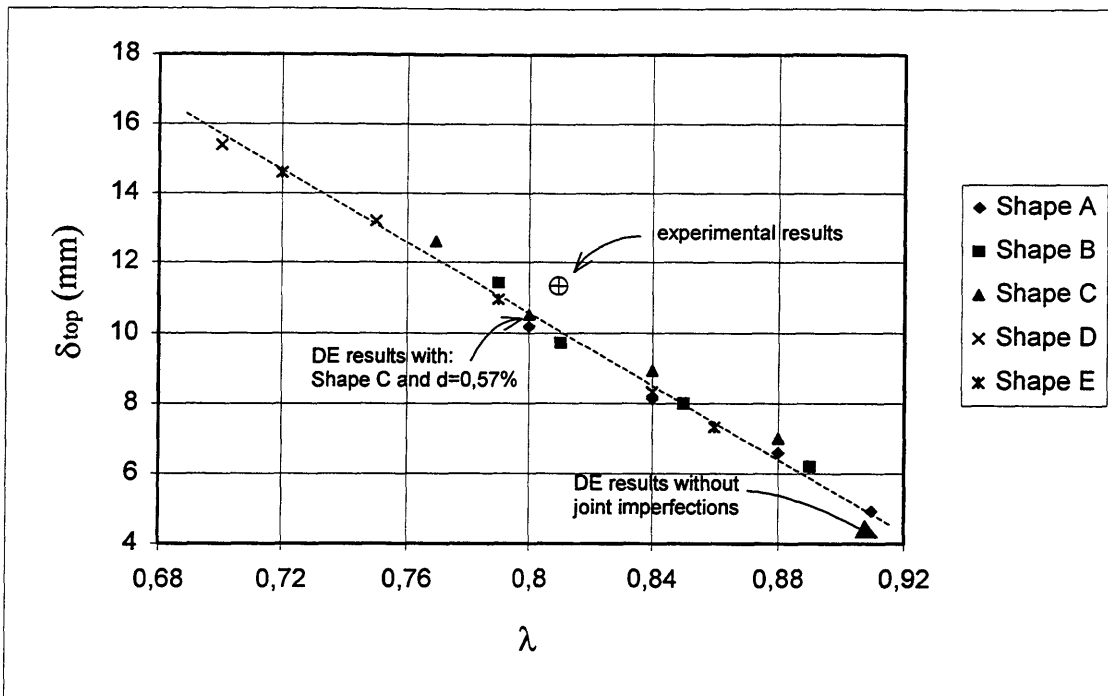


Figure 7-40. Relationship between maximum top lateral displacements δ_{top} and failure loads λ in 20 out-of-plane DE analyses with non coplanar joint model of a 14-layer wall. Analyses were performed with 5 shapes of reference polygon and 4 values of max joint aperture for each shape (0.34%, 0.46%, 0.57%, 0.69% of block height).

example, of shape A with $d=0.69\%$ and shape C with $d=0.57\%$, which both give a failure load $\lambda = 0.80$. The corresponding values of the top lateral displacement for such cases are very similar: $\delta_{top} = 10.2$ mm and 10.5 mm. It is also recalled that the maximum lateral displacement δ_g of the centroid of the wall before failure, which is a function of λ (see equation 7-4), must be identical for the two cases. If both δ_g and δ_{top} are very close for the two cases it appears that, not only the failure load, but also the deformed failure configuration of both walls were essentially the same even if two different type of shapes were assumed for the reference polygon. Therefore, in this series of tests, we are observing a low sensitivity of the system response with respect to the shape of the reference polygon of the non coplanar joint model.

Finally, the calibration of the joint model has been performed by minimizing the distance in the λ - δ_{top} plane, between experimental and numerical results. As shown in Figure 7-40, the point which minimize such distance is the one associated to shape C ($n=3$; $L=20\%$) and $d = 0.57\%$. These values have been used in all of the following analyses.

Case	Failure load λ	Top lateral displacement before failure δ_{top} (mm)
Experimental values	0.81	11.5
Non coplanar model (with calibrated parameters)	0.80	10.5
Planar joint model (no imperfections)	1.00	0.0

Table 7-3. Summary of experimental and numerical results in out-of-plane test of a 14-layer wall.

In conclusion, from the data summarized in Table 7-3 we can observe: (a) the good agreement between the results predicted by the non coplanar model with the calibrated parameters, and the experimental results; and (b) the substantial improvement of such results with respect to those obtained with the planar joint model. Obviously these results have to be confirmed on cases which were not used to calibrate the model as it will be shown in section 7.5.

7.4.2 Sensitivity with respect to number of blocks

In the previous section we studied the effect of varying the geometrical parameters of the joint on the out-of-plane response of a wall with a fixed number of joints along its height. It is also of interest to evaluate the effect of the number of joints assuming fixed parameters for the geometrical irregularities⁵. Two series of analyses have been performed: the first with constant block height h , while the second with constant wall height H .

In the first series of quasistatic DE analyses the slenderness $r = h/b$ of the block has been assumed equal to the one of the blocks used for the experimental tests: $r=0.44$ (corresponding to $b=40\text{mm}$ and $h=17.5\text{mm}$). Four cases have been considered with $n= 1, 5, 10, 20$. For each case the percentage reduction ζ of the lateral failure load obtained with the non coplanar joint model with respect to the one obtained with the planar joint model is provided in Table 7-4.

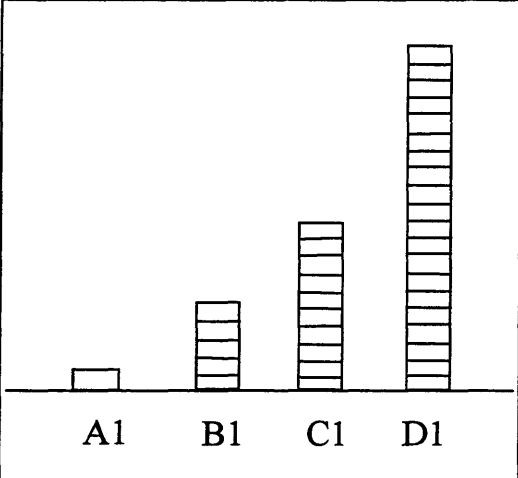
	CASE	n. of blocks	% reduction of failure load ζ
	A1	1	0.91
	B1	5	3.09
	C1	10	10.31
	D1	20	39.62

Table 7-4. Percentage reduction ζ (due to joint irregularity) of out-of-plane failure load in walls with blocks with constant height and increasing number of joints (from 1 to 20).

⁵ Such parameters have been assigned to the calibrated values obtained in the previous section.

ζ is defined as:

$$\zeta = \frac{\lambda_{pl} - \lambda_{nc}}{\lambda_{pl}} \quad (7-16)$$

where λ_{pl} is the failure load obtained with the planar DE model,
and λ_{nc} is the failure load obtained with the new non coplanar model.

It can be observed that for this value of slenderness ratio ($r=0.44$) the effect of joint imperfections is negligible for 1 to 5 blocks ($\zeta < 5\%$), noticeable for about 10 blocks ($\zeta = 10\%$) and significant for $n=20$ ($\zeta = 39\%$).

In the previous series of tests, it is noted that ζ is a function of both n and H (the total height of the column). Since such quantities were increasing simultaneously, their effects could not be separated. In order to distinguish them a second series of tests with walls with constant height $H=20h$, and base $b=40\text{mm}$ (as in the previous series) was performed. Three new cases with $n=1, 5$, and 10 were studied. The results in terms of percentage reduction of failure load ζ are shown in Table 7-5.

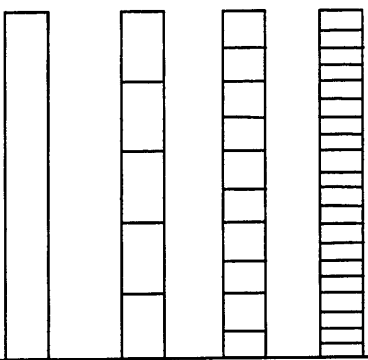
				CASE	n. of blocks	% reduction of failure load ζ
A2	B2	C2	D2	A2	1	6.37
				B2	5	13.37
				C2	10	22.12
				D2=D1	20	39.62

Table 7-5. Percentage reduction ζ (due to joint irregularity) of out-of-plane failure load in walls with constant height and increasing number n of joints (n varies from 1 to 20).

In Figure 7-41, showing ζ as a function of the number of blocks n for both series of tests, it can be observed that ζ has a linear dependency with n for the case of constant column height ($H=\text{const}$), while in the case of constant block height ($h=\text{const}$), the simultaneous increase of number of blocks and column height determines, as expected, a higher order dependency of ζ with n .

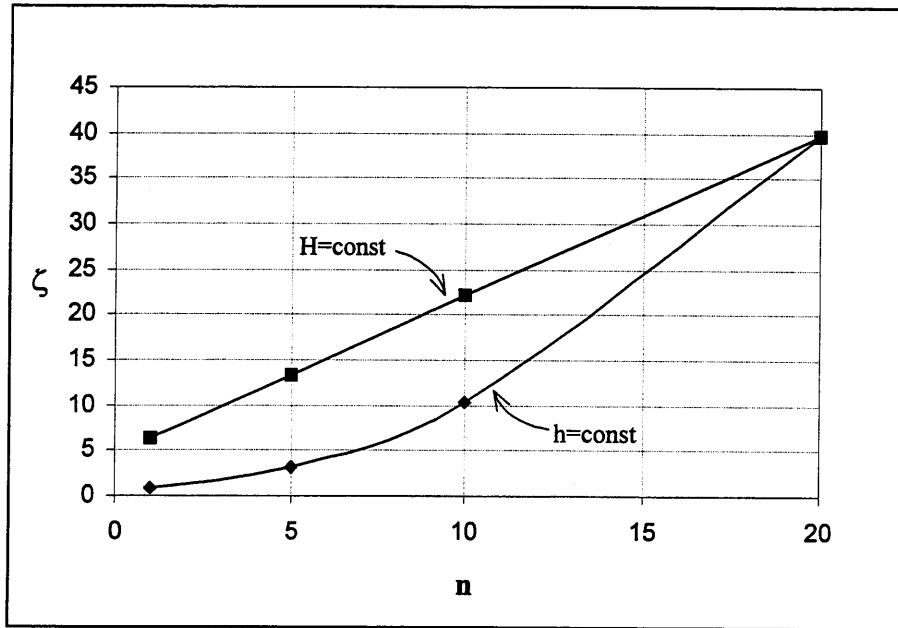


Figure 7-41. Percentage reduction ζ (due to joint irregularity) of out-of-plane failure load as a function of the number of joints n . Case of blocks with constant height ($h=\text{const}$), and case of walls with constant height ($H=\text{const}$). Curves are obtained by interpolation of DE results.

7.4.2.1 Instability of a block column due to contact non coplanarity

In the previous series of tests we observed a remarkable reduction of the lateral failure load, due to imperfections, as the number of blocks increased up to $n = 20$. It is of interest to investigate what happens when the number of layers increases further. For such problem we can attempt to obtain an explicit expression of ζ as a function of n and of the geometry of the wall.

If we make the simplifying assumption that the irregular contact can be modeled with a polygon with only 2 sides, as illustrated in Figure 7-42 when L tends to zero, it appears that a slight lateral force will cause the closure of all joints, and this configuration will remain unchanged until collapse.

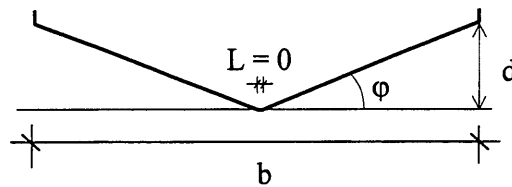


Figure 7-42. Joint profile assumed for the explicit expression of the failure load reduction ζ .

Knowing the configuration of the system at collapse we can compute the corresponding horizontal displacement of the wall centroid δ_g , and then with Eq. 7-4 the lateral failure load λ_{nc} :

$$\lambda_{nc} = \frac{1 - 2\delta_g}{b} \lambda_{pl} \quad (7-17)$$

Substituting the previous expression in the definition of ζ (Eq. 7-16) we obtain:

$$\zeta = \frac{2\delta_g}{b} \quad (7-18)$$

The horizontal displacement of the wall centroid δ_g can be computed from the horizontal displacements δ_i of the centroid of each block i according to:

$$\delta_g = \frac{1}{n} \sum_{i=1}^n \delta_i \quad (7-19)$$

with $i=1$ for the lower block and $i=n$ for the top one.

Assuming small rotations, the displacement δ_i is given by the sum of the displacements $\delta_{i,j}$ of the centroid of block i due to the rotations φ_j of each joint j located below block i :

$$\delta_i = \sum_{j=1}^i \delta_{i,j} \quad (7-20)$$

If $h_{i,j}$ is the distance between joint j and the centroid of block i , we have:

$$\delta_{i,j} = h_{i,j} \varphi_j \quad (7-21)$$

where

$$h_{i,j} = \left(i - j + \frac{1}{2} \right) h \quad (7-22)$$

h being the height of a block.

Substituting back from 7-22 to 7-18 we obtain the expression of the reduction of failure load ζ due to the non coplanarity of the joints:

$$\zeta = \frac{2}{nb} \sum_{i=1}^n \left[\sum_{j=1}^i \left(i - j + \frac{1}{2} \right) h \varphi_j \right] \quad (7-23)$$

which, assuming equal rotations $\varphi_j = \varphi$, and introducing the block aspect ratio $r = h / b$, yields the following expression:

$$\zeta_r = r \varphi \left(\frac{n^2}{3} + \frac{n}{2} + \frac{1}{6} \right) \quad (7-24)$$

We can also obtain ζ as a function of the wall aspect ratio $R = H/b$, where H is the height of the wall, by substituting $r = R/n$ in 7-24:

$$\zeta_R = R\varphi\left(\frac{n}{3} + \frac{1}{2} + \frac{1}{6n}\right) \quad (7-25)$$

The previous expressions have been obtained for the case of a joint profile as in Figure 7-42, however for the case of $L = 0.2 b$, which corresponds to the shape adopted for the DE analyses previously described in this section, they constitute a good approximation. In fact, by replacing in 7-24 and 7-25 the values of r , R , and φ used in the DE analyses we obtain values of ζ very close to those obtained with the DEM, as shown in Figure 7-43, where triangles and circles represent DE results for the two series of tests, and the curves represent the previous expressions.

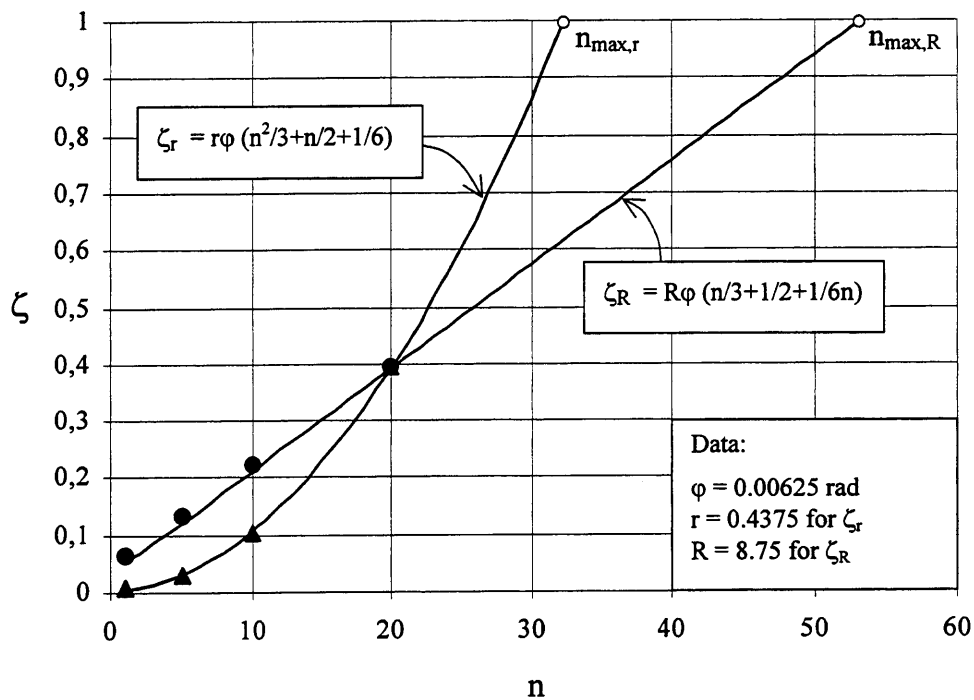


Figure 7-43. Plots of approximate expressions of failure load reduction as a function of number of joints n : ζ_r for the case of constant block aspect ratio r , and ζ_R for the case of constant wall aspect ratio R . Markers indicate results of DE analyses illustrated in the previous section for $n=1, 5, 10, 20$ blocks.

From the previous expressions we can observe that the failure load reduction ζ increases with the number of blocks n , and for a given value of $n = n_{\max}$, ζ assumes a unit value: $\zeta(n_{\max}) = 1$, and the corresponding failure load is reduced to zero⁶. This means that given a specific type of blocks characterized by a certain aspect ratio r and joint imperfection φ , there is a limit to the height of a column which can be built using such blocks. We can say that when this limit is reached the column becomes unstable even in absence of lateral force since any slight vibration or construction imperfection causes the column to collapse.

Assigning $\zeta_r(n) = 1$, in Eq. 7-24, and solving for n we obtain:

$$n_{\max,r} = -\frac{1}{3} + \sqrt{\frac{1}{16} + \frac{3}{r\varphi}} \quad (7-26)$$

analogously, Eq. 7-25 yields:

$$n_{\max,R} = \frac{3}{2R\varphi} - \frac{3}{4} + \sqrt{\frac{1}{16} + \left(\frac{3}{2R\varphi}\right)^2} (1 - R\varphi) \quad (7-27)$$

The maximum number of blocks n_{\max} for which the column is stable in absence of lateral load, as obtained from the previous expressions, is plotted (in logarithmic scale) as a function of $(r \cdot \varphi)$ in Figure 7-44, and as a function of $(R \cdot \varphi)$ in Figure 7-45. Note that in such functions n_{\max} decreases very rapidly with increasing joint rotation φ . As an example the values of n_{\max} for the two series of DE tests have been indicated on the plots. Note that, as shown in Figure 7-44, for the case of the blocks used in the experiments, ($h=17.5$ mm; $b=40$ mm; $\varphi=6.25 \cdot 10^{-3}$ rad), despite an apparently insignificant joint imperfection (joint aperture $d = 0.1$ mm), it appears to be impossible to build a stable column with more than just 32 blocks.

This is an additional confirmation that microrotations at the joints due to non coplanarity of the contacts play an important role in the stability of block structures and cannot be neglected.

⁶ This is the case when point C tends to B in Figure 7-2.

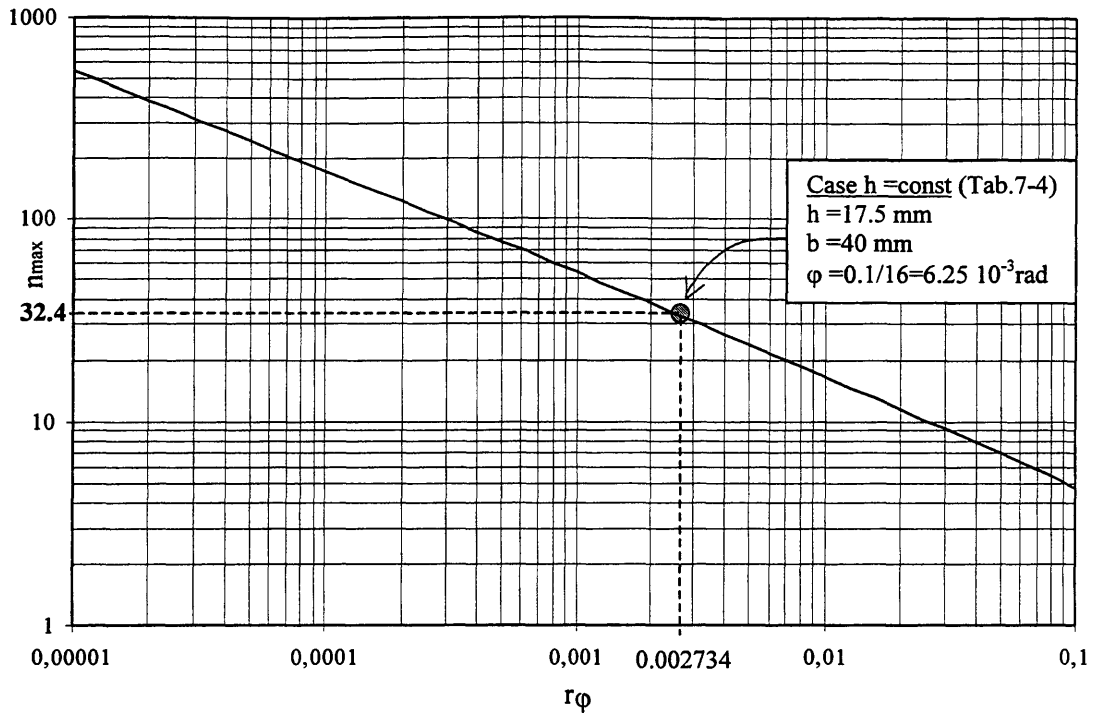


Figure 7-44. Maximum number, n_{max} , of blocks for a stable column with non coplanar contacts and in absence of lateral forces. n_{max} is given as a function of the product of the block aspect ratio $r=h/b$, and the joint rotation ϕ .

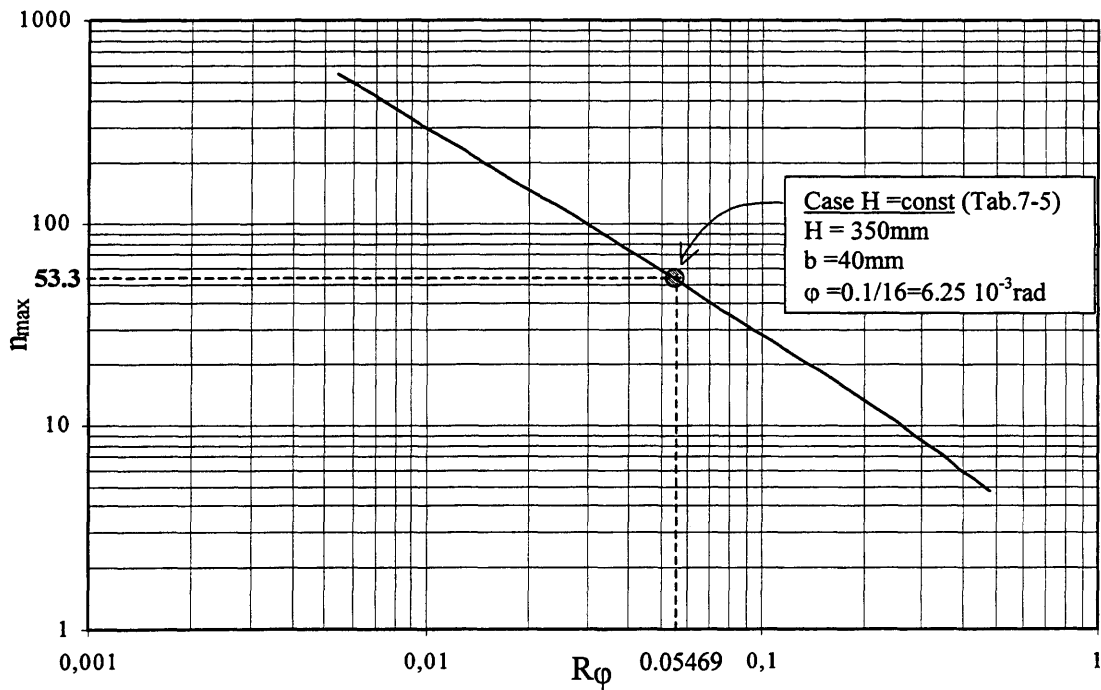


Figure 7-45. Maximum number, n_{max} , of blocks for a stable column with non coplanar contacts and in absence of lateral forces. n_{max} is given as a function of the product of the column aspect ratio $R=H/b$, and the joint rotation ϕ .

7.5 APPLICATIONS

At the beginning of this chapter, based on the work previously presented, it was recognized that the Discrete Element Method is an innovative and promising approach to the study of the seismic response of structures constituted by assemblages of blocks interacting only through frictional contacts. It was noted however that certain discrepancies existed between the experimental findings and the DE results (obtained with the existing joint model) relating to the behavior of walls subjected to in-plane quasistatic loading (see section 7.1). In the attempt to improve such predictions a new joint model, accounting for the non coplanarity of the contact surfaces, has been proposed, as illustrated in the previous sections (7.2, 7.3 and 7.4). It is now important to evaluate the performances of such model in those cases in which the mentioned discrepancies had been observed. This is the purpose of the DE analyses of the 3 opus quadratum walls (with respectively 21, 110, and 231 blocks) which will be presented in sections 7.5.2, 7.5.3, and 7.5.4.

Another objective of this section is that of using the 14-block case, briefly presented in a previous section devoted to the model calibration, as an example to illustrate the details of the DE response of a block structure, and in particular to compare and contrast the differences in the system behavior obtained with and without the adoption of the non coplanar joint model.

It is recalled that in all these applications, due to the relatively low stress level and high material stiffness, the deformations are negligible. This allowed to model the interior of the blocks as rigid bodies, and the deformability of the joints with arbitrarily high values of the contact elastic stiffnesses K_{nc} and K_{tc} . Their values have been assigned by satisfying the need to obtain negligible elastic joint deformations, and, at the same time, to avoid computational inefficiencies.

In Table 7-6 the calibrated parameters for the new joint model, as obtained from the sensitivity study on the 14-block case, and the block data used in the applications presented in the following of this chapter are summarized.

<u>Block data:</u>	
Base:	$b = 40 \text{ mm},$
Height:	$h = 17.5 \text{ mm},$
Mass density:	$M = 1 \text{ kg / mm}^2$
Contact elastic interaction stiffness:	$K_{ne} = K_{te} = 10^6 \div 10^8 \text{ N/m}$
Friction coefficient:	$f = 0.6$
<u>Calibrated reference polygon parameters:</u>	
Number of sides:	$n = 3$
Lengths of each side:	$l_1 = 16 \text{ mm}; l_2 = 8 \text{ mm}; l_3 = 16 \text{ mm}$
Maximum joint aperture:	$d = 0.1 \text{ mm}$
Angle between 2 adjacent sides:	$\varphi_1 = d/l_1 = 0.00625 \text{ rad}$

Table 7-6. Summary of data used for the modeling of the blocks with the calibrated non coplanar joint model in the 14 block-case, and in the 3 opus quadratum walls.

7.5.1 14-block case

In section 7.4.1 the results of a sensitivity study with respect to the geometrical parameters of the joint model were presented. The study consisted in the evaluation of the influence of such parameters on the response of a column of 14 blocks subjected to gravity and slowly increasing lateral loads. For the purpose of the sensitivity study, and model calibration, only the failure load λ and the top lateral displacement at failure δ_{top} , had been reported for each of the 20 cases which were considered (see Table 7-2). We will present here, also as an example for all other analyses, the details of the DE response with the help of the following 16 figures (from 7-46 to 7-61).

7.5.1.1 14-block case with planar joint model

To better appreciate the features of the system response which have been introduced by the new joint model, it is first presented the behavior obtained without accounting for the joint imperfections, that is by employing the existing planar joint model. The details of the analysis for this case are illustrated in the following figures showing: (a) the system configuration before and after failure (Figure 7-46 and 7-48); (b) the time history of the top lateral displacement $\delta_{top}(t)$ for various time intervals (from Figure 7-49 to 7-51); and (c) the force-displacement relationship λ - δ_{top} (Figure 7-47). Note that each figure reports also the values of the lateral force F_x acting on each block, the simulation time, and the cycle number, corresponding to the time in which the figure was generated during the solution process¹.

¹ More specifically, the lateral force F_x (which is provided in the title of each figure) is related to λ by the relation: $F_x = 10\lambda$. The simulation time, and the cycle number are given in the top of the left panel of the figure. In addition, if the figure represents an x-y plot, the left panel contains also the maximum and minimum values of the quantities represented on each Cartesian axis.

We can summarize the essential results obtained with such model in:

1. Absence of any appreciable top lateral displacement δ_{top} before failure as opposed to the experimental response ($\delta_{top}=0.0173\text{mm}$ vs. $\delta_{top-exp}=11.5\text{mm}$)
2. Correct prediction of the failure mode (rigid body overturning)
3. Overestimation of the failure load ($\lambda = 0.163$ vs. $\lambda_{exp} = 0.132$)

Such results can be illustrated with the help of the figures in the following.

Regarding the first point, observing the system configuration just before failure (Figure 7-46), corresponding to an applied lateral load $\lambda = 0.162$, we can observe that the column appears undeformed. The maximum value of the time history of the top lateral displacement δ_{top} (Figure 7-50), confirms that only a negligible top lateral displacement, $\delta_{top} = 0.0173$ mm, takes place before failure due to the elastic deformations of the joints². The linearity of the response is clearly illustrated in the force-displacement, λ - δ_{top} , relationship shown in Figure 7-47.

² The predicted maximum top lateral displacement is less than 10^{-4} H, H being the height of the column.

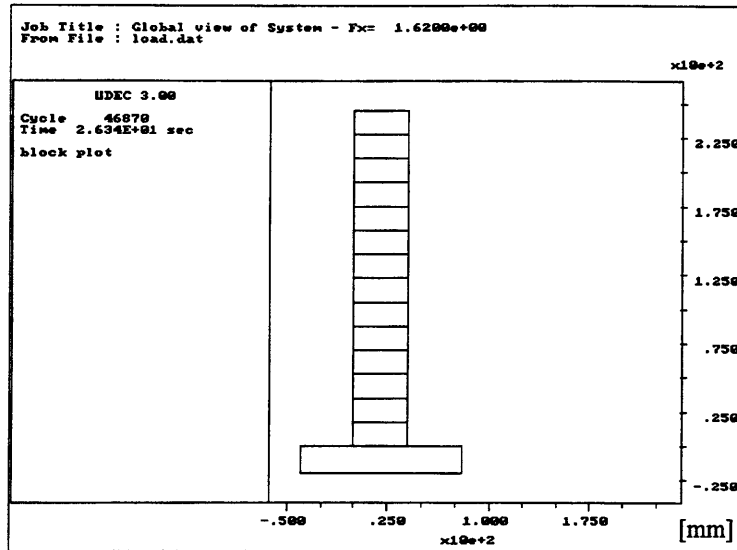


Figure 7-46. 14-block case, no imperfections: system configuration with maximum lateral load ($\lambda = 0.162$; $t = 26$ sec).

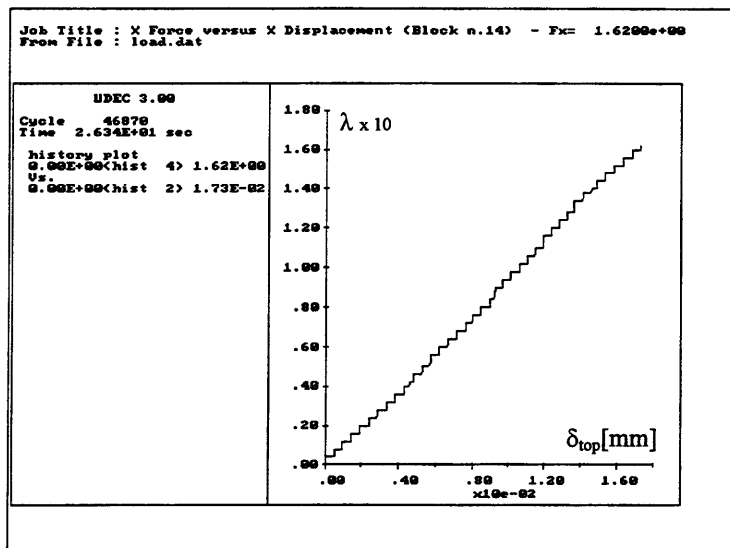


Figure 7-47. 14-block case, no imperfections: top horizontal displacement δ_{top} vs. horizontal lateral load λ up to maximum force before failure (from $\lambda = 0$, to $\lambda = 0.162$).

With respect to the second point (failure mode) we can observe in Figure 7-48 that the system fails by rotation of the entire column around its base corner without any rotation or sliding occurring at the intermediate joints. This is in agreement with the experimental response.

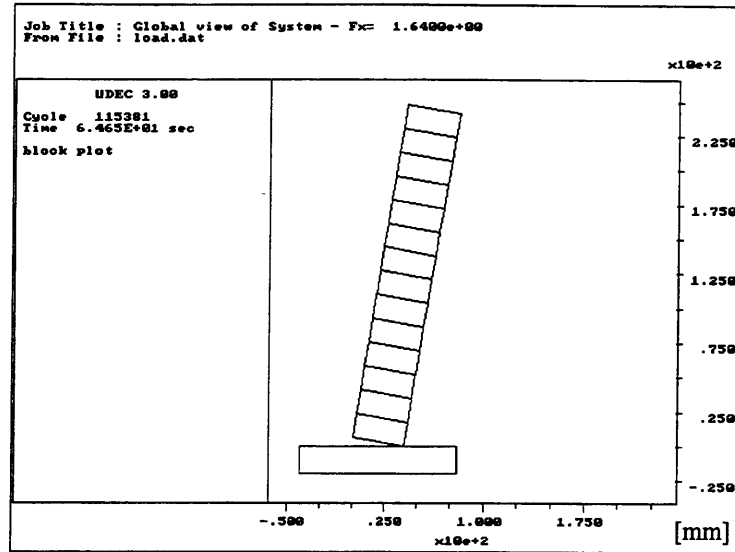


Figure 7-48. 14-block case, no imperfections: initiation of failure mechanism ($\lambda=0.164$; $t=65$ sec).

Concerning the third point (failure load), we illustrate here in detail (as an example for all other analyses), how the failure load is recognized by monitoring the time history of δ_{top} for each new increment of lateral load.

First, in Figure 7-49 the time history of the top lateral displacements for the initial loadsteps (up to 3.1sec of simulation) is presented. Note that after each load step $\Delta\lambda=0.004$, which is applied instantaneously, it takes a certain amount of time for the system to reach a new stable configuration, corresponding to a constant value of δ_{top} . Subsequently, the failure load is clearly detected by comparing Figure 7-50 and 7-51. The first one shows that the system has reached a stable configuration for a lateral load $\lambda=0.162$, and a simulation time $t=2.63$ sec, while Figure 7-51 shows that, with a lateral

load $\lambda=0.164$, and after more than 3.8 sec of additional simulation time, the top lateral displacement has increased of 3 orders of magnitude and is clearly diverging. Therefore, having used a final increment of lateral load $\Delta\lambda=0.02$, we can conclude that the analysis with the planar joint model has predicted a failure load $0.162 < \lambda_{pl} < 0.164$.

As already mentioned, such value is higher (+20%) than the experimental one, $\lambda_{exp} = 0.132$, however it is interesting to observe that the DE prediction is correct if no microrotations at the joints are assumed. In fact in this case, if b and H are respectively the base and the height of the column, the exact failure load, assuming a failure mode of rigid rotation of the entire column, is simply $\lambda_{rig} = b/H = 40/245 = 0.163$.

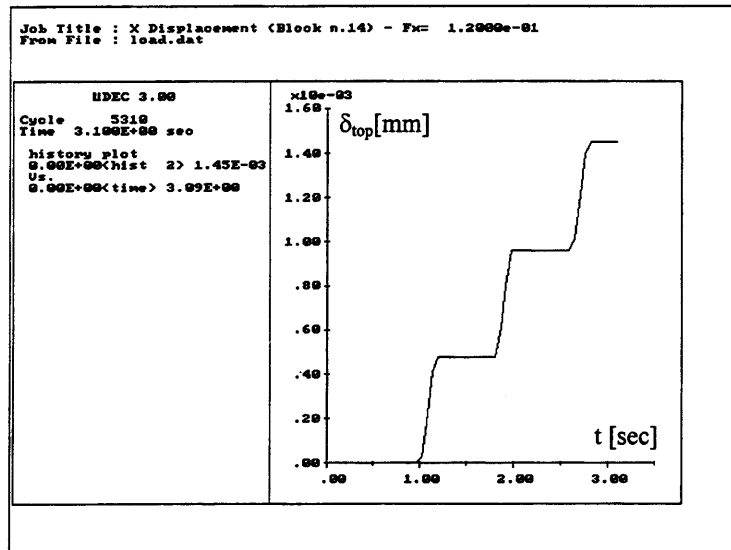


Figure 7-49. 14-block case, no imperfections: time history of top horizontal displacement δ_{top} during initial loadsteps (from $\lambda = 0$, to $\lambda = 0.012$).

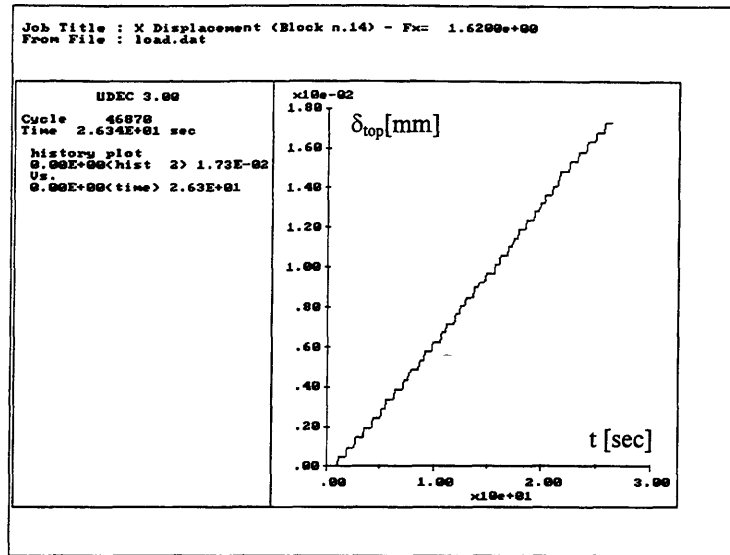


Figure 7-50. 14-block case, no imperfections: time history of top horizontal displacement δ_{top} during incremental application of lateral load (from $\lambda=0$ to $\lambda=0.162$). Final constant value of δ_{top} indicates that the system has reached a stable configuration for $\lambda = 0.162$.

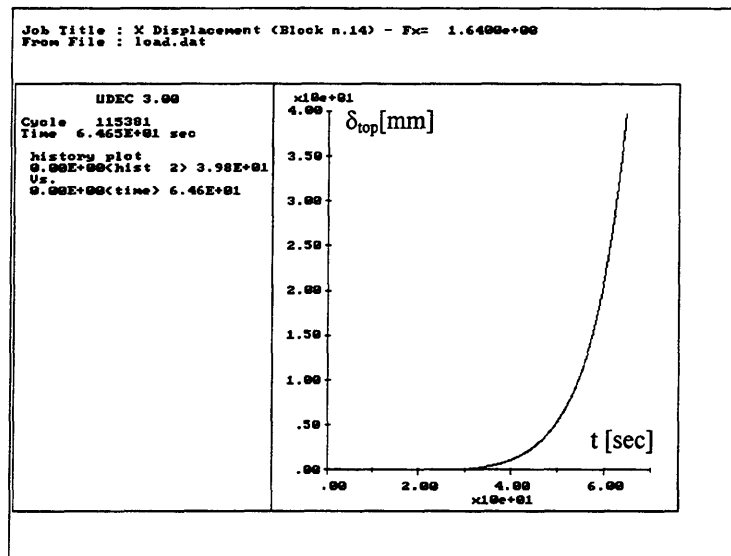


Figure 7-51. 14-block case, no imperfections: time history of top horizontal displacement δ_{top} during incremental application of lateral load (from $\lambda=0$ to $\lambda=0.164$). Diverging response indicates initiation of failure mechanism for $\lambda = 0.164$.

7.5.1.2 14-block case with non coplanar joint model

In this section the details of the response obtained in the modeling of the 14-block column subjected to gravity and quasistatic lateral load with the new non coplanar joint model are presented. It is recalled that for the purpose of a sensitivity study several analyses had been performed with different values of the joint parameters. The results of those analyses were summarized in Table 7-2, where the failure load λ , and the top lateral displacement before failure δ_{top} were reported for each of the 20 cases³. Since the essential features of the response were the same for all cases, only one will be presented here. In particular we will refer to the case corresponding to the Shape E (see Figure 7-38) with a reference polygon with 5 sides, a central base measuring $0.2b$, (where b is the joint length), and a maximum joint aperture $d=0.1$ mm (or 0.57% of the block height). Note that this is not the case which best approximates the experimental values of λ and δ_{top} , but it is suitable for the purpose of illustrating the features of the new joint model.

Similarly to the case of the planar joint model presented in the previous section, the details of the analysis are illustrated by⁴: (a) the system configuration at various levels of lateral load (Figure 7-52 and 7-55); (b) the time history of the top lateral displacement $\delta_{top}(t)$ for various time intervals (from Figure 7-56 to 7-58); and (c) the force-displacement relationship λ - δ_{top} also reported for various time intervals (Figure 7-59 to 7-61).

³ Note that the failure load λ reported in Table 7-2 is normalized with respect to the failure load $\lambda_{pl} = 0.163$ obtained with the planar joint model.

⁴ Note that each figure reports also the values of the lateral load λ , the simulation time, and the cycle number, corresponding to the time in which the figure was generated during the solution process. More specifically, λ can be obtained from the value of $F_x=10\lambda$ (the lateral force acting on a single block) which is provided in the title of each figure. The simulation time, and the cycle number are given in the top of the left panel of the figure. If the figure represents an x-y plot, the left panel contains also the maximum and minimum values of the quantities represented on each Cartesian axis.

The main features in the system response due to the new joint model are:

1. The progressive formation of microrotations at the joints associated to the increase of lateral load, which cause an apparent bending of the column before failure ($\delta_{top}=14.6$ mm as opposed to a negligible displacement with the planar model)
2. A substantially reduced failure load λ_{nc} with respect to the one obtained with the planar joint model ($\lambda_{nc}=0.117$ as opposed to $\lambda_{pl}=0.163$).

Such characteristics of the system response are in agreement with the experimental behavior and were, in fact, the intended objectives in the development of the new joint model. It is noted that the failure mode - consisting in a rotation around the base corner with no sliding or joint opening - is also correctly predicted.

More in detail with the help of the figures, we can observe that up to a lateral load $\lambda=0.032$ (27% of failure load) the column is practically undeformed (Figure 7-52) with a negligible top lateral displacement $\delta_{top}=0.113$ mm (see $\delta_{top}(t)$ in Figure 7-56 up to $t=25$ sec), but when $\lambda=0.040$ (34% of failure load), and $t=99$ sec, a noticeable apparent deformation can be seen in Figure 7-53 due to the formation of microrotations at the joints which yield a $\delta_{top}=8.2$ mm (see $\delta_{top}(t)$ in Figure 7-57 for $t=99$ sec). Subsequently, when the lateral load assumes its maximum value $\lambda=0.116$, for $t=270$ sec, (Figure 7-54), the top lateral displacement reaches the value of $\delta_{top}=14.6$ mm (see $\delta_{top}(t)$ in Figure 7-57 for $t=270$ sec).

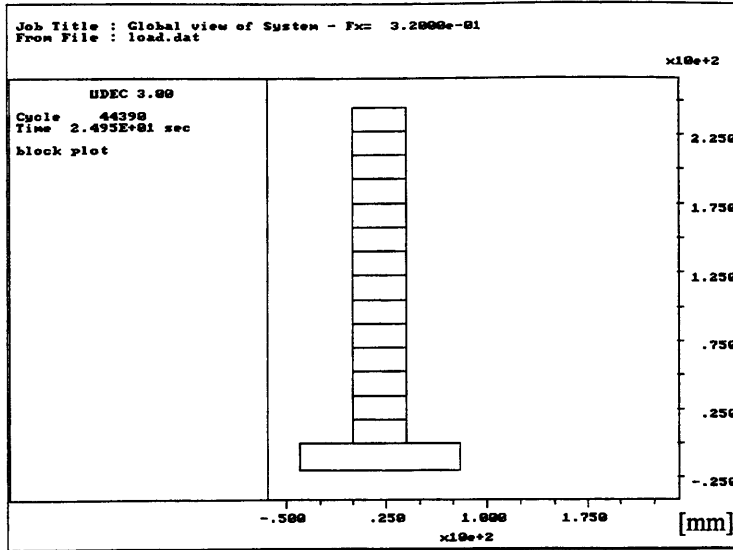


Figure 7-52. 14-block case, with imperfections: system configuration with low level of lateral load ($\lambda=0.032$; 27% of failure load; $t=25$ sec). No microrotations.

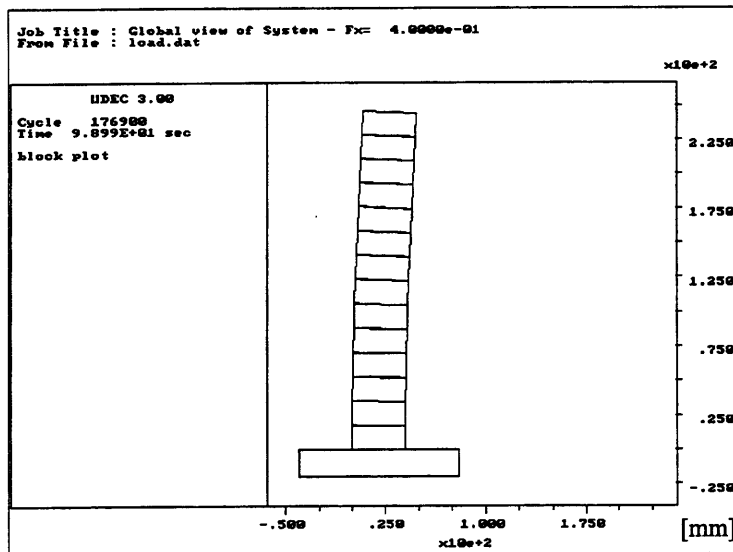


Figure 7-53. 14-block case, with imperfections: system configuration corresponding to intermediate lateral loading ($\lambda = 0.040$; 34% of failure load; $t=99$ sec). Apparent bending due to microrotations.

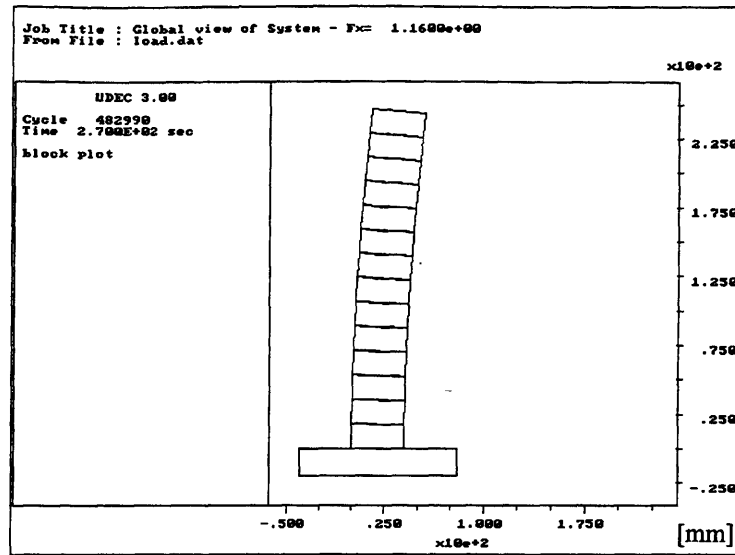


Figure 7-54. 14-block case, with imperfections: system configuration corresponding to maximum lateral load before failure ($\lambda = 0.116$; $t = 270$ sec). Apparent bending due to microrotations.

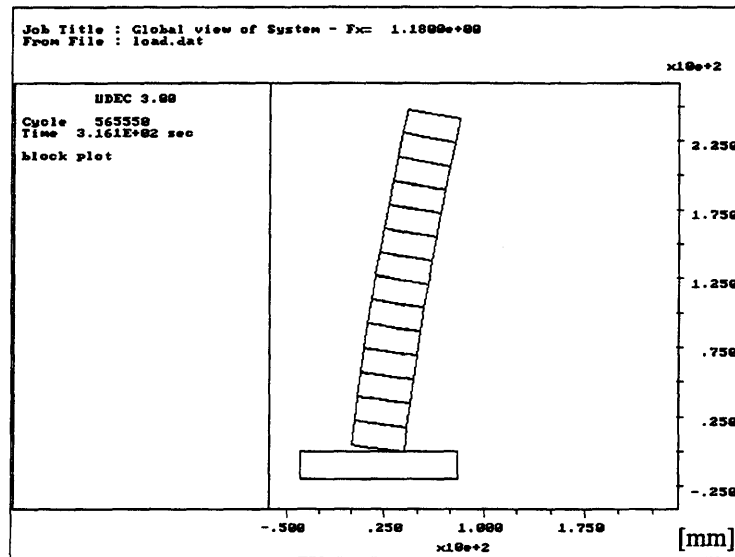


Figure 7-55. 14-block case, with imperfections: initiation of failure mechanism ($\lambda = 0.118$; $t = 316$ sec).

From the time history of the top lateral displacement $\delta_{top}(t)$ we can observe an initial linear elastic phase up to 27% of the maximum lateral load (Figure 7-56), characterized by negligible displacements due to the elasticity of the joints, followed by a nonlinear phase due to the microrotations showed in Figure 7-57, where horizontal segments indicate stable configurations. The value of the failure load ($0.116 < \lambda < 0.118$) is obtained by comparing the stable configuration at $\lambda = 0.116$ corresponding to a constant value of δ_{top} showed in Figure 7-57, and the unstable configuration at $\lambda = 0.118$ corresponding to a diverging value of δ_{top} as showed in Figure 7-58.

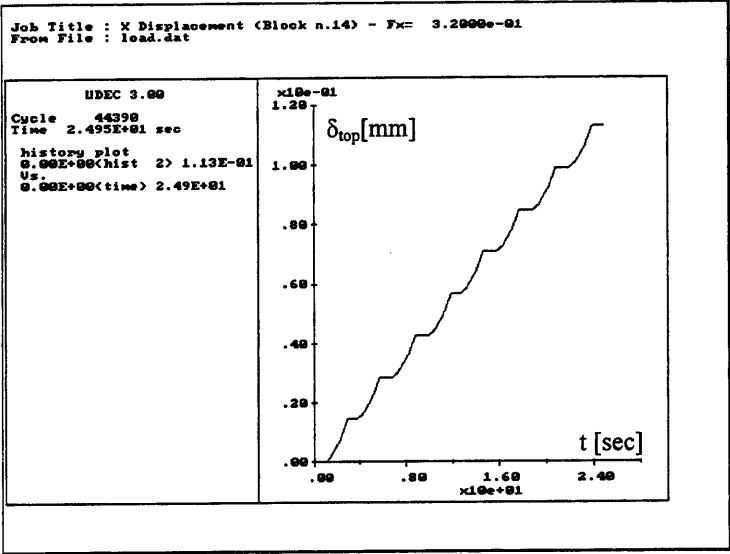


Figure 7-56. 14-block case, with imperfections: time history of top horizontal displacement δ_{top} during initial load steps (from $\lambda = 0$, to $\lambda = 0.032$). Linear response, no microrotations.

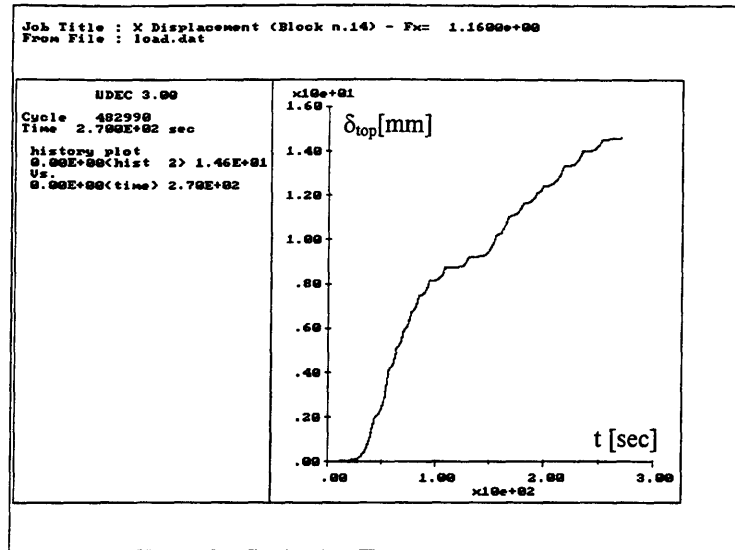


Figure 7-57. 14-block case, with imperfections: time history of top horizontal displacement δ_{top} up to maximum lateral load (from $\lambda = 0$, to $\lambda = 0.116$). Nonlinear response due to microrotations.

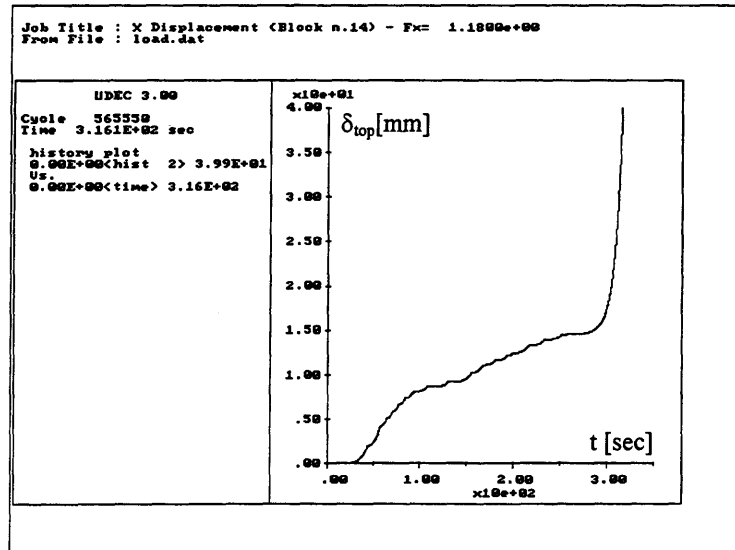


Figure 7-58. 14-block case, with imperfections: time history of top horizontal displacement δ_{top} up to failure load with initiation of failure mechanism (from $\lambda = 0$, to $\lambda = 0.118$).

The highly nonlinear response of the system due to the accumulation of microrotations at the joints is even more evident in the force-displacement (λ - δ_{top}) relationship, where stable configurations are associated to vertical segments. The initial linear elastic phase is showed in Figure 7-59 (up to $\lambda=0.032$ or 27% of maximum lateral load). Subsequently, in Figure 7-60 the horizontal segments indicate increasing displacements associated to constant lateral loads. Clearly such levels of lateral loads are those which caused the formation of one or more microrotations. Finally the failure load is recognized in the increasing displacement occurring for a constant lateral load $\lambda=0.118$ shown in Figure 7-61.

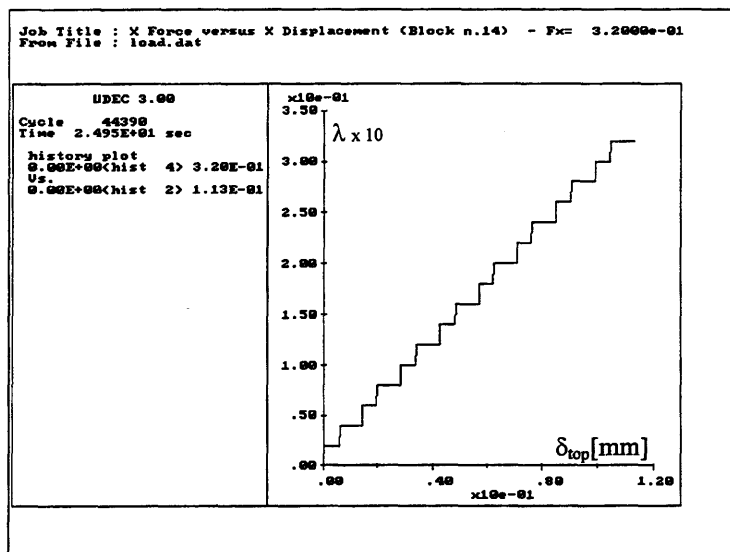


Figure 7-59. 14-block case, with imperfections: top displacement vs. lateral load in the initial loading phase (from $\lambda = 0$, to $\lambda = 0.032$). No microrotations take place, the system behaves linearly.

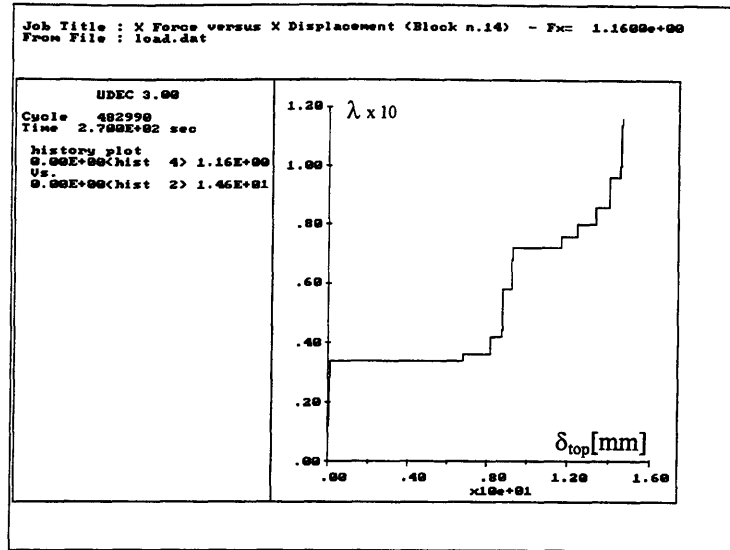


Figure 7-60. 14-block case, with imperfections: top displacement vs. lateral load up to maximum lateral load (from $\lambda = 0$, to $\lambda = 0.116$). The system behaves nonlinearly due to accumulation of microrotations.

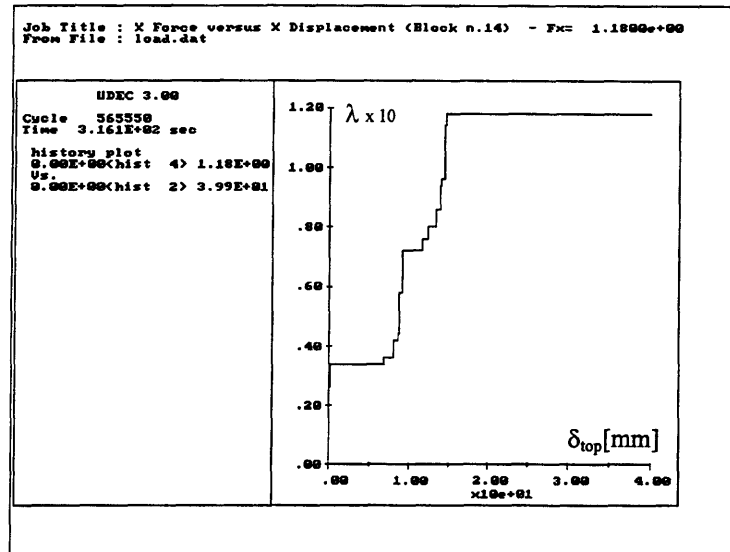


Figure 7-61. 14-block case, with imperfections: top displacement vs. lateral load up to failure load with initiation of failure mechanism (from $\lambda = 0$, to $\lambda = 0.118$).

7.5.2 21-block case

In this section we will illustrate the results obtained from the DE modeling of the in-plane loading test of a 21-block wall adopting the new non coplanar joint model. The joint parameters calibrated on the 14-block case (as described in the section 7.4) will be used in the following analysis.

In Chapter 5 we described the experimental observations and the DE analyses with the planar joint model related to the same 21-block wall. It is recalled that the experimental tests yielded a failure load $\lambda_{\text{exp}}=0.5$ and either a mixed sliding-rotating failure mode or a partial rotating failure mode involving only the 2 top left blocks as illustrated in Figure 7-62a, and 7-62b. This variability was explained by a high sensitivity of the system behavior with respect to the geometric imperfections of the experimental model, and the accuracy in repositioning the blocks⁵.

The DE analysis with the planar joint model predicted, instead, a diffuse sliding failure mode at a failure load $\lambda=0.6$ (which was equal to the friction coefficient $\alpha=0.6$) as shown in Figure 7-63a. In addition no displacement was observed before failure as opposed to the experimental case where some internal displacements were observed starting from 80% of the ultimate lateral load. Rotating or mixed sliding-rotating failure modes were obtained with the DE planar model by adopting higher values of the friction coefficient: $\alpha=0.65$, and $\alpha=0.75$ (see Figure 7-63b and 7-63c). As shown in Chapter 5, limit analysis confirmed that the results predicted by the DE planar model were exact assuming that the system had no geometric imperfections.

⁵ In Figure 7-62a, it is reported a wall with 7 instead of 6 layers, however it should be noticed that the bottom layer was fixed to the test plane (and therefore it behaved as a 6-layer wall). In addition it was found experimentally that, in this case, the length of the base of the wall did not influence the failure response of the system if it was longer or equal to the length of 3 blocks. Therefore the wall in Fig. 7-62a had the same failure behavior of a 21-block wall.

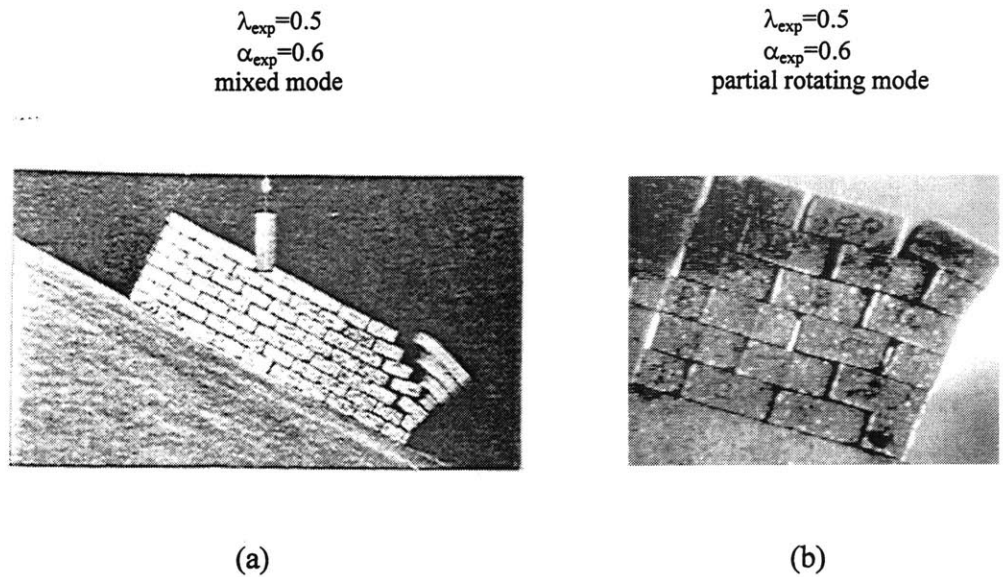


Figure 7-62. Experimental failure modes and failure loads λ_{exp} for the 6-layer opus quadratum wall: (a) mixed sliding-rotating mode; (b) partial rotating mode. Experimental friction coefficient: $\alpha_{exp}=0.6$.

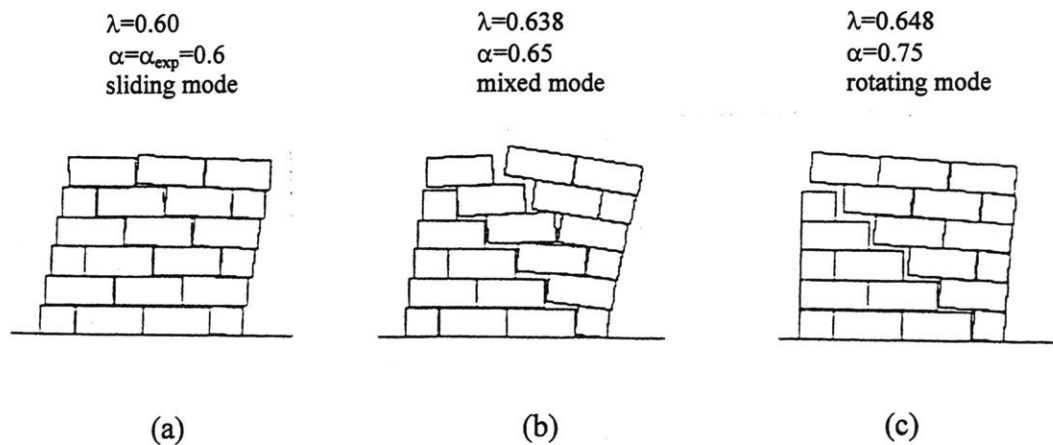


Figure 7-63. DE results with planar joint model: failure modes and failure loads λ for the 6-layer opus quadratum wall with various friction coefficients α .

In summary the planar joint model, for the 21-block case, had shown the following limitations:

- a 20% overestimation of the failure load,
- a misprediction of a diffuse sliding failure mode,
- a misprediction of a sudden collapse as opposed to a progressive failure.

The results obtained with the new joint model are illustrated in Figure 7-64 where a sequence of system configurations at various levels of lateral load λ are presented.

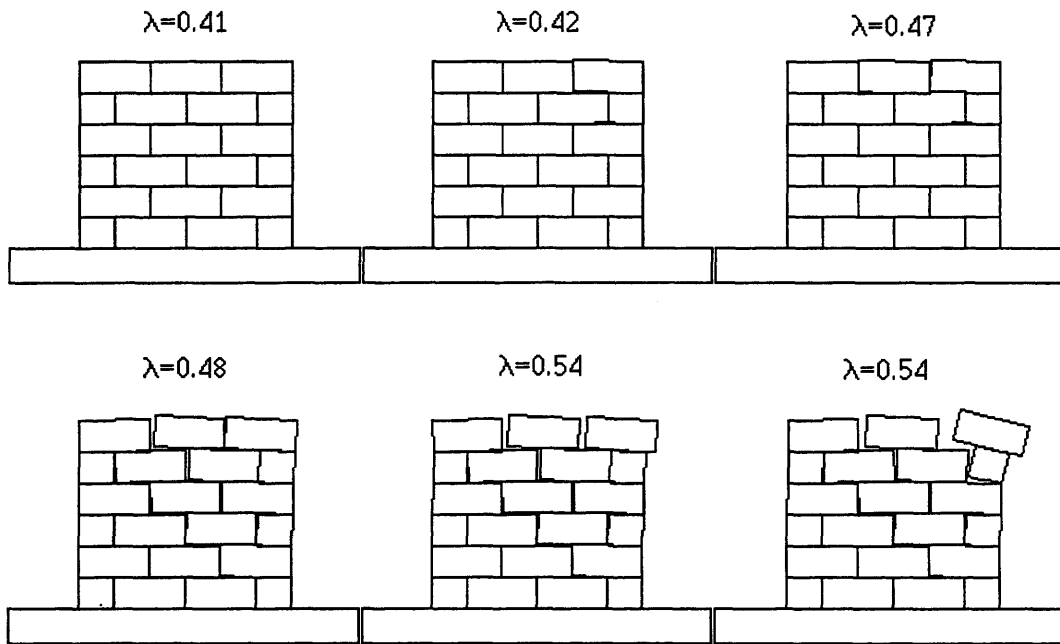


Figure 7-64. 21-block case with imperfections: progressive failure under increasing lateral load. Initiation of microrotations for lateral load $\lambda=0.42$, development of fracture lines for $\lambda=0.48$, and failure for $\lambda=0.54$.

First it is noted that the process of development of microrotations at the joints initiates for $\lambda = 0.42$. It initially interests the two top right blocks and progressively extends to about half of the wall. When λ is increased from 0.47 to 0.48 a pronounced rotation of the 6 top right blocks is observed and a new fracture line along the diagonal of

the wall is also noticed. The system eventually fails due to the sliding and rotation of the 2 top right blocks for $\lambda = 0.54$.

Based on such results we can observe that with the new model:

- the overestimation of the failure load is reduced from 20% to less than 8%
- one of the two experimental failure modes (the one in Figure 7-62b) is correctly predicted
- the process of progressive failure is also correctly predicted.

In addition we noticed that the pronounced rotation of the 6 top right blocks, which was predicted for $\lambda = 0.48$, appears to be the initiation of the experimental failure mode shown in Figure 7-62a which involves the rotation of the same group of blocks, and is obtained for a similar value of lateral load $\lambda = 0.50$. The reason why in the experimental modeling the system does not find a configuration of equilibrium after such rotation may be related to the dynamic effects of the impact which are not addressed in the quasistatic simulation.

Finally it is reported that by increasing the size of the joint irregularity, by assigning the maximum joint aperture $d=0.2\text{mm}$ (instead of the calibrated value of $d=0.1\text{mm}$ used in the previous analysis), we obtain a failure load $\lambda = 0.50$ which coincides with the experimental one, while the rotation of the 6 blocks still occur at $\lambda = 0.48$. Therefore the residual difference between predicted and experimental failure load may be associated to a high sensitivity of the failure load with respect to the joint irregularity due to the small number of block involved in the failure mechanism.

7.5.3 110-block case

This case refers to a wall constituted by the same peperino blocks, with dimensions of 17.5 x 40 x 80 mm, used in the previous cases, with the difference that the longer side of the block is now parallel (instead of perpendicular) to the plane of the wall. In the 2D representation the base of the block is now 80 mm instead of 40 mm long (as in the other cases) while the height is the same (17.5mm). The dimensions of the wall are: B = 400 mm, and H = 350 mm, and it is constituted by 20 layers of 5 full blocks each, for a total of 110 blocks including the half blocks at the edges.

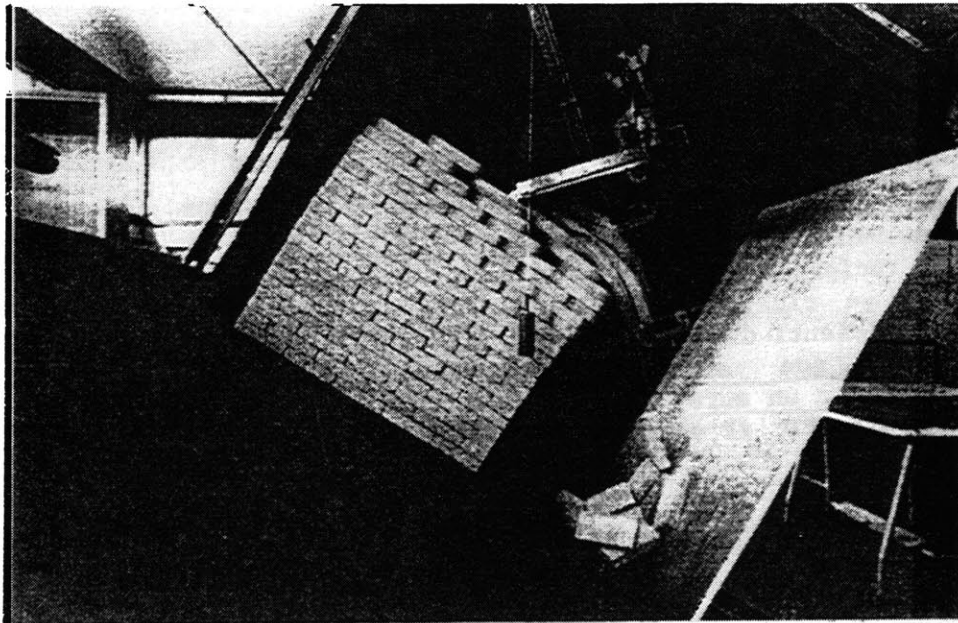


Figure 7-65. Experimental failure mode of a 110-block wall subjected to in plane loading. Failure occurs for a lateral load $\lambda=0.55$.

The wall was tested on an inclined table to simulate an increasing lateral load (Ceradini, V. 1992). The failure occurred for a lateral load $\lambda = 0.55$, after that some small internal displacements had occurred at lower values of lateral load. Failure initiated by sliding of the top right blocks (see Figure 7-65) and gradually extended to the rest of the wall without increase of lateral load.

More precisely, after 10 repetitions of the same test, the average failure load was $\lambda = 0.555$, and the standard deviation $\sigma = 0.0137$ (or 2.5%). Apparently, this result is in contrast with the value of the friction coefficient which, as already reported, has an average value $f=0.6$, and a standard deviation of 0.0069 (or 1.2%). In fact, a failure mechanism of pure sliding should take place when $\lambda = f$.

The DE analysis, with the planar joint model, confirmed this expectation, and predicted a failure load $\lambda = 0.6$ with a diffuse sliding mechanism occurring simultaneously between all layers, and with no displacements before failure. Therefore the differences between the DE predictions with the planar joint model, and the experimental results were:

- a failure to predict internal displacements before collapse,
- a failure to predict the initiation of the sliding in the top layer, and
- an overestimation of the failure load.

The results obtained with the new joint model are illustrated in Figure 7-66, where a series of system configurations for various levels of lateral load λ are presented.

It is observed that failure occurs for a lateral load $\lambda = 0.55$, due to the sliding of the top right block which involves also the rotation of the half block of the second layer. Internal displacements due to the formation of microrotations are visible also at lower values of lateral load as shown in Figure 7-66 in the configuration corresponding to $\lambda = 0.52$.

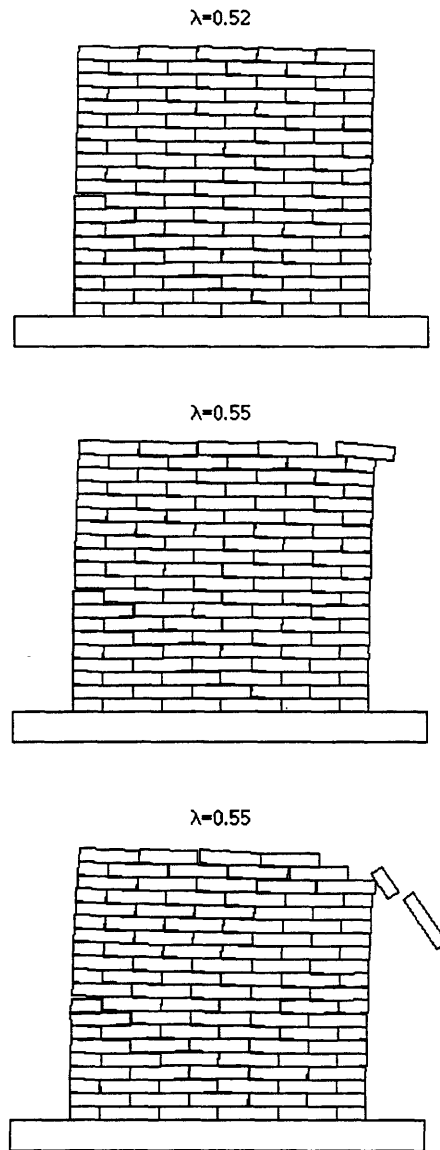


Figure 7-66. 110-block case with imperfections: at lateral load $\lambda=0.52$ initiation of internal displacements due to microrotations; at lateral load $\lambda=0.55$ failure mechanism takes place due to accumulation of microrotations.

This result can be explained with the formation and accumulation of microrotations (in particular in the blocks along the free edge on the right side) which cause the top right block to rotate slightly. Such inclined configuration allowed the initiation of sliding for a lateral load $\lambda = 0.55$ which is lower than the friction coefficient $f=0.6$.

An hypothesis to explain the fact that in the numerical prediction only the 2 top right blocks slide (at the correct value of lateral load $\lambda = 0.55$), may be that in reality such motion causes vibrations (not captured by the DE model) which could induce sliding in the adjacent blocks which are very close to the sliding condition.

In conclusion it appears quite clearly that also for the 110-block wall the new joint model has improved the DE predictions. In fact we can observe that:

- as opposed to the planar model prediction, a process of increasing internal displacements before failure is predicted,
- the new model predicts a sliding process initiating from the top layer, and
- the failure load λ , which was previously overestimated ($\lambda_{pl} = 0.60$), is now in agreement with the experimental results: $\lambda = \lambda_{exp} = 0.55$.

7.5.4 231-block case

In this section the results obtained from the DE modeling of the in-plane loading test of a 231-block wall adopting the new non coplanar joint model will be illustrated. In Chapter 5 we described the experimental observations and the DE analyses with the planar joint model related to the same case, which was indicated as WALL3. It is recalled that the experimental model of the wall was built with the same peperino blocks used in the previous cases, therefore, also the values of the joint parameters adopted for the DE analysis were the same used in the previous cases, which were obtained from the calibration on the 14-block case (see section 7.4). The blocks, in the plane of the wall, measured 40 x 17.5 mm, and the dimensions of the wall were: base B = 400 mm, and height H = 385 mm. The wall was constituted by 22 layers of 10 full blocks each, for a total of 231 blocks including the half blocks at the edges⁶. The experimental failure mode obtained with the tilting table is shown in Figure 7-67.

$$\lambda=0.35$$



Figure 7-67. 231-block case: experimental failure mode and failure load λ .

⁶ Note that in Chapter 5 WALL3 was modeled with 21 instead of 22 brick layers. However, in this section all analyses, with and without contact imperfections, refer to a wall with 22 layers. Note, also, that in the experimental model the first of the 23 layers is fixed to the testing table, and therefore it behaves as a 22 layer wall.

The wall failed at $\lambda = 0.35$ after small internal displacements had taken place at lower levels of lateral loads. It appears as if the right portion of the wall, for a width of approximately 2 or 3 full blocks along the free edge, behaved as a column which tends to separate itself from the rest of the wall through a complex mechanism involving sliding and rotation of many blocks.

The failure load obtained with the DE analysis using the planar joint model was $\lambda = 0.46$. The corresponding failure mode is represented in Figure 7-68 and it appears to be in reasonable agreement with the experimental one. Such failure occurred without prior displacements of the blocks at lower levels of lateral loads.

In comparing these results with the experimental response we can observed that:

- the DE failure load is substantially higher than the experimental one (23%) ,
- the DE response does not predict internal displacements before failure, and
- the area where sliding take place at failure is wider in the numerical prediction.

$\lambda=0.46$

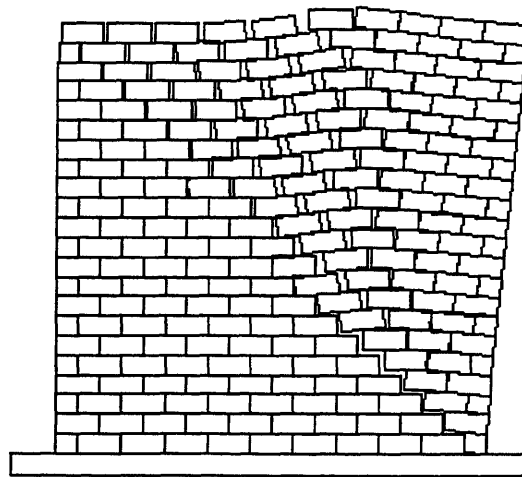


Figure 7-68. 231-block case, DE prediction with no imperfections: failure mode and failure load λ .

The results obtained with the new non coplanar joint model are reported in Figure 7-69 where the system configuration at various levels of lateral load are presented. The failure load is obtained for $0.37 < \lambda < 0.38$, while some internal displacements are observed for lower values of lateral load.

It appears that the new model allowed:

- a better estimation of the failure load with a residual difference of 7% with respect to the 23% overestimation of the planar model ,
- the prediction of a process of progressive internal displacements as opposed to a sudden failure, and
- a narrower area of internal sliding at failure.

It is noted however that experimental failure mode exhibits an even narrower failure band. As already mentioned this phenomenon of localization of the sliding band may be related to the friction softening behavior of the joint, which was not accounted for in the previous analyses, but will be addressed in the next section.

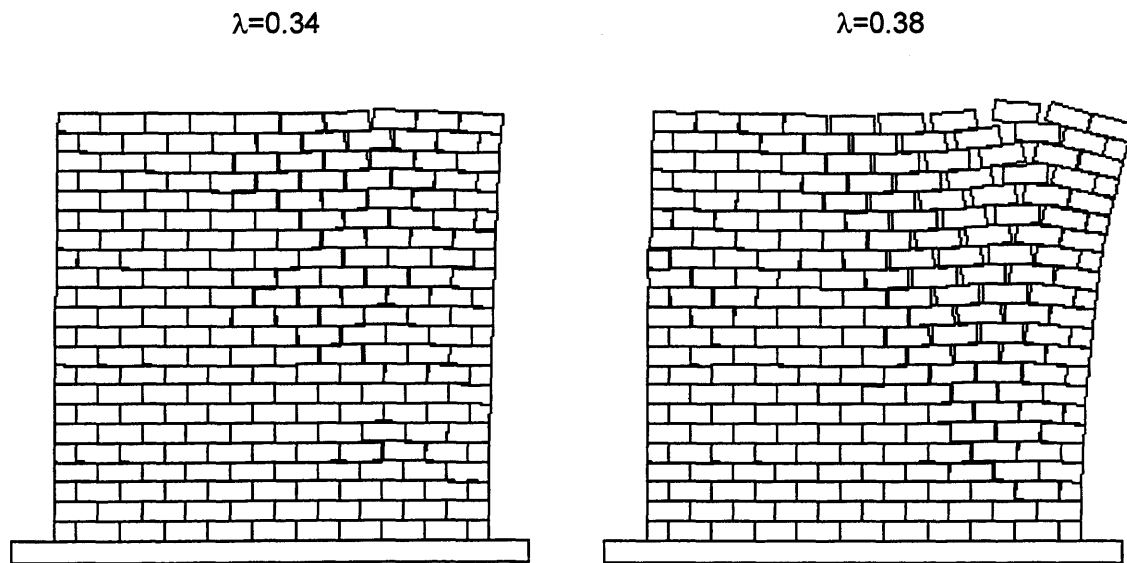


Figure 7-69. 231-block case, DE prediction with imperfections: system configurations at various levels of lateral load λ .

7.5.5. Assessment of friction softening

In the formulation of the new joint model, as illustrated in section 7.2.3 (see equations 7-13, 7-14, and Figure 7-10), a modification of the behavior in the tangential direction was introduced in order to allow for the reduction of the friction force after some sliding distance had taken place. In the 231-block case, where a localization of the sliding band is observed in the experimental response, it may be interesting to observe the effect of friction softening on the width of such sliding area.

First a simple sliding test of a single block on a fixed base is performed in order to verify that the expected softening behavior is obtained (see Figure 7-70). The friction softening parameters for such test are the following:

$$\phi = 0.6 \text{ (friction coefficient)}$$

$$\Delta U_1 = 0.0225 b = 0.9 \text{ mm}$$

$$\Delta U_1 + \Delta U_2 = 0.025 b = 1.0 \text{ mm}$$

$$\beta = 0.8$$

where $b = 40 \text{ mm}$ is the block base.

The tests consists in the application of the gravity force followed by an increasing lateral load up to the initiation of sliding. In Figure 7-71 the plot of the friction force vs. sliding distance, shows that the expected reduction of the friction force is obtained after a sliding distance $U_s = \Delta U_1 + \Delta U_2$ had occurred.

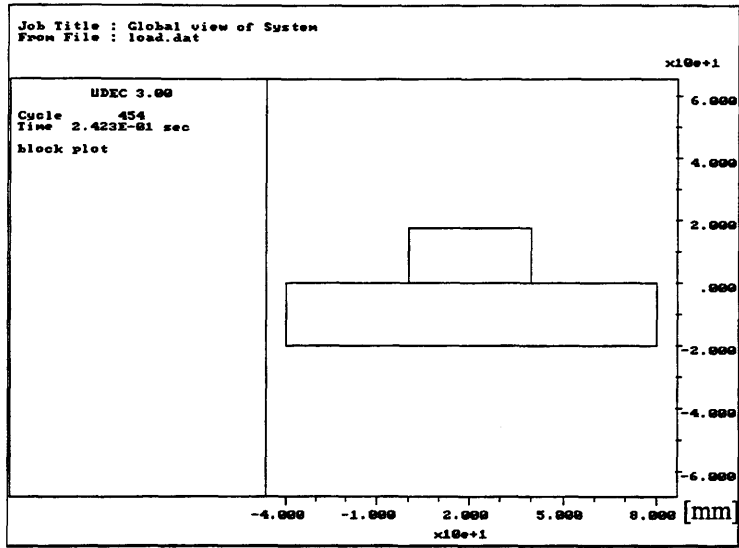


Figure 7-70. Sliding test of a single block on a fixed base with friction softening: system configuration.

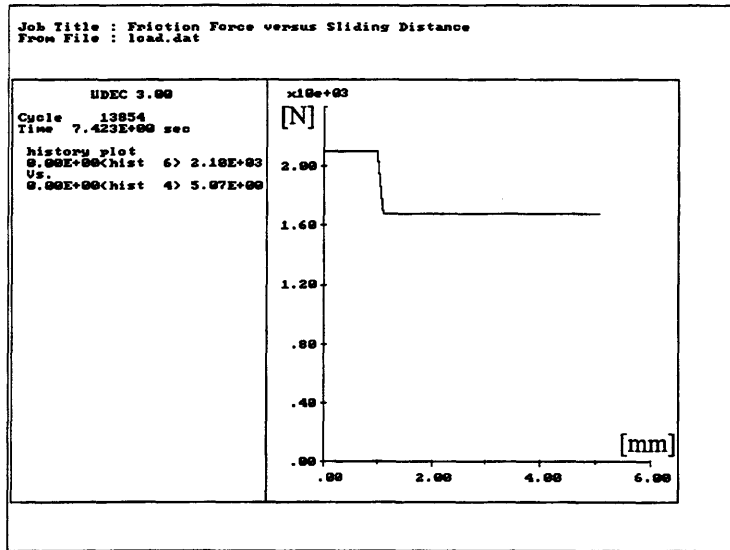


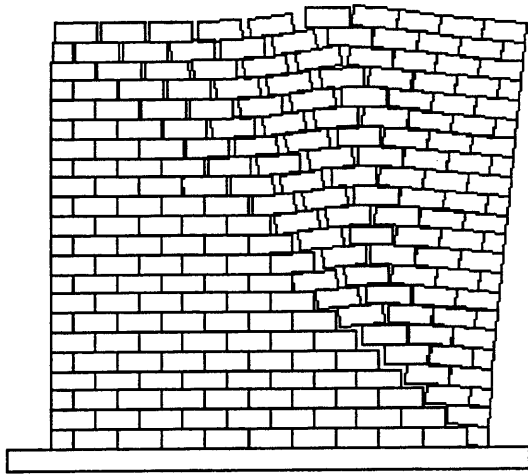
Figure 7-71. Sliding test of a single block on a fixed base with friction softening: friction force versus sliding distance.

In order to assess the effect of friction softening on the localization of the sliding band on the in-plane failure response of opus quadratum walls, the analysis of the 231-block wall has been repeated, accounting for both geometric imperfections, as in section 7.5.4, and friction softening. Two values of the friction reduction parameter β have been considered: $\beta = 0.9$ and $\beta = 0.8$. As expected no variation of the failure load was observed, but an increasingly narrower sliding band was obtained as the friction softening effect became more pronounced.

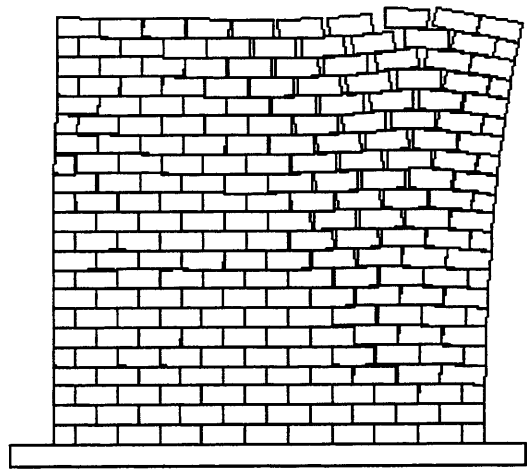
A comparison of the failure modes obtained with and without friction softening and with and without geometric imperfections is presented in Figure 7-72. Case (a) is obtained with the planar joint model and no friction softening; case (b) with the non coplanar model and no friction softening; while case (c) and (d) are obtained with the non coplanar model and friction reduction parameter $\beta = 0.9$ and $\beta = 0.8$ respectively. For the purpose of comparison, the horizontal displacement of the top right corner of the wall is the same (40 mm) for each configuration shown in figure. For qualitatively compare the extent of the sliding areas for the various cases a count of the vertical joints which appeared opened in the top 5 layers was performed as reported in Table 7.7. Based on these results it can be concluded that the width of the sliding band decreases with the accounting of the joint imperfections, but, as expected, is particularly sensitive to the introduction of the friction softening behavior. In particular for $\beta = 0.8$ (Figure 7-72d) we observe a failure mode which is in very good agreement with the experimental one shown in Figure 7-67.

CASE	a	b	c	d
Imperfections	NO	YES	YES	YES
Frict. softening	NO	NO	YES ($\beta = 0.9$)	YES ($\beta = 0.8$)
layer 1	6	5	3	3
layer 2	5	5	5	2
layer 3	5	4	4	2
layer 4	5	4	3	2
layer 5	4	3	4	3
Top 5 layers	25	21	19	12

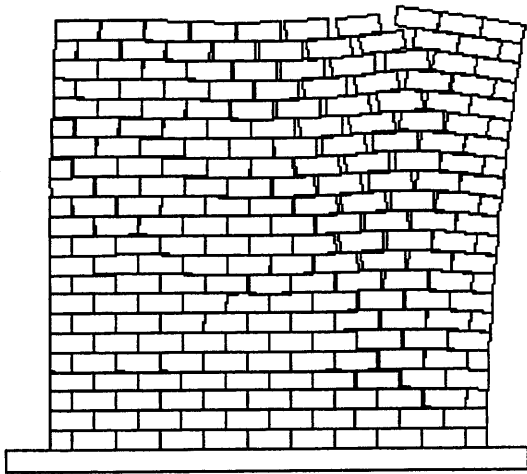
Table 7-7. 231-block case: number of opened vertical joints at failure for a top right block displacement of 40mm. Cases a, b, c, d refer to Figure 7-72.



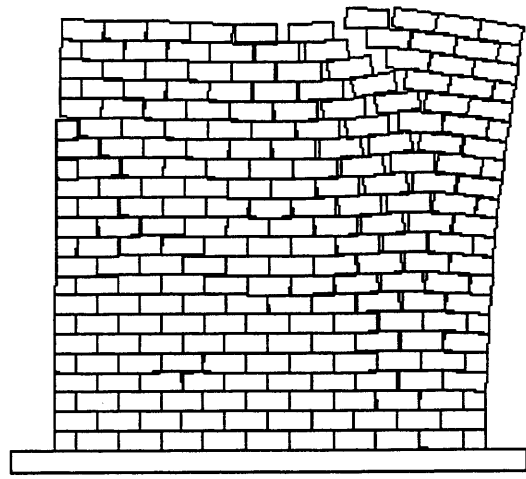
(a) No imperfections and no friction softening



(b) With imperfections and no friction softening



(c) With imperfection and friction softening ($\beta=0.9$)



(d) With imperfect. and friction softening ($\beta=0.8$)

Figure 7-72. 231-block case: comparison of 4 failure modes for evaluating the effects of joint imperfections and friction softening. The horizontal displacement of the top right corner of the wall is the same (40 mm) for each configuration.

7.6 CONCLUSION

In the previous chapters the application of the Discrete Element Method to the study of the seismic vulnerability of historical structures has been proposed and verified. It was observed that for masonry structures without mortar, such as opus quadratum constructions, or structures made by few large blocks such as the megalithic constructions, the DEM allows a more realistic modeling than competing methods based on equivalent continuum models. However, certain discrepancies were observed when comparing the DE predictions with experimental results, as summarized in section 7.1. Referring to the study of walls subjected to quasistatic in-plane loading the main observed limitations of the DEM were: (a) a systematic overestimation of the maximum lateral load; (b) the failure to predict progressive internal displacements before collapse; (c) the failure to predict a localization of sliding in narrow diagonal bands.

Based on the observation of the experimental response of walls subjected to out-of-plane loading (as described in sections 7.2.1 and 7.2.2) it appeared that, as the lateral load increased, small relative rotations between blocks were occurring at the joints due to geometric irregularities of the contact surfaces. An hypothesis was made that such behavior, not accounted for in existing DE formulations, would play an important role in overcoming the observed discrepancies.

Consequently, a new joint model was developed for including the possibility of relative microrotations between blocks due to contact non coplanarity. It is reminded that in the DEM a linear joint is represented by two contact points placed at its ends, and that at each contact point there are two interaction stiffness elements K_n and K_t , in the normal and tangential direction respectively, which represent in a lumped form the material behavior of the joint. The essential concept of the new joint formulation (described in detail in sections 7.2 and 7.3) consists in allowing microrotations to take place by assigning a plastic behavior to one of the two normal stiffness K_n when the conditions for rotation are met. This formulation is similar, in a sense, to the standard DE modeling of Coulomb friction, where relative tangential displacements are obtained by

assigning a plastic behavior to the tangential stiffness K_t when the conditions for sliding are met.

For calibrating the parameters of the non coplanar joint model for a given type of blocks, a simple procedure was proposed. It requires the availability of the experimental failure load λ and the maximum top displacement δ_{top} of a column constituted by such blocks when subjected to gravity and slowly increasing lateral load. After performing a series of DE simulations with various values of joint parameters, such parameters are selected by minimizing the distance between numerical and experimental results in the $\lambda - \delta_{top}$ plane. For calibrating the new joint model for the applications considered in this study, the experimental results related to a 14-block column have been used as described in section 7.4.1 and illustrated in Figure 7-40.

In order to evaluate the effectiveness of the proposed non coplanar joint model, three opus quadratum walls, for which experimental results were available, have been studied with the new model. The results obtained with both the planar and non coplanar joint model, as well as the experimental data, are summarized in Table 7-8.

	21-block case	110-block case	231-block case
λ_{exp}	0.50	0.55	0.35
λ_{nc}	0.54	0.55	0.38
λ_{pl}	0.60	0.60	0.46
$\lambda_{nc,disp}$	$0.78\lambda_{nc}$	$0.95\lambda_{nc}$	$0.89\lambda_{nc}$
Experimental failure mode	partial mode or mixed mode (Fig.7-62)	sliding from top layer down (Fig.7-65)	mixed (Fig.7-67) localized sliding band
Failure mode with non coplanar joint	partial mode (Fig.7-64) (initial mixed at $\lambda=0.48$)	sliding top layer followed by diffuse sliding (Fig.7-66)	mixed (Fig.7-72d) localized sliding band
Failure mode with planar joint	diffuse sliding (Fig.7-63a)	diffuse sliding	mixed (Fig.7-68) broad sliding band

Table 7-8. Summary of experimental and numerical results for 3 opus quadratum walls subjected to in-plane loading. λ_{exp} is the experimental failure load, λ_{nc} , λ_{pl} are the failure loads obtained with the new non coplanar and the planar joint models respectively. $\lambda_{nc,disp}$ is the load level corresponding to the initiation of internal displacements due to microrotations.

Such results confirms that the non coplanar joint model effectively contributes to overcome the observed limitations of the planar joint model. In fact the following comments can be made:

1. The failure load λ_{nc} obtained with the new model is more accurate than the one obtained with the planar joint model in all three cases, with a failure load reduction of 10% in the 21-block case, 8% in the 110-block case and 17% in the 231-block case;
2. The new joint model correctly predicts a process of progressive internal displacements before failure (initiating at load levels $\lambda_{nc,disp}$ given in Table 7-8) which was observed experimentally and was not described by the planar joint model;
3. The failure modes obtained with the new model for the 21-block case and the 110-block case are in better agreement with the experimental results than those obtained with the planar joint model;
4. The new joint model, due to microrotations and friction softening, correctly predicts, in the 231-block case, the formation of a localized sliding band as opposed to the broad sliding area obtained with the planar joint model.

In conclusion, it is important to underlie the remarkable sensitivity of the system response with respect to the size of the joint imperfections. In fact, for the walls studied in this chapter, the reduction of the failure load, due to a maximum joint aperture⁷ of only 0.1 mm, was quite significant, ranging from 8% to 20%. But the effect of joint imperfections became particularly substantial when we considered the case of a column with many blocks (section 7.4.2.1). For such case, the closed form expression which was derived for the failure load reduction (eq. 7-24), showed that, even with a relatively small imperfection, the lateral failure load rapidly goes to zero as the number of blocks increases⁸. Such result further confirmed that even apparently negligible joint

⁷ For the definition of maximum joint aperture see section 7.3.1 and Figure 7-11.

⁸ As an example, for the type of blocks used in the experimental models studied in this chapter, ($b=40\text{mm}$; $h=17.5\text{mm}$; maximum joint aperture $d=0.1\text{mm}$) - according to eq. 7-24 - a column of only 33 (or more) blocks is unstable even with a negligible lateral load (see section 7.4.2.1 for more details).

imperfections should not be ignored since they may cause significant modifications in the response of a block structure subjected to gravity and lateral loading.

Finally, among other aspects which require further work for improving the DE analysis of block structures, we should remind: the definition of a procedure, based on experimental tests, for the calibration of the friction softening parameters; and the extension of the non coplanar joint model to the three-dimensional case.

8. CONCLUSION

A review of current analysis methods for both the static and dynamic analysis of block structures has shown various limitations:

- Limit analysis [Baggio, C., 2000], in addition to being restricted to static equilibrium problems, can predict only the initial motion of the system, without being able to capture a subsequent stabilization of the structure and a possible different global failure mechanism for higher loads.
- Deformable contact models, such as specialized finite elements ("gap elements"), are not particularly suited for automatically detecting the activation and deactivation of a large number of contact surfaces during the evolution of the system response [Mamaghani, I., 1999].
- The method of finite elements with the smeared crack approach is limited by the impossibility of considering the effects of the layout of the bricks and of the presence of well defined lines of fracture within the structure.
- Specialized analytical formulations for predicting the dynamic behavior of multi-block systems are mainly restricted to predefined structural typologies such as the multi-block column or the trilite ([Manos, 1994], [Wilson, 1999]).

The Discrete Element Method, originally developed in the field of rock mechanics, appeared as a good candidate for overcoming some of the limitations of currently used methods, and its applicability to the seismic vulnerability assessment of historical block structures was investigated by performing a series of experimental and numerical tests both on the quasistatic and the dynamic response of block structures. For the quasistatic case (illustrated in Chapter 5) the objective has been the determination of the lateral failure loads and associated failure mechanisms of opus quadratum walls subjected to gravity and slowly increasing lateral load. It was concluded that DEM predictions are in good agreement with limit analysis results.

Based on this results two pilot studies (presented in the Appendices) have been performed with the quasistatic DE analysis, addressing, respectively, the out-of-plane and the in-plane behavior of opus quadratum walls.

In Appendix A the DEM has been applied to the study of the seismic vulnerability of a medieval church. Since such construction represents a class of numerous similar historical buildings it is expected that the approach adopted in this study may be useful for future similar investigations. With this application it has been demonstrated how the DEM can effectively account for structural details (such as the type of connections between a wooden beam and a masonry wall, or the out-of-plumb of a wall, or the exact number and size of the elements of a column) which may significantly affect the failure load of the system, and therefore how DEM may contribute to a more realistic modeling of a specific historical structure.

In Appendix B, it was illustrated how the DEM may also be employed for improving the understanding of the complex in-plane behavior of the opus quadratum wall. We focused our attention on the causes which may determine an undesired failure of the wall constituted by diffuse sliding and rotations of the blocks (as in Figure B-1e) as opposed to a collapse due to the monolithic rotation of a large portion of the wall (as in Figure B-2c) which is associated to a higher value of the lateral strength of the wall. Three aspects have been investigated: the aspect ratio (b/h) of the bricks, the loading condition, and the presence of an horizontal connection along the top portion of the wall. A parametric study which included 3 values of the aspect ratio ($b/h=1.0$; 2.3 ; 4.6), and 4 loading conditions, has been performed both numerically and experimentally. The following qualitative conclusions have been drawn:

1. The wall subjected to self weight only, fails - under increasing lateral load - by disgregation and cannot sustain the rigid body failure load unless it posses a high value of the aspect ratio (e.g $b/h = 4.6$ which indicates a good interlocking and therefore a good construction quality);

2. The presence of additional vertical load (due to floors, other walls or roof) tends to increase the wall capability of behaving as the rigid body model, and only poor quality walls (characterized by brick aspect ratio $b/h = 1$) still fail by disgregation;
3. The presence of an horizontal connection along the top portion of the wall (for example a rod acting in the plane of the wall) facilitates the rigid body response, which has been achieved even in the case of poor interlocking among bricks ($b/h=1$).

The two above mentioned studies have demonstrated the potentials of the DEM for both assessing the seismic vulnerability of specific historical building, and investigating fundamental aspects of the behavior of historical block structures, which cannot be addressed by other methods of analysis. In fact in comparing the numerical and experimental results, a good capability of DEM in predicting complex failure modes involving rotation and sliding of many blocks was observed. However, several discrepancies between the DEM results and the experimental response were observed:

1. The numerical predictions systematically overestimated the actual experimental failure load;
2. At failure, the sliding and rotations among blocks were generally localized in relatively narrow diagonal bands, on the contrary the numerical model predicted sliding and rotations over a wider area of the wall;
3. Micro-sliding progressively developed starting from 80% of the failure load, while in the numerical model the wall remained practically undeformed up to failure;
4. For the case of long and short walls with long blocks (where collapse occurred by sliding only) the failure load was 10% lower than the friction coefficient, whereas the numerical model did not predict this apparent shear strength reduction; and

5. In the case of the in-plane loading of the 21-block wall the failure mode was incorrectly predicted as pure sliding while in fact it was a mixed sliding and rotating mode.

For the dynamic case (illustrated in Chapter 6) an attempt has been made, in the context of the DEM, to model the internal material damping with a lumped viscous element acting at the interface between the blocks, and retaining a simple representation of the block interior. For the case of rocking of a slender block on a rigid base an empirical expression for the parameter of the viscous element has been obtained by minimizing errors of predicted restitution ratios with respect to “exact” values obtained with the Housner model. Good agreement with experimental results has been found for a range of slenderness ratios (from 2 to 5). Using the same parameter, acceptable agreement with experimental results has also been found for the case of harmonic base shaking of the single block. For a case of a multibody arch structure subjected to ground shaking the same viscous parameter obtained for the case of a single block has been assumed. A reasonable agreement was found with experimental results, however it was noted that for this particular case the system response was dominated by the rocking of the two columns, which, as previously reported, is well described by this model.

Based on the previous observations it appeared that the quasistatic approach was promising even if a number of discrepancies in the response prediction needed to be resolved. Since the problems identified in the quasistatic analyses will have an impact also on the dynamic case it was decided to approach them first.

As illustrated in Chapter 7, based on the observation of the experimental response of walls subjected to out-of-plane loading (as described in sections 7.2.1 and 7.2.2) it was recognized that, as the lateral load increased, small relative rotations between blocks were occurring at the joints due to geometric irregularities of the contact surfaces. An hypothesis was made that such behavior, not accounted for in existing DE formulations, would play an important role in overcoming the observed discrepancies.

Consequently, a new non coplanar joint model was developed for including the possibility of relative microrotations between blocks due to contact non coplanarity and for accounting for friction softening. In section 7.3 the implementation and verification are illustrated.

For calibrating the parameters of the non coplanar joint model for a given type of blocks, a simple procedure was proposed. It requires the availability of the experimental failure load λ and the maximum top displacement $\bar{\delta}_{top}$ of a column constituted by such blocks when subjected to gravity and slowly increasing lateral load. The calibrated joint parameters are obtained by minimizing the distance between numerical and experimental results in the $\lambda - \delta_{top}$ plane. For calibrating the new joint model for the applications considered in this study, the experimental results related to a 14-block column have been used as described in section 7.4.1 and illustrated in Figure 7-40.

In order to evaluate the effectiveness of the proposed non coplanar joint model, three opus quadratum walls (with respectively 21, 110, and 231 blocks), for which experimental results were available, have been studied with the new model. By comparing the results obtained with both the planar and non coplanar joint model, as well as the experimental data (see Table 7-8) it is confirmed that the non coplanar joint model effectively contributes to overcome the observed limitations of the planar joint model. To this respect the following comments can be made:

1. The failure load λ_{nc} obtained with the new model is more accurate than the one obtained with the planar joint model in all three cases, with an overestimation which is reduced from 20% to 8% in the 21-block case, from 9% to 0% in the 110-block case and from 31% to 8% in the 231-block case;
2. The new joint model correctly predicts a process of progressive internal displacements before failure which was observed experimentally and was not described by the planar joint model;

3. The failure modes obtained with the new model for the 21-block case and the 110-block case are in better agreement with the experimental results than those obtained with the planar joint model;
4. The new joint model, due to microrotations and friction softening, correctly predicts, in the 231-block case, the formation of a localized sliding band as opposed to the broad sliding area obtained with the planar joint model.

In conclusion, it is important to underline the remarkable sensitivity of the system response with respect to the size of the joint imperfections. In fact, for the 3 walls studied in chapter 7, the reduction of the failure load, due to a maximum joint aperture¹ of only 0.1 mm, was quite significant (up to 20%). But the effect of joint imperfections became particularly substantial when we considered the case of a column with many blocks (section 7.4.2.1). For such case, the closed form expression which was derived for the failure load reduction (eq. 7-24), showed that, even with a relatively small imperfection, the lateral failure load rapidly goes to zero as the number of blocks increases² determining a condition of intrinsic instability of the system. Such result further confirmed that even apparently negligible joint imperfections should not be ignored since they may cause significant modifications in the response of a block structure subjected to gravity and lateral loading.

¹ For the definition of maximum joint aperture see section 7.3.1 and Figure 7-11.

² As an example, for the type of blocks used in the experimental models studied chapter 7, (b=40mm; h=17.5mm; maximum joint aperture d=0.1mm) - according to eq. 7-24 - a column of only 33 (or more) blocks is unstable even with a negligible lateral load (see section 7.4.2.1 for more details).

9. RECOMMENDATIONS

Among other aspects which require further work for improving the DE analysis of block structures, we should remind:

- the investigation of the effects of the random variability of the model parameters on the system response;
- the definition of a procedure, based on experimental tests, for the calibration of the friction softening parameters;
- the refinement of the friction behavior of the model by accounting for the joint length, dilatancy, surface degradation, and the relative velocity of the blocks for the case of dynamic simulations; and
- the extension of the non coplanar joint model to the three-dimensional case.

Finally, it is recalled that in the dynamic modeling with DEM (chapter 6) a strong assumption was made in the representation of the damping at impact, and while it may be acceptable for single block structures or for certain types of multibody systems, additional work is needed for defining a more general interface dissipation mechanism.

Appendix A: OUT-OF-PLANE BEHAVIOR OF HISTORICAL MASONRY WALLS

A1. BACKGROUND

A2. THE OUT-OF-PLANE MODEL

A3. NUMERICAL ANALYSES

A4. DISCUSSION OF RESULTS

A5. CONCLUSIONS

A1. BACKGROUND

In the appendixes it will be illustrated how the DEM may be effectively applied to the study of the seismic vulnerability of historical structures constituted of blocks, or of masonry without (or with ineffective) mortar. As previously illustrated, in a masonry construction subjected to lateral forces, the walls may fail out of the plane (due to their slenderness and/or poor connection to the rest of the structure) or in the plane of the wall if the previous failure mode is prevented¹. In this section, the application of the DEM to the study of the out-of-plane failure of the main walls of a masonry church will be illustrated, while the case of in-plane failure of historical masonry walls will be addressed in Appendix B. The scope of the analyses will be limited to the determination of the lateral failure mechanism and corresponding failure loads in two dimensional DE models, with planar joints, and with quasistatic application of the lateral forces.

The determination of the out-of-plane failure load of a single wall which collapses by rigid body overturning is a simple task. However, if we consider the response to lateral loads of the entire structural system, constituted by the main walls (which are supposed to fail by out-of-plane overturning), and by the horizontal connecting elements like roofs and floors, then the failure mode² (and its associated failure load) is not easily predictable. Many different failure modes may take place depending from a variety of aspects including (a) the type of the interconnections, (b) the friction coefficients between

¹ These are the so called "first collapse mode", and "second collapse mode" respectively which were described in more detail in a previous section.

the various materials, and (c) the geometrical details, all of which can be accounted for with the DEM as it will be illustrated in the following study of a typical medieval church.

The church selected for this study is Santa Maria Maggiore in Tuscania³ (Figure A-1), which is situated in a moderately seismic active area. The reason for this choice is related to the architectural importance of the construction, and to the fact that many medieval churches possess similar layout, structural typology, and materials, and therefore it is hoped that certain aspects of this study may be of guidance in the evaluation of the seismic vulnerability of this typology of important historical constructions.

² see as an example the predicted failure mode shown in Figure A-15a

³ The church, consecrated in 1206, is a monument of Romanesque age that is of primary importance in Italy's architectural history.

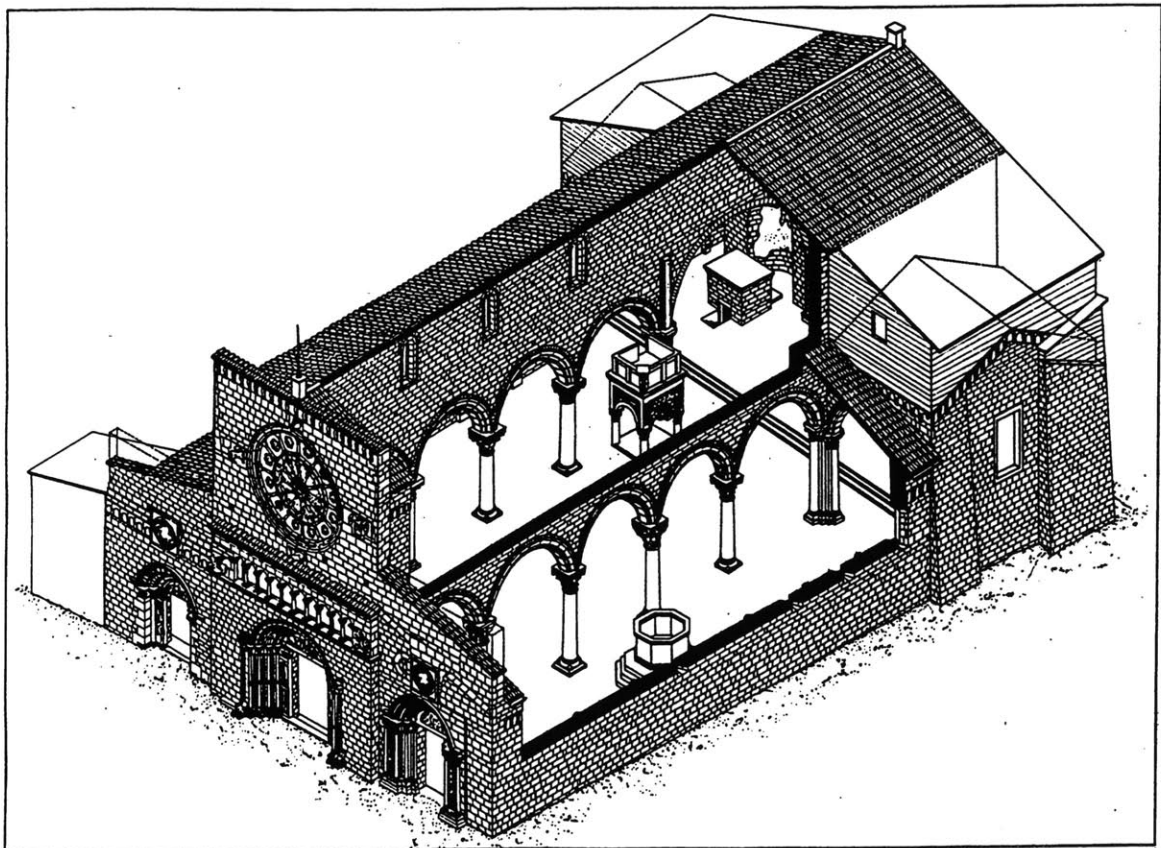
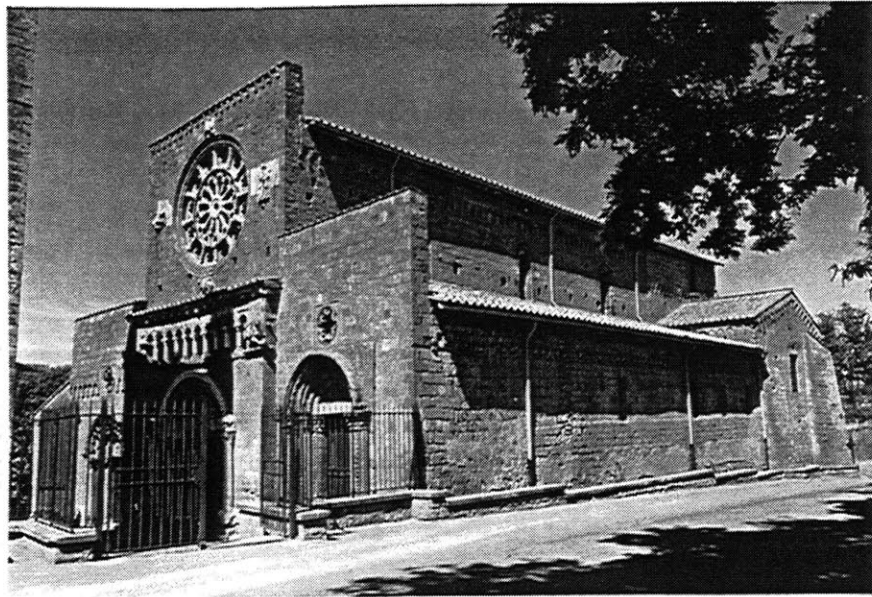


Figure A-1. Axonometric view of the church of S. M. Maggiore.

A2. THE OUT-OF-PLANE MODEL

Due to the practical difficulty in analyzing a 3D model of the entire construction, it is suggested that simpler 2D models of the structure are developed (if possible) with the objective of describing the most critical failure modes of the system. In this case it appears that the construction is most vulnerable when it is subjected to lateral forces acting in the transverse direction (orthogonal to the nave), causing an out-of-plane failure of the main longitudinal walls. Several reasons have led to this hypothesis:

- (a) the significant height and slenderness of the main walls;
- (b) the considerable distance between the structural elements resisting to transverse forces (front wall and transept); and
- (c) the poor structural connections between such elements and the longitudinal walls.

It is worthwhile to illustrate, in particular, the last point which is also the most critical. To this purpose it is necessary to briefly recall the history of the construction whose main phases, illustrated in the schematic layouts of Figures A-2, A-3 and A-4 have contributed to generate the weaknesses mentioned above. It should be noticed that practically all historical constructions are the results of several modifications occurred over the centuries, and therefore the study of the history of the construction with the objective of discovering structural problems in the contemporary configuration is an essential phase for the vulnerability study of any historical construction.

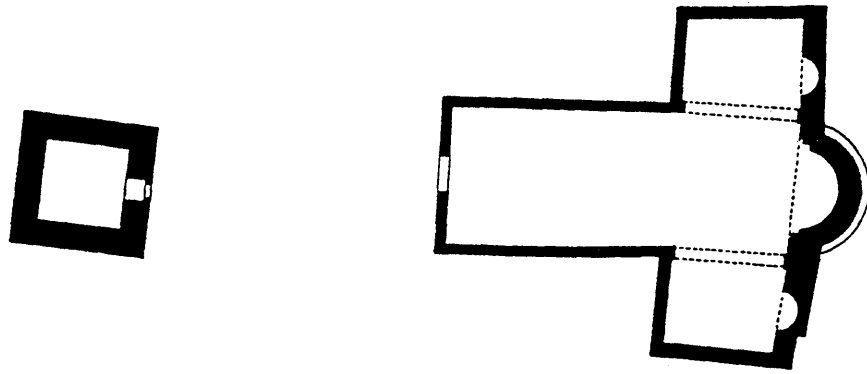


Figure A-2. Church of S. M. Maggiore, starting core (end of 11th, beginning of the 12th centuries).

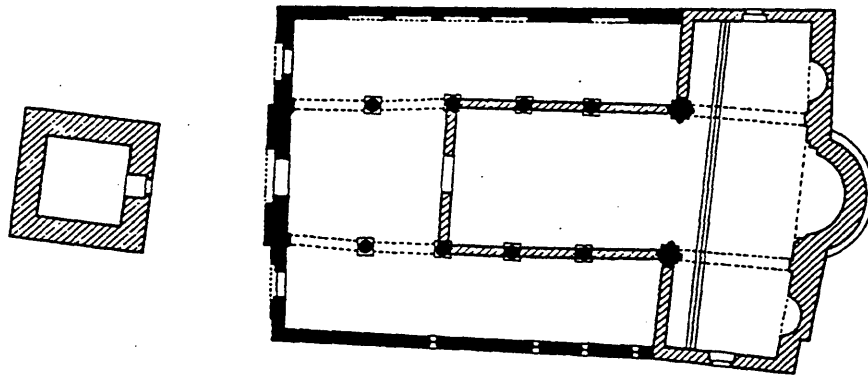


Figure A-3. Church of S. M. Maggiore, adoption of basilica plan (second half of 12th century).

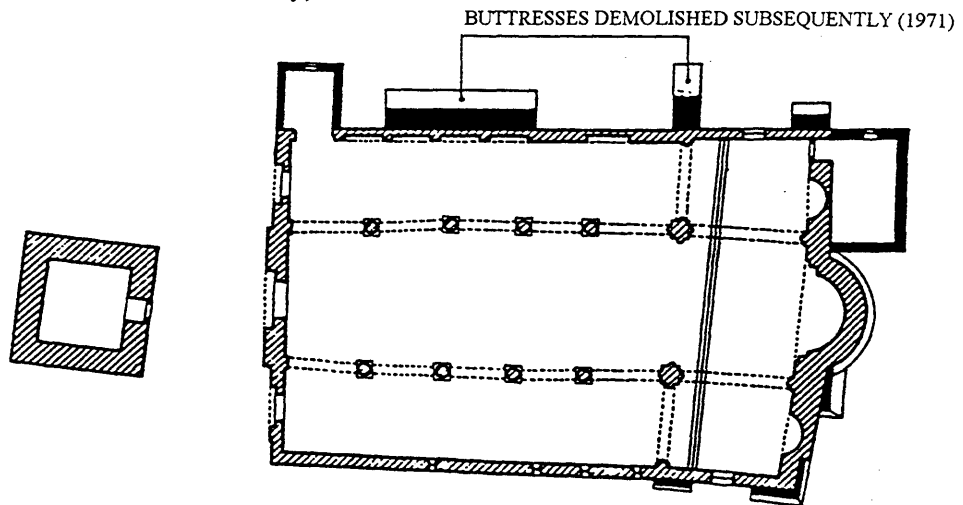


Figure A-4. Church of S. M. Maggiore, subsequent additions.

The original church was built between the end of the 11th and the start of the 12th centuries, and it adopted a nave with no aisles system with a three-apse projecting transept (Figure A-2). Of this first phase the current structure conserves the apse zone and the head ends of the transept, as is clearly seen from the typology of the masonry members.

During the second half of the twelfth century the building was almost totally redone, its plan being modified to form that of a basilica (Figure A-3). The aisles were added and these incorporate the projecting transept. The church was also lengthened with the addition of the first two arch spans.

During subsequent centuries it was redone a number of times, the most obvious of these efforts involving the first two spans (starting from the facade), which differ from the others both in their construction technique and in their decoration. The reason for this could be found in a collapse that occurred after an earthquake. Other interventions which occurred over the centuries have involved the modification of the transept roof and the raising of the aisle roofs, the addition of the body of the sacristy in the apse area and the addition of the chapel in the left aisle and of the numerous outside buttresses, added after structural impairments had been detected (Figure A-4).

Due to the various interventions mentioned above, and to the damages from past earthquakes it can be recognized that the central portion of the longitudinal walls, as

already anticipated, are not well connected with the rest of the structure. In fact we can observe:

- (a) a total lack of connection (scarfing) between the blocks of the two distinct portions of the tall walls of the nave at the height of the transept (Figure A-5) which were constructed in different phases;
- (b) a lack of scarfing on the same crosswise alignment, between the outside walls of the aisles and the transept headends also built at different times (Figure A-5);
- (c) vertical cracks in the masonry of both longitudinal central walls at the second column (starting from the facade) (Figure A-6), due to the different characteristics, both in the dimensions of the blocks and in the care taken in their workings, of the first two spans of masonry walls (probably rebuilt as a consequence of a past earthquake, as already noted).

Based on the previous considerations it appears that the central portion of the church is not effectively connected to the facade nor to the transept, therefore, in order to describe its most critical failure mechanism (when subjected to lateral forces), it is reasonable to consider a planar model representing a transverse "slice" of the church as indicated in Figure A-7.

It is of interest to note other details of the construction which influence its vulnerability to lateral forces, and which it was possible to include in the DE model. The first one is the out-of-plumb of the lateral wall on the left side of the church which is clearly seen in Figure A-8. It extends for about 10 meters and it has a maximum magnitude of 20 centimeters. The second one is related to the change in the connection

between the roofs of the lateral aisles and the central tall walls which was operated during a restoration in 1954 as shown in Figure A-9. The roofs were lowered (to bring them back to their original height), and the wooden beams, which before were inserted well inside the masonry, after the intervention were simply supported by small brackets, causing a drastic reduction of the horizontal forces which can be transferred from the roof to the wall. Another change operated in 1954 was the elimination of the lateral battresses.

It was found interesting to model both the configurations before and after the 1954 restoration, also to illustrate how the DEM may describe the effect of structural details, such as the ones mentioned above, on the failure mechanism and corresponding failure load. In Figure A-10 and A-11 the two DE models are shown.

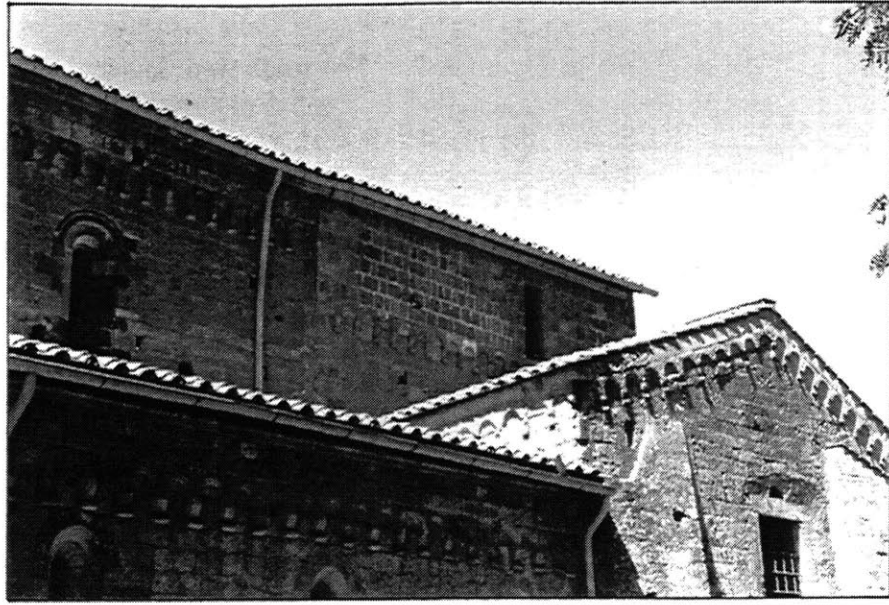


Figure A-5. Transept-nave discontinuity.

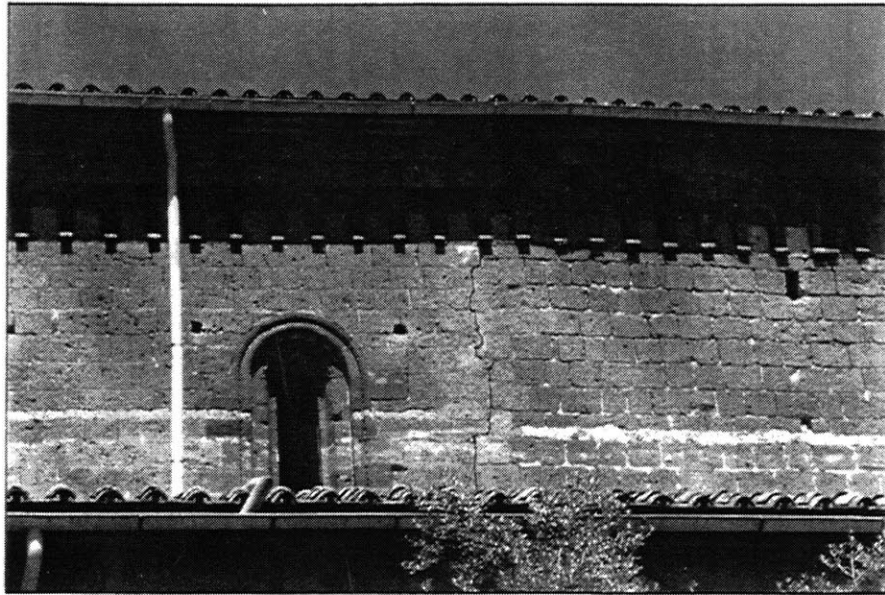


Figure A-6. Vertical cracks in the nave walls.

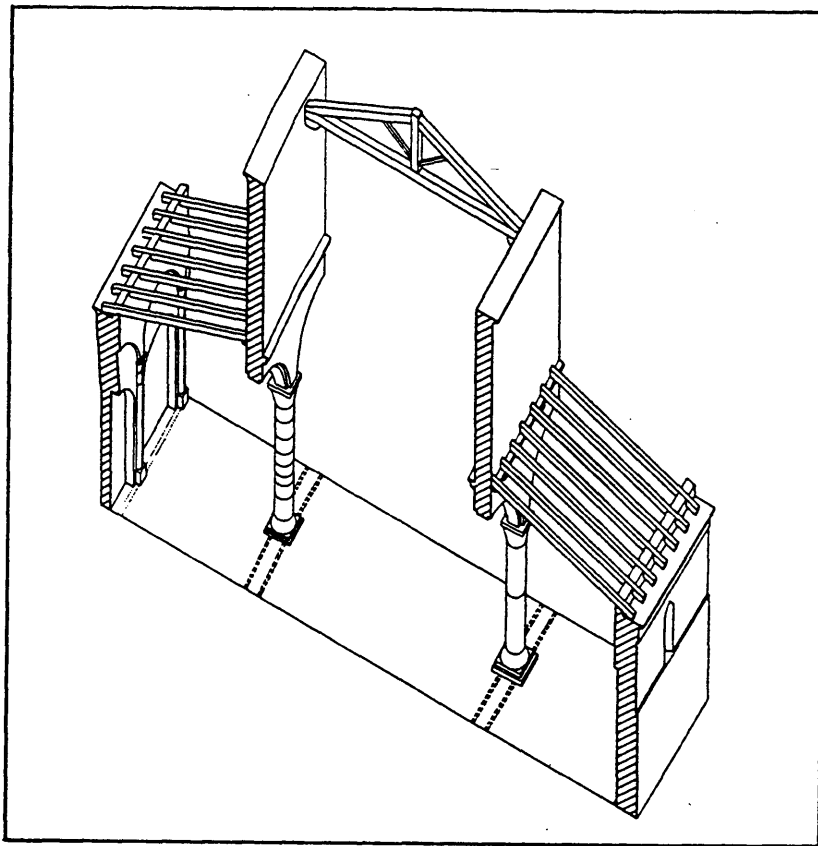


Figure A-7. Axonometric view of a transversal "slice" of the church of S. M. Maggiore, subjected to out-of-plane failure under lateral loads, and its corresponding Discrete Elements model with indication of distribution of weights and materials.

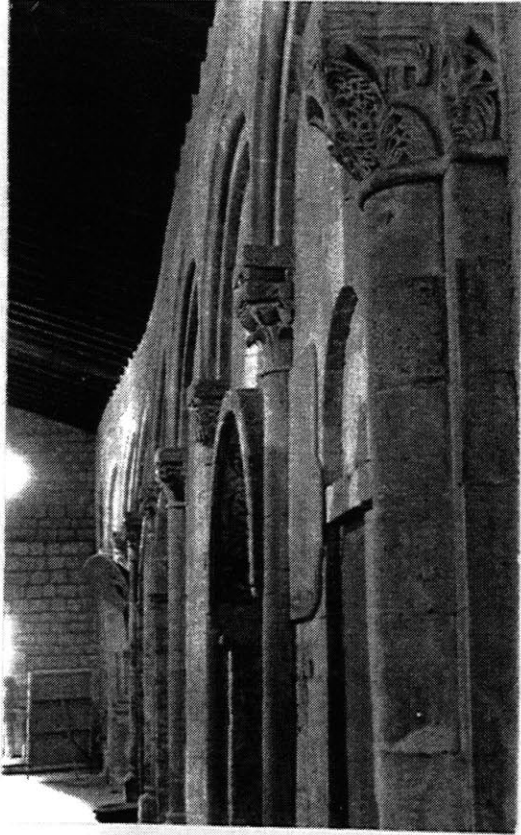


Figure A-8. Church of S. M. Maggiore, out-of-plumb of external left wall.

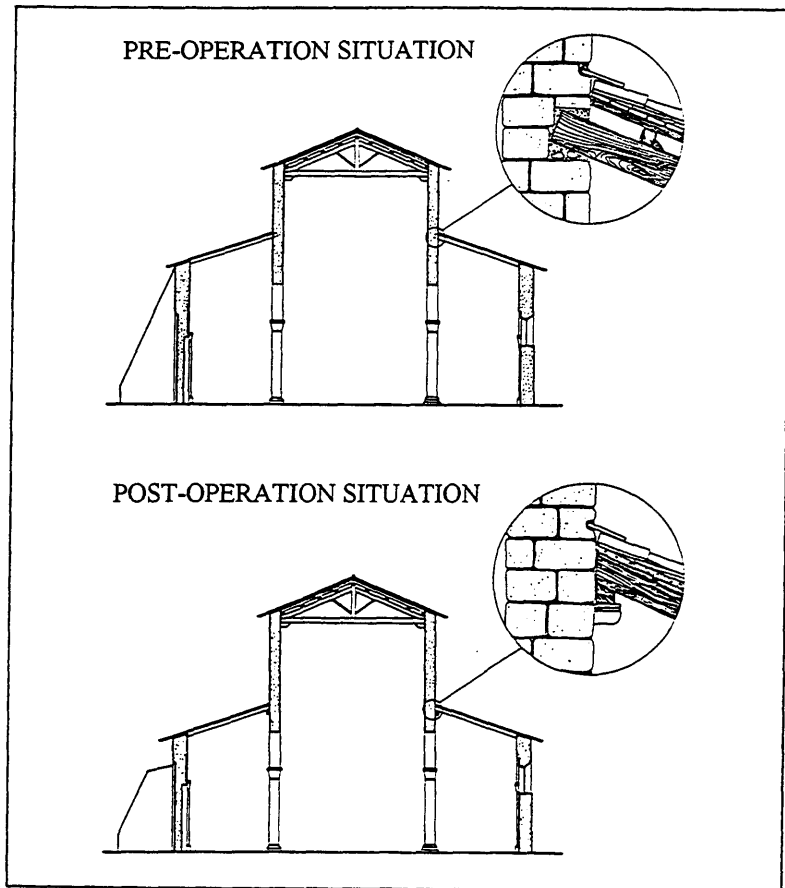


Figure A-9. Church of S. M. Maggiore, modification to the joint between the roof beams and the nave walls in 1954 restoration.

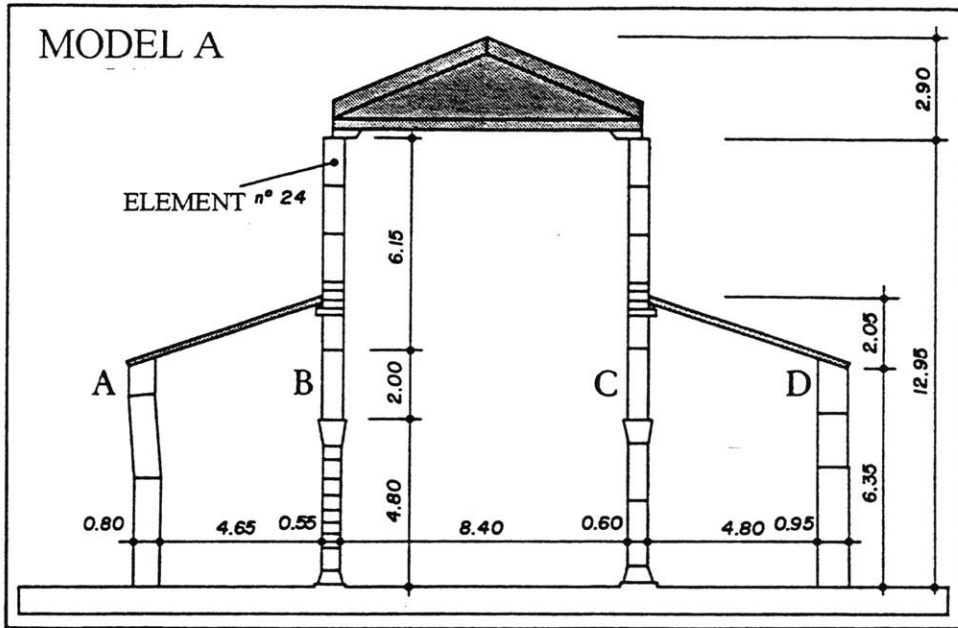


Figure A-10. Church of S. M. Maggiore, DE model of current configuration.

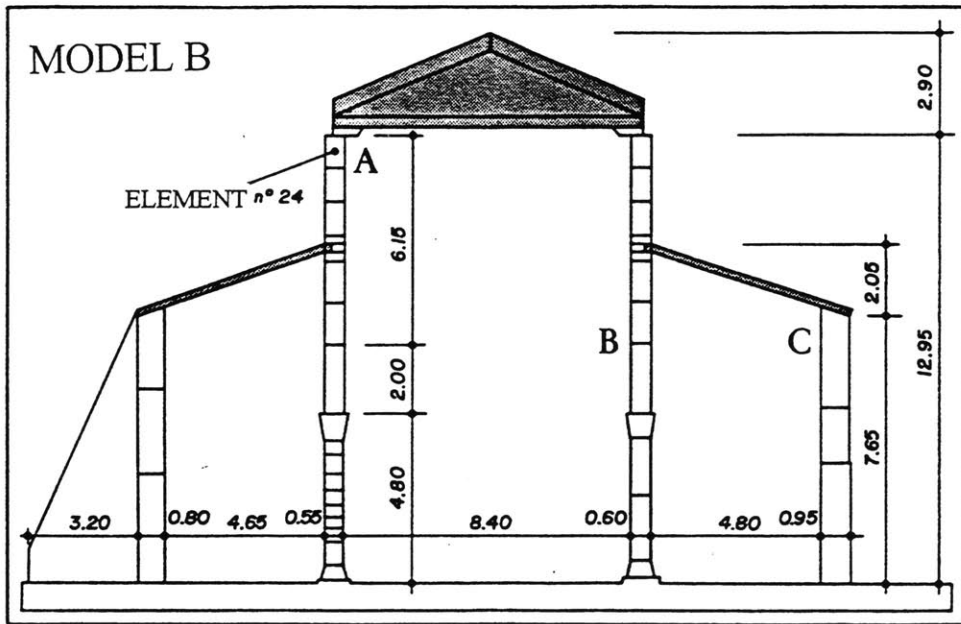


Figure A-11. Church of S. M. Maggiore, DE model of pre-1954 configuration.

A3. NUMERICAL ANALYSES

Two distinct configurations of the church of S. Maria Maggiore - as previously mentioned - have been taken into consideration: one regarding the current configuration (model A), and the other regarding the situation existing before 1954 (model B)⁴.

Model A (Figure A-10) is constituted by 48 elastic elements with four nodes, plus one rigid base element with 12 nodes, which is fixed in its initial position. Model B (Figure A-11) has one additional element representing the outside buttress, which before 1954 was still in existence.

The choice of adopting a simple elastic constitutive relationship for the material as opposed to a more complex one, it is quite inessential because, for this typology of structure, collapse is likely to occur for loss of equilibrium (at a relatively low stress level) rather than for internal material failure of the elements which may therefore be essentially treated as rigid bodies.

A substantial difference between the two configurations involves the morphology of the joint between the aisle roofs and the nave wall (as illustrated by Figure A-9), which was accounted for in the 2 DE models (compare Figures A-10 and A-11). Furthermore, in model A the out-of-plumb of the lateral wall on the left side was also taken into consideration (Figure A-10).

Where necessary, several elements were assembled to form "macroelements" which behave as single discrete elements with complex shapes; in Figures A-10, and A-11 the gray areas identifies the macroelements created.

In the DE model, the columns dividing the nave from the aisles have the same number of elements observed in reality. The walls instead have been modeled with a few blocks along their height in order to save computational resources, but at the same time to allow rotation to take place at various locations inside the wall (in addition to the most probable case of rotation around its base). Near the joint between the nave wall and the aisle roofs the height of the blocks was taken identical to that of the real tuff blocks in order to capture possible complex failure mechanisms involving block displacements in this area. Clearly, it would be possible to model each block of every portion of the walls as a separate DE element at the only cost of employing additional computational resources in the analyses, however, also based on the results which have been obtained, the level of detail which has been adopted here seems adequate for the scope of the study.

The materials are travertine for the right column (two drums), peperino stone for the left column (eight drums), chestnut wood for the roof members, and tuff for the masonry members. Table A-1 shows the elastic moduli and the densities used in the analysis as obtained from values reported in the literature.

⁴ The DE program used was DECICE, developed by Intera Technologies.

Material	Elastic modulus (kg/cm ²)	Density (kg/cm ²)
Tuff masonry	27,000	1700
Peperino stone	279,000	2112
Travertine marble	586,000	2420
Chestnut wood	110,000	650

Table A-1. Materials parameters.

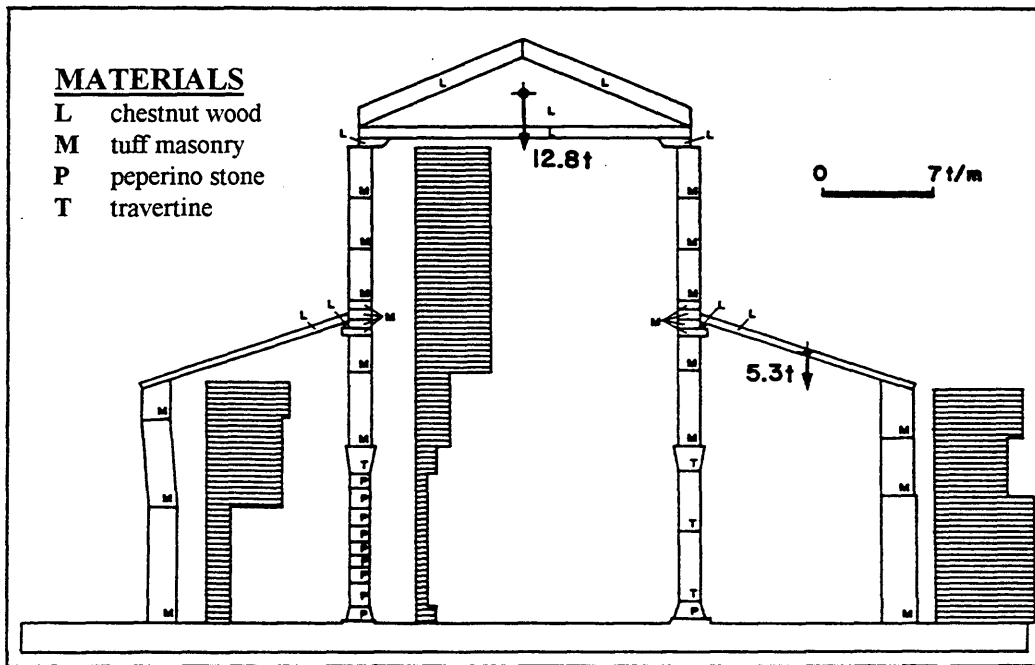


Figure A-12. Church of S. M. Maggiore: materials and distribution of weights in the Discrete Element model.

The blocks interact through a Coulomb friction mechanism; the friction coefficients used, also obtained from the literature, are: 0.45 for wood, 0.6 for the other materials, and 0.4 for the interaction between wood and other materials. Cohesion between the blocks was not introduced since the mortar was either absent or totally deteriorated.

The normal and tangential interaction stiffness between the blocks was chosen high (6×10^5 t/m), for the purpose of limiting the deformation in the joint relative to that inside the element. Considering, for example, one of the central walls it is observed that the contribution of the joints deformability to the vertical displacement of the top of the wall is less than 10%.

In order to illustrate in detail the typical loading procedure and corresponding system response we refer in the remaining of this section to the case of model A (current configuration) in which sliding between roof and walls was prevented with an high friction coefficient (see Figure A-15 b) as it will be explained in more detail in the next section.

According to the procedure illustrated in previous sections, the system was first subjected to gravity loads and to viscous forces, proportional to their mass, acting for the time necessary to damp the vibrations of the system. A damping of 0.3 of critical damping for a frequency of 20 Hz was used, this being the lowest frequency of the system subjected to gravity only. The response during this phase is given in Figure A-13,

in which it may be observed that the vertical oscillations of the top of the wall (element n. 24) disappear after 0.18 seconds of simulation.

Subsequently, each element was subjected to a stepwise increasing horizontal force up to the failure of the system. Again, at each step vibrations were damped out by viscous forces proportional to their masses. If N_i is the vertical gravity force acting on the centroid of element i , the lateral force applied at the same element is $F_i = \lambda N_i$, where λ is a function of time $\lambda = \lambda(t)$ common to all elements. It is, therefore, convenient to refer to λ as a normalized lateral load.

In Figure A-14, the dashed line indicates the increase with time of the lateral forces, $\lambda(t)$, while the continuous one shows the response of the structure in terms of horizontal displacements, $\Delta x(t)$, measured at the top of the wall (element n. 24). The first ramp brought the horizontal forces to 5% of the gravity load, causing a horizontal displacement of 0.54 cm of the top of the wall. The lateral forces were subsequently increased in smaller ramps until failure was reached for a failure load λ included in the range: 5.6 % to 5.7 %. Note that the last stable configuration (with $\lambda = 5.6\%$) showed only a minimal top displacement of 0.83 cm which is less than 0,06 % of the height of the wall.

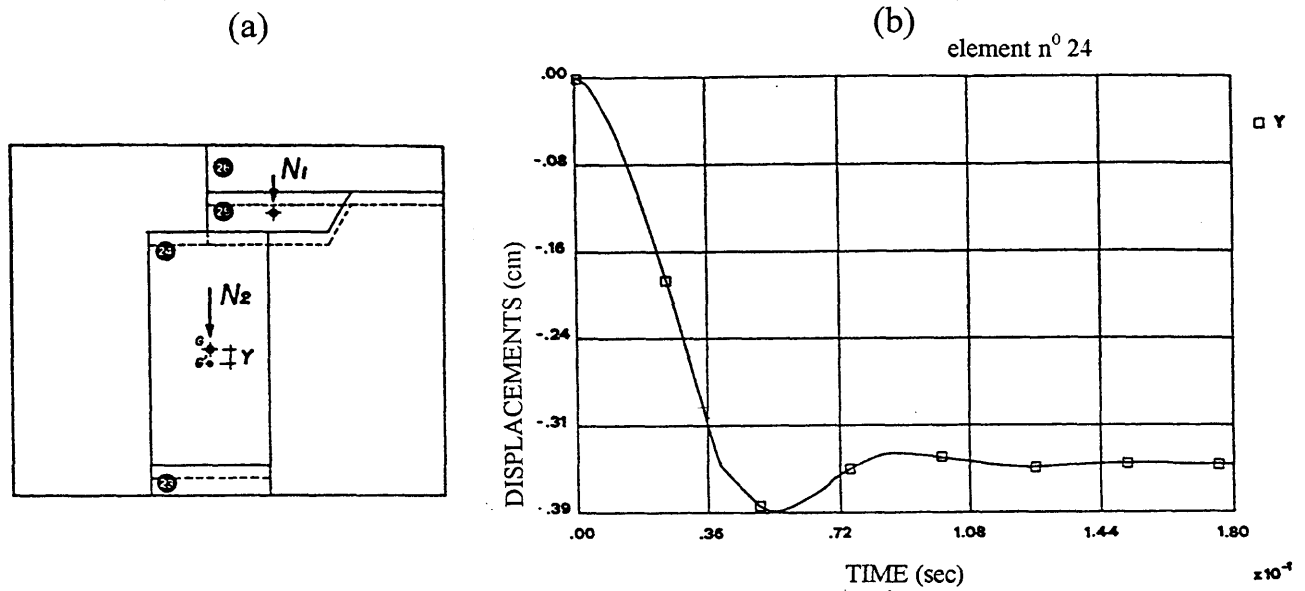


Figure A-13. (a) Detail of the top of the left central wall (element n° 24): dashed line indicates configuration after application of gravity load (note that displacements are magnified).
 (b) Time history of vertical displacement of element n° 24 during the application of gravity load.

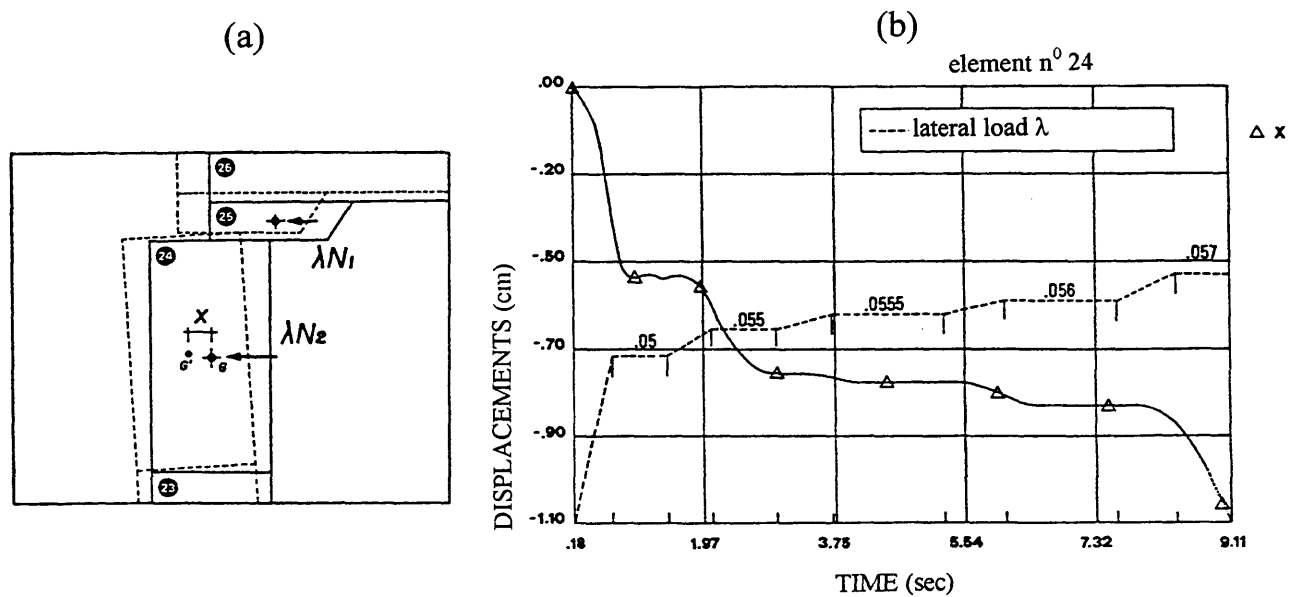


Figure A-14. (a) Detail of the top of the left central wall (element n° 24): dashed line indicates the configuration after application of lateral loads before failure (Note that displacements are magnified).
 (b) The solid line indicates the time history of horizontal displacement ΔX of element n° 24 caused by the application of lateral load λ . The dashed line indicates the time history of the applied lateral load λ .

A4. DISCUSSION OF RESULTS

The failure load λ for the case of the current configuration (model A) with the friction coefficient previously defined was found to lie between 3.7% and 3.8%. The failure mechanism is shown in Figure A-15a, while the failure loads for the various cases are presented in Table A-4. It can be observed a monolithic behavior of the central walls which rigidly rotate around the second element (from the bottom) of the columns (note that the first element has a larger base). It can also be observed how the friction coefficient between masonry and wood ($c=0.4$) was not adequate to prevent sliding of the aisle roof beams. As a consequence the roof of the left aisle slides over the lateral wall, while the right one disconnects from the support at the central wall. The certainly positive cooperation between the central and side walls thus fails, and the result of this is that the system failure load ($\lambda = 3.8\%$) is only slightly higher than that ($\lambda = 3.05\%$) of the individual high walls, considered as monolithic. Monolithic failure loads of individual walls (obtained from simple equilibrium considerations) are given in Tables A-2, and A-3.

It is therefore evident that the wall-roof connections (currently relying upon the rather uncertain wood-masonry friction coefficient) sensibly conditions the system behavior, and in a retrofitting intervention should certainly be improved.

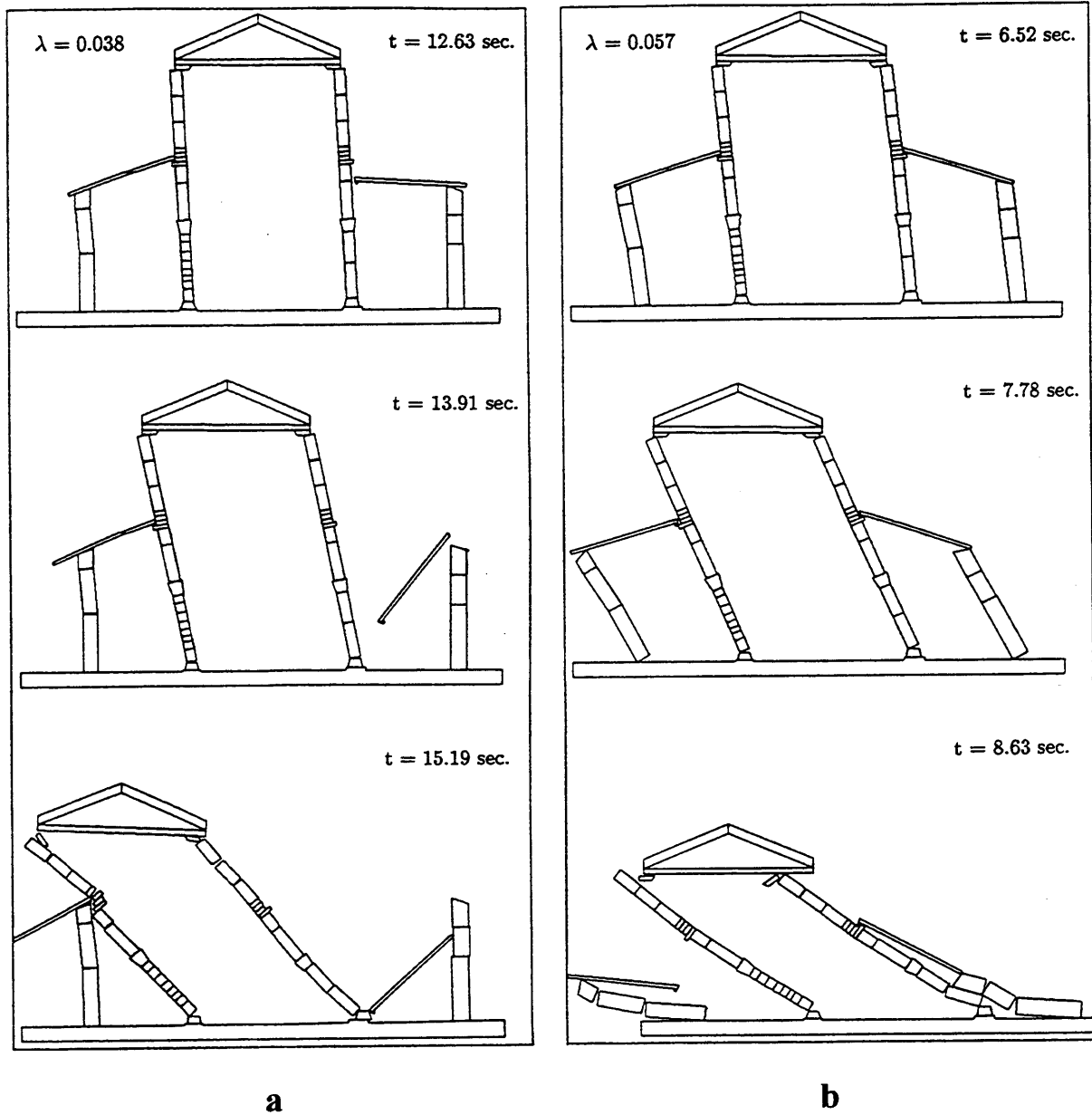


Figure A-15. Collapse mechanisms, and failure loads λ , for model A (current configuration) with two values of wood-masonry friction coefficient c : (a) $c = 0.4$; (b) $c = 10$.

Such considerations have suggested a second analysis, still using model A, but considering a fictitious high friction coefficient ($c = 10$), which would certainly be able to prevent the sliding that took place in the previous case, and simulating the effect of a retrofitting intervention aimed at creating a perfect lateral continuity between roof beams and walls.

The results show that with such modification the system behaves, at least in the first phase of the collapse, as an assembly of seven rigid bodies connected by hinges as illustrated in Figure A-15b. The collapse mechanism is substantially that of a one degree of freedom system, and the failure load increases up to $\lambda = 5.6\% - 5.7\%$. This is clearly due to the cooperation of the side walls which have an individual monolithic failure load of 6.2% and 13.9% respectively (the lower value corresponding to the out-of-plumb one).

A confirmation of the DE results is obtained by considering the one degree of freedom system (constituted by 7 bodies connected by hinges) and computing the corresponding failure load with the principle of virtual work which yielded a value of $\lambda = 5.5\%$, very close to the one obtained with the DE model.

It is also interesting to compare the previous results, referring to the current configuration, (model A) with those related to the configuration before the 1954 restoring (model B). The failure mechanism, for the last case, is illustrated in Figure A-16, where two differences may be observed. First, the effect of the buttress that, reaching up to the

roof, blocks the possible sliding of the beam⁵ and prevents a large portion of the central wall from rotating. Second, the fact that, due to the better connection between the roof beams and the central walls (see Figures A-9, A-10 and A-11), even with a wood-masonry friction coefficient of 0.4, the right roof beam does not disconnect from the wall, and causes the right lateral wall to participate in the failure mechanism. These differences have the effect of sensibly raising the failure load of the structure, which in this case is $\lambda = 7.3\% - 7.4\%$ (compared to $\lambda = 3.7\% - 3.8\%$ of the current configuration).

⁵ It is to be noted that this buttress was about nine meters long and thus covered a significant part of the church's left outside wall.

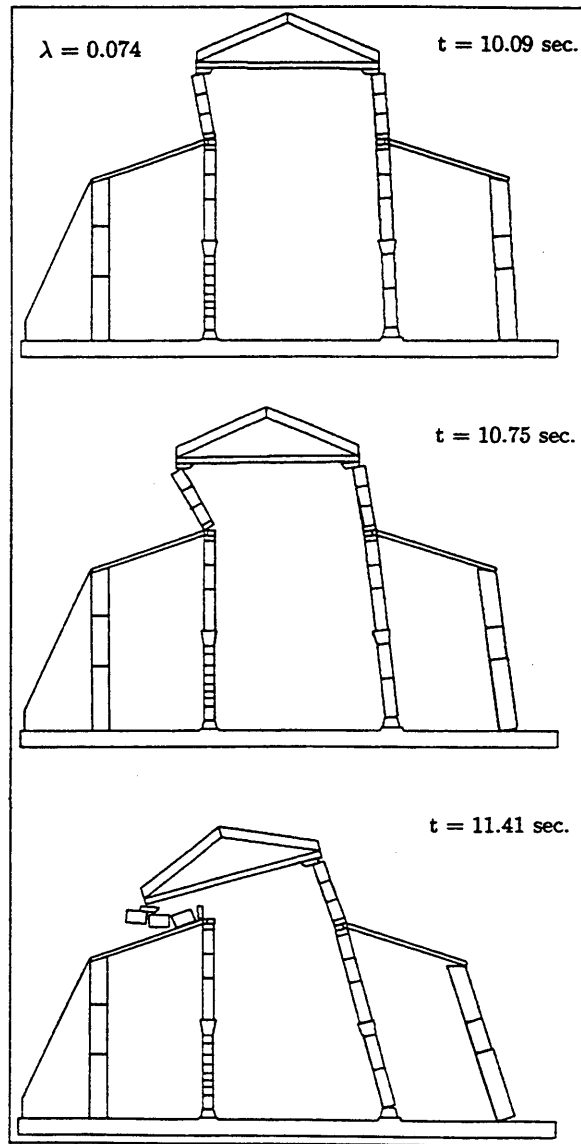


Figure A-16. Collapse mechanisms, and failure loads λ , for model B (pre-1954 configuration).

A5. CONCLUSIONS

In this section the practical application of DEM, as an innovative analysis method for the study of the seismic vulnerability of a medieval church, has been presented. Since such construction represents a class of numerous similar historical buildings it is hoped that the approach adopted in this study may be useful for future similar investigations.

The objective of the study has been the investigation of the response of the structure when subjected to lateral forces acting in the direction perpendicular to the main longitudinal walls, and therefore determining an out-of-plane failure of such walls. Care has been taken to illustrate when, - on the base of the structural features, the history of the construction, and the survey of damages occurred in past earthquakes - this simple two-dimensional out-of-plane model of the masonry construction may be employed.

Finally it has been demonstrated how the DEM can effectively account for structural details (such as the type of connections between a wooden beam and a masonry wall, or the out-of-plumb of a wall, or the exact number and size of the elements of a column) which may significantly affect the failure load of the system, and therefore how DEM may contribute to a more realistic modeling of historical buildings.

After having applied the DEM to the study of the *out-of-plane* behavior of historical masonry walls, in the next section (Appendix B), it will be illustrated how the

DEM may also be effectively employed for improving the understanding of fundamental aspects of the more complex *in-plane* behavior of this structural typology.

Walls	A	B	C	D
$\lambda\%$	6.2	3.05	3.4	13.9

Table A-2. Model A (current configuration): failure loads of individual walls rotating as simple rigid bodies (see wall labels in Figure A-10)

Walls	A	B	C
$\lambda\%$	16.5	3.2	11.5

Table A-3. Model B (pre-1954 configuration): failure loads of individual walls rotating as simple rigid bodies (see wall labels in Figure A-11)

Models	Failure load $\lambda\%$
Model A - Current configuration	3.7÷3.8
Model A - Current configuration (with higher friction)	5.6÷5.7
Model B - Pre-1954 configuration	7.3÷7.4

Table A-4. DEM failure loads of various models of the church of S. M. Maggiore.

Appendix B: IN-PLANE BEHAVIOR OF HISTORICAL MASONRY WALLS

B1. BACKGROUND

B2. EXPERIMENTAL INVESTIGATION

B3. NUMERICAL ANALYSIS

B4. DISCUSSION OF RESULTS

B5. CONCLUSION

B. IN-PLANE BEHAVIOR OF HISTORICAL MASONRY WALLS

In this section we illustrate the application of the DEM to the study of the in-plane failure of the *opus quadratum* wall¹ (a wall made of regular squared blocks without mortar). More specifically we focused our attention on the causes which may determine an undesired failure of the wall constituted by diffuse sliding and rotations of the blocks (as in Figure B-1e) as opposed to a collapse due to the monolithic rotation of a large portion of the wall (as in Figure B-2c) which is associated to a higher value of the lateral strength of the wall. Furthermore, it is suggested that the results obtained from the parametric study of the *opus quadratum* wall may be - qualitatively - extended to the more complex case of the irregular stone wall.

This study is proposed for both the interest of the specific problem, and for illustrating how the DEM can be employed for gaining a better understanding of a variety of fundamental aspects of the seismic response of historical constructions which cannot be approached with conventional analysis methods.

B1. BACKGROUND

The first concern in the seismic retrofitting of historical masonry buildings is to provide an adequate connection between orthogonal walls in order to prevent the out-of-plane overturning of the walls when struck by a lateral seismic force. However, when adequate provisions are taken to prevent the previous collapse mode, the seismic

¹ See Chapter 2, page 2-4, for a description of the *opus quadratum* wall.

vulnerability of the building depends on the in-plane behavior of the walls parallel to the direction of the earthquake. Numerous studies - both analytical, such as [Mann, W., 1982; Page, A., 1981, 1982, 1983], and experimental as in [Anthoine, A., 1991; Ganz, H., 1989; Hamid, A., 1981] - have been devoted to this subject. Most of the methods currently used for the assessment of the in-plane strength of a masonry wall are based on the hypothesis of a continuous medium and consists, at various levels of detail, in (a) evaluating the stress state inside the wall, and (b) applying a material failure criteria usually based either on maximum shear stress or maximum principal tensile stress. This approach, while reasonable for the case of regular brick masonry with effective mortar, it appears inappropriate for the irregular stone masonry without, or with scarcely effective mortar as found in many Italian historical urban centers (Figure B-4).

From the observation of the damages suffered in past earthquakes it appears that a certain class of buildings found in several small historical urban centers in Italy do not collapse due to extensive material failure, but rather for loss of equilibrium and overturning of entire walls or large portions of them. For such rigid body behavior, a lateral failure load - for any given collapse mechanism - can be easily determined based only on system geometry and equilibrium considerations. If this rigid body behavior could be assumed, the vulnerability assessment, based on the comparison between the lowest failure load and a given seismic action for the site, would therefore be extremely simplified and would not require a stress analysis and material modeling. It is clearly very important to identify the conditions under which the previous hypothesis may be valid. To this respect some work has already been conducted concerning the out-of-plane

behavior [Ceradini, V., 1992], however, for the in-plane behavior whether and under which circumstances the collapse may take place through overturning of large portions of the walls without substantial diffuse internal failure is still to be clarified and it will be part of the objective of this study.

B2. EXPERIMENTAL INVESTIGATION

The main objective of the experimental program has been the investigation of the influence of the type of arrangement of the bricks, and of the load distribution on the in-plane lateral failure load and corresponding failure mechanism of a regular brick wall without mortar. It was of particular interest to find out the conditions under which an assemblage of bricks, kept together by friction only, could fail - under lateral load - by separating into two monolithic parts instead of disgregating in many bricks sliding and rotating one respect to the other.

It has been used the experimental technique of the inclined plane previously presented (see Chapter 2). The same small scale bricks measuring 17.5 x 40 x 80 mm made of peperino have been assembled to build walls measuring 40 x 59.5 cm. The average value of the friction coefficient was 0.6. Two wall patterns have been tested:

- 1) with stretchers only (Figure B-1)
- 2) with headers only (Figure B-2).

In the first case the ratio of base over height of the brick (in the plane of the wall) was 4.6 and the wall was constituted by 187 bricks, in the second one the ratio was 2.3 and the

number of bricks was 357. The base over height ratio of the bricks is an important parameter since it determines the amount of overlapping and the degree of interlocking among bricks which provide both the capability of resisting horizontal forces (through friction) and the possibility of establishing a monolithic behavior under lateral loads.

Four load conditions have been considered: ..

- (A) self weight only (Figure B-1a),
- (B) distributed vertical load on the upper base of the wall, applied with 5 separate loads (Figure B-1b),
- (C) like (B), but applied with 5 loads acting on a connecting beam (Figure B-2c),
- (D) like (C), but with a single off center load (Figure B-2d).

In condition (B) the load was applied on 5 steel bricks attached with mortar on the top course, for cases (C) and (D) the loads were applied on a metal beam also attached with mortar to the top course. Case (B) is representative of the typical situation of a wall carrying the load of the floor through wood beams inserted in the masonry, whereas the metal beam attached to the bricks used in cases (C) and (D) simulates an horizontal connection along the top portion of the wall (for example with a steel rod acting in the

plane of the wall) which could be adopted to prevent the separation of the bricks of the top course.

The test has been repeated with 3 different vertical loads of 250, 500, and 750 kg. By gradually inclining the testing table horizontal forces have been generated proportional to the masses of the wall and of the top loads. The failure load was determined by measuring the inclination angle which determined the collapse of the wall. The small reduction of the vertical load component due to the rotation did not affect the results because of its negligible effect on the friction coefficient.

A total of ten different walls have been tested. The collapse mechanisms of representative cases are shown in Figure B-1 to Figure B-3, and the results - compared with the numerical analysis - are discussed in a following section.

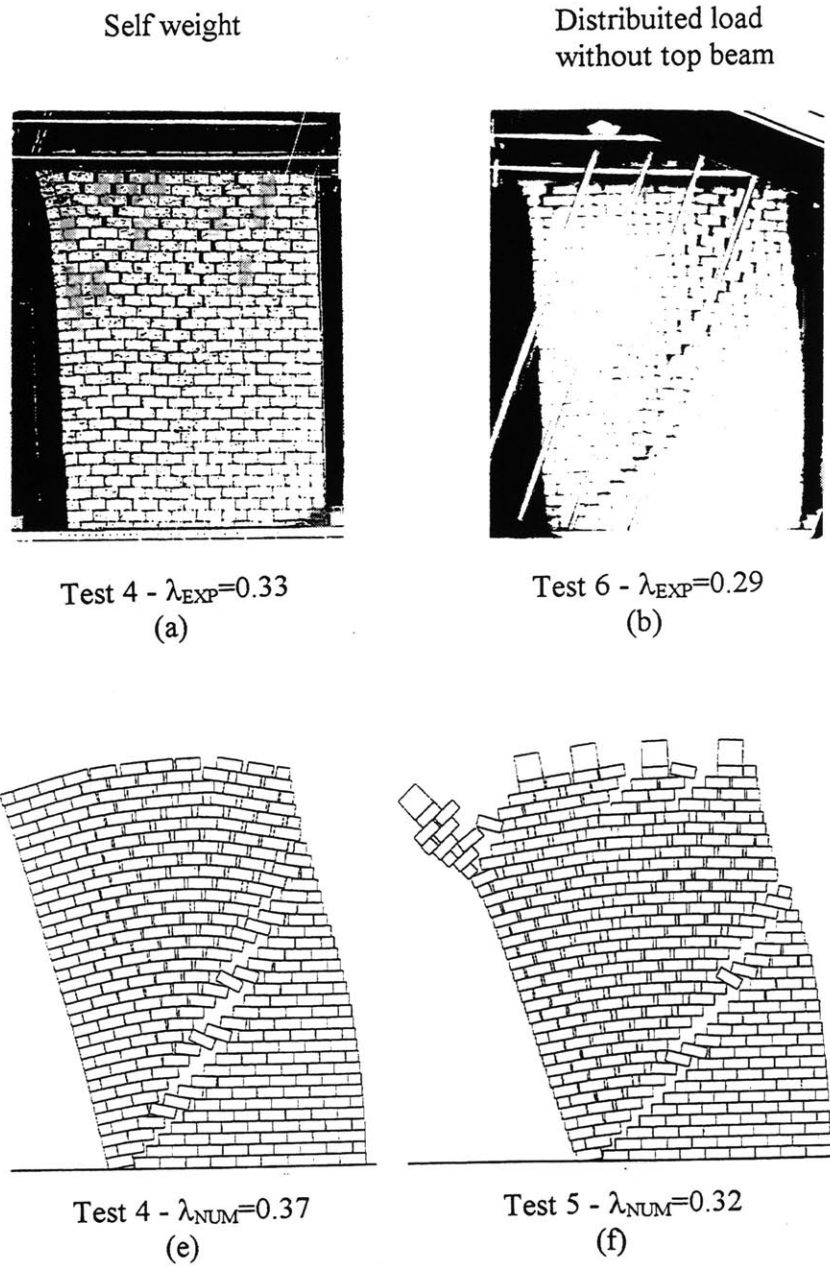
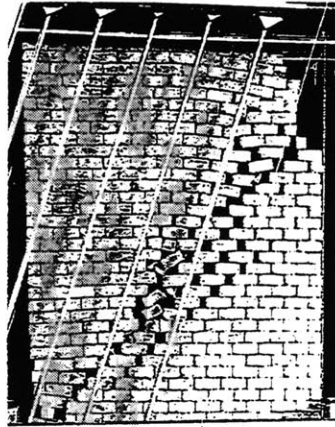


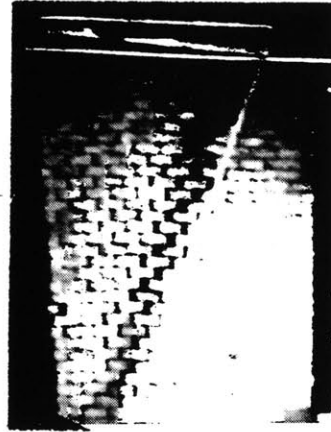
Figure B-1. Collapse mechanisms and failure loads λ for experimental and numerical models made with bricks with $b/h = 2.3$: cases of self weight and distributed load without top beam.

Distributed load
without top beam

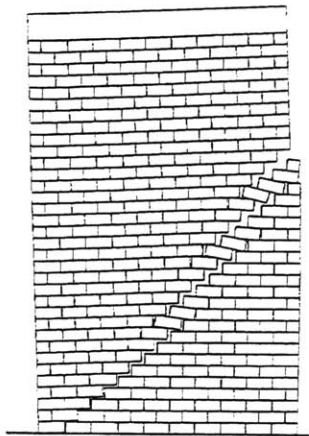


Test 9 - $\lambda_{EXP}=0.30$
(c)

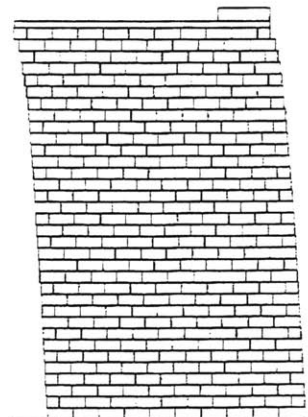
Eccentric load



Test 12 - $\lambda_{EXP}=0.44$
(d)



Test 8 - $\lambda_{NUM}=0.33$
(g)



Test 10 - $\lambda_{NUM}=0.50$
(h)

Figure B-2. Collapse mechanisms and failure loads λ for experimental and numerical models made with bricks with $b/h = 2.3$: cases of distributed load with top beam, and eccentric load.

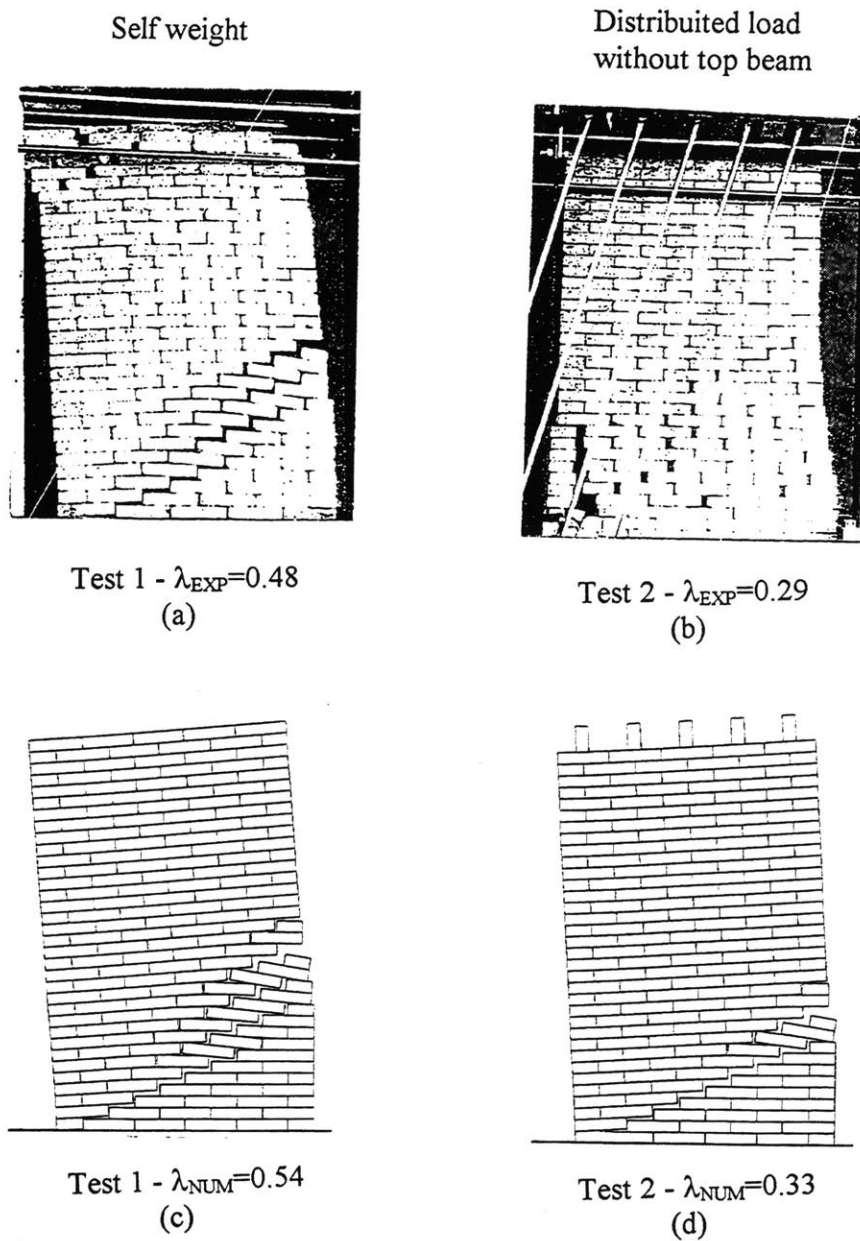


Figure B-3. Collapse mechanisms and failure loads λ for experimental and numerical models made with bricks with $b/h = 4.6$.

B3. NUMERICAL ANALYSIS

A conventional DEM procedure (without the irregular joint model) has been adopted for a detailed mechanical modeling and analysis of the previously described physical tests. Besides all experimental cases an additional brick ratio $b/h = 1$ has been analyzed. After some preliminary analyses, it was noticed that the intensity of the top load did not significantly affect the results, therefore, only one load intensity (250 kg) has been considered for each case in the numerical analyses².

Since the deformation of the single brick is negligible at the load level of the test, rigid elements have been selected, and the joints among bricks, according to the DEM, were modeled with a no tension normal spring and an elastoplastic tangential spring simulating a Coulomb's friction mechanism. The criterion for assigning the values of the interaction stiffness has been that of limiting the maximum horizontal displacement of the top course at failure to 0.5% of the height of the wall; it has been found that further increase of the stiffness would require more computing time with negligible increase in accuracy.

The friction coefficient value was set to 0.6 except in one case as it will be indicated later.

The external loads applied on the top course were simulated with the weight of elements with appropriate density with centroids located in the same position of the points of application of the weight in the physical experiment. The effect of the mortar

² This is explained by two facts: (a) the friction coefficient does not vary significantly in the range of loads which has been considered; (b) the weight of the wall is small with respect to the top load.

between the connecting beam and the bricks was simulated with a high friction coefficient. The loading sequence closely followed the experimental one: first gravity and then horizontal forces proportional to the mass of each element were applied step-by-step to the system up to failure. After each load step - before failure - static equilibrium was reached using an appropriate damping mechanism in order to stabilize any residual vibrations.

As it will be discussed in the next section, the analyses performed, in addition to providing a better insight on the interpretation of some experimental results, have given a further verification of the accuracy and reliability of the DEM simulation for masonry walls for systems with a significant number of elements (up to 357) and for various type of boundary conditions.

In addition to the discrete element analysis, a simple rigid body model of the wall has been studied to determine a failure load λ_{rig} , for each test case. The basic assumption of the model is that, under increasing lateral loads, the wall fails by separating into two monolithic portions along a line passing through the center of rotation, and, inclined of an angle α with respect to the base, where α is $\arctg(2h/b)$ (with h and b the brick height and base). Note that, except for the self-weight load condition, the failure load λ_{rig} is very close to that of the entire wall rotating rigidly. In the following section results from the rigid body model are compared with those obtained from both the physical experiments and the discrete element analysis.

B4. DISCUSSION OF RESULTS

Failure loads λ are presented, for walls with brick ratio $b/h = 4.6$, and $b/h = 2.3$, in Table B-1 and Table B-2 respectively. Results are organized by load condition, and load intensity. For each test the failure loads obtained from the discrete element model, λ_{num} , the experimental model, λ_{exp} , and the rigid body model, λ_{rig} , are presented. The ratio $\lambda_{\text{exp}}/\lambda_{\text{num}}$, with an average value of 0.89, indicates a reasonable agreement between experimental and numerical results except for a systematic overestimation of the failure load. As previously discussed the difference between the two sets of values is essentially due to the geometrical irregularities of the physical model, which have not been included in this discrete element analysis. The collapse mechanisms obtained experimentally and numerically are represented in Figure B-1, Figure B-2 and Figure B-3. Finally, in Figure B-4 the numerical results regarding two walls with brick ratio $b/h = 1$ are reported.

Considering the cases with brick ratio $b/h = 2.3$, the following comments can be made. In test 4, we notice that, if the wall is not loaded, it fails by disgregation and a large portion of the wall is interested by diffuse brick sliding and rotations (Figure B-1 a, B-1 e). This failure mode, although the experimental fractures appear more localized, is indicated by both the physical (Figure B-1 a) and the numerical model (Figure B-1 e). It appears that the wall cannot sustain the rigid body failure load $\lambda_{\text{rig}} = 0.49$ since an "internal failure" occurs earlier at $\lambda_{\text{num}} = 0.37$.

In test 6 it can be observed that by applying a distributed vertical load (without connecting beam), which is approximately 6 times the weight of the wall, the experimental collapse mechanism becomes closer to that of the rigid body model (Figure B-1 b).

Test number	Load condition	Load intensity (kg)	λ_{num}	λ_{exp}	λ_{rig}	$\lambda_{exp}/\lambda_{num}$
1	A	0	0.52÷0.54	0.48	0.54	0.88
2	B	250	0.32÷0.34	0.28	0.33	0.88
3		500		0.29		

Table B-1. Failure loads of walls with bricks ratio $b/h = 4.6$: discrete element model λ_{num} , experimental model λ_{exp} , rigid body model λ_{rig} .

The numerical mechanism (Figure B-1 f) is still affected by internal sliding, but since the failure load $\lambda_{num} = 0.32$ is very close to the rigid body one, $\lambda_{rig} = 0.33$, it may be considered a borderline case between the two types of collapse. In test 8, and 9, preventing the bricks of the top course to separate, determines a pure rigid body failure mechanism as it can be seen both in the experimental and numerical results (cases c and g in Figure B-2).

Test number	Load condition	Load intensity (kg)	λ_{num}	λ_{exp}	λ_{rig}	$\lambda_{exp}/\lambda_{num}$
4	A	0	0.37÷0.38	0.33	0.49	0.87
5	B	250	0.30÷0.33 (0.32)		0.33	0.90
6		500		0.29		
7		750		0.27		
8	C	250	0.32÷0.34		0.33	0.90
9		500		0.30		
10	D	250	0.49÷0.51 ($tg\phi = 0.50$)		0.57	
11			0.56÷0.58 ($tg\phi = 0.65$)			
12		500		0.44		
13				0.39		
14			750		0.44	

Table B-2. Failure loads of walls with bricks with $b/h = 2.3$: discrete element model λ_{num} , experimental model λ_{exp} , rigid body model λ_{rig} .

In Figure B-3 the results concerning walls with bricks ratio $b/h = 4.6$ are shown. In both the self weight load condition and the distributed load without connecting beam the wall fails in the rigid body mode with λ_{num} very close to λ_{rig} . Note the failure of the bricks (case b in Figure B-3) occurring at the beginning of the collapse mechanism in the bottom left portion of the wall. Load conditions C and D were not tested since a rigid body failure mode was certainly expected.

Finally, Figure B-4 shows that the wall with brick ratio $b/h = 1$ collapses much earlier ($\lambda_{\text{num}} = 0.22$) than the rigid body failure load when subjected to distributed load without connecting beam. However, if the top connection is provided (Figure B-4 b), the wall behaves according to the rigid body model and the failure load raises to $\lambda_{\text{num}} = \lambda_{\text{rig}} = 0.32$.

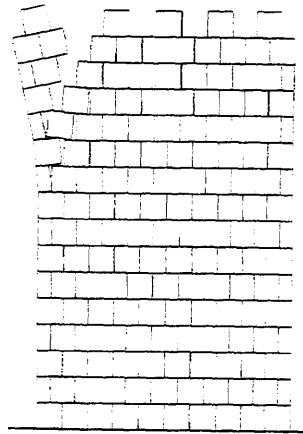
The eccentric load condition simulates the case of a wall between rigid floors which, under lateral loads, remain parallel and cause the load resultant to move towards the edge of the wall as this initiates to rotate. This case, even though it is not typical of the irregular stone masonry houses of the historical urban centers which are primarily considered here, it has been included because it resembles a common testing technique of masonry walls. Due to the eccentricity of the top load, the rigid body failure load raises to $\lambda_{\text{rig}} = 0.57$. In this case the friction coefficient $\text{tg}\phi$, which was assumed 0.6 for all other cases, plays an important role, in fact, the discrete element analysis shows that if the friction coefficient $\text{tg}\phi$ is greater than λ_{rig} , a pure rigid body rotation failure mode takes place (with $\lambda_{\text{num}} = \lambda_{\text{rig}}$), whereas, a value of $\text{tg}\phi$ lower than λ_{rig} determines a pure distributed sliding failure mode (case h in Figure B-2) with $\lambda_{\text{num}} = \text{tg}\phi$ (see Table B-2: test 10 and 11). In the experimental tests it has been found an average value of the failure load $\lambda_{\text{exp}}=0.43$.

If we assumed a friction coefficient $\text{tg}\phi = 0.6$, the predicted failure load $\lambda_{\text{num}} = 0.57$, substantially overestimates the experimental one $\lambda_{\text{exp}}=0.43$. This could be

explained by the geometrical irregularities of the physical model, as in the other cases, but also by the presence of higher normal stresses on the horizontal joints of the compressed diagonal of the wall where a reduction of the friction coefficient³ may have initiated the collapse mechanism.

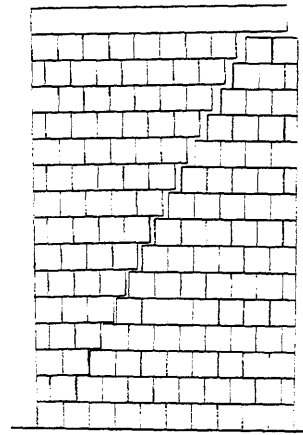
³ According to the Barton's law the friction coefficient decreases with increasing normal stress.

Distributed load
without top beam



$\lambda_{NUM}=0.22$
(a)

Distributed load
with top beam



$\lambda_{NUM}=0.32$
(b)

Figure B-4. Collapse mechanisms and failure loads λ for numerical models made with bricks with $b/h = 1$.

B5. CONCLUSION

The parametric study which has been conducted has provided some indications on the tendency of the *opus quadratum* wall to fail by rigid rotation of a large portion of the wall as opposed to diffuse sliding and rotation of bricks. Within the limits of the experimentation which has been performed, the following conclusions can be drawn:

- (1) the wall subjected to self weight only fails - under increasing lateral load - by disgregation and cannot sustain the rigid body failure load λ_{rig} unless it posses a very good construction quality (such as in the wall with bricks with $b/h = 4.6$);
- (2) the presence of additional vertical load (due to floors, other walls or roof) tends to increase the wall capability of behaving as the rigid body model, and only poor quality walls (with brick ratio $b/h = 1$) still fail for disgregation;
- (3) the presence of an horizontal connection along the top portion of the wall (for example with a rod acting in the plane of the wall) facilitates the rigid body response, which has been achieved even in the case of poor interlocking among bricks ($b/h=1$).

Finally, it is of interest to remind that the *opus quadratum* has been proposed as a qualitative model of the irregular stone masonry⁴, and, as suggested in Figure B-5, an analogy may be established between the quality of the irregular wall (intended as the

⁴ The irregular stone masonry without, or with scarcely effective mortar is found in many Italian historical centers.

degree of interlocking of the blocks) and the aspect ratio b/h of the bricks of the opus quadratum. In this light the previous results provide qualitative indications also for the irregular stone masonry, but additional experimental data and more complex numerical models are clearly needed for reaching conclusive recommendations in this case. Nevertheless these results are a first step toward a more realistic modeling of the historical masonry constructions which only an in-depth understanding of the ancient construction techniques coupled with an appropriate mechanical modeling of discontinuous media will allow.

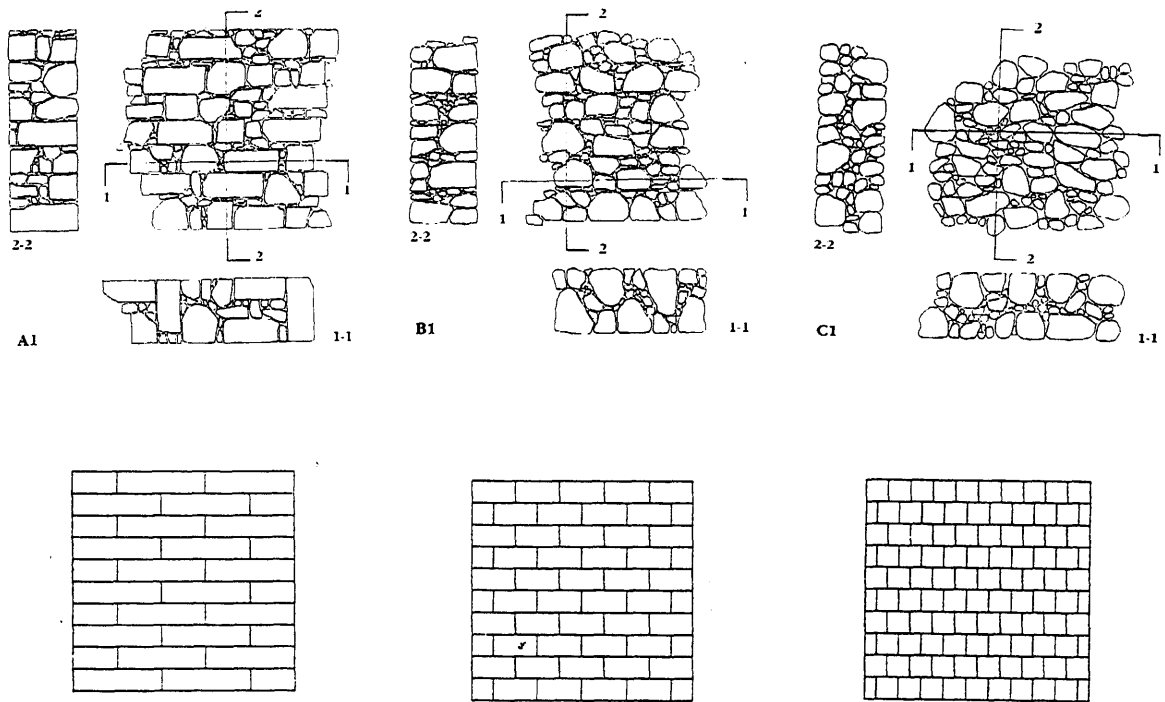


Figure B-5. Irregular stone masonry with good (A1), average (B1), and poor (C1) interlocking, and their corresponding opus quadratum models with brick ratio $b/h=4, 2,$ and $1.$

REFERENCES

[Abrams,D.P.,1994]

Abrams,D.P., Calvi, M.,eds., Proceedings of the US-Italy Workshop on Guidelines for Seismic Evaluation and Rehabilitation of Unreinforced Masonry Buildings;University of Pavia, Italy, June 22-24, 1994. National Center for Earthquake Engineering Research, State University of New York at Buffalo, July 1994.

[Adam, J.P.,1984]

Adam, J.P., 1984, *L' arte di costruire presso i romani*, Longanesi & C., Milan.

[Ageno, A.,1991]

Ageno, A., Sinopoli, A., 1991, Indagina teorica e sperimentale sul problema dell'urto fra blocchi rigidi, *Proceedings of the V Convegno Nazionale, L'Ingegneria Sismica in Italia*, Palermo, 1991.

[Allen, R.H.,1984]

Allen, R.H., Oppenheim, I.J., Bielak, J., 1984, Rigid body mechanism in structural dynamics, *Proceedings of the 8th World Conf. Earth. Eng.*, San Francisco, 1984.

[Allen, R.H.,1986]

Allen, R.H., Oppenheim, I.J., Parker, A.R., Bielak, J., 1986, "On the dynamic response of rigid body assemblies", *Earth. Eng. St. Dyn* 14.

[Andreaus, U.,1987]

Andreaus, U., Di Paolo, A., 1987, Analisi critica dei modelli per lo studio dinamico dei sistemi di conci a secco, *Proceedings of the III Conv. Naz. "L'Ingegneria Sismica in Italia"*, Rome, 1987:649-663.

[Andreaus, U.,1988]

Andreaus, U., 1988, A 3-D finite element model for the analysis of masonry structures, *Proceedings of the 8th IBrMac*, Dublin, 1988:1405-1416.

[Andreaus, U.,1988]

Andreaus, U., 1988, "Mechanical behaviour of block-work structures: a brief review of experimental results and phenomenological aspects", in *Omaggio a Giulio Cerradini*. (Dipartimento di Ingegneria Strutturale e Geotecnica, Università degli studi di Roma "La Sapienza", Rome) pp. 37-48.

[Andreaus, U.,1989]

Andreaus, U., 1989, A frictional model for sliding of jointed blocks, *Proceedings of the ICCLEM (Asia)*, Chongqing, China, 1989.

[Andreas, U.,1989]

Andreas, U., 1989, Analisi dinamica di blocchi lapidei su base attritiva, *Proceedings of the IV Conv. Naz. "L'Ingegneria Sismica in Italia"*, Milan, 1989.

[Andrews, D.,1982]

Andrews, D., 1982, "L'evoluzione della tecnica muraria nell'Alto Lazio", in *Quaderni di biblioteca e società*. (Viterbo), vol. 1-2, IV.

[Angeletti, P., 1994]

Angeletti, P., Cherubini, A., "Proposed method for assessing the vulnerability of historical masonry buildings: churches", Proceedings of the 10th European Conference on Earthquake Engineering; Vienna, Austria, September 1994, Duma,G., ed. A A Balkema, Rotterdam, 1995, volume 2, pages 977-980.

[Angotti, F.,1982]

Angotti, F., Toni, P., 1982, Oscillazioni non lineari di corpi rigidi su semi spazi elastici monolaterali, *Proceedings of the VI Congr. Naz. AIMETA*, Genova, 1982:134-143.

[Angotti, F.,1984]

Angotti, F., Chiostrini, S., Toni, P., 1984, Analisi dinamica e sismica di strutture a deformabilità limitata su suolo monolaterale, *Proceedings of the VII Congr. Naz. AIMETA*, Trieste, 1984:409-420.

[Angotti, F.,1985]

Angotti, F., Chiostrini, S., 1985, Oscillazioni libere e forzate di strutture rigide su suolo monolaterale, *Proceedings of the Convegno "Stato dell'arte in Italia sulla meccanica delle murature"*, Rome, 1985:615-613.

[Anthoine,A.,1991]

"In-plane behavior of masonry: a literature review"; Report EUR 13840 EN, Commission of the European Communities, JRC - ISPRA SITE, 1991

[Applied Technology Council, 1999]

Evaluation of Earthquake Damaged Concrete and Masonry Wall Buildings, Technical Resources. Prepared for The Partnership for Response and Recovery by The Applied Technology Council (ATC): Redwood City, California, 1999. 271 pages.

[Aslam, M.,1980]

Aslam, M., Godden, W.G., Scalise, T., 1980, "Earthquake rocking response of rigid bodies", J. of the Struct. Div., ASCE 106:ST2, 377-392.

[Augusti, G.,1988]

Augusti, G., Sinopoli, A., 1988, "Analisi di strutture costituite da blocchi lapidei", in *Omaggio a Giulio Cerradini*. (Dipartimento di Ingegneria Strutturale e Geotecnica, Università degli studi di Roma "La Sapienza", Rome) pp. 79-97.

[Augusti, G.,1992]

Augusti, G., Sinopoli, A., 1992, "Modelling the dynamics of large block structures", *Meccanica* 27:3, 195-211.

[Baggio, C.,1990]

Baggio, C., 1990, "Sullo studio del comportamento sismico delle strutture murarie: Risposta sismica di catene cinematiche di corpi rigidi" *Report 11* (Dipartimento di Ingegneria strutturale e geotecnica, Università di Roma "La Sapienza").

[Baggio, C.,1993]

Baggio, C., Trovalusci, P., 1993, "Discrete Models for Jointed Masonry Walls", Proc. of the 6th North American Masonry Conference, The Masonry Society, Philadelphia, Pennsylvania.

[Baggio, C.,2000]

✓ Baggio, C., Trovalusci, P., 2000, "Collapse behaviour of three-dimensional brick-block systems using non-linear programming", *Structural Engineering and Mechanics*, 10, 2, Aug.2000, pages 181-195.

[Baratta, M.,1901]

Baratta, M., 1901, *I terremoti d'Italia*, F.lli Bocca, Turin.

[Bartolucci, G.,1972]

Bartolucci, G., Camponeschi, B., Sonaglia, A., 1972, "Il terremoto di Tuscania", *Rassegna min LL.PP.* 5.

[Barton, N.R.,1978]

Barton, N.R., Choubey, V., 1978, "The shear strength of rock joints in theory and practice", *Rock Mech.* 10, 1-54.

[Bathe, K.J.,1982]

Bathe, K.J., 1982, *Finite element procedures in engineering analysis*, Prentice-Hall, New Jersey.

[Beer,1957]

Beer, Johnston, 1957, *Mechanics for Engineers*, McGraw-Hill Book Company.

[Blasi, C.,1984]

Blasi, C., Spinelli, P., 1984, Analisi dinamica di colonne formate da blocchi lapidei, *Proceedings of the II Conv. Naz. "L'Ingegneria Sismica in Italia"*, Rapallo, 1984:6.33-6.45.

[Blasi, C.,1986]

Blasi, C., Spinelli, P., 1986, "Un metodo di calcolo dinamico per sistemi formati da blocchi rigidi sovrapposti", *Ingegneria sismica* III:1, 12-21.

[Brebbia,C.,1991]

Brebbia, C A. , Dominguez, J., Escrig, F, eds., Proceedings of the Second International Conference on the Structural Repair and Maintenance of Historical Buildings, Seville, Spain,14-16, May 1991, Computational Mechanics Publications, Southampton, UK, 1991.

[Brookes, C. L., 1998]

Brookes, C. L.; Mehrkar-Asl, S., *Numerical modelling of masonry using discrete elements*, Seismic Design Practice into the Next Century: Research and Application, Proceedings of the Sixth SECED Conference, A. A. Balkema, Rotterdam, 1998, pages 131-137.

[Caleca, L., 1983]

Caleca, L., de Vecchi, A., 1983, *Tecnologie di consolidamento delle strutture murarie*, edizioni Dario Flaccovio, Palermo.

[Campanari, S., 1856]

Campanari, S., 1856, *Tuscania e i suoi monumenti*, Montefiascone.

[Carvalho, F.J., 1979]

Carvalho, F.J., "Adaptive control in the simulation of seismic actions", 1979, Thesis, LNEC, Lisbon.

[Ceradini, V., 1992]

Ceradini, V., "Modellazione e sperimentazione per lo studio della struttura muraria storica", 1992, Doctoral Thesis, Università di Roma "La Sapienza".

[Cigni, G., 1983]

Cigni, G., 1983, *Il consolidamento murario. Tecniche di intervento*, Kappa, Rome.

[CNR, 1985]

CNR - Progetto finalizzato Geodinamica, 1985, *Catalogo dei terremoti italiani dall'anno 1000 al 1980*, CNR, Bologna.

[Colomi, A.,]

Colomi, A., *Ricerca Operativa*, ed. clup, Milan.

[Colville, J., 1991]

Colville, J., and Samarasinghe, W., "Finite Element Model for Brick Masonry", 9th Int. Brick/Block Masonry Conf., Vol. 2, Berlin, pp. 726-734.

[Console, R., 1972]

Console, R., Sonaglia, A., 1972, "Studio del terremoto di Tuscania", *Annali di geofisica* XXV:3.

[Cundall, P.A., 1979]

Cundall, P.A., Strack, O.D., 1979, "A discrete numerical model for granular assemblies", *Gèotechnique* 29:1, 47-65.

[Cundall, P.A., 1988]

Cundall, P.A., 1988, "Formulation of a three-dimensional distinct element model - Part I: A scheme to detect and represent contacts in a system composed of many polyhedral blocks", *Int. J. Rock Mech. Sc. & Geomech. Abstr.* 25:3, 107-116.

[Cundall, P.A., 1988]

Cundall, P.A., 1988, "Formulation of a three-dimensional distinct element model - Part II:

Mechanical calculations for motion and interaction of a system composed of many polyhedral blocks”, *Int. J. Rock Mech. Sc. & Geomech. Abstr* 25:3, 117-125.

[Cundall, P.,1989]

Cundall, P., Hart, D., 1989, Numerical modeling of discontinua, *Proceedings of the 1st U. S. Conf. on Discrete Element Methods*, Golden, CO, 1989 (CSM Press).

[de Coulomb, C.A.,1776]

de Coulomb, C.A., 1776, “Essai sur une application de maximis et minimis à quelques problèmes de statique, relatifs à l'Architecture”, in *Mémoires de Mathématique et de Physique présentés à l'Académie Royale des Sciences, par divers Savans, et lus dans les Assemblées, Année 1773*. (Paris) pp. 343-382.

[Defez, A.,1982]

Defez, A., 1982, “Protezione dal rischio sismico dei beni culturali”, *Campo* 9/10.

[Den Hartog, J.P.,1931]

Den Hartog, J.P., 1931, “Forced vibrations with combined Coulomb and viscous friction”, *Trans. ASME* 53, 107-115.

[Drucker, D.C.,1954]

Drucker, D.C., 1954, “Coulomb friction, plasticity, and limit loads”, *Journal of Applied Mechanics*:March, 71-74.

[Duarte, R.T.,1992]

Duarte, R.T., Ritto-Correa, M., V., C.T., Campos-Costa, A., 1992, Shaking Table testing of Structures, *Proceedings of the 10th World Conf. Earthquake Engineering*, Madrid, Spain, 1992:6837-6846.

[Essawy, A.,1985]

Essawy, A., Drysdale, R., Mirza, F., 1985, “Nonlinear macroscopic finite element model for masonry walls”, in *New analysis techniques for structural masonry*, S. Anand, Ed. (ASCE, New York) pp. 19-45.

[Fardis and Buyukozturk, 1979]

Fardis, M., Buyukozturk, O., "Shear Transfer Model for Reinforced Concrete", *Journal of the Engineering Mechanics Division*, pp.255-275, ASCE, April, 1979.

[Franciosi, V.,1985]

Franciosi, V., Sinopoli, A., 1985, “Una introduzione alla stabilità e dinamica delle strutture in pietra monodimensionale”, in *Atti dell'Istituto di Scienza delle Costruzioni*. (Istituto Univers. di Architettura di Venezia,), vol. 75.

[Franciosi, V.,1986]

Franciosi, V., Sinopoli, A., 1986, “The stability degree of masonry structures: the earthquake as crisis parameter”, *Mechanics Research Communications* 13.

- [Ganz, H., 1989]
 Ganz, H., 1989, "Failure criteria for masonry", Proc. of the 5th Canadian Masonry Symposium; Vancouver.
- [Gavarini, G.,1991]
 Gavarini, G., 1991, *Ingegneria antisismica*, Editoriale ESA, Milan.
- [Ghaboussi, J.,1990]
 Ghaboussi, J., Barbosa, R., 1990, "Three-dimensional discrete element method for granular materials", *International Journal for Numerical and Analytical Methods in Geomechanics* 14, 451-472.
- [Giannini, R.,1984]
 Giannini, R., 1984, Analisi dinamica di sistemi di blocchi sovrapposti, *Proceedings of the 2nd Italian Conf. on Seismic Eng.*, Rapallo, 1984.
- [Giannini, R.,1985]
 Giannini, R., 1985, Considerazioni sulla modellazione numerica di sistemi di blocchi rigidi sovrapposti, *Proceedings of the Convegno "Stato dell'arte in Italia sulla meccanica delle murature"*, Rome, 1985:677-685.
- [Giannini, R.,1986]
 Giannini, R., Giuffrè, A., Masiani, R., 1986, La dinamica delle strutture composte di blocchi sovrapposti: studi in corso sulla Colonna Antonina, *Proceedings of the VIII Congr. Naz. AIMETA*, Turin, 1986:299-304.
- [Giannini, R.,1988]
 Giannini, R., Masiani, R., 1988, La dinamica delle oscillazioni dei blocchi rigidi, *Proceedings of the IX Congr. AIMETA*, Bari, 1988.
- [Giannini, R.,1989]
 Giannini, R., Masiani, R., 1989, Risposta subarmonica del blocco rigido, *Proceedings of the Conv. Naz. in ricordo di Riccardo Baldacci e Michele Capurso*, Rome, 1989.
- [Giannini, R.,1990]
 Giannini, R., Masiani, R., 1990, Risposta in frequenza del blocco rigido: stabilità delle soluzioni, *Proceedings of the X Congr. AIMETA*, Pisa, 1990.
- [Giannotti, F.,1969]
 Giannotti, F., 1969, *Storia di Tuscania scritta nel 1500*, Archivio Capitolare di Tuscania, Tuscania.
- [Giuffrè, A.,1988]
 Giuffrè, A., Ceradini, V., Jacovoni, F., Pugliano, A., 1988, "Centri storici in zona sismica. Analisi tipologico della danneggiabilità e tecniche di intervento conservativo. Casteltevete sul Calore" *Report 8* (Dipartimento di ingegneria strutturale e geotecnica, Università di Roma "La Sapienza").

[Giuffrè, A.,1988]

Giuffrè, A., 1988, *Monumenti e terremoti - aspetti statici del restauro*, Multigrafica editrice, Rome.

[Giuffrè, A.,1989]

Giuffrè, A., Baggio, C., Masiani, R., 1989, Dynamic Features of historical masonry, *Proceedings of the XV Regional Seminary on Earthquake Engineering*, Ravello, Italy, 1989:92-109.

[Giuffrè, A.,1990]

Giuffrè, A., 1990, *Lecture sulla meccanica delle murature storiche*, Rome.

[Giuffrè, A.,1994]

Actuality and modelling of historical masonry, Giuffrè, A., Carocci, C., De Felice, G., Tocci, C.; Proceedings of the US-Italy Workshop on Guidelines for Seismic Evaluation and Rehabilitation of Unreinforced Masonry Buildings; Abrams, D.P., Calvi, M., eds., University of Pavia, Italy, June 22-24, 1994. National Center for Earthquake Engineering Research, State University of New York at Buffalo, July 1994.

[Hamid, A., 1981]

Hamid, A., Drysdale, R.G., [7] - A. A. HAMID, R. G. DRYSDALE, "Proposed failure criteria for concrete block masonry under biaxial stress", *Journal of the Structural Division, ASCE*, 107(ST8), 1981

[Heyman, J.,1966]

Heyman, J., 1966, "The stone skeleton", *Int. J. Solids & Structures* 2:2, 249-279.

[Heyman, J.,1969]

Heyman, J., 1969, "The safety of masonry arches", *Int. J. Mech. Sci.* 11:4, 363-385.

[Heyman, J.,1982]

Heyman, J., 1982, "The masonry Arch", Chichester.

[Hocking, G.,1993]

Hocking, G., 1993, Collision Impact of a Ship with Multi-Year Sea Ice, *Proceedings of the 2nd Int. Conf. on Discrete Element Methods*, Boston, 1993 (M.I.T.):369-378.

[Hocking, G., Sulistijo B., 1993]

Hocking, G. and Sulistijo B., 1993, Progressive Failure Analysis of Rock Slopes, *Proceedings of the 2nd Int. Conf. on Discrete Element Methods*, Boston, 1993 (M.I.T.):489-497.

[Hogan, S.J.,1989]

Hogan, S.J., 1989, "On the dynamics of rigid block motion under harmonic forcing", *Proc. R. Soc. Lond.* A425, 441-476.

[Housner, G.W.,1963]

Housner, G.W., 1963, "The behaviour of inverted pendulum structures during earthquakes", *Bulletin of the Seismological society of America* 53:2, 403-417.

- [INTERA Technologies,1988]
INTERA Technologies, 1988, *DECICE Distinct Element Code: user's manual*, Denver, CO.
- [Ishiyama, Y.,1982]
Ishiyama, Y., 1982, "Motions of rigid bodies and criteria for overturning by earthquake excitations", *Earthquake Engr. and Struct. Dynamics* 10.
- [Jervis Pereira, J.,1977]
Jervis Pereira, J., Oliveira, C.S., Duarte, R.T., 1977, Direct and inverse conversion from power spectra to response spectra, *Proceedings of the 6th World Conf. on Earthquake Engrg*, New Delhi, India, 1977:279-285.
- [Jervis Pereira, J.,1984]
Jervis Pereira, J., Carvalhal, F.J., 1984, Adaptive control techniques for the simulation of seismic actions, *Proceedings of the Seminar on Design of Concrete Structures - The Use of Model Analysis*, London, 1984.
- [Ji-Cheng, G.,1984]
Ji-Cheng, G., Rice, J.R., Ruina, A.L., Tse, S.T., 1984, "Slip motion and stability of a single degree of freedom elastic system with rate and state dependent friction", *J. Mech. Phys. Solids* 32:3, 167-196.
- [Kelly,T.,1996]
Kelly, T. E., "Earthquake resistance of unreinforced masonry buildings", Pergamon, Elsevier Science Ltd.,Oxford, England, *Proceedings Eleventh World Conference on Earthquake Engineering* , 1996.
- Koh, A., Spanos, P.D., Roesset, J.M., 1986, "Harmonic rocking of rigid block on flexible foundation", *Journal of Engineering Mechanics* 112:11.
- [Koh, A.,1986]
Koh, A., Spanos, P.D., Roesset, J.M., 1986, "Harmonic rocking of rigid block on flexible foundation", *Journal of Engineering Mechanics* 112:11.
- [Levi-Civita,1927]
Levi-Civita, Amaldi, 1927, *Lezioni di meccanica razionale*, Zanichelli, Bologna.
- [Lipscombe, P.R.,1990]
Lipscombe, P.R., "Dynamics of rigid block structures", 1990, Doctoral Thesis, Cambridge.
- [Livesley, R.K.,1975]
Livesley, R.K., 1975, *Matrix Methods of Structural Analysis*, Pergamon, Oxford, ed. 2, vol..
- [Livesley, R.K.,1978]
Livesley, R.K., 1978, "Limit analysis of structures formed from rigid blocks", *Int. J. Num. Meth. Engng.* 12, 1853-1871.

[Livesley, R.K.,1992]

Livesley, R.K., 1992, "A computational model for the limit analysis of three-dimensional masonry structures", *Meccanica* 27:3, 161-172.

[Lo Bianco, M.,1984]

Lo Bianco, M., Mazzarella, C., 1984, Tecniche di delimitazione del carico di collasso delle strutture murarie, *Proceedings of the VII Congr. Naz. AIMETA*, Trieste, 1984:361-373.

[Lo Bianco, M.,1985]

Lo Bianco, M., Mazzarella, C., 1985, Sulla sicurezza sismica delle strutture in murature a blocchi, *Proceedings of the Convegno "Stato dell'arte in Italia sulla meccanica delle murature"*, Rome, 1985:577-596.

✓ [Mamaghani,I.,1999]

Mamaghani, I., Aydan,O.,Kajikawa,Y.,"Analysis of masonry structures under static and dynamic loading by discrete finite element method", *Structural Engineering/Earthquake Engineering*, 16, 2, Oct.1999, pag.75S-86S.

[Mann,W., 1982]

Mann,W., Muller,H., 1982,"Failure of shear-stressed masonry - An enlarged theory, tests and applications to shear walls"; *Proc. of the British Ceramic Society*, No. 30.

[Mannoni, T.,1984]

Mannoni, T., 1984, "Metodi di datazione dell'edilizia storica", *Archeologia medioevale* XI.

[Manos, G C., 1995]

Manos, G C., Demosthenous, M., "Comparative Study of the Global Dynamic Behavior of Solid and Sliced Rigid Bodies", *Proceedings of the 10th European Conference on Earthquake, Engineering*; Duma, Gerald, ed. A A Balkema, Rotterdam, 1995, volume 2, pages 1087-1092.

[Marta, R.,1987]

Marta, R., 1987, *Tecnica costruttiva a Roma nel medioevo*, Edizioni Kappa, Rome.

[Marta, R.,1989]

Marta, R., 1989, *Tecnica costruttiva romana*, Edizioni Kappa, Rome.

[Mastrodicasa, S.,1960]

Mastrodicasa, S., 1960, *Dissesti statici delle strutture edilizie*, Ed. Hoepli, Milan.

[Milne, J.,1881]

Milne, J., 1881, "Experiments in observational seismology", *Trans. Seism. Soc., Japan* 3, 12-64.

[Moretti, M.,1984]

Moretti, M., 1984, *Chiese di Tuscania*, Istituto Geografico De Agostini, Novara.

[Muto, K.,1960]

Muto, K., Umemura, H., Sonobe, Y., 1960, Study on the overturning of slender structures, *Proceedings of the 2nd WCEE*, Tokyo/Kyoto, 1960:1239-1261.

[Muto, K.,1981]

Muto, K., Takase, H., Horikoshi, K., Ueno, H., 1981, 3-D non linear dynamic analysis of stacked blocks, *Proceedings of the 2nd Special Conf. on "Dynamic response of structures: experimentation, observation, prediction and control"*, Mech. div of ASCE, Atlanta, Georgia, 1981:917-930.

[Nizzi Grifi, L.,1981]

Nizzi Grifi, L., 1981, *Restauro statico dei monumenti. Diagnosi e consolidamento*, Florence.

[Ogawa, N.,1980]

Ogawa, N., 1980, A study on overturning vibration of rigid structures, *Proceedings of the 7th WCEE*, Istanbul, 1980:205-208.

[Oliveira-Costa, C.,1994]

Oliveira-Costa, C., Carvalhal, F.J., Duarte, R.T., 1994, The performance of an adaptive control system on shaking table testing of structure elements, *Proceedings of the 10th European Conf. on Earthquake Engineering*, Vienna, Austria, 1994.

[Page, A.,1978]

Page, A., 1978, "A Finite Element Model for Masonry", J. Struct. Div., ASCE, Vol. 104, No. ST8, pp.1267-1285.

[Page, A.,1981]

Page, A., 1981, "The biaxial compressive strength of brick masonry"; Proc. Instn. of Civ. Engrns, 71.

[Page, A.,1982]

Page, A., 1982, "An experimental investigation of the biaxial strength of brick masonry; Proc. of the 6th I.B.Ma.C. , Rome.

[Page, A.,1983]

Page, A., 1983, "The strength of brick masonry under biaxial tension-compression", Int. Journal of Masonry Construction, 3.

[Page, A.,1985]

Page, A., Kleeman, P., Dhanasekar, M., 1985, "An in-plane finite element model for brick masonry", in *New analysis techniques for structural masonry*, S. Anand, Ed. (ASCE, New York) pp. 1-18.

[Pan, X.D.,1991]

Pan, X.D., Reed, M.B., 1991, "A coupled distinct element-finite element method for large deformation analysis of rock masses", *Int. J. Rock Mech. Min. Sci. & Geomech. Abstr.* 28:1, 93-99.

- [Perry, J.,1881]
Perry, J., 1881, "Note on the rocking of a column", *Trans. Seism. Soc., Japan* 3, 103-106.
- [Plesha, 1987]
Plesha, M., "Constitutive Models for Rock Discontinuities with Dilatancy and Surface Degradation", *International Journal for Numerical and Analytical Methods in Geomechanics*, vol.11, 345-362, 1987.
- [Psycharis, I.N.,1983]
Psycharis, I.N., Jennings, P.C., 1983, "Rocking of slender rigid bodies allowed to uplift", *Earthqu. Eng. Struct. Dyn.* 11:1, 57-76.
- [Psycharis, I.N.,1990]
Psycharis, I.N., 1990, "Dynamic behaviour of rocking two-block assemblies", *Earthqu. Eng. Struct. Dyn.* 19, 555-575.
- [Psycharis, I.N.,1991]
Psycharis, I.N., 1991, "Dynamic behaviour of rocking structures allowed uplift" *Report EERL 81-02* (Earthquake Engineering Research Laboratory, California Institute of Technology, Pasadena, CA).
- [Raspi Serra, J.,1971]
Raspi Serra, J., 1971, *Tuscania - Cultura ed espressione di un centro medievale*, ERI Edizioni Rai, Rome.
- [Rice, J.R.,1983]
Rice, J.R., Ruina, A.L., 1983, "Stability of steady frictional slipping", *Journal of Applied Mechanics* 50, 343-349.
- [Rondelet, J.,1802]
Rondelet, J., 1802, *Traité théorique et pratique del l'art de batir*, Paris.
- [Ruina, A.L.,1985]
Ruina, A.L., 1985, "Constitutive relations for frictional slip", in *Mechanics of Geomaterials*, Z. Bazant, Ed. (John Wiley & Sons Ltd,) pp. 169-187.
- [Sepe, V.,1991]
Sepe, V., Sinopoli, A., 1991, La dinamica del trilitte: Modello generale e limiti di validità del modello ad un grado di libertà, *Proceedings of the V Convegno Nazionale, L'Ingegneria Sismica in Italia*, Palermo, 1991.
- [Sepe, V.,1992]
Sepe, V., "Comportamento dinamico di strutture costituite da blocchi rigidi sovrapposti: il trilitte", 1992, Doctoral Thesis, Università degli Studi, Florence.
- [Silvitrelli, G.,1940]
Silvitrelli, G., 1940, *Città, castelli e terre della regione romana*, Rome.

- [Sinclairian, G.E., 1999]
Sinclairian, Gabriela E.; Lemos, J. V. , *Seismic analysis of a stone masonry aqueduct using discrete elements*, Earthquake Engineering: Eighth Canadian Conference, Canadian Association for Earthquake Engineering, Vancouver, British Columbia, Canada, 1999, pages 131-136
- [Sinopoli, A.,1989]
Sinopoli, A., 1989, Analisi dinamica di colonne multiblocco, *Proceedings of the IV Convegno Nazionale, L'Ingegneria Sismica in Italia*, Milan, 1989.
- [Sinopoli, A.,1989]
Sinopoli, A., 1989, "Kinematic approach in the impact problem of rigid bodies", *Applied Mechanics Review*, ASME 42:11, Part 2.
- [Sinopoli, A.,1990]
Sinopoli, A., 1990, Modello analitico per la dinamica forzata di una colonna lapidea, *Proceedings of the X Congresso Nazionale AIMETA*, Pisa, 1990.
- [Sinopoli, A.,1990]
Sinopoli, A., 1990, Non linear dynamic analysis of multiblock structures, *Proceedings of the European Conference on Structural Dynamics Eurodyn'90*, 1990 (Bochum):127-134.
- [Sinopoli, A.,1991]
Sinopoli, A., 1991, "Dynamic analysis of a stone column excited by a sine wave ground motion", *Applied Mechanics Review*, ASME 44:10, Part 2.
- [Spanos, P.D.,1984]
Spanos, P.D., Koh, A., 1984, "Rocking of rigid blocks due to harmonizing shaking", *Journ. of Eng. Mech.*, ASCE 110:11, 1627-1643.
- [Tampone, G.,1977]
Tampone, G., 1977, "Aspetti formali nei dissesti sismici", in *Bolletino degli ingegneri*. (Florence), vol. 2/3.
- [Tassios, T.,1985]
Tassios, T., Mamillan, M., 1985, *Valutazione strutturale dei monumenti antichi*, Ed. Kappa, Rome.
- [Trovalusci, P.,1992]
Trovalusci, P., "Modelli matematici per la muratura a blocchi considerata come sistema dotato di struttura", 1992, Doctoral Thesis, Università degli studi, Florence.
- [Tso, W.K.,1989]
Tso, W.K., Wong, C.M., 1989, "Steady state rocking response of rigid blocks, Part 1: Analysis", *Earthqu. Eng. Struct. Dyn*, 18, 89-106.
- [Tso, W.K.,1989]
Tso, W.K., Wong, C.M., 1989, "Steady state rocking response of rigid blocks, Part 2: Experiment", *Earthqu. Eng. Struct. Dyn*, 18, 107-120.

[UDEEC,1996]

User Manual, Itasca Consulting Group, Inc., Minneapolis, Minnesota, USA, 1996.

[Vieira Pinto, A.,1987]

Vieira Pinto, A., Gil Saraiva, J.A., Duarte, R.T., 1987, Seismic tests on physical models, *Proceedings of the 9th Int. Conf. on Structural Mechanics in Reactor Technology*, Lausanne, Switzerland, 1987.

[Villaggio, P.,1979]

Villaggio, P., 1979, "An elastic theory of Coulomb friction", in *Archive for Rational Mechanics and Analysis*. (Springer-Verlag,), vol. 70, pp. 135-143.

[Williams, J.R.,1985]

Williams, J.R., Hocking, G., Mustoe, G.G.W., 1985, The theoretical basis of the discrete element methods, *Proceedings of the NUMETA Conference*, Swansea, 1985 (Balkema).

[Wilson, J.F., 1999]

Wilson, James F. , "Gross dynamic failure of toppling block structures", *Structural Engineering and Mechanics*, 8, 5, Nov. 1999, pages 491-504.

[Yim, C.S.,1980]

Yim, C.S., Chopra, A.K., Penzien, J., 1980, "Rocking response of rigid blocks to earthquakes", *Earthqu. Eng. Struct. Dyn.* 8:6, 565-587.